Radio-frequency fluxonium superconducting qubit for AC-charge sensing applications

Baldo Luis Najera Santos

SORBONNE UNIVERSITÉ

THÈSE DE DOCTORAT
DE SORBONNE UNIVERSITÉ

Spécialité : Physique

École doctorale nº564: Physique en Île-de-France

réalisée au Laboratoire Kastler Brossel

présentée par

Baldo Luis NAJERA SANTOS

Sujet de la thèse :

Radio-frequency fluxonium superconducting qubit for AC-charge sensing applications

soutenue le 31 5 2024

devant le jury composé de :

Nicolas	ROCH	Rapporteur
Johannes	FINK	Rapporteur
Agnès	MAÎTRE	Examinatrice
Audrey	BIENFAIT	Examinatrice
Antoine	HEIDMANN	Directeur de thèse
Thibaut	JACQMIN	Co-directeur de thèse
Samuel	DELÉGLISE	Co-directeur de thèse

Contents

Introduction

Context of this work

Probing quantum-gravity with electromechanical systems

The quest to reconcile Quantum Mechanics (QM) and General Relativity (GR) remains one of the grand challenges in contemporary physics. These foundational theories describe the universe at vastly different scales and under distinctly different conditions, yet a unified framework that incorporates both remains elusive. A particular stumbling block in this endeavor is the integration of GR's prediction of time dilation—where the flow of time is altered by the presence of mass—with the quantum mechanics paradigm. This integration is crucial, as GR-induced time dilation introduces ambiguities when massive objects are placed in quantum superpositions, conflicting with the defined temporal framework required by Schrödinger's equation [58].

There is no consensus at present regarding what effects will emerge when the phase shift due to time-dilation becomes experimentally relevant (see Figure 0.1a). However, several theoretical insights point towards a fundamental gravitational decoherence mechanism [38]. Such gravity-induced decoherence would bestow a purely mass-related origin to the quantum-to-classical boundary [27, 60]. In the model proposed by Penrose, a massive object placed in a quantum superposition $|\Psi\rangle = |\Psi_1\rangle + |\Psi_2\rangle$ would undergo a gravitational collapse over a time-scale $\tau_G = \hbar/\Delta E$, where ΔE is the gravitational self-energy of the quantum superposition [21, 44].

Experimental tests of such ideas are challenging because relativistic effects such as time-dilation are only significant for massive objects, whereas quantum effects on macroscopic systems tend to be blurred over very short time-scales due to environmental decoherence. The effects of relativistic time dilation become substantial only with massive objects; however, observing quantum phenomena in such objects is complicated by rapid environmental decoherence. In practice, two conditions need to be fulfilled to test these theories with massive quantum superpositions: 1. The spatial separation Δx between the states in the superposition needs to exceed the typical width of the mass distribution. 2. the standard decoherence time τ_{dec}—due to the unavoidable interactions with the environment—must occur on a slower timescale than the gravitational collapse itself.

Both conditions depend crucially on the mass distribution of the object, and there is much debate regarding what form this mass distribution should take for a macroscopic object [28, 44]. However, a plausible assumption is that the mass is distributed over a regular array of spheres, each of mass m_i, and radius r_{n} representing the nuclei of the considered material (see Figure 0.1b). In practice, an experimental test of gravitational decoherence

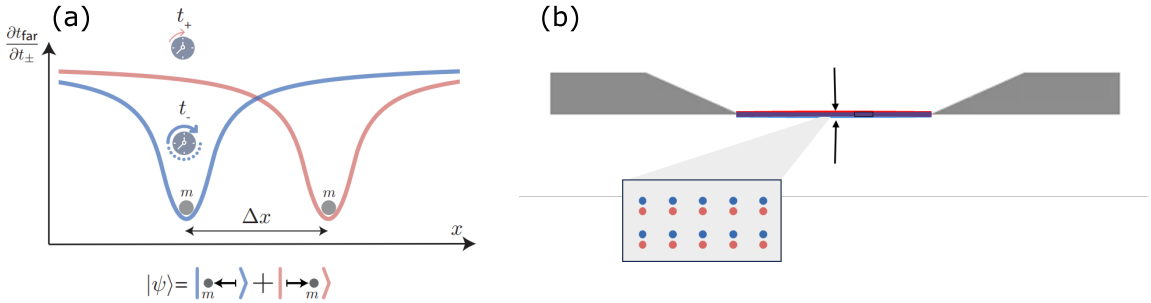

Fig. 0.1 *(a) Gedanken experiment: we consider a mass in a quantum superposition of being displaced in two opposite directions. The rate of evolution of the proper time $t_\pm$ with respect to the proper time $t_{\rm far}$ of a reference location far away is represented in blue (red) for the left (right) position of the mass. There is an ambiguity, quantified by $t_+ - t_-$ in the definition of local time close to the locations of each parts of the superposition. (b) Exprimental test with a mechanical oscillator: a mechanical resonator in a Schrödinger-cat state can be seen as an assembly of N nucleis placed in a quantum superposition similar to (a). Figure adapted from ref. [35].*

requires to prepare a massive object in a quantum superposition, where the spatial extent Δx of the wavefunction exceeds the typical width $2r_{\rm n}$ of the mass distribution. Under this assumption, the gravitational self-energy of each nucleus is given in good approximation by $\Delta E = 48\pi G m_i^2/5r_{\rm n}$ [44], leading to a *total* gravitational decoherence time:

$$\tau_G \approx \frac{5\hbar r_{\rm n}}{48\pi G m m_i} = \frac{1}{m} \cdot 3. \times 10^{-15}\,\text{kg.s}, \tag{0.1}$$

where m is the total mass of the object, G the gravitational constant, and the atomic mass $m_i = 4.6 \times 10^{-26}$ kg and nuclear radius $r_{\rm n} = 2.7$ fm of silicon ($A = 28, Z = 14$) have been taken for the numerical calculation.

Circuit Quantum Acousto Dynamics (cQAD) is a powerful experimental framework, where the quantum state of a mechanical system is probed and manipulated thanks to its nearly resonant coupling to a superconducting qubit [9, 23, 59, 67]. Recently, this framework has been used to prepare a 16 μg piezo-mechanical resonator in a Schrödinger-cat state [10] $|\Psi^+_{\rm cat}\rangle = (|\alpha\rangle + |-\alpha\rangle)/\mathcal{N}$, where $|\alpha\rangle$ is a coherent state of complex amplitude α and $\mathcal{N}$ is a normalization factor with $\mathcal{N} \simeq 1/\sqrt{2}$ for $|\alpha| \gg 1$. In this state, the spatial separation between the classical components $|\alpha\rangle$ and $|-\alpha\rangle$ is given by $\Delta x = 2|\alpha| x_{\rm zpf}$, with $x_{\rm zpf}$ the zero-point fluctuations of the mechanical system. This parameter describing the width of the ground state wavefunction $x_{\rm zpf} = \sqrt{\hbar/2m\Omega_m}$ plays a crucial role, as this is the natural length-scale of low-energy quantum states. For instance, in the Zürich experiment, the large mass (16 µg) combined with large mechanical frequency ($\Omega_m/2\pi \sim 6$ GHz) results in a small value of $x_{\rm zpf} \sim 3 \cdot 10^{-19}$ m. Consequently, the extent of the quantum superposition, was only $\Delta x \sim 10^{-18}$ m, approximately 4 orders of magnitude short of condition (1). In other words, achieving a spatial separation of $\Delta x \geq 2r_{\rm n}$ with such a device would require to prepare a Schrödinger-cat state with $|\alpha|^2 \gtrsim 10^8$ phonons. Even if successfully prepared, such a highly excited quantum state would suffer very fast environmental decoherence masking a possible

gravitational collapse.

In order to estimate the potential of various systems to observe quantum gravitational effects, we compare the gravitational decoherence time predicted by eq. 0.2 to the thermal decoherence time [35, 41] in a pure quantum state satisfying $\Delta x > 2r_{\mathrm{n}}$

$$\tau_{\mathrm{dec}} = \frac{1}{\Gamma_m} \frac{1}{(n+1)n_{\mathrm{th}} + n(n_{\mathrm{th}}+1)}. \tag{0.2}$$

The previous formula is the exact expression for the lifetime of the Fock state $|n\rangle$ in the presence of a thermal environment of occupation n_{th}, and constitutes a good approximation for the decoherence time of the quantum superposition $|\Psi_{\mathrm{cat}^+}\rangle$ [25]. The main mechanical parameters for various cQAD systems are summarized in Figure 0.2. The two last columns of the table correspond to the parameters τ_{dec}, as calculated for a quantum superposition with a 5-fm spatial separation using formula (0.2) and the Penrose gravitational decoherence time predicted by Formula (0.1). This table confirms what was illustrated in the previous example: only the low-frequency ($\lesssim$ MHz) mechanical resonators, which feature a zero-point fluctuation sizeable with the nuclear radius, stand a chance to reach condition (1) with a reasonable-sized quantum superposition. Furthermore, as highlighted in red, one type of mechanical resonator already combines all the characteristics to fulfill condition (2). These are so-called softly-clamped membranes [74]: highly stressed, ultra-thin silicon-nitride membranes, with a phononic crystal directly patterned on the suspended film. Owing to a phenomenon known as dissipation dilution, the quality factor of such mechanical resonators can reach extremely high values (up to 10^9) at cryogenic temperature, bringing their thermal decoherence time in the 100 ms range. The group at LKB where I have conducted this thesis has already demonstrated the design and fabrication of such softly-clamped mechanical resonators [43] and the long-term objective of the group is to perform an experimental test of quantum-gravitational collapse with such a mechanical system.

Interfacing low-frequency mechanical systems with superconducting qubits

State-of-the art Numerous experimental works have strived to extend the quantum control achieved with GHz cQAD systems towards low-frequency mechanical resonators. Here, the main difficulty stems from the large frequency imbalance between the mechanical resonator and the superconducting qubit, typically operating at GHz frequency. For instance, the group of Gary Steele in Delft has proposed to interface indirectly a low-frequency mechanical resonator to a transmon qubit via an electromagnetic resonator operating in the RF frequency range, as recently demonstrated with a 200 MHz electromagnetic cavity [34]. Pioneering works in the group of Konrad Lehnert have also demonstrated that the phononic excitations of a 20-MHz DC-biased aluminium-drum capacitor could be detected thanks to its dispersive coupling to a Cooper-pair box at 4.6 GHz [51, 77]. This work was the first to demonstrate a direct interface between a superconducting qubit and a MHz mechanical resonator. In this experiment, the ubiquitous transmon was replaced with a Cooper-pair box (CPB), a strongly anharmonic qubit behaving as a quasi-ideal two-level system, even in the regime $\Omega_m \ll \omega_q$. Unfortunately, the sensitivity of the CPB to low-frequency environmental charge noise is also its Achilles' heel. In the previous example, the $\sim$ 40 ns CPB coherence time was insufficient to perform coherent manipulation of the mechanical system.

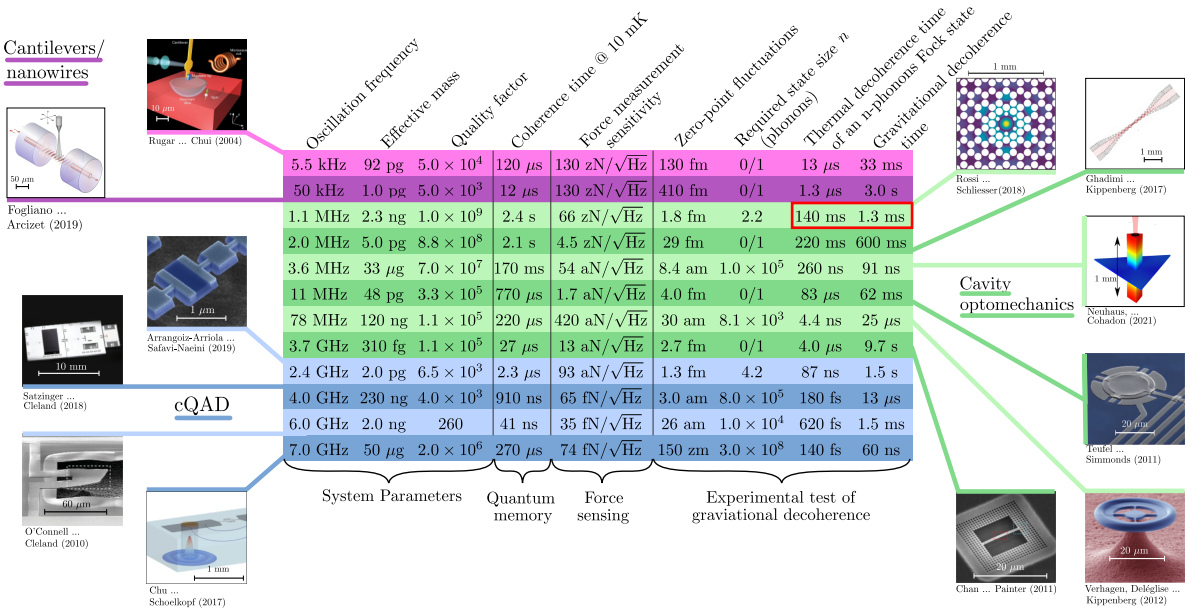

Fig. 0.2 *Comparison between various mechanical systems for quantum memory, sensing, and quantum gravity applications. The force sensitivity is calculated using the formula* $F_{\text{min}} = \sqrt{\hbar m \Omega_m^2 (2n_{\text{th}} + 1)/Q}$ *(see ref. [70]). The state size required for quantum gravity experiments is* $n = (2.7\,\text{fm}/\text{x}_{\text{zpf}})^2$*. The corresponding thermal, and gravitational decoherence times are extracted from* (0.2) *and* (0.1) *respectively. For mechanical systems where small cat states* $n < 1$*, or even the ground state are sufficient to observe quantum gravitational effects, we write* $n = 0/1$ *and calculate the decoherence time in state* $|1\rangle$*. The performances of the system envisioned in this proposal are framed in red (see text for details). Images and system parameters are extracted from the following references: Rugar et al. [66], Fogliano et al. [32], Rossi et al. [65], Ghadimi et al. [37], Neuhaus et al. [56], Teufel et al. [73], Verhagen et al. [75], Chan et al. [20], Arrangoiz et al. [6], Satzinger et al. [67], O'Connell et al. [59], Chu et al. [22]. Figure adapted from ref. [35].*

The fluxonium qubit The group at LKB is pursuing a new approach where the mechanical system would be coupled to a radically different qubit architecture enabling direct resonant strong coupling: the fluxonium qubit. This circuit developed in the group of Michel Devoret at Yale in 2009 [52] is composed of a Josephson junction (JJ) (Josephson energy E_J, capacitive energy E_c) shunted by an extremely large inductance (inductive energy E_L), fulfilling the high-impedance condition $E_L < E_c$. In this configuration, the two conjugate circuit variables—the superconducting phase $\hat{\varphi}$ and the charge $\hat{N}$ across the junction—play a role analogous to the position and momentum of a particle moving in a potential that is the sum of the sinusoidal Josephson energy $-E_J \cos(\hat{\varphi})$ and the parabolic inductive energy $E_L(\hat{\varphi} - \varphi_{\text{ext}})^2$, with φ_{ext} the magnetic flux threading the superconducting loop. In this physical picture, the capacitive energy $4E_c(\hat{N} - n_g)^2$ plays a role analogous to a kinetic energy. Here, n_g is the offset charge due to the capacitive coupling of the circuit to an external potential.

Very recently, several experimental groups have explored an unprecedented parameter

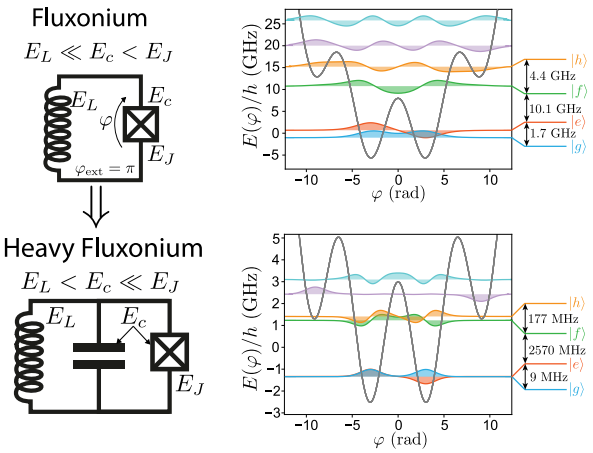

Fig. 0.3 *Circuit diagrams (left): in the heavy fluxonium, a large capacitance supplements the intrinsic junction capacitance. Energy-levels and flux wavefunctions (right) calculated at* $\varphi_{\text{ext}}/2\pi = 0.5$. *Fluxonium parameters (in GHz):* $E_L/h = 0.5$, $E_C/h = 5$, $E_J/h = 8$, *heavy fluxonium parameters:* $E_L/h = 0.1$, $E_C/h = 0.4$, $E_J/h = 3$.

regime, coined the "heavy fluxonium" [30]. In this regime, identified by $E_c \ll E_J$, each potential well contains several bound states (see Fig. 0.3). The singularity of the heavy fluxonium is most apparent at the flux-frustration point $\varphi_{\text{ext}}/2\pi = 0.5$, where the phase $\hat{\varphi}$ is subjected to a degenerate double-well potential. At this point, the two lowest energy eigenstates $|g\rangle$ and $|e\rangle$ are the symmetric and anti-symmetric superpositions of the left- and right-well eigenstates (or fluxons, hence the name fluxonium). The energy difference between $|g\rangle$ and $|e\rangle$ being given by the tunneling rate through the central barrier, it is exponentially reduced as a function of $\frac{E_J}{E_C}$ in the heavy fluxonium regime. At this bias point, where the qubit frequency is insensitive to first-order to changes in flux, a coherence time > 250 μs, with a qubit frequency as low as $\omega_q/2\pi = 15$ MHz has recently been demonstrated [81].

The mecaflux project The Mecaflux project, as illustrated in Figure 0.4, focuses on probing and manipulating the quantum state of a mechanical oscillator by interfacing it resonantly with a superconducting fluxonium qubit. The heavy-fluxonium, located on the bottom chip, is composed of an individual Josephson junction (energy E_J), shunted by a large capacitor (energy E_C) and a super-inductor in parallel (inductive energy E_L). Furthermore, the fluxonium electrode is capacitively coupled via a moving gap capacitor $C(x)$ to a nearby electrode maintained at a DC-voltage V_g. In this configuration, the motion $\hat{x}$ is transduced into a charge modulation $\hat{N}_g = \frac{V_g}{2e}\frac{\partial C}{\partial x}\hat{x}$ on the fluxonium electrode.

The membrane/fluxonium interaction is thus described by a motion-dependent offset charge:

$$\hat{H} = 4E_c(\hat{N} - \hat{N}_g(t))^2 - E_J\cos(\hat{\varphi} - \varphi_{\text{ext}}) + \frac{E_L}{2}\hat{\varphi}^2 + \hbar\Omega_m\hat{b}^\dagger\hat{b}. \tag{0.3}$$

In this expression, $\hat{N}_g(t) = N_{\text{zpf}}(\hat{b}+\hat{b}^\dagger)$ represents the offset-charge induced by the mechanical motion, where $\hat{b}$ is the annihilation operator for phonons in the mechanical mode, and $N_{\text{zpf}} = \frac{V_g}{2e}\frac{\partial C}{\partial x}x_{\text{zpf}}$ stands for the "zero-point charge fluctuations" (in units of Cooper pairs) that

are induced by the electromechanical system on the fluxonium electrode as a result of the mechanical zero-point fluctuations. With realistic experimental conditions, this parameter remains exceedingly small, with an estimated value of $N_{\mathrm{zpf}} \sim 10^{-2}$.

Interestingly, this experiment highlights a somewhat paradoxical aspect of fluxonium-based systems: while the fluxonium is inherently immune—or insensitive—to a static (DC) charge offset, the focus here is to detect exceedingly small, mechanically induced charge modulations at the MHz frequency of the mechanical system. This is made possible by the peculiar frequency response of the circuit inductive shunt, which filters efficiently the environmental noise at audio frequency while being maximally sensitive at the resonant qubit frequency in the MHz range.

Objectives of this work

This PhD work is mainly centered on the qubit side of the experiment, and in particular, it aims at demonstrating the following pre-requisites:

1. Low-operational frequency: the goal is to demonstrate the feasibility of a superconducting qubit resonant at –or below– the mechanical resonance frequency of a softly-clamped membrane ($\sim$ 5 MHz).

2. Demonstrating the possibility to drive the qubit transitions directly with a nearly-resonant AC charge-offset.

3. Ensuring sufficient charge sensitivity to detect the tiny charge modulation induced by the mechanical motion in the final experiment.

This PhD project necessitated the implementation of a number of techniques that were new to the host laboratory (Josephson junction fabrication and characterization, simulation of complex circuit QED devices, pulsed microwave experiments and cryogenic quantum measurements). This manuscript is structured to provide a comprehensive examination of each aspect involved in the development of heavy-fluxonium qubits and their application in sensing protocols. Chapters 1 and 2 review essential theoretical concepts on circuit Quantum ElectroDynamics (cQED), and Fluxonium qubits respectively. Chapter 3 and 4 cover various design and experimental techniques that are pivotal for our experiments. In chapters 5 and 6, we present the experimental characterization of the circuit at cryogenic temperature. In particular, chapter 5 focuses on the GHz transitions to from the low-energy qubit manifold to higher excited states that are pivotal for the readout and manipulation of the qubit manifold, as demonstrated in chapter 6. Finally, in chapter 7, we demonstrate the exquisite charge sensitivity of the heavy-fluxonium qubit to a nearly resonant MHz charge modulation.

Summary of the main results

1 A record-low frequency superconducting qubit (1.8 MHz)

The main focus of this work is to push the operational boundaries of superconducting qubits towards the low-frequency spectrum. Whereas typical circuit Quantum Electrodynamics (cQED) systems operate in the 5-10 GHz range, extending their operation into the radio-frequency domain introduces distinct challenges: Firstly, adapting readout techniques to

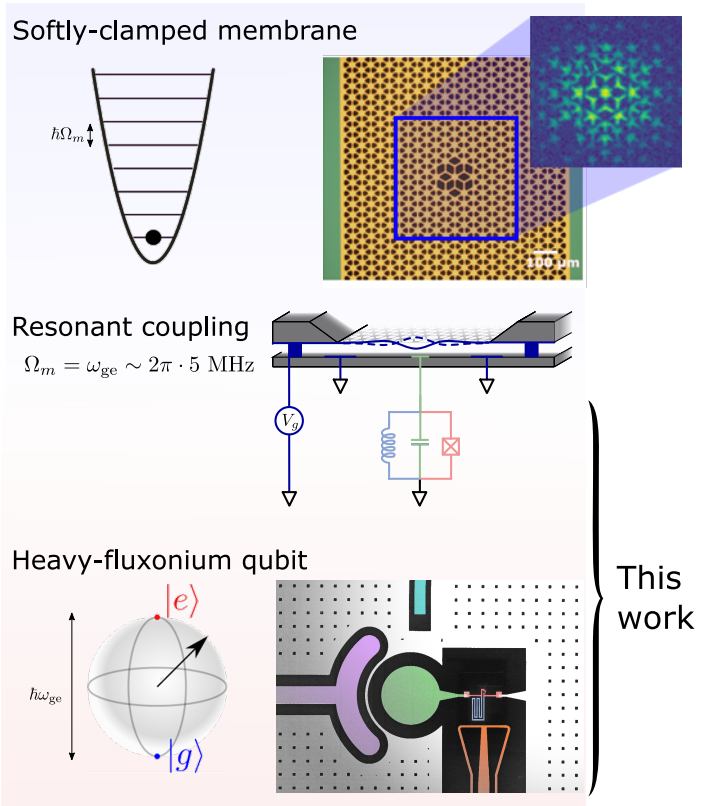

Fig. 0.4 *Concept of the mecaflux project. The mechanical oscillator developed in the LKB group (top) consists of a suspended silicon-nitride film (orange) suspended above a silicon substrate (green). A 5 MHz out-of-plane vibrational mode is confined close to a phononic-crystal defect directly etched in the membrane (the inset shows the color-coded displacement profile). The quantum state of this mechanical oscillator is probed and manipulated thanks to its coupling to a resonant heavy-fluxonium qubit (bottom). In order to couple the two systems, a metalized membrane is integrated as one electrode of a vacuum gap capacitor (middle). By applying a voltage bias across this capacitor, the motion of the membrane translates into a charge modulation. I have developed and optimized the qubit component of this setup, ensuring it operates at sufficiently low frequencies and possesses the requisite charge sensitivity to detect the motion of the membrane.*

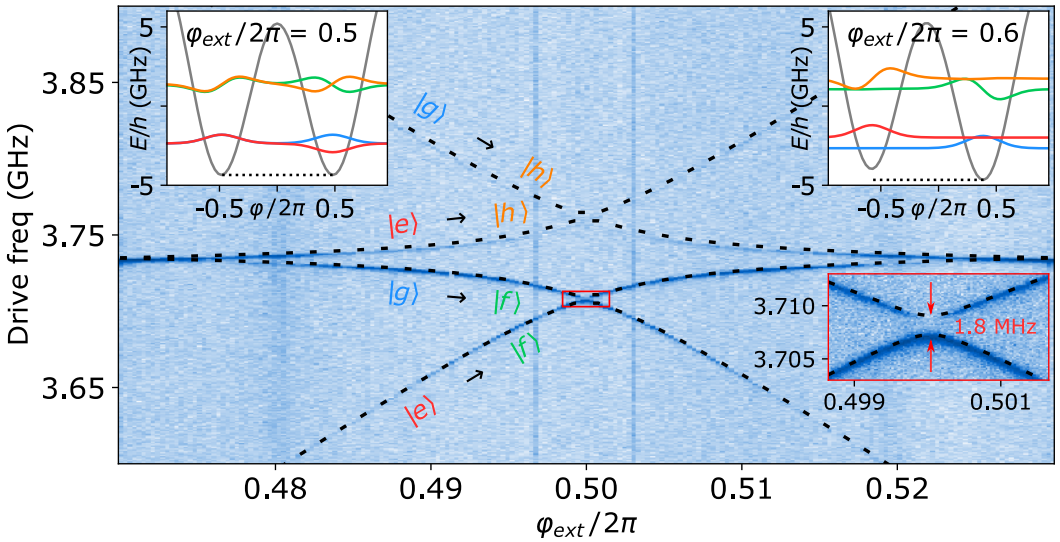

Fig. 0.5 *Two tone spectrum of the microwave transitions of a heavy fluxonium centered on the flux frustration point* $\varphi_{\text{ext}}/2\pi = 0.5$. *The various qubit transitions are well explained by a 3 parameters model with* $E_J/h = 5.178$ *GHz,* $E_C/h = 0.4144$ *GHz, and* $E_L/h = 0.18$ *GHz. The magnitude of the avoided-crossing near the flux frustration point (inset) corresponds to the low-frequency qubit transition of 1.8 MHz*

.

lower frequencies is non-trivial. Traditional cQED setups rely on the dispersive shift imparted to a nearby superconducting resonator for qubit state readout. At lower frequencies, this dispersive shift diminishes significantly when the cavity detuning exceeds the qubit anharmonicity. In such cases, maintaining resonant conditions for the resonators would require impractically large physical dimensions—for example, achieving resonance at 1 MHz would necessitate a coplanar cavity approximately 100 meters long. Secondly, systems operating below $k_{\text{B}}T/\hbar$ (where T denotes the environmental temperature) face severe thermal noise issues. At these frequencies, the qubit is effectively coupled to a hot thermal bath, stimulating random photon exchanges that can rapidly degrade quantum states into statistical mixtures.

Thankfully, owing to its highly non-linear spectrum–the transition to the second excited state lies 3-orders of magnitude above the qubit transition, the fluxonium can be manipulated and readout using standard microwave techniques. These technics are reminiscent to optical manipulations of spin degrees-of-freedom in atomic systems. In this work, we have achieved a significant milestone by realizing a heavy-fluxonium with a qubit transition frequency as low as 1.8 MHz [55], marking an unprecedented achievement for superconducting qubits, as highlighted in Figure 0.5. The manipulation and characterization of this low-frequency qubit are extensively detailed across several chapters.

In Chapter 5, we describe the successful implementation of a single-shot projective measurement of the qubit state. This is accomplished by selectively addressing a specific transition to a higher excited state of the circuit, followed by a conventional circuitQED readout process. Prior to these manipulations, as detailed in Chapter 6, we implemented a side-

band cooling protocol which effectively reduced the qubit's effective temperature, achieving a final ground state population of 97.7 % and corresponding to an effective temperature of 23 μK. This protocol was critical in preparing the qubit system in a low-entropy state for high-fidelity operations. Moreover, we demonstrated the direct manipulation of the qubit's degrees of freedom, showcasing its robustness with coherence times of T_1 = 34 µs and T_2 = 39 µs. These results confirm that, despite the qubit's operation within a "hot" thermal environment, it retains sufficient coherence to permit effective manipulation and readout.

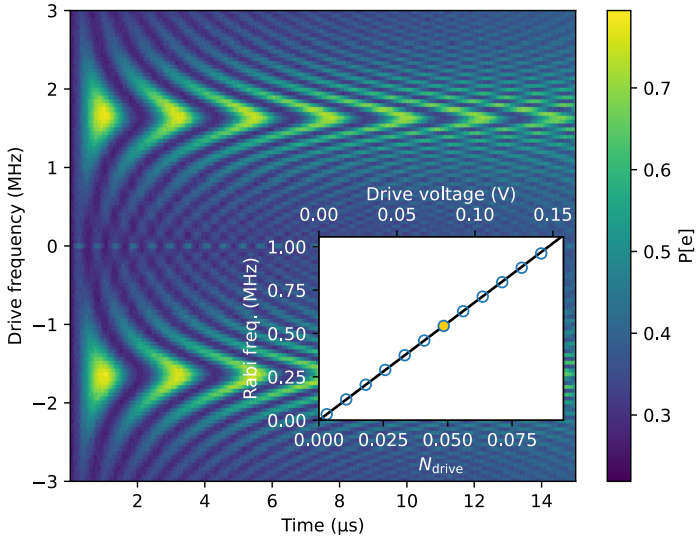

Fig. 0.6 *Direct Rabi manipulation of the radio frequency qubit transition. after initial preparation in* $|g\rangle$*, the qubit is driven via a charge port with a MHz pulse of variable duration and frequency. The colorscale indicates the final qubit population. The negative frequency part of the graph is here to highlight the validity range of the rotating-wave approximation. The inset shows the Rabi frequency for a resonant drive at 1.8 MHz, as a function of the drive voltage amplitude (upper horizontal axis) and in units of Cooper-pairs on the fluxonium electrode (lower horizontal axis). The yellow dot is obtained for the parameters of the main figure. The negative-frequency half is just a reflection of the positive-frequency half, it was added for visualization porpuses only.*

2 Ultra-sensitive nearly resonant charge sensing

In chapter 7, we demonstrate direct Rabi oscillations by driving the MHz fluxonium qubit close to resonance via a capacitively coupled waveguide (see Fig. 0.6). This experiment can be seen as a simplified version of the Mecaflux setup, where the mechanical charge modulation is replaced by the classical drive through this port. By relating the voltage amplitude on the digital-to-analog converter and the equivalent number of Cooper pairs on the fluxonium electrode, we extract a single-shot charge sensitivity of $N_{\min} \sim 5 \times 10^{-3}$ cooper pairs. This is the smallest charge modulation required to observe coherent Rabi

flipping. This highlights the capability of the fluxonium qubit to respond to less than 1 % of a Cooper pair, reflecting its exceptional ac-charge sensitivity. Specifically, this sensitivity aligns with the charge fluctuations N_{zpf} expected from mechanical zero-point fluctuations, suggesting that achieving strong coupling in the Mecaflux project is a feasible target.

This value corresponds to a single-shot charge sensitivity of 10^{-2} e. In order to compare our qubit-based sensor to other more conventional charge sensors, we have implemented a quantum sensing protocol, similar to those routinely used in nitrogen-vacancy center magnetometry [14] and similar methodologies [62]. Via the application of a cyclic qubit preparation and interrogation sequence, we are able to accumulate statistical data on the weak modulation signal (see Figure 0.7). This enables us to report a sensitivity of δq =33 $\mu\mathrm{e}/\sqrt{\mathrm{Hz}}$, indicating that our quantum sensor can detect charge modulations as low as 33 millionths of an elementary charge over a 1-second integration period.

This sensitivity rivals that of the most advanced transport-based devices [1, 4, 12, 16, 19, 39, 46, 50, 68, 76, 78], while maintaining intrinsic insensitivity to dc-charge noise. Furthermore, the capacitance $C \sim 50$ fF of the fluxonium electrode exceeds the typical gate capacitance of single-electron transistors (SETs) [1, 68] by approximately 2 orders of magnitude, resulting in a record-low energy sensitivity $\delta q^2/2C \sim 2.8\hbar$. This metric can be regarded as more fundamental than the bare charge sensitivity, which gets diluted when the self-capacitance of the probed system exceeds that of the sensor in a real-world charge-sensing scenario. Beyond the application of this work within the Mecaflux project, the high charge sensitivity combined with large capacitive shunt unlocks new avenues for exploring quantum phenomena in the 1–10 MHz, for instance in spin sensing protocols.

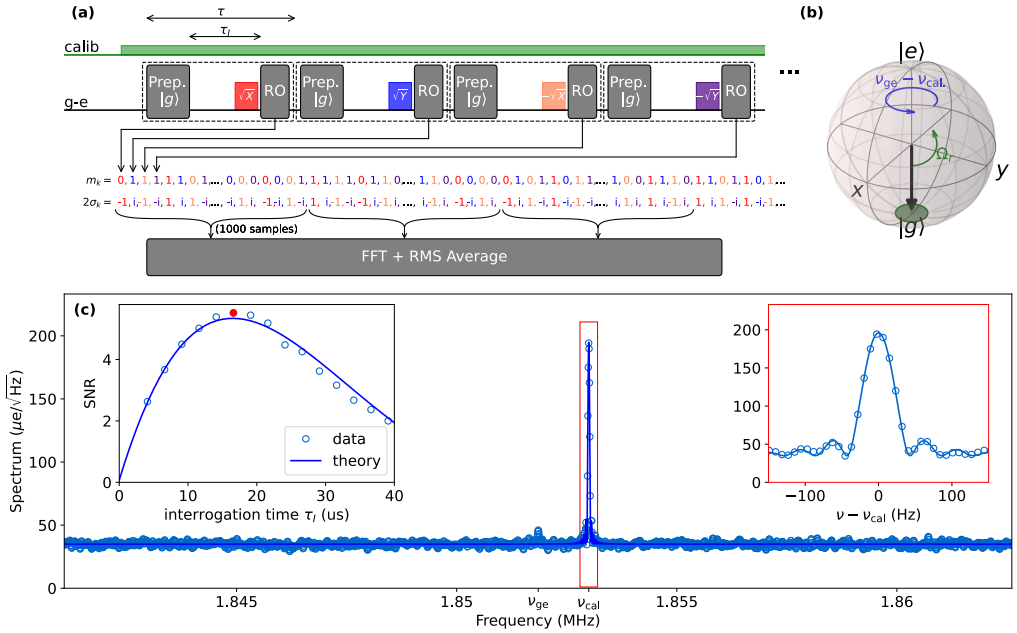

Fig. 0.7 *AC-charge sensing. (a) A weak monochromatic charge-drive (also referred to as calibration tone) is detected thanks to a repeated pulse sequence: the qubit is prepared in* $|\mathrm{g}\rangle$ *(black arrow in the Bloch sphere (b)). After interacting for a time* τ_I *with the tone, a partial information on the qubit state is obtained by performing a* $\pi/2$ *pulse in one of the 4 directions* $+X, +Y, -X, -Y$*, followed by a qubit state readout in the eg basis. From the measurement samples* $m_k \in \{0, 1\}$*, a complex telegraphic signal* $\sigma_k = i^k(m_k - 1/2)$ *is constructed. The noise spectrum centered around the qubit frequency is estimated by the Bartlett's-method, with periodograms of 1000 non-overlapping consecutive samples. (c) The estimated noise spectrum presents a residual-bandwidth-limited peak at the calibration tone frequency* $\nu_{\mathrm{cal}} = 1.853$ *MHz. Red inset: zoom on the calibration peak and sinus-cardinal fit (solid line). Left and right insets: signal-to-noise-ratio (SNR) for the calibration peak as a function of interrogation time* τ_I *and calibration peak amplitude respectively. The red dots in the insets correspond to the parameters used in the main graph of panel (c). The solid lines are the results of an analytic model taking into account the evolution of the qubit during the interrogation time. Signal cancellation occurs when the calibration tone amplitude is a multiple of that of a pi-pulse. The spectrum in (c) is calibrated using the known variance of the calibration tone.*

Chapter 1

Superconducting circuits fundamentals

Introduction

The goal of the following section is to give a short introduction to the superconducting circuits platform and the theoretical and experimental techniques which describe the most simple experiments in circuit QED. We will discuss the basic building blocks which are microwave cavities (harmonic oscillators), the heavily used Transmon qubit (anharmonic oscillators) and the procedure with which we can control the states of qubits (Rabi oscillations) as well as measure the state of the qubit (dispersive readout). Each of these topics will only be convered briefly, a very thorough treatment of some of the theory can be found in (Girvin les Houches 2011) [43] and (Blais et al. CQED) [44].

1.1 The quantum LC harmonic oscillator

This section explains the basic concepts and the elementary physical description of the superconducting circuits by considering the simplest kind of circuit, the quantum harmonic oscillator. We start wit the minimalist but useful description of the circuit in terms of lumped elements. Then, we consider the degrees of freedom of the circuit and the classical approach to the circuit dynamics. We finalize the section with the quantization of the circuit. This is nothing but the quantum-mechanical description of the circuit, which turns around two core properties: The energy spectrum of the circuit and quantum fluctuations of the circuit variables.

1.1.1 Flux variable in electrical circuits

The most elementary version of an electrical harmonic oscillator is a lumped-element LC-resonator. This circuit consists of an inductance L and a capacitance C in parallel connection. The LC-resonator has a single degree of freedom: either the voltage drop V between the two electrodes of the capacitor or the current I flowing through the inductor. However, when it comes to superconducting circuits, we prefer a description in terms of either accumulated

charge Q at the capacitor electrodes or the flux ϕ threading the inductor. The flux ϕ is defined as the time-integral of the voltage V

$$\phi =: \int_{-\infty}^{t} dt' \, V(t') \, . \tag{1.1}$$

This equation means that the voltage V is the derivative of the flux with respect to time, $\dot{\phi} = V$. For example, in the case of a solenoid, the flux ϕ coincides with the external flux ϕ_{ext} of the magnetic field $\vec{B}$ threading the wire-loop of the solenoid:

$$\phi_{\text{ext}} =: \int_{\Omega} d\vec{\sigma} \cdot \vec{B}(\vec{r}) \tag{1.2}$$

On the one hand, the voltage drop V across the capacitor electrodes is related to the accumulated charge at electrodes Q as:

$$Q = C \, V = C \, \dot{\phi} \tag{1.3}$$

On the other hand, the flux ϕ threading through the inductor is related to the circulating current I as:

$$\phi = L \, I = L \, \dot{Q} \tag{1.4}$$

The stored energy in a lumped-element is calculated as:

$$U \equiv \int_{-\infty}^{t} dt' \, V(t') I(t') \, . \tag{1.5}$$

Thus, the energy stored in the capacitor is

$$U_C = \frac{Q^2}{2C} = \frac{C\dot{\phi}^2}{2} \tag{1.6}$$

Moreover, the energy stored in the inductor is

$$U_L = \frac{\phi^2}{2L} = \frac{L\dot{Q}^2}{2} \tag{1.7}$$

As we will see in the following, the circuit description in terms of charge Q or flux ϕ is equivalent.

1.1.2 Classical dynamics of the LC-resonator

This section is about the classical dynamics of the LC-resonator, which is governed by its Lagrangian $\mathscr{L}$. The Lagrangian $\mathscr{L}$ contains the kinetic energy $\mathrm{T}(\dot{x})$ minus the potential energy $\mathrm{V}(x)$ of the circuit, where "x" represents either the flux ϕ or the charge Q. For instance, the Lagrangian of the LC-resonator in terms of flux ϕ reads:

$$\mathscr{L}_{\phi} = \frac{C\dot{\phi}^2}{2} - \frac{\phi^2}{2L} \tag{1.8}$$

Notice that the conjugated variable of the flux ϕ is nothing but the charge Q,

$$\partial_{\dot{\phi}} \mathscr{L} = C\dot{\phi} = Q \tag{1.9}$$

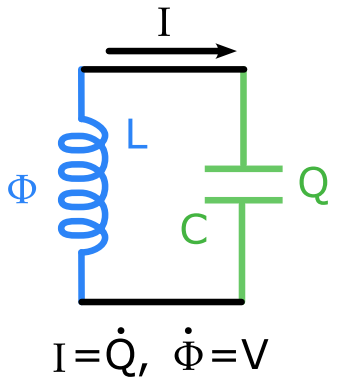

Fig. 1.1 ***Lumped-element LC-resonator:*** .

Similarly, the Lagrangian of the LC-resonator in terms of charge Q reads:

$$\mathscr{L}_{\mathrm{Q}} = \frac{L\dot{Q}^2}{2} - \frac{Q^2}{2C}. \tag{1.10}$$

The conjugated variable of the charge Q is nothing but the flux ϕ,

$$\partial_{\dot{Q}}\mathscr{L} = L\dot{Q} = \phi \tag{1.11}$$

The description of the LC-resonator in terms of flux ϕ or charge Q is thus equivalent. By using the Euler-Lagrange equation, we obtain the equation ruling the time evolution of the flux ϕ:

$$\frac{d}{dt}\partial_{\dot{\phi}}\mathscr{L}_{\phi} - \partial_{\phi}\mathscr{L}_{\phi} = 0 \quad \rightarrow \quad C\,\ddot{\phi} + \frac{\phi}{L} = 0 \tag{1.12}$$

The solution of this equation is then:

$$\phi(t) = \phi_{\max}\,\cos(\omega_0\,t + \theta) \tag{1.13}$$

This means that the flux ϕ threading the inductor oscillates at an angular frequency ω_0,

$$\omega_0 \equiv \frac{1}{\sqrt{L\,C}}. \tag{1.14}$$

The accumulated charge Q on the capacitor electrodes (Eq. 1.3) is then:

$$Q(t) = C\,\dot{\phi}(t) = -\frac{\phi_{\max}}{Z_0}\,\sin(\omega_0\,t + \theta), \tag{1.15}$$

where Z_0 is the resonator impedance,

$$Z_0 \equiv \sqrt{\frac{L}{C}}. \tag{1.16}$$

Notice that the flux ϕ in the inductor and the charge Q in the capacitor oscillate in quadrature. The energy stored in the inductance $U_L(t)$ and the energy stored in the capacitance $U_C(t)$ as functions of time are:

$$U_L(t) = \frac{\phi_{\max}^2}{2L}\,\cos(\omega_0\,t + \theta)^2 \;, \quad U_C(t) = \frac{\phi_{\max}^2}{2C\,Z_0^2}\,\sin(\omega_0\,t + \theta)^2. \tag{1.17}$$

Thus, the total energy stored in the LC-resonator is a constant of motion:

$$E = \frac{Q(t)^2}{2C} + \frac{\phi(t)^2}{2L} = \frac{\phi_{\max}^2}{2L}. \tag{1.18}$$

Eq. 1.13, 1.15 and 1.18 correspond to the intuitive picture of the harmonic oscillator where the energy flows back and forth between the inductor and the capacitor but the total energy is conserved. The initial flux, at time $t = 0$, is $\phi(0) = \phi_{\max}\cos(\theta)$, while the initial charge is $Q(0) = -\frac{\phi_{\max}}{Z_0}\sin(\theta)$. Therefore, the flux $\phi(t)$ and the charge $Q(t)$ as functions of time (Eqs. 1.13 and 1.15) can be written as:

$$\begin{aligned} \phi(t) &= \phi(0)\,\cos(\omega_0\,t) + Z_0\,Q(0)\,\sin(\omega_0\,t), \\ Q(t) &= -\frac{\phi(0)}{Z_0}\,\sin(\omega_0\,t) + Q(0)\,\cos(\omega_0\,t). \end{aligned} \tag{1.19}$$

These two equations together describe an elliptical trajectory $(\phi(t),\, Q(t))$ in phase space, the space given by the pairs $(\phi,\, Q)$, such that the energy E of the LC-resonator is conserved and it is given by:

$$E = \frac{\phi(0)^2}{2L} + \frac{Q(0)^2}{2C}. \tag{1.20}$$

Only the initial conditions $\phi(0)$ and $Q(0)$ are needed to determine the time evolution of the LC-resonator.

1.1.3 Quantum-mechanical description of the LC-resonator

In this section, we consider the quantum mechanical description of the LC-resonator. The main difference of the quantum-mechanical theory with respect to the classical theory is that the energy E of the LC-resonator can't take arbitrary values but it is quantized in units of $\hbar\omega_0$, where $\hbar$ is the Planck's constant and ω_0 is the resonance frequency of the LC-resonator (Eq. 1.14).

We start by obtaining the classical Hamiltonian of the LC-resonator from its Lagrangian $\mathscr{L}$ (Eq. 1.8) via the Legendre transform, $\mathscr{H} = Q\dot{\phi} - \mathscr{L}$,

$$\mathscr{H} = \frac{\phi^2}{2L} + \frac{Q^2}{2C} \tag{1.21}$$

Firstly, notice that the Hamiltonian just has the sign of the potential energy inverted with respect to the Lagrangian (Eq. 1.8), such that the Hamiltonian is just the total energy of the LC-resonator. Secondly, notice that describing the LC-resonator in terms of flux or charge leads to the same Hamiltonian. We obtain the quantum Hamiltonian of the LC-resonator H via the canonical quantization, where the conjugated variables ϕ and Q are replaced by conjugated operators $\hat{\phi}$ and $\hat{Q}$[1], such that, the canonical commutation relation between the operators is:

$$\left[\hat{\phi},\, \hat{Q}\right] = \hat{\phi}\,\hat{Q} - \hat{Q}\,\hat{\phi} \equiv i\hbar \tag{1.22}$$

[1]For the sake of simplicity, we will drop the hat of the operators in the following sections, but the reader must be aware that an operator (typically a matrix) is a different mathematical object than a variable (typically a real number).

This equation implies that the operators $\hat{\phi}$ and $\hat{Q}$ don't have the same eigenvalues, meaning that is not physically possible to determine with infinite precision both the flux ϕ and the charge Q at the same time. This is nothing but the Heisenberg's indeterminacy principle: Q_{zpf}, the quantum fluctuations of the charge Q in the capacitor electrodes, and ϕ_{zpf}, the flux ϕ threading the inductor, must fulfil the inequality $\phi_{\text{zpf}}\, Q_{\text{zpf}} \geq \hbar/2$.

In the quantum-mechanical picture, we do not describe the state of the LC-resonator with a pair of variables (ϕ, Q), but rather with a vector $|\psi\rangle$. Such vector is normalized $\langle\psi|\psi\rangle = 1$ and lives in a Hilbert space representing all the allowed states of the LC-resonator. In this thesis, the considered Hilbert spaces are discrete. Moreover, the physical observables, such as the flux ϕ and the charge Q, are related to the mean values of their corresponding operators, in this case $\hat{\phi}$ and $\hat{Q}$, respectively. For example, the mean value of the flux $\langle\phi\rangle$, at a given time "t", is calculated as:

$$\langle\phi\rangle = \langle\psi|\hat{\phi}|\psi\rangle \tag{1.23}$$

The time evolution of the wavefunction, thus the evolution of the observables over time, is governed by the Schrödinger equation:

$$i\hbar\,\partial_t\ |\psi\rangle = \hat{H}\ |\psi\rangle \tag{1.24}$$

This equation is in general complicated to handle, however, it simplifies a lot if the wavefunction $|\psi\rangle$ is written in the basis of eigen-states of the Hamiltonian H. An eigen-state $|E\rangle$ of the Hamiltonian H with eigenvalue E, satisfies the relation:

$$\hat{H}\ |E\rangle = E\ |E\rangle \tag{1.25}$$

This equation is also known as the time-independent Schrödinger equation.

1.1.4 Energy spectrum of the quantum LC-resonator

This section focuses on the eigen-values and the eigen-vectors of the Hamiltonian H of the LC-resonator. We also introduce the useful ladder operators. Since the Hamiltonian H (Eq. 1.21) is the operator representing the total energy of the LC-resonator, therefore, the eigen-values E represent the allowed energies of the LC-resonator. The set of all the eigen-values {E} is the referred to as the spectrum of the Hamiltonian H. In order to find the spectrum corresponding to the LC-resonator, we introduce the ladder operators $\hat{a}$ and $\hat{a}^\dagger$:

$$\begin{aligned}\hat{a} &= \sqrt{\frac{1}{2\hbar Z_0}}\left(\hat{\phi} + iZ_0\hat{Q}\right)\\ \hat{a}^\dagger &= \sqrt{\frac{1}{2\hbar Z_0}}\left(\hat{\phi} - iZ_0\hat{Q}\right)\end{aligned} \tag{1.26}$$

Where Z_0 is the impedance of the LC-resonator (Eq. 1.16). The operator $\hat{a}^\dagger$ is the hermitian adjoint of $\hat{a}$. The ladder operators satisfy the commutation relation:

$$\left[\hat{a},\, \hat{a}^\dagger\right] = \hat{a}\,\hat{a}^\dagger - \hat{a}^\dagger\,\hat{a} = 1 \tag{1.27}$$

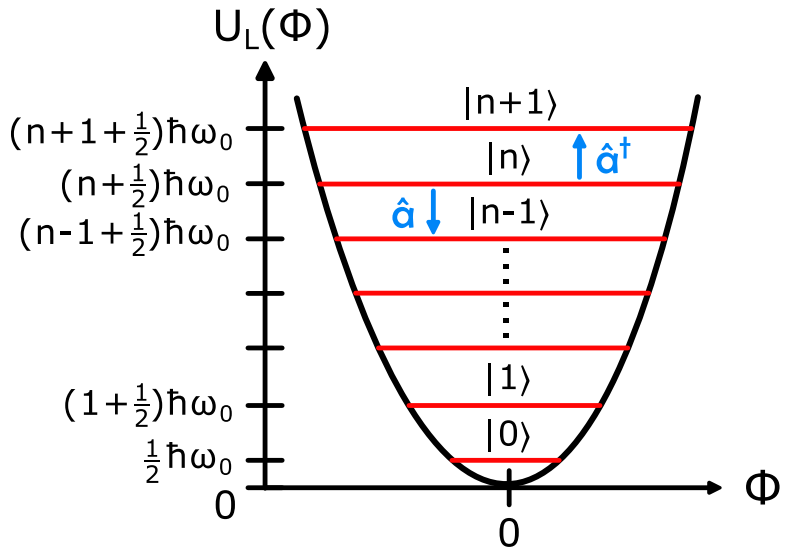

Fig. 1.2 ***Spectrum of the LC-resonator:*** *The harmonic oscillator Hamiltonian has a discrete spectrum, with equally spaced eigen-energies. The ladder operators allow to go up or down the ladder of eigenstates. The ground state has an energy that is higher than the minimum of the potential energy.*

One can write the Hamiltonian of the LC-resonator (Eq. 1.21) in terms of the ladder operators:

$$\hat{H} = \hbar\omega_0 \left(\hat{a}^\dagger \hat{a} + \frac{1}{2}\right) \tag{1.28}$$

The eigen-energies E_n are given by

$$E_n = \hbar\omega_0 \left(n + \frac{1}{2}\right). \tag{1.29}$$

Notice that the smallest energy E_0 is not zero, the value of the potential energy minimum, but $\frac{1}{2}\hbar\omega_0$. It is commonly referred as the vacuum energy or the zero-point energy. The eigenstates of the LC-resonator are labeled as $|n\rangle$, with "n" representing the number of energy quanta of the mode. The quantization of the energy spectrum is a consequence of the commutation relations between a and $a^\dagger$ and H:

$$\begin{aligned} [\hat{H},\, \hat{a}\,] &= -\hbar\omega_0\, \hat{a} \\ [\hat{H},\, \hat{a}^\dagger] &= +\hbar\omega_0\, \hat{a}^\dagger \end{aligned} \tag{1.30}$$

The first relation 1.30 implies that the operator $\hat{a}$ subtracts an energy quantum from the LC-resonator, i.e.:

$$\hat{H}\,\hat{a}\,|n\rangle = \hat{a}\,(H - \hbar\omega_0)\,|n\rangle = (E_n - \hbar\omega_0)\;\hat{a}\,|n\rangle \tag{1.31}$$

Eq. 1.31 means that applying the operator $\hat{a}$ to an eigen-state $|n\rangle$ with energy E_n produces other eigen-state $|n-1\rangle$ that has 1 less energy quantum, $|n-1\rangle \propto \hat{a}\,|n\rangle$ with energy $E_{n-1} = E_n - \hbar\omega_0$. In particular

$$\hat{a}\,|n\rangle = \sqrt{n}\,|n-1\rangle \tag{1.32}$$

Because of this, the operator $\hat{a}$ is referred to as the annihilation operator. The second relation 1.30 implies that the operator $\hat{a}^\dagger$ adds an energy quantum to the LC-resonator, i.e.:

$$\hat{H}\,\hat{a}^\dagger\,|n\rangle = \hat{a}^\dagger\,(H + \hbar\omega_0)\,|n\rangle = (E_n + \hbar\omega_0)\;\hat{a}^\dagger\;|n\rangle \tag{1.33}$$

Eq. 1.33 means that applying the operator $\hat{a}^\dagger$ to a state $|n\rangle$ with energy E_n produces other eigen-state $|n+1\rangle$ that has 1 more energy quantum, $|n+1\rangle \propto \hat{a}^\dagger\,|n\rangle$ with energy $E_{n+1} = E_n + \hbar\omega_0$. In particular,

$$\hat{a}^\dagger\,|n\rangle = \sqrt{n+1}\,|n+1\rangle \tag{1.34}$$

1.1.5 Quantum fluctuations of the energy eigen-states

In the previous section we saw that the spectrum of the quantum LC-resonator is discrete and their energy levels are equally spaced by $\hbar\omega_0$ (see Figure 1.2). This result differs from the classical LC-resonator whose energy E (Eq. 1.18 and 1.20) can take any arbitrary value. Moreover, there is another fundamental difference between the quantum LC-resonator and the classical one: the so-called quantum fluctuations. In this section, we consider the (quantum) fluctuations of both the flux $\Delta\phi$ and the charge ΔQ of the energy eigen-states $|n\rangle$ of the LC-resonator. We also discuss the relation between each other, which is nothing but the Heisenberg's uncertainty principle.

We start by writing the flux $\hat{\phi}$ and charge $\hat{Q}$ operators in terms of the ladder operators $\hat{a}$ and its hermitian adjoint $\hat{a}^\dagger$ (Eq. 1.26):

$$\begin{aligned}\hat{\phi} &= \frac{\phi_{\text{zpf}}}{\sqrt{2}}\left(\hat{a} + \hat{a}^\dagger\right)\\ \hat{Q} &= \frac{Q_{\text{zpf}}}{i\sqrt{2}}\left(\hat{a} - \hat{a}^\dagger\right)\end{aligned} \tag{1.35}$$

Where the parameters ϕ_{zpf} and Q_{zpf} are named the "flux zero-point-fluctuations" and the "charge zero-point-fluctuations", respectively. These parameters are related to the LC-resonator impedance Z_0 (Eq. 1.16 and 1.26) as:

$$\begin{aligned}\phi_{\text{zpf}} &\equiv \sqrt{\hbar\,Z_0}\\ Q_{\text{zpf}} &\equiv \sqrt{\frac{\hbar}{Z_0}}\end{aligned} \tag{1.36}$$

We can then calculate the mean value of the flux $\langle\phi\rangle$ and the mean value of the charge $\langle Q\rangle$ for an energy eigen-state $|n\rangle$:

$$\begin{aligned}\langle\phi\rangle_{nn} &= \langle n|\hat{\phi}|n\rangle = \frac{\phi_{\text{zpf}}}{\sqrt{2}}\;\langle n|\hat{a} + \hat{a}^\dagger|n\rangle = 0\\ \langle Q\rangle_{nn} &= \langle n|\hat{Q}|n\rangle = \frac{Q_{\text{zpf}}}{i\sqrt{2}}\,\langle n|\hat{a} - \hat{a}^\dagger|n\rangle = 0\end{aligned} \tag{1.37}$$

Notice that the ladder operators $\hat{a}$ and $\hat{a}^\dagger$ cause a jump from $|n\rangle$ to a state with 1 less $|n+1\rangle$ or 1 more $|n+1\rangle$ energy quantum, respectively, and the eigen-states are orthogonal to each other:

$$\langle m|n\rangle = \delta_{m,\,n} \tag{1.38}$$

Where $\delta_{m,n}$ is a Kronecker delta (an identity matrix), such that $\delta_{n,n} = 1$ and $\delta_{m\neq n,n} = 0$. Eq. 1.37 mean that the energy eigen-states $|n\rangle$ represent states of the LC-resonator with both zero mean-flux $\langle\phi\rangle$ and zero mean-charge $\langle Q\rangle$, nevertheless, those states still have an energy $E_n \propto n\hbar\omega_0$ which is conserved over time[2]. These states have no-classical equivalent, since in the case of the classical LC-resonator, the energy E is also fixed but it is related to the mean values of the flux $\langle\phi\rangle$ and the charge $\langle Q\rangle$ (Eq. 1.18) as:

$$E_{nn}^{\text{classic}} = \frac{\langle\phi\rangle_{nn}^2}{2L} + \frac{\langle Q\rangle_{nn}^2}{2C} \tag{1.39}$$

The energy of the Hamiltonian eigen-states $|n\rangle$ is actually related to the quantum fluctuations of the charge ΔQ and the flux $\Delta\phi$,

$$\begin{aligned} \Delta\phi_{nn}^2 &\equiv \langle n|\hat{\phi}^2 - \langle\phi\rangle^2|n\rangle = \frac{\phi_{\text{zpf}}^2}{2}\langle n|\hat{a}\hat{a}^\dagger + \hat{a}^\dagger\hat{a}|n\rangle = \phi_{\text{zpf}}^2\left(n+\frac{1}{2}\right) \\ \Delta Q_{nn}^2 &\equiv \langle n|\hat{Q}^2 - \langle Q\rangle^2|n\rangle = \frac{Q_{\text{zpf}}^2}{2}\langle n|\hat{a}\hat{a}^\dagger + \hat{a}^\dagger\hat{a}|n\rangle = Q_{\text{zpf}}^2\left(n+\frac{1}{2}\right) \end{aligned} \tag{1.40}$$

By combining Eq. 1.36 and 1.40 we find the relations between the flux and charge fluctuations of the energy eigen-states $|n\rangle$:

$$\begin{aligned} \frac{\Delta\phi_{nn}}{\Delta Q_{nn}} &= Z_0 \\ \Delta\phi_{nn}\,\Delta Q_{nn} &= \hbar\left(n+\frac{1}{2}\right) \geq \frac{\hbar}{2} \end{aligned} \tag{1.41}$$

Firstly, notice that the ratio between the flux $\Delta\phi$ and charge ΔQ fluctuations is determined by the impedance Z_0 but it is independent of the number of energy quanta "n" in the LC-resonator. Secondly, the product of the flux $\Delta\phi$ and charge ΔQ fluctuations scales proportionally to the number of energy quanta "n", but it is independent of the parameters of the LC-resonator, which are the resonance frequency ω_0 and the impedance Z_0. Since the Hamiltonian $\hat{H}$ is the operator related to the total energy of the LC-resonator, the mean energy $\langle E\rangle$ of the Hamiltonian eigen-states $|n\rangle$ is actually

$$\langle E\rangle_{nn} = \langle n|\hat{H}|n\rangle = \frac{\Delta\phi_{nn}^2}{2L} + \frac{\Delta Q_{nn}^2}{2C} = \hbar\omega_0\left(n+\frac{1}{2}\right) \tag{1.42}$$

Thus, the Hamiltonian eigen-states $|n\rangle$ represent cases where the LC-resonator has no net charge $\langle Q\rangle = 0$ nor net flux $\langle\phi\rangle = 0$, so that it's classical energy E_{nn}^{classic} is zero as well, nonetheless, the LC-resonator still has some energy $E_{nn}^{\text{quantum}} = \hbar\omega_0\left(n+\frac{1}{2}\right)$ that is stored in the form of quantum fluctuations of the flux $\Delta\phi_{nn}$ and the charge ΔQ_{nn}. Notice that, in virtue of Heisenberg's uncertainty principle, $\Delta\phi\,\Delta Q \geq \hbar/2$, the energy stored in the quantum fluctuations E^{quantum} has always a minimum value greater than zero, the so-called "vacuum energy" or zero-point energy. In the case of the LC-resonator, the zero-point energy is $E_0 = \frac{1}{2}\hbar\omega_0$. Although the ladder operators $\hat{a}^\dagger$ and $\hat{a}$ can rise or decrease, respectively, the energy stored in the quantum fluctuations by quanta $\hbar\omega_0$, nonetheless, the vacuum $|0\rangle$ is the

[2]We well see this in a following section.

state with the minimal energy of quantum fluctuations and no energy can be extracted from it, such that

$$\hat{a}\,|0\rangle = 0\,|0\rangle = 0 \tag{1.43}$$

Notice that the vacuum state $|0\rangle$ is an eigen-state of the annihilation operator $\hat{a}$ with eigenvalue $\alpha = 0$. In the more general case of an arbitrary state of the LC-resonator $|\psi\rangle$ that is not an eigen-state of the Hamiltonian $\hat{H}$, such that mean values of the flux $\langle\phi\rangle$ and the charge $\langle Q\rangle$ are not zero, the mean energy $\langle E\rangle$ is:

$$\langle E\rangle = \langle\psi|\hat{H}|\psi\rangle = \frac{\langle\psi|\hat{\phi}^2|\psi\rangle}{2L} + \frac{\langle\psi|\hat{Q}^2|\psi\rangle}{2C} = \frac{\langle\phi\rangle^2 + \Delta\phi^2}{2L} + \frac{\langle Q\rangle^2 + \Delta Q^2}{2C} = E^{\text{classic}} + E^{\text{quantum}} \tag{1.44}$$

1.1.6 The vacuum-state of the LC-resonator

This section is about the wavefunction of the vacuum state $|0\rangle$ in either charge $\langle Q|0\rangle$ or flux $\langle\phi|0\rangle$ representation. The vacuum state is interesting because it represents the state with the minimum energy of the quantum fluctuations. In general, the wavefunction in the charge representation $\langle Q|\psi\rangle$ is the Fourier transform of the wavefunction in the flux representation $\langle\phi|\psi\rangle$:

$$\langle Q|\psi\rangle = \int_{-\infty}^{\infty} d\phi\ \langle\phi|\psi\rangle\ \exp\left(\frac{-i\phi\,Q}{\hbar}\right) \tag{1.45}$$

The wave function of the vacuum-state $|0\rangle$ in the flux ϕ representation (in the basis of the flux operator $\hat{\phi}$) is:

$$\psi_0(\phi) \equiv \langle\phi|0\rangle = \frac{\pi^{-\frac{1}{4}}}{\sqrt{\phi_{\text{zpf}}}}\, e^{-\frac{1}{2}\left(\frac{\phi}{\phi_{\text{zpf}}}\right)^2} \tag{1.46}$$

The wave function $\psi_0(\phi)$ is a Gaussian centered at $\phi = 0$ with a standard deviation $\phi_{\text{zpf}} = \sqrt{\hbar Z_0}$ (Eq. 1.36). Similarly, the wave function of the vacuum-state $|0\rangle$ in the charge Q representation (in the basis of the charge operator $\hat{Q}$) is:

$$\Psi_0(Q) \equiv \langle Q|0\rangle = \frac{\pi^{-\frac{1}{4}}}{\sqrt{Q_{\text{zpf}}}}\, e^{-\frac{1}{2}\left(\frac{Q}{Q_{\text{zpf}}}\right)^2} \tag{1.47}$$

The wave function $\Psi_0(Q)$ is a Gaussian centered at $Q = 0$ with a standard deviation $Q_{\text{zpf}} = \sqrt{\hbar/Z_0}$ (Eq. 1.36).

1.2 Non-linear circuits

The Section 1.1 was about the most elementary superconducting circuit, the LC-resonator, that is made of a linear inductance L and a linear capacitance C in parallel connection. However, the more involved and interesting superconducting circuits are typically anharmonic oscillators: They have a more complicated lower energy spectrum that results from the inclusion of a non-linear element in the circuit components. This non-regularity (anharmonicity) of the spectrum allows to drive and manipulate an individual pair of levels, realising what is known as a two-level system. This last one is also referred to as a pseudo-spin or a qubit and it is at the core of the field of quantum information. In practice, the non-linearity of a circuit

originates from a small tunnel-effect junction, named a Josephson junction, that is made of a thin insulating barrier (I) separating two superconducting electrodes (S). The junction behaves as a non-linear inductance that depends on the superconducting phase difference across the junction. This chapter is about the fundamentals of the Josephson junctions and how they allow the realisation of anharmonic circuits that can be used as two-level systems.

1.2.1 Josephson junction

This section is about the fundamentals of the Josephson junctions. A Josephson junction is a tunnel-effect junction made of a thin insulating barrier (I) between two superconducting electrodes (S). B. Josephson showed in 1962 [Jos62] that a phase difference $\varphi = \varphi_{S1} - \varphi_{S2}$ between the two superconducting electrodes can produce a super-current of pairs of electrons (Cooper pairs) through the junction. This is the case even if the transmission of single electrons through the tunnel barrier is very small. The super-current of Cooper pairs is proportional to the normal-state tunnel conductance of the junction [3]. The so-called Josephson relations characterize the behavior of the junction:

$$\begin{aligned} I &= I_c \, \sin(\varphi) \\ \partial_t \varphi &= \frac{V}{\Phi_0}, \end{aligned} \tag{1.48}$$

where V and I are the voltage and current through the junction, respectively, and $\Phi_0 = \hbar/2e$ is the reduced flux quantum. The parameter I_c is named the critical current of Cooper pairs through the junction and it is given by

$$I_c = \frac{\pi \Delta}{2eR_N}, \tag{1.49}$$

where Δ is the BCS gap of the superconducting electrodes and R_N is the normal state resistance of the junction. Notice that the superconducting phase difference φ across the junction is proportional to the flux $\phi = \Phi_0 \, \varphi$ (Eq. 1.1). Then, the phase operator is defined as $\hat{\varphi} = \hat{\phi}/\Phi_0$. According to the relations 1.48, the time derivative of the super-current $\partial_t I$ is written:

$$\partial_t I = I_c \cos(\varphi) \, \frac{V}{\Phi_0} \tag{1.50}$$

This equation suggests that the junction behaves approximately as a linear inductance $V = L\dot{I}$ as long as the superconducting phase difference φ is small. In general, a Josephson junction behaves as a non-linear inductance $L(I)$ which depends on the value of the super-current I through the junction. By combining the Eq. 1.48 and 1.50, we obtain an expression for the inductance corresponding to the junction:

$$L(I) = \frac{\Phi_0}{I_c \, \cos(\varphi)} = \frac{\Phi_0}{I_c \sqrt{1 - \left(\frac{I}{I_c}\right)^2}} \tag{1.51}$$

Using Eq. 1.5, we can calculate the energy stored in the junction:

$$U_J(\phi) = \int_{-\infty}^{t} dt' \, V(t') \, I(t') = -E_J \cos\left(\frac{\phi}{\Phi_0}\right), \tag{1.52}$$

where

$$Ej \equiv \Phi_0 \, I_c \tag{1.53}$$

is the so-called Josephson energy. In the regime where the flux ϕ across the junction is small, $\phi \ll \Phi_0$, the energy of the junctions is approximately $U_J(\phi) \approx E_J \phi^2 / 2\Phi_0^2$, meaning that the junction behaves as a linear inductance L_J, such that

$$L_J \equiv \frac{\Phi_0^2}{E_J} = \frac{\Phi_0}{I_c} \tag{1.54}$$

Note that this Josephson junction inductance is a kinetic inductance. In the work described in this thesis, Josephson will be used either as non-linear inductors, or as large linear inductors.

1.2.2 Anharmonic oscillator: The transmon

Building upon the non linearity provided by Josephson junctions, one can create a wide variety of circuits that behave as artificial atoms. For instance, the charge circuit of a superconducting island that is allowed to exchange Cooper pairs with a superconducting reservoir (e.g., another superconducting island) through a Josephson junction. These elementary kind of circuits can be modeled by the Hamiltonian:

$$H = \frac{\hat{Q}^2}{2C} - E_J \cos\left(\frac{\hat{\phi}}{\Phi_0}\right) \tag{1.55}$$

Where the charge $\hat{Q}$ and flux $\hat{\phi}$ operators satisfy the canonical commutation relation $\left[\hat{\phi}, \hat{Q}\right] = i\hbar$. When it comes to describing a superconducting circuit with a Josephson junction, it is more natural to express its Hamiltonian with dimensionless variables that are the (superconducting) phase operator $\hat{\varphi} = \hat{\phi}/\Phi_0$ and the operator representing the number of extra Cooper pairs on the capacitor $\hat{N} = \hat{Q}/2e$,

$$\hat{H} = 4E_C \hat{N}^2 - E_J \cos\left(\hat{\varphi}\right) \tag{1.56}$$

Where $E_C \equiv e^2/2C$ is the so-called charging energy. Notice that the phase $\hat{\varphi}$ and Cooper-pair number operator $\hat{N}$ satisfy the commutation relation

$$\left[\hat{\varphi}, \hat{N}\right] = i \tag{1.57}$$

The ratio between the tunneling energy and the charging energy, E_J/E_C, controls the Hamiltonian spectrum. In the so-called "transmon regime", $E_J/E_C \gg 1$ (typically $E_J/E_C \approx 50$), a charge circuit described by the Hamiltonian 1.56 behaves as a weakly non-linear LC-resonator (also referred to as "anharmonic" resonator). This circuit, named transmon, is insensitive to external charge noise at the expense of having a reduced non-linear behaviour (the spectrum anharmonicity). Nowadays, most of the quantum computing architectures based on superconducting circuits are built upon circuits made of several coupled transmons. Similarly to the case of the quantum LC-resonator, the phase $\hat{\varphi}$ and Cooper-pair number $\hat{N}$ operators

can be written in terms of the ladder operators $\hat{a}$ and its hermitian adjoint $\hat{a}^\dagger$ (see Eq. 1.26 and 1.35):

$$\begin{aligned}\hat{\varphi} &= \frac{\phi_{\text{zpf}}}{\Phi_0}\frac{\left(\hat{a}+\hat{a}^\dagger\right)}{\sqrt{2}} \\ \hat{N} &= \frac{Q_{\text{zpf}}}{2e}\frac{\left(\hat{a}-\hat{a}^\dagger\right)}{i\sqrt{2}}\end{aligned} \tag{1.58}$$

Where the zero-point fluctuations of the flux $\phi_{\text{zpf}} = \sqrt{\hbar Z_0}$ and the charge $Q_{\text{zpf}} = \sqrt{\hbar/Z_0}$ are related to the circuit impedance Z_0 (see Eq. 1.36). In this case, the circuit impedance is given by:

$$Z_0 = \sqrt{\frac{L_J}{C}} = \mathscr{R}_Q \left(\frac{2E_C}{E_J}\right)^{1/2} \tag{1.59}$$

Where $\mathscr{R}_Q \equiv \hbar/2e^2$ is the reduced quantum of resistance and $2\pi\cdot\mathscr{R}_Q \approx 12.9\,\text{k}\Omega$. The charge circuit Hamiltonian $\hat{H}$ (Eq. 1.56) in terms of the ladder operators $\hat{a}$ and $\hat{a}^\dagger$ (Eq. 1.58) is written:

$$\hat{H} = -4E_C N_{\text{zpf}}^2 \frac{\left(\hat{a}-\hat{a}^\dagger\right)^2}{2} - E_J \cos\left(\varphi_{\text{zpf}}\frac{\left(\hat{a}+\hat{a}^\dagger\right)}{\sqrt{2}}\right) \tag{1.60}$$

Where the parameters φ_{zpf} and N_{zpf} are defined as:

$$\begin{aligned}\varphi_{\text{zpf}} &\equiv \frac{\phi_{\text{zpf}}}{\Phi_0} = \left(\frac{8E_C}{E_J}\right)^{1/4} \\ N_{\text{zpf}} &\equiv \frac{Q_{\text{zpf}}}{2e} = \left(\frac{E_J}{8E_C}\right)^{1/4}\end{aligned} \tag{1.61}$$

Notice that in the transmon regime $\varphi_{\text{zpf}} \ll 1$. Then, the junction potential in the transmon Hamiltonian (Eq. 1.60) can be expanded in power series. In a first approximation, the cosine is approximated to the 4th order yielding:

$$\hat{H} \approx \sqrt{8E_C\,E_J}\left(\hat{a}^\dagger\hat{a}+\frac{1}{2}\right) - \frac{E_J\,\varphi_{\text{zpf}}^4}{24}\frac{\left(\hat{a}+\hat{a}^\dagger\right)^4}{4} \tag{1.62}$$

The first term in the RHS represents the linear part of the Hamiltonian $\hat{H}_0$ and it is nothing but the Hamiltonian of an LC-resonator (see Eq. 1.28) with a resonance frequency ω_0 given by:

$$\omega_0 \equiv \frac{1}{\hbar}\sqrt{8E_C\,E_J} \tag{1.63}$$

The second term in the RHS is the non-linear part of the Hamiltonian $\hat{H}_{\text{nl}}$ and it is written as:

$$\hat{H}_{\text{nl}} = -\frac{E_C}{3}\frac{\left(\hat{a}+\hat{a}^\dagger\right)^2}{4} \tag{1.64}$$

The transmon Hamiltonian (Eq. 1.62) can be seen as a quantum harmonic oscillator $\hat{H}_0$ perturbed by a weak non-linearity $\hat{H}_{\text{nl}}$. We expand the non-linear part $\hat{H}_{\text{nl}}$ and keep only the

terms with equal number of creation and annihilation operators (in virtue of the rotating-wave approximation), and after simplifying a bit by taking into account the commutator between $\hat{a}$ and $\hat{a}^\dagger$ (Eq. 1.27), we finally obtain a simplified form of the transmon Hamiltonian:

$$\hat{H} \approx \sqrt{8E_C\,E_J}\left(1-\sqrt{\frac{E_C}{8E_J}}\right)\hat{a}^\dagger\hat{a} - \frac{E_C}{2}\hat{a}^{\dagger\,2}\hat{a}^2 \tag{1.65}$$

Firstly, notice that the frequency related to the linear part of the Hamiltonian has been reduced as:

$$\hbar\omega_{\rm tr} \equiv \hbar\omega_0 - E_C = \sqrt{8E_C\,E_J} - E_C \tag{1.66}$$

This means that the spectrum of linear part $\hat{H}_0 \propto \hat{a}^\dagger\hat{a}$ has been re-scaled according to the factor $(1-\sqrt{E_C/8E_J})$, this effect is referred to as Lamb shift. Secondly, to first order in perturbation, notice that the nonlinear part $\hat{H}_{\rm nl} \propto \hat{a}^{\dagger\,2}\hat{a}^2$ has the same eigen-states $|n\rangle$ as the linear part $\hat{H}_0$. Thus, the eigen-states $|n\rangle$ of the transmon Hamiltonian (Eq. 1.65) are the same as the states of a harmonic-oscillator with resonance frequency $\omega_{\rm tr}$ (Eq. 1.66) and impedance Z_0 (Eq. 1.59). However, the energies E_n of the eigen-states $|n\rangle$ now scale quadratically with the number of energy quanta "n":

$$E_n \approx \left(\sqrt{8E_C\,E_J} - E_C\right)n - E_C\frac{n(n-1)}{2} \qquad (n \geq 1) \tag{1.67}$$

The transition frequency between ground state $|g\rangle = |0\rangle$ and the first excited state $|e\rangle = |1\rangle$ is $\omega_{ge} = \omega_{\rm tr}$, while the transition frequency between first excited state $|e\rangle = |1\rangle$ and the next excited state $|f\rangle = |2\rangle$ is $\omega_{ef} = \omega_{\rm tr} - E_C/\hbar$. The difference between these two frequencies is referred to as the *anharmonicity* α of the transmon:

$$\alpha \equiv \omega_{ge} - \omega_{ef} \approx \frac{E_C}{\hbar} \tag{1.68}$$

The key result is that the spectrum of the transmon is sufficiently non-linear to be used as a two level system, also referred to as a qubit. In practice, the two lower energy states $|g\rangle$ and $|e\rangle$ are typically chosen as qubit states. The anharmonicity of the transmon spectrum makes it possible to address the qubit transition without exciting higher energy transitions, such that it can legitimately be regarded as a two-level system.

1.3 Two-level system manipulation

In this section, we describe the physics of an ideal two-level system: time evolution, state representation in the Bloch sphere, arbitrary state preparation with Rabi oscillation. We also describe the physics of a two-level system coupled to an environment: either a microwave resonator used to readout its state, or a thermal bath leading to relaxation and decoherence.

1.3.1 Mathematical description of a two level system

The quantum state of a two-level system is represented by a normalized vector in complex 2-dimensional space, such that

$$|\psi\rangle = \alpha_0\,|0\rangle + \alpha_1\,|1\rangle = \begin{bmatrix}\alpha_1\\ \alpha_0\end{bmatrix} \tag{1.69}$$

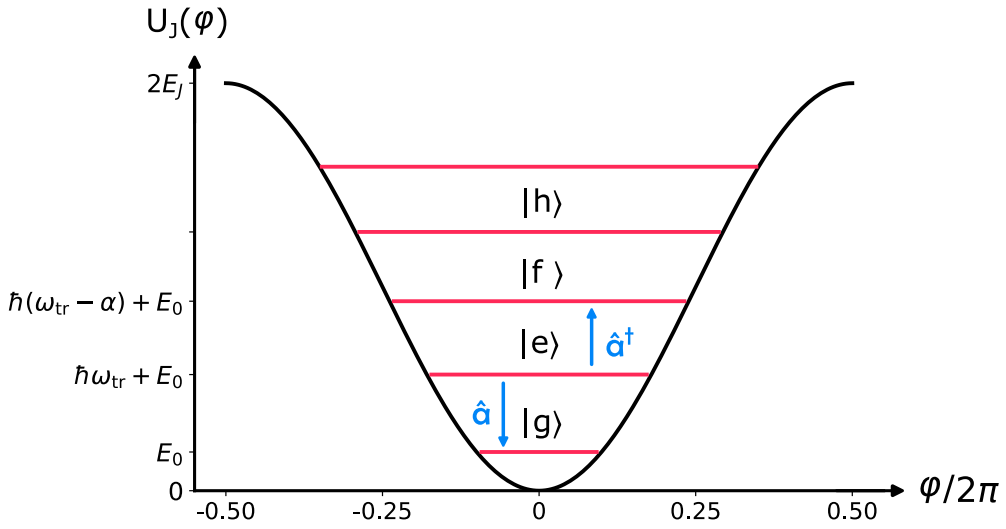

Fig. 1.3 ***Spectrum of the transmon circuit:*** .

Where the base vectors $|0\rangle$ and $|1\rangle$ represent the allowed states of the two level system. They are normalized $\langle 1|1\rangle = \langle 0|0\rangle = 1$ and they are orthogonal to each other $\langle 0|1\rangle = \langle 1|0\rangle = 0$. The coefficients satisfy $|\alpha_0|^2 + |\alpha_1|^2 = 1$, such that they can be rather written as:

$$\alpha_0 = \cos\left(\frac{\theta}{2}\right) \qquad \alpha_1 = e^{i\gamma}\,\sin\left(\frac{\theta}{2}\right) \tag{1.70}$$

Where the term $e^{i\gamma}$ represents the relative phase between the two terms in the decomposition. In general, the Hamiltonian of a two-level system is a 2×2 matrix that is hermitian (self-adjoint), $\hat{H}^\dagger = \hat{H}$:

$$\hat{H} = \frac{1}{2}\hbar\omega_0 \begin{bmatrix} -A & B - iC \\ B + iC & +A \end{bmatrix} \tag{1.71}$$

Where the coefficients A, B and C are real numbers satisfying $A^2 + B^2 + C^2 = 1$, such that the eigen-values of the Hamiltonian are always $E_\pm = \pm\frac{1}{2}\hbar\omega_0$. When dealing with a two-level system, it is convenient to use the formalism of the Pauli matrices:

$$\hat{\sigma}_x = \begin{bmatrix} 0 & 1 \\ 1 & 0 \end{bmatrix}, \quad \hat{\sigma}_y = \begin{bmatrix} 0 & -i \\ i & 0 \end{bmatrix}, \quad \hat{\sigma}_z = \begin{bmatrix} 1 & 0 \\ 0 & -1 \end{bmatrix}, \quad \hat{I}_2 = \begin{bmatrix} 0 & 1 \\ 1 & 0 \end{bmatrix} \tag{1.72}$$

Where $\hat{I}_2$ is the 2×2 identity matrix. One can show that $\hat{H}$ can be written in terms of Pauli matrices as:

$$\hat{H} = -\frac{1}{2}\hbar\omega_0\,\left(-\sin(\theta)\,\cos(\gamma)\,\hat{\sigma}_x - \sin(\theta)\,\sin(\gamma)\,\hat{\sigma}_y + \cos(\theta)\,\hat{\sigma}_z\right). \tag{1.73}$$

The coefficients of the Pauli operators resemble the coordinates of vector laying on the unit sphere, where $\cos(\theta)$ is the projection on the z-axis, $\sin(\theta)$ is the transversal projection on the

x-y plane, and γ is the component of the transverse projection on the x-axis. The eigen-states of the two-level Hamiltonian $\hat{H}$ (Eq. 1.75) are given by:

$$\begin{aligned} |-\rangle &= \cos\left(\frac{\theta}{2}\right)|0\rangle - \sin\left(\frac{\theta}{2}\right) e^{i\gamma}\,|1\rangle \\ |+\rangle &= \sin\left(\frac{\theta}{2}\right)|0\rangle + \cos\left(\frac{\theta}{2}\right) e^{i\gamma}\,|1\rangle\,. \end{aligned} \tag{1.74}$$

Finally, there exists a basis set where the Hamiltonian reduces to

$$\hat{H} = -\frac{1}{2}\hbar\omega_0\,\hat{\sigma}_z. \tag{1.75}$$

Problems are usually parametrized such that $|0\rangle$ and $|1\rangle$ are the eigenstates of this Hamiltonian. The eigen-energies associated to the states $|0\rangle$ and $|1\rangle$ are $E_0 = -\frac{1}{2}\hbar\omega_0$ and $E_1 = +\frac{1}{2}\hbar\omega_0$, such that the qubit transition frequency is ω_0.

1.3.2 Bloch sphere representation

It is useful to consider the Bloch sphere representation of a two-level system for a better visualization of its dynamics (see Figure 1.4). Any state of a two level system $|\psi\rangle$ can be written:

$$|\psi\rangle = \cos\left(\frac{\theta}{2}\right)|0\rangle + \sin\left(\frac{\theta}{2}\right) e^{i\gamma}\,|1\rangle \quad \rightarrow \quad \hat{e}_r \equiv \begin{bmatrix} \sin(\theta)\cos(\gamma) \\ \sin(\theta)\sin(\gamma) \\ \cos(\theta) \end{bmatrix}, \tag{1.76}$$

where $\theta \in [0, \pi]$ and $\phi \in [0, 2\pi[$ are angles having same interval of definition than radial and azimuthal angles of the spherical coordinates system. Thus, each state vector of the two-level system can be mapped onto a unique vector of the unite sphere. In this representation, the eigen-states of the Hamiltonian $\hat{H} = -\frac{1}{2}\hbar\omega_0\hat{\sigma}_z$ are located the south pole $|1\rangle$ and the north pole $|0\rangle$ of the unit sphere.

1.3.3 Dynamics of the two-level system

In general, the dynamics of a two-level system is governed by the Schrödinger equation 1.24. Firstly, we consider the natural time evolution of the state $|\psi\rangle$ of the two-level system that is driven by its time-independent Hamiltonian $\hat{H}$ (Eq. 1.75). Finally, we consider the time evolution of the state of the two level system when affected by an external coherent drive.

The time evolution of the two level system is described by the Schrödinger equation $i\hbar\,\partial_t\,|\psi\rangle = \hat{H}\,|\psi\rangle$. We start by considering the time evolution of the states $|0\rangle$ and $|1\rangle$. We recall that these are the eigen-states of the Hamiltonian $\hat{H} = -\frac{1}{2}\hbar\omega_0\hat{\sigma}_z$. In this case, the equations describing the dynamics of the states $|0\rangle$ and $|1\rangle$, respectively, are:

$$\begin{aligned} i\hbar\,\partial_t\,|0\rangle &= -\frac{1}{2}\hbar\omega_0\,|0\rangle \quad \rightarrow \quad |0(t)\rangle = e^{+\frac{i}{2}\omega_0 t}\,|0\rangle \\ i\hbar\,\partial_t\,|1\rangle &= +\frac{1}{2}\hbar\omega_0\,|1\rangle \quad \rightarrow \quad |1(t)\rangle = e^{-\frac{i}{2}\omega_0 t}\,|1\rangle \end{aligned} \tag{1.77}$$

The states $|0\rangle$ and $|1\rangle$ remain invariant up to a global phase $\exp(\pm\frac{i}{2}\omega_0 t)$, respectively. This stems from the fact that the energy of the eigen-states of the Hamiltonian is conserved. Next,

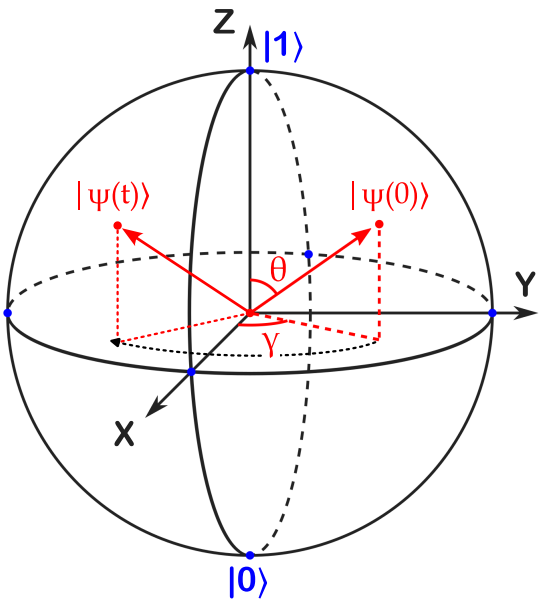

Fig. 1.4 ***Bloch sphere representation of a two-level system:*** .

we consider the time evolution of an arbitrary state $|\psi\rangle = \alpha_0 |0\rangle + \alpha_1 |1\rangle$, which is a linear combination of the eigen-states of the Hamiltonian $|0\rangle$ and $|1\rangle$. The equation governing the dynamics of the state $|\psi\rangle$ is:

$$i\hbar\,\partial_t |\psi\rangle = i\hbar\,(\dot{\alpha}_0 |0\rangle + \dot{\alpha}_1 |1\rangle) = \frac{1}{2}\hbar\omega_0\,(-\alpha_0 |0\rangle + \alpha_1 |1\rangle) \tag{1.78}$$

Since the states $|0\rangle$ and $|1\rangle$ are orthogonal to each other, we can separate the dynamics of the two coefficients α_0 and α_1, resulting in:

$$\begin{aligned} \dot{\alpha}_0 &= +\frac{i}{2}\hbar\omega_0\alpha_0 \quad \rightarrow \quad \alpha_0(t) = e^{+\frac{i}{2}\omega_0 t}\,\alpha_0(0) \\ \dot{\alpha}_1 &= -\frac{i}{2}\hbar\omega_0\alpha_1 \quad \rightarrow \quad \alpha_1(t) = e^{-\frac{i}{2}\omega_0 t}\,\alpha_1(0) \end{aligned} \tag{1.79}$$

If the initial value of the state $|\psi(0)\rangle = \cos(\theta/2)\,|0\rangle + \sin(\theta/2)\,e^{i\gamma}\,|1\rangle$, meaning that $\alpha_0(0) = \cos(\theta/2)$ and $\alpha_1(0) = \sin(\theta/2)\,e^{i\gamma}$, then, the state of the two-level system at a later time $|\psi(t)\rangle$ is, up to a global phase, given by:

$$|\psi(t)\rangle = \cos(\theta/2)\,|0\rangle + \sin(\theta/2)\,e^{i(\gamma-\omega_0 t)}\,|1\rangle \tag{1.80}$$

Notice that the relative phase between the two states $|0\rangle$ and $|1\rangle$ grows proportionally to the elapsed time as $\omega_0 t$. The complex number $e^{i\omega_0 t}$ represents a clockwise-rotation around the unit circle with angular velocity ω_0. The Bloch sphere representation of the state vector $|\psi(t)\rangle$ at a time "t" is:

$$|\psi_{\mathrm{d}}(t)\rangle = \begin{bmatrix} +\sin(\theta)\,\cos(\omega_0\,t-\gamma) \\ -\sin(\theta)\,\sin(\omega_0\,t-\gamma) \\ \cos(\theta) \end{bmatrix} \tag{1.81}$$

The pseudo-spin representing the state of the two level system $|\psi(t)\rangle$ follows a clock-wise precession around the z-axis of the Bloch sphere (see Figure 1.4) with frequency ω_0. This rotation of the pseudo-spin is naturally driven by its own Hamiltonian (Eq. 1.75) $\hat{H} = -\frac{1}{2}\hbar\omega_0\hat{\sigma}_z$.

1.3.4 Sinusoidal drive of a two-level system: Rabi oscillations

Here we describe the major qubit state manipulation used in this work: Rabi oscillations. We consider the time evolution of the state of a two level system when it is subject to a coherent drive. We encounter this situation often in the experiments, for instance, when applying a microwave pulse to drive a transition of a non-linear circuit, such as a transmon (see 1.2.2).

1.3.4.1 Out of resonance case

The Hamiltonian of a two level system under a coherent drive is:

$$\hat{H} = -\frac{1}{2}\hbar\omega_0\hat{\sigma}_z + \hbar\Omega_\mathrm{r}\,\cos(\omega_\mathrm{d})\;\hat{\sigma}_x \tag{1.82}$$

The time-independent part of the Hamiltonian is $\hat{H}_0 = -\frac{1}{2}\hbar\omega_0\hat{\sigma}_z$. The coherent drive is represented by the interaction Hamiltonian:

$$\hat{H}_\mathrm{I} = \hbar\Omega_\mathrm{r}\,\cos(\omega_\mathrm{d})\;\hat{\sigma}_x \tag{1.83}$$

Where the drive frequency is ω_d and the drive amplitude is Ω_r, the so-called Rabi frequency. The time-evolution of the two-level system is governed by the Schrödinger equation 1.24, however, the interaction Hamiltonian $\hat{H}_\mathrm{I}$, as it is, is too complicated for us to find an analytical solution. We start by performing a transformation of the state vector $|\psi\rangle$ as:

$$\begin{aligned} |\psi\rangle &= \hat{U}_\mathrm{d}(t)\;|\psi_\mathrm{d}\rangle \\ \hat{U}_\mathrm{d}(t) &\equiv \exp\left(+\frac{i}{2}\omega_\mathrm{d}t\,\hat{\sigma}_z\right) \end{aligned} \tag{1.84}$$

The term $\hat{U}_\mathrm{d}(t)$ is a unitary operator, such that $\hat{U}_\mathrm{d}(t)^\dagger = \hat{U}_\mathrm{d}(t)^{-1}$. In the general case, the operator $\hat{U}_\mathrm{d}(t)$ can be regarded as a generalized rotation of the Hilbert space representing the allowed states of a quantum system. In this particular case, the transform given by $\hat{U}_\mathrm{d}(t)$ translates into a rotation of the state vector $|\psi\rangle$ around the z-axis of the Bloch sphere (see Figure 1.4) with an angular velocity ω_d, the frequency of the coherent drive. Next, we substitute the explicit form of the wave vector (Eq. 1.84) in the Schrödinger equation 1.24, and after multiplying by $\hat{U}_\mathrm{d}^\dagger(t)$, we finaly obtain:

$$i\hbar\,\partial_t\,|\psi_\mathrm{d}\rangle = \hat{U}_\mathrm{d}^\dagger(t)\,\hat{H}\,\hat{U}_\mathrm{d}(t)\;|\psi_\mathrm{d}\rangle - i\hbar\,\hat{U}_\mathrm{d}^\dagger(t)\,\partial_t\,\hat{U}_\mathrm{d}(t)\;|\psi_\mathrm{d}\rangle \tag{1.85}$$

Notice that the operator $\hat{U}_\mathrm{d}(t)$ is time-dependent, thus, it produces an additional term in the equation governing the time evolution of the state vector $|\psi_\mathrm{d}\rangle$. In order to simplify Eq. 1.85, we consider the Baker-Hausdorff Lemma:

$$e^{+i\lambda\,\hat{G}}\,\hat{A}\,e^{-i\lambda\,\hat{G}} = \sum_{n=0}^{\infty}\frac{(i\lambda)^n}{n!}\;\left[\hat{G},\,\hat{A}\right]_n\,, \tag{1.86}$$

Where the term $\left[\hat{G},\,\hat{A}\right]_n$ represent the nested commutator between $\hat{G}$ and $\hat{A}$ of n-th order:

$$\begin{aligned}\left[\hat{G},\,\hat{A}\right]_0 &\equiv \hat{I}\\ \left[\hat{G},\,\hat{A}\right]_n &\equiv \left[...\left[\left[\left[\hat{A},\hat{G}\right],\hat{G}\right],\hat{G}\right],...\hat{G}\right] \quad \text{(n times)}\end{aligned} \tag{1.87}$$

By substituting Eq. 1.82, 1.84 and 1.86 into Eq. 1.85, we obtain:

$$i\hbar\,\partial_t\,|\psi_{\rm d}\rangle = \frac{\hbar}{2}\left(-\Delta\,\hat{\sigma}_z + \Omega_{\rm r}\,\hat{\sigma}_x\right)\,|\psi_{\rm d}\rangle + \frac{\hbar}{2}\left(-\Omega_{\rm r}\,\sin(2\omega_{\rm d})\,\hat{\sigma}_y + \Omega_{\rm r}\,\cos(2\omega_{\rm d})\,\hat{\sigma}_x\right)\,|\psi_{\rm d}\rangle \tag{1.88}$$

Where the detuning Δ is defined as $\Delta \equiv \omega_0 - \omega_{\rm d}$. Finally, we drop the quickly rotating terms at frequency $2\omega_{\rm d}$ conserving only the time-independent terms in virtue of the rotating-wave approximation (RWA):

$$i\hbar\,\partial_t\,|\psi_{\rm d}\rangle = \frac{\hbar}{2}\left(-\Delta\,\hat{\sigma}_z + \Omega_{\rm r}\,\hat{\sigma}_x\right)\,|\psi_{\rm d}\rangle \tag{1.89}$$

This equation corresponds to the Schrödinger equation 1.24 of a two level system with the effective Hamiltonian:

$$\hat{H}_0' = -\frac{1}{2}\hbar\,\Delta\,\hat{\sigma}_z + \frac{1}{2}\hbar\,\Omega_{\rm r}\,\hat{\sigma}_x \tag{1.90}$$

In the frame rotating at $\omega_{\rm d}$, we see that the Hamiltonian acquires a term proportional to $\hat{\sigma}_x$ which gives rise to oscillations between the qubit states, that are named Rabi oscillations. In the next subsection, we explicitly derive this result in the resonant case.

1.3.4.2 Resonant case

In the resonant driving regime, the detuning Δ between the drive frequency $\omega_{\rm d}$ and the bare frequency ω_0 of the two-level system is equal zero. Thus, the Hamiltonian driving the dynamics of the qubit is only

$$\hat{H}_0' = \frac{1}{2}\hbar\,\Omega_{\rm r}\,\hat{\sigma}_x \tag{1.91}$$

By substituting the explicit form of the state vector $|\psi_{\rm d}\rangle = \alpha_0\,|0_{\rm d}\rangle + \alpha_0\,|1_{\rm d}\rangle$ into Eq. 1.89 and separating the equations for $|0_{\rm d}\rangle$ and $|1_{\rm d}\rangle$, we obtain:

$$\dot{\alpha}_0 = -i\frac{\Omega_{\rm r}}{2}\alpha_1 \qquad \dot{\alpha}_1 = -i\frac{\Omega_{\rm r}}{2}\alpha_0 \tag{1.92}$$

The solutions of these equations are, up to a global phase:

$$\begin{aligned}\alpha_0(t) &= \alpha_0(0)\,\cos\left(\frac{\Omega_r\,t}{2}\right) - i\,\alpha_1(0)\,\sin\left(\frac{\Omega_r\,t}{2}\right)\\ \alpha_1(t) &= \alpha_1(0)\,\cos\left(\frac{\Omega_r\,t}{2}\right) - i\,\alpha_0(0)\,\sin\left(\frac{\Omega_r\,t}{2}\right)\end{aligned} \tag{1.93}$$

Where $\alpha_0(0)$ and $\alpha_1(0)$ represent the initial state $|\psi_{\rm d}(0)\rangle$ of the two-level system. For instance, when the two-level system is initially in the south pole of the Bloch sphere $|\psi_{\rm d}(0)\rangle = |0_{\rm d}\rangle$, the state of the two level system at a later time "t" is:

$$|\psi_{\rm d}(t)\rangle = \cos\left(\frac{\Omega_r\,t}{2}\right)|0_{\rm d}\rangle - i\,\sin\left(\frac{\Omega_r\,t}{2}\right)|1_{\rm d}\rangle \tag{1.94}$$

The Bloch sphere representation of the state vector $|\psi_{\rm d}(t)\rangle$ is:

$$|\psi_{\rm d}(t)\rangle = \begin{bmatrix} 0 \\ -\sin(\Omega_r\, t) \\ \cos(\Omega_r\, t) \end{bmatrix} \tag{1.95}$$

Notice that the pseudo-spin representing the state of the two-level system $|\psi_{\rm d}(t)\rangle$ is undergoing a counter-clockwise rotation around the x-axis of the Bloch sphere with angular frequency $\Omega_{\rm r}$. This rotation of the pseudo-spin, in the frame rotating at the drive frequency, is generated by the effective Hamiltonian $\hat{H}_0' = \frac{1}{2}\hbar\,\Omega_{\rm r}\,\hat{\sigma}_x$ (Eq. 1.91).

1.4 Qubit readout

In the previous section we have seen how to initialize any qubit state by driving Rabi oscillations, in this section we describe how the state of a qubit can be readout by coupling it to a far-detuned microwave resonator.

1.4.1 Jaynes-Cummings Hamiltonian

The interaction between a qubit and a single cavity mode is captured by the Jaynes-Cummings Hamiltonian. The qubit Hamiltonian is $\hat{H}_0 = (-\hbar\omega_0/2)\hat{\sigma}_z$, the micowave resonator mode Hamitonian is $\hat{H}_r = \hbar(\hat{a}^\dagger\hat{a} + 1/2)$. The non-trivial dynamics of the system stems from an additional term in the Hamiltonian, accounting for the coupling between the qubit and the resonator mode. This interaction Hamiltonian writes $\hat{H}_{\rm int} = \hbar g(\hat{a}\hat{\sigma}^+ + \hat{a}^\dagger\hat{\sigma}^-)$, where $\hat{\sigma}^+$ and $\hat{\sigma}^-$ are the ladder operators for the qubit states, and where g denotes the coupling strength. g has the dimension of a frequency, and represents the energy exchange rate between the qubit and the resonator mode. If $g \gg \omega_0, \omega_r$, we get

$$\hat{H} = -\frac{\hbar\omega_0}{2}\hat{\sigma}_z + \frac{\hbar\omega_r}{2}(\hat{a}^\dagger\hat{a} + 1/2) + \hbar g(\hat{a}\hat{\sigma}^+ + \hat{a}^\dagger\hat{\sigma}^-). \tag{1.96}$$

Note that, in order to make sure that the system dynamics is not predominantly influenced by the interaction with the environment, such that the Jaynes-Cummings Hamiltonian accurately describes the system's time evolution, it is crucial to achieve the strong coupling limit. In this regime, the coupling strength must exceed the decay rates of the qubit and the losses in the cavity ($g > \kappa, \Gamma_1, \Gamma_2$).

1.4.2 Far-detuned limit, dispersive coupling

In the far-detuned regime, application of a unitary transformation followed by perturbation theory[11] yields an effective Hamiltonian:

$$\hat{H}_{\rm eff} = \hbar\left(\omega_r + \frac{g^2}{\Delta}\hat{\sigma}_z\right)\hat{a}^\dagger\hat{a} + \frac{\hbar}{2}\left(\omega_0 + \frac{g^2}{\Delta}\right)\hat{\sigma}_z.$$

The frequency of the resonator is shifted by $\chi = 2g^2/\Delta$ when changing the qubit state from $|0\rangle$ to $|1\rangle$. It is usually referred to as as the dispersive shift. It enables the readout of the qubit state by monitoring the resonator frequency, as shown in Fig. 1.5.

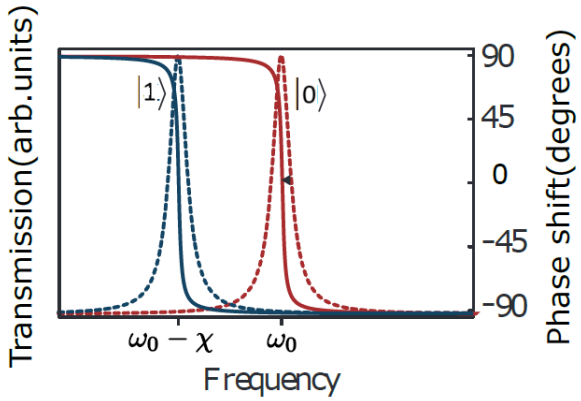

Fig. 1.5 *Reproduced from [7].* ***Dispersive shift of and ancillary resonator dispersively coupled to a qubit:*** *Amplitude (dashed lines) and phase (solid lines) of the readout resonator field as a function of the frequency of the drive signal when the qubit is in state $|0\rangle$ (red lines) or $|1\rangle$ (blue lines). The readout resonator resonance frequency shift depends on the qubit state ($|0\rangle$ or $|1\rangle$). The signal is mostly absorbed at frequency ω_0 (resp $\omega_0 - \chi$) when the qubit is in the ground (resp excited) state.*

1.5 Qubit coherence properties

In the last section, we have seen how to extract information regarding the qubit state through the coupling of an additional resonator. In this section, we describe the decoherence of the qubit induced by the interaction with its global environment.

We will consider two mechanisms, relaxation and dephasing. Relaxation is an energy exchange between the qubit and the environment that occurs at a rate γ_1. Dephasing corresponds to the loss of information about the phase of the superposition of the qubit basis states at a rate of γ_ϕ. It is caused by fluctuations in the qubit frequency due to fluctuations in the environment state.

1.5.1 Lindblad Master Equation

The qubit-environment interaction is described by the Linblad master equation [49], which introduces some decoherence terms, namely the jump operators $\hat{L}$, into the Schrödinger evolution equation of the density matrix $\hat{\rho}$:

$$\frac{\partial \hat{\rho}}{\partial t} = \frac{-i}{\hbar}[\hat{H}_0, \hat{\rho}] + \sum_{\hat{L}} \mathcal{D}_{\hat{L}}(\hat{\rho}), \tag{1.97}$$

with:

$$\mathcal{D}_{\hat{L}}(\hat{\rho}) = \hat{L}\hat{\rho}\hat{L}^\dagger - \frac{1}{2}\hat{L}^\dagger\hat{L}\hat{\rho} - \frac{1}{2}\hat{\rho}\hat{L}^\dagger\hat{L}. \tag{1.98}$$

and $\hat{H}_0 = (-\hbar\omega_0/2)\hat{\sigma}_z$ the qubit Hamiltonian. the jump operators describing the relaxation and dephasing phenomena can be written as:

$$\hat{L}_{\mathrm{r}_-} = \sqrt{\gamma_1(n_{\mathrm{th}}+1)}\hat{\sigma}^- \tag{1.99}$$

$$\hat{L}_{\mathrm{r}_+} = \sqrt{\gamma_1 n_{\mathrm{th}}}\hat{\sigma}^+ \tag{1.100}$$

$$\hat{L}_{\Phi} = \sqrt{\frac{\gamma_{\Phi}}{2}}\hat{\sigma}_{\mathrm{z}}. \tag{1.101}$$

Due to the non-zero temperature of the environment, the relaxation operator is split into two parts, describing the gain ($\hat{L}_+$) and loss ($\hat{L}_-$) of a qubit excitation. The evolution rates $\Gamma_\downarrow = \sqrt{\gamma_1(n_{\mathrm{th}}+1)}$ and $\Gamma_\uparrow = \sqrt{\gamma_1 n_{\mathrm{th}}}$ are determined by the environment mode occupancy $n_{\mathrm{th}} = 1/(e^{\hbar\omega_0/k_{\mathrm{b}}T}-1)$ (following Bose-Einstein statistics), for an environment at temperature T.

The master equation 1.97 and the trace properties of the density matrix ($Tr(\hat{\rho}) = 1$) gives the following first-order derivatives:

$$\frac{d\rho_{00}}{dt} = -\gamma_1 n_{th}\rho_{00} + (1-\rho_{00})\gamma_1(n_{th}+1) \tag{1.102}$$

$$\frac{d\rho_{01}}{dt} = -\frac{\gamma_1 n_{th}\rho_{01} + \gamma_1\rho_{01}\,(n_{th}+1)}{2} - \gamma_\phi\rho_{01} - i\omega_q\rho_{01} \tag{1.103}$$

where ρ_{ij} represents the density matrix components. We solve the first order differential equation for each components. The final density matrix reads:

$$\rho_{00}(t) = A_1 e^{-(\gamma_1+2\gamma_1 n_{\mathrm{th}})t} + \frac{n_{\mathrm{th}}+1}{2n_{\mathrm{th}}+1} \tag{1.104}$$

$$\rho_{01}(t) = A_2 e^{-(i\omega_{\mathrm{q}}+\gamma_\Phi+\frac{\gamma_1}{2}+\gamma_1 n_{\mathrm{th}})t} \tag{1.105}$$

with the A_1 and A_2 defined by the initial conditions.

1.5.2 Relaxation time, and impact of a non-zero thermal populations

From the density matrix calculated in the last section, several characteristic times can be defined. $1/\gamma_1$ is the pure relaxation time of the qubit at zero-temperature, while $T_1 = 1/(\gamma_1 + 2\gamma_1 n_{\mathrm{th}})$ is the total relaxation time in the presence of a non-negligible average occupancy of the bath modes. In the following, this work presents the manipulation of a very low frequency qubit (1.8 MHz) in a cryogenic environment (10 mK). Under these conditions, $\hbar\omega_0/(k_{\mathrm{b}}T) \ll 1$ and we can make the approximation: $n_{\mathrm{th}} \sim k_{\mathrm{b}}T/(\hbar\omega_0) \gg 1$.

In this particular case, the qubit has almost equal ground and excited state populations at equilibrium. The relaxation time is reduced to $T_1 \sim 1/(2\gamma_1 n_{\mathrm{th}})$, much smaller than the pure zero-temperature relaxation time $1/\gamma_1$ (see Figure 1.6), and is completely dominated by the thermal effect.

Experimentally, the relaxation time is determined by initially placing the qubit in its excited (or ground) state, allowing some time to elapse, and then employing the measurement technique described in section 1.4.

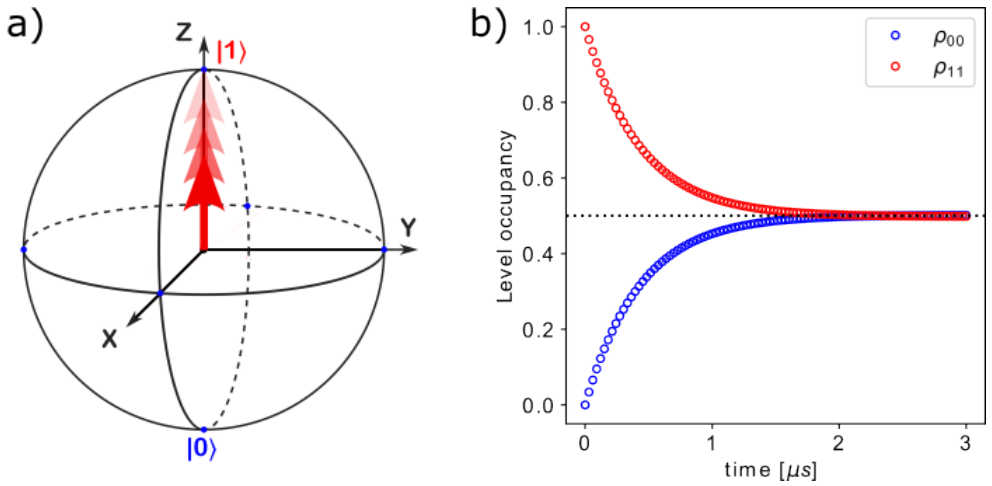

Fig. 1.6 ***Qubit relaxation in presence of a thermal bath*** *a) Bloch sphere representing a qubit in its excited state, which relaxes to a statistical mixture of excited and ground states. b) Evolution of the diagonal matrix element when* $n_{\mathrm{th}} = 115$ *and* $1/\gamma_1 = 100$ μs*. Due to the thermal bath, the observed relaxation time would be reduced to* $T_1 = 0.43$ μs*.*

1.5.3 Dephasing time and Ramsey sequence

In a similar way, we can define $T_\Phi = 1/\gamma_\Phi$, the pure dephasing time. The total dephasing time, $1/T_2 = 1/2T_{1,\mathrm{tot}} + 1/T_\Phi$ includes the pure dephasing time but also an energy relaxation component which ultimately limits its value to $2T_1$.

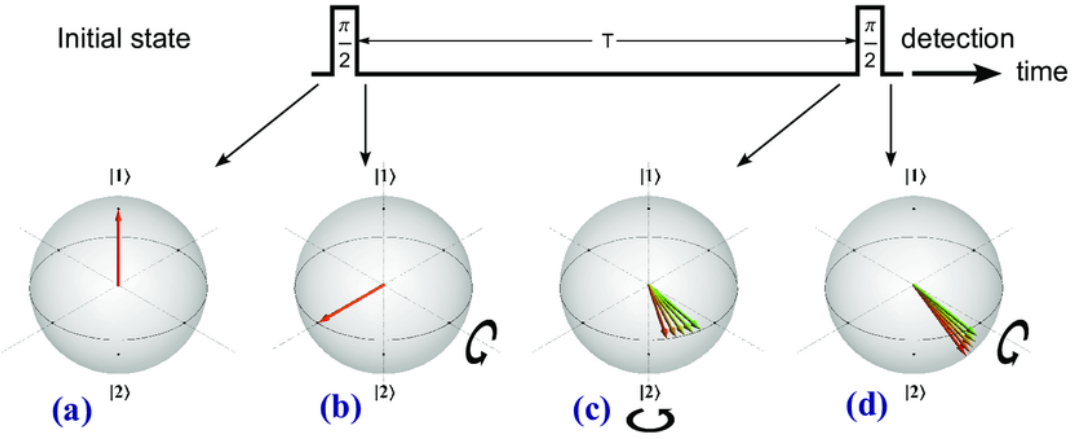

Fig. 1.7 ***Bloch sphere representation of a Ramsey interferometer.***

The coherence time T_2 can be determined experimentally using the Ramsey sequence (see Figure 1.7), which is well known in the field of magnetic resonance [63]. The qubit is first initialized in its fundamental state, then placed in the equator of the Bloch sphere by means of a resonant pulse (see section 1.3.4). After a waiting period, another pulse identical to the first is applied. If the qubit does not change of frequency during the waiting time, it will be in its excited state at the end of the sequence. On the other hand, if a frequency

fluctuation occurs, it will have a non-zero probability of being in its ground state.

The coherence time T_2 is the characteristic time after which the qubit is measured equally in its fundamental and excited states at the end of the Ramsey sequence.

Conclusion In this chapter, we have established the fundamentals of superconducting circuits, emphasizing the role of the Josephson junction in introducing non-linearity crucial for the realization of two-level quantum systems. We have also introduced various techniques that are pivotal to circuit quantum electrodynamics (circuitQED), such as qubit readout, manipulation, and the measurement of coherence properties. These techniques will be implemented in the experimental contexts of Chapters 5 and 6. However, before delving into these applications, the next chapter will focus on the specific type of qubit used in our investigations—the fluxonium qubit.

Chapter 2

Fluxonium fundamentals

In this chapter, we introduce the Fluxonium circuit—a distinct type of superconducting qubit where the Josephson junction is shunted by an inductive element. We begin by addressing a fundamental limitation of traditional charge qubits in section 2.1: their susceptibility to offset-charge fluctuations due to random voltage noise on the capacitor electrodes. These fluctuations often result in significant dephasing and operational instability. While transmons are engineered to be exponentially protected against charge noise, this design inherently involves a trade-off between dephasing rate and anharmonicity. In section 2.2, we delve into the Fluxonium's Hamiltonian, illustrating its intrinsic protection against charge offset that does not compromise anharmonicity. Next, in section 2.3, we explore the excitation spectrum of the Fluxonium, providing a phenomenological description of its diverse transitions. Finally, in section **??**, we introduce the heavy-Fluxonium regime, which plays a pivotal role in the context of this work. In particular, we show the exponential dependence of the qubit frequency as a function of circuit parameters.

2.1 Limitations of charge qubits

The development of one of the earliest quantum superconducting circuits, the charge qubit, often referred to as the *Cooper-pair box* (CPB) [15], heralded potential breakthroughs in the domains of quantum information [8, 57] and high-sensitivity measurements, such as quantum metrology. Essentially, the CPB operates by manipulating the quantum state of a pair of superconducting electrons, known as a Cooper pair, across a small insulating barrier (see Fig. 2.1). However, it was quickly realized that such devices were strongly limited by dephasing, the loss of quantum coherence that destroys interference and makes quantum systems to behave as classical ones. In the case of the Cooper-pair box, the dephasing was mainly the effect of slowly drifting microscopic charges, the offset charges, which were common to solid states systems [**?**]. To address this issue, substantial advancements were initially directed towards the design of superconducting qubits. A critical milestone was achieved in 2007 when Koch et al. [45] demonstrated that shunting the Cooper pair box with a large capacitance offers some protection to the qubit against the decoherence effects due to charge noise. This insensitivity is achieved by diminishing the energy associated with offset charge fluctuations, thereby broadly de-localizing the wave function over several states in charge states (effectively reducing the phase zero-point fluctuations).

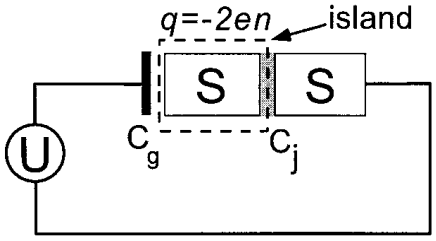

Fig. 2.1 ***The Cooper pair box:*** *In a piece of isolated a superconducting metal, the box (dashed line), the charge is quantized in units of* $2e$*. The box is allowed to exchange Cooper-pairs with another piece of superconducting material, a reservoir, through a Josephson junction. An electrode shunted to the island by the gate capacitance* C_g *controls the potential* U*, or equivalently the offset charge on the island,* $n_g = C_g U/2e$*, in units of Cooper pairs. The junction favors the tunneling of pairs of electrons, however, the addition of an extra Cooper-pair on the box rises the electrostatic energy by the amount* $4E = (2e)^2/2C_j$*, representing the Coulomb repulsion, where* C_j *is the capacitance between the islands.*

The Hamiltonian of the transmon and the Cooper pair box is:

$$\hat{H} = 4E_C(\hat{N} - n_g)^2 - E_J \cos(\hat{\varphi}) \tag{2.1}$$

Where E_C is the capacitive energy, E_J is the Josephson energy and $\hat{N}$ and $\hat{\varphi}$ are conjugated operators. This Hamiltonian describes the scenario of a superconducting island, a box, that is allowed to exchange Cooper-pairs through a Josephson junction with another piece of superconducting material acting as a reservoir (see Figure 2.2). The $\hat{N}$ operator corresponds to the excess of Cooper pairs in the island, and n_g is the offset charge in units of Cooper pairs, it represents the potential at the island. The operator $\hat{\varphi}$ is related to the superconducting phase difference between the two sides of the junction, which is the conjugated variable of charge on the island. The operator $\hat{N}$ has a discrete set of eigenvalues resulting from the quantization of the charge in the island in units of $2e$. Reciprocally, the wave function $\psi(\varphi)$ in phase space is periodic, up to a global phase, with a period of 2π. The coefficient $4E_C$ is the change of the island electrostatic energy associated to the excess of 1 Cooper-pair:

$$E_C = \frac{e^2}{2C} \tag{2.2}$$

Where C is the total capacitance of the island and e is the electron charge. The coefficient E_J is the energy gain when a Cooper pair tunnels across the junction. Both the Cooper-pair box and the transmon are described by the same hamiltonian 2.1, but at different regimes of the parameters E_C and E_J. This hamiltonian describes a Cooper-pair box when $E_J/8E_J \gtrsim 1$, while it describes a transmon when $E_J/8E_J \gg 1$. The coefficient $E_J/8E_J$ determines the ratio between the phase zero-point fluctuations φ_{zpf} and the charge zero-point fluctuations N_{zpf}, and it is related to the impedance of the circuit Z_0.

An offset charge n_g in the island translates into a complex phase $e^{in_g\varphi}$ affecting the the boundary conditions of the wavefunction $\psi(\varphi)$. This effect is less detrimental for the transmon as it is for the Cooper pair box, since this last one presents smaller phase zero-point

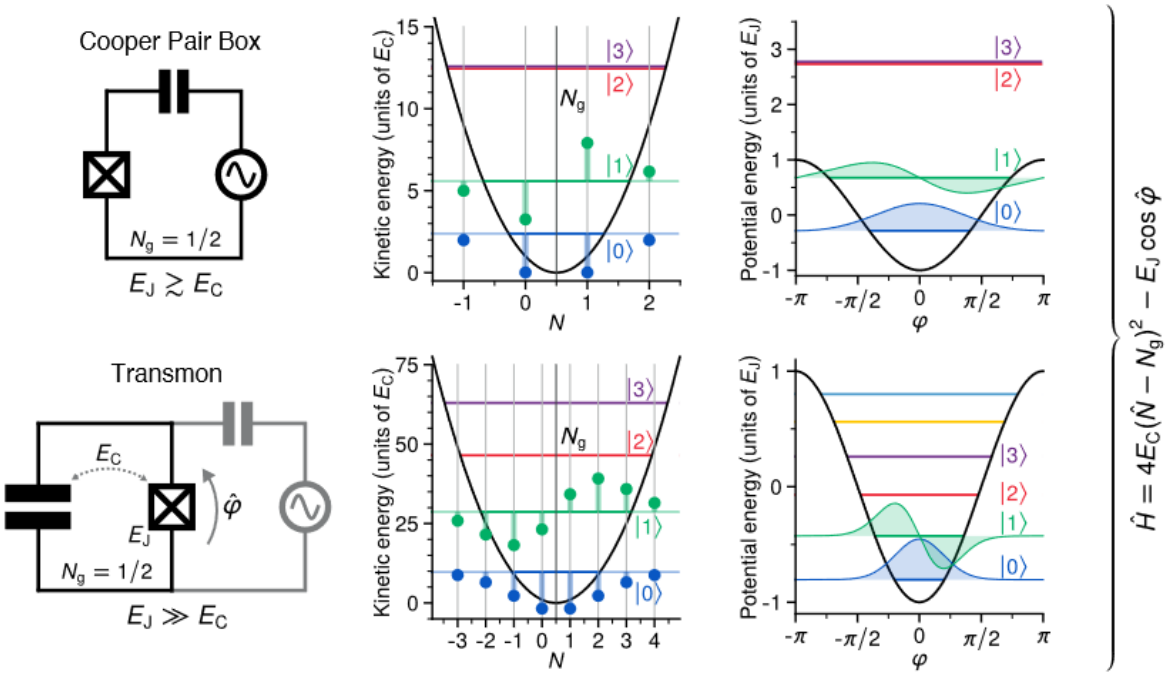

Fig. 2.2 ***Transmon vs Cooper-pair box:*** *Both quantum circuits are described by the same hamiltonian, but at different parameter regimes: $E_J/E_C \gtrsim 1$ for the Cooper-pair box, while $E_J/E_C \gg 1$ for the transmon. In the limit of an opaque junction $E_J \ll E_C$, the circuit hamiltonian 2.1 is dominated by the Coulomb repulsion between the Cooper pairs. In this case, charge fluctuations are very small $N_{\text{zpf}} \ll 1$, and the charge of the island $\langle N \rangle$ is essentially fixed at the value N_0 that minimizes the electrostatic energy, $4E_C(N_0 - n_g)^2$. When the junction transparency is high $E_J \gtrsim E_C$, in the Cooper-pair box regime, the junction favors the tunneling of Cooper pairs into the island, generating charge fluctuations around around the mean value $\langle N \rangle \approx n_g$, such that the wavefunction is a linear combination of few charge states $|N\rangle$. In the limit of when the junction transparency is very high, in the transmon regime, $E_J/E_C \gg 1$, the wavefunction is broadly delocalized over many charge states $|N\rangle$. Because of Heisenberg's indeterminacy principle, the wavefunction is then more confined around its mean value in φ-space. These reduced phase zero-point fluctuations $\varphi_{\text{zpf}} \ll 1$ of the transmon wavefunctions results in less sensitivity to offset charges. Both the Cooper-pair box and the transmon are operated at the sweet spot, $n_g = 0.5$, such that they are (first-order) insensitive to offset-charge noise.*

fluctuations $\varphi_{\text{zpf}} = \sqrt{8E_C/E_J}$, having states that are more confined in the phase φ-space. However, the increased insensitivity to offset charges of the transmon comes at the price of a lower anharmonicity. While $\psi(\varphi)$ becomes more localized in phase φ space, the high-order terms of the cosine potential in Equation 2.1 become less relevant, such that $\cos(\varphi)$ can be well approximated as $\varphi^2/2 - \varphi^4/24$. In this limit case, the Hamiltonian of the transmon 2.1 resembles the one of a linear LC-resonator with only a small distortion of the parabolic potential. Thus, the energies of the eigen-states are almost equally spaced (see Figure 2.2), resulting in small anharmonicity. The small anharmonicity is a limiting factor when the superconducting circuit is intended to be used as a qubit, a two-level system for quantum information applications. The anharmonicity determines how fast one can drive the two-level

system without pumping other higher energy levels. In the transmon regime, the sensitivity to offset charges reduces exponentially with E_J/E_C, while the anharmonicity only decreases algebraically with a slow power law in E_J/E_C. Therefore, there is always a compromise between noise sensitivity and anharmonicity for the Cooper-pair box and the transmon circuits [45].

2.2 A DC charge-offset free superconducting circuit: the fluxonium

In 2009, the group of Michel Devoret proposed a new device for reducing the sensitivity to offset-charges [52]: the fluxonium circuit. This circuit is realised by shunting the Josephson junction of a transmon with a large inductance (see Figure 2.3). The effect of this inductance is to cancel out DC offset charges. This work was very challenging, since it required to fabricate a super inductance, that is to say an on-chip component with a high impedance that behaves like a linear pure inductance.

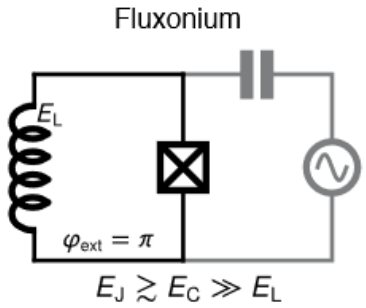

Fig. 2.3 ***Fluxonium circuit:*** *The Hamiltonian in Eq. 2.3 describes the scenario of two superconducting electrodes (nodes) shunted by a Josephson junction and an inductive "wire" at the same time. The variable φ is the flux circulating in the loop between the wire and the Josephson junction, and its conjugated variable N is the displacement charge on the junction electrodes. The fluxonium regime corresponds to $E_J > E_C \gg E_L$.*

2.2.1 Hamiltonian

The fluxonium circuit is described by the following Hamiltonian

$$\hat{H} = 4E_C(\hat{N} - n_g)^2 + \frac{E_L}{2}(\hat{\varphi} - \varphi_{\text{ext}})^2 - E_J \cos(\hat{\varphi}) \tag{2.3}$$

This Hamiltonian describes two superconducting electrodes connected by a Josephson junction and an inductance L. The variable φ represents the flux across the Josephson junction, and its conjugated variable N is the displacement charge on the capacitor plate in units of Cooper pairs. This Hamiltonian is analogous to that of a particle moving in a 1D potential. The particle has a position(-like variable) φ and a momentum(-like variable) N. In this picture, the inductance, with associated energy E_L, results in a parabolic contribution to

the potential energy (second term in Eq. 2.3). Also, note that E_L represents the energy of one flux quantum threading the fluxonium loop:

$$E_L = \frac{\phi_0^2}{4\pi^2 L} = \frac{\Phi_0^2}{L} \tag{2.4}$$

where L is the inductance, $\phi_0 = h/2e$ is the quantum of flux, and $\Phi_0 = \hbar/2e$ is the reduced flux quantum. The Josephson junction, with associated energy E_J, results in a sinusoidal potential energy (third term in Eq. 2.3). The first term in Eq. 2.3, that is quadratic in the momentum-like variable, is analogous to the kinetic energy of the particle. Overall, the fluxonium physics is equivalent to a particle evolving in a potential landscape that is the sum of a parabola and a sinusoid (see Figure 2.4). In this scenario, there are typically a few trapped states within the wells defined by the deeps of the sinusoidal potential.

Note that shunting the junction by an inductance has two main consequences: First, compared to the transmon case, the flux representation of the wave-function $\psi(\varphi)$ is no longer periodic. As a consequence, the charge operator N has no longer a discrete set of eigenvalues, but a continuous spectrum, and the wave functions $\psi(\varphi)$ and $\psi(N)$ (flux and charge representations) are connected by a conventional Fourier transform. Second, an external magnetic flux φ_{ext} can be threaded into the superconducting loop made by the inductor and the Josephson junction. This provides an additional external control parameter that allows to shift the parabolic term of the potential energy with respect to the sinusoidal one. The third consequence is an intrinsic immunity to DC offset-charges. It will be the subject of the next section, but we can intuitively think of the inductance as a perfect wire for

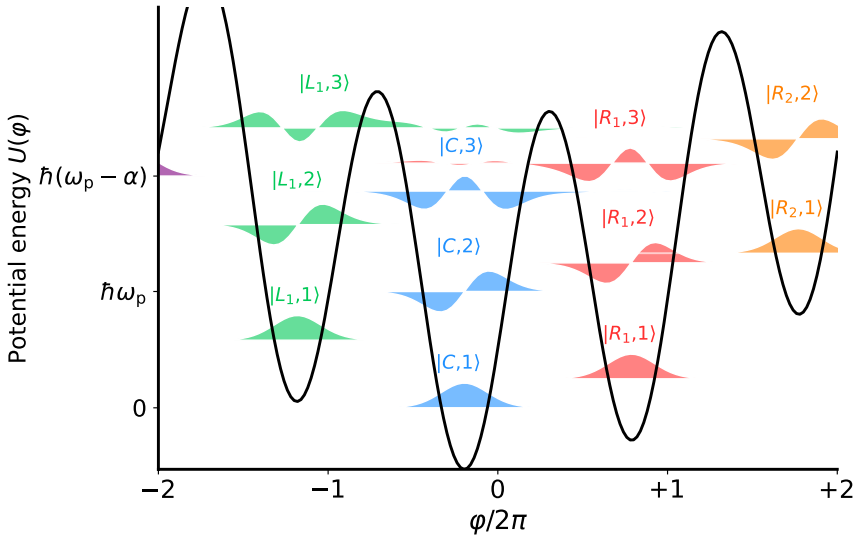

Fig. 2.4 ***Potential energy and few levels of the fluxonium:*** *The potential energy of the fluxonium is the sum of a parabola and a sinusoid. This particular mixture results in a set of wells that are defined by the deeps of the sinusoidal potential. Each well contain few trapped states that are practically localized within the well. In this schematics, the trapped states are labeled with a letter referring for the well, "L" for right, "C" for center, "R" for right, and a number labeling the different states within each well.*

slowly varying offset-charge fluctuations, keeping both electrodes of the junction at the same potential.

2.2.2 Intrinsic insensitivity to DC charge offset

Let us consider the Hamiltonian of the fluxonium (Eq. 2.3) at zero offset-charge ($n_g = 0$), $\hat{H}(n_g = 0) = \hat{H}(0)$. Given that $|\Psi(0)\rangle$ is an eigenfunction of $\hat{H}(0)$ with energy $E(0)$, we have

$$\hat{H}(0)\,|\Psi(0)\rangle = E(0)\,|\Psi(0)\rangle\,. \tag{2.5}$$

We then consider the unitary transformation:

$$|\Psi(0)\rangle = \hat{U}_{n_g}\,|\Psi(n_g)\rangle \quad , \qquad \hat{U}_{n_g} \equiv e^{-in_g\hat{\varphi}} \tag{2.6}$$

This transform represents a charge displacement by n_g (being equivalent to a translation in momentum space in the analogous mechanical problem). Adding a charge n_g thus amounts to applying the following transform to $\hat{H}(0)$:

$$\hat{U}^{\dagger}_{n_g}\,\hat{H}(0)\,\hat{U}_{n_g} = \hat{H}(n_g) \tag{2.7}$$

By applying the gauge transform 2.6 to the eigen-value Equation 2.5, we find the $\hat{U}_{n_g}$ adds an offset charge to the hamiltonian, $\hat{H}(0) \to \hat{H}(n_g)$, while leaving the energy E of the state invariant $E(n_g) = E(0)$. This matches the intuitive picture of the inductance acting as a perfect wire that keeps the two electrodes of the junction at the same electrostatic potential. Now, let us consider a time-dependent charge modulation, e.g., $n_g = n_g(t)$ is a slowly varying function of time. For instance, let us consider the Hamiltonian of the fluxonium $\hat{H}(n_g)$ with a time-dependent offset-charge $n_g(t) = A\cos\omega_d t$. The time-independent Schrodinger equation must be replaced by the time-dependent one:

$$i\hbar\partial_t\,|\Psi\rangle = \hat{H}(n_g(t))\,|\Psi\rangle\,. \tag{2.8}$$

However, when trying to get rid of the offset-charge term in the R.H.S by applying the unitary transform $\hat{U}(-n_g)$ as $|\Psi\rangle = \hat{U}\,|\psi\rangle$, a new term proportional to the time derivative of n_g arises in the L.H.S. of the Schrodinger equation, specifically $-\hbar\,\dot{n}_g(t)\hat{\varphi}\,|\psi\rangle = i\hbar\,\omega_d\,n_g\hat{\varphi}\,|\psi\rangle$. This term has to be compared to the inductive energy of the qubit E_L. Finally, the hamiltonian effectively transforms as

$$\hat{H}(n_g) \to \hat{H}(0) - i\,E_L\left(\frac{LI_g}{\phi_0/2\pi}\right)\hat{\varphi} \tag{2.9}$$

The previous equation means that a time-dependent offset-charge $n_g(t)$ generates a current $I_g \equiv 2e\,\omega_d\,n_g$, that is then turned into a flux-offset $\varphi_g \equiv 2\pi\,L\,I_g/\phi_0$ by the inductance. This result agrees with the classical intuition about an inductance. Therefore, the fluxonium remains insensitive to offset-charge fluctuations, as long as the corresponding current in the inductance remains small, e.g., $I_g \ll I_c = \phi_0/(2\pi L)$, or equivalently, as long as the corresponding flux-offset $\phi_g = 2\pi L I_g$ is much smaller than the flux quantum ϕ_0.

2.2.3 Fluxonium-regime

In this section, we will explain that what we name fluxonium regime, corresponds to the following parameter regime of the Hamiltonian of Eq. 2.3:

$$\frac{E_J}{E_L} \gg 1 \; ; \qquad \frac{E_J}{E_C} > 1 \tag{2.10}$$

This conditions can also be stated as $E_J > E_C \gg E_L$ (see Figure 2.5). The first inequality, $E_J/E_L \gg 1$, means that the potential energy, $\frac{E_L}{2}(\varphi - \varphi_{\text{ext}})^2 - E_J \cos(\varphi)$, resembles a series of potential wells at locations close to $\varphi = (2m-1)\pi$, with "m" an integer. The parabolic term, proportional to E_L, shifts the height of the wells with respect to each other. We typically refer to the well that contains the absolute minimum of the potential energy as the central well. Notice that the potential energy is a periodic function of the external flux φ_{ext} with a period of 2π.

The second inequality, $E_J/E_C > 1$, means that each potential well contains at least one trapped state. In general, these states have a non-zero mean value of the flux $\Phi_0 \langle\varphi\rangle$, but a zero mean value of the charge $2e \langle N\rangle$. They represent states of a frictionless current circulating in the loop made by the Josephson junction and the superinductance (see Figure 2.3). If we take $2E_J$ as the approximate depth of a well, and we consider that inside the well the levels are almost equally spaced by:

$$\hbar\omega_{\text{plasmon}} \equiv \sqrt{8E_C(E_J + E_C)} \approx \sqrt{8E_C E_J} \tag{2.11}$$

This results from approximating the cosine potential with related energy E_J around the center of the well as a parabola. The number of levels inside each well ℓ_{well} then scales as:

$$\ell_{\text{well}} \sim \frac{2E_J}{\sqrt{8E_C E_J}} = \sqrt{\frac{E_J}{2E_C}} \tag{2.12}$$

Thus, for a fixed E_J, decreasing E_C (increasing the capacitance C) makes the spectrum of levels inside each well more dense. This corresponds to increasing the mass of the particle in the equivalent mechanical problem. Therefore, the capacitance C plays the role of the mass of the particle, and E_C is equivalent to the reciprocal of the particle mass.

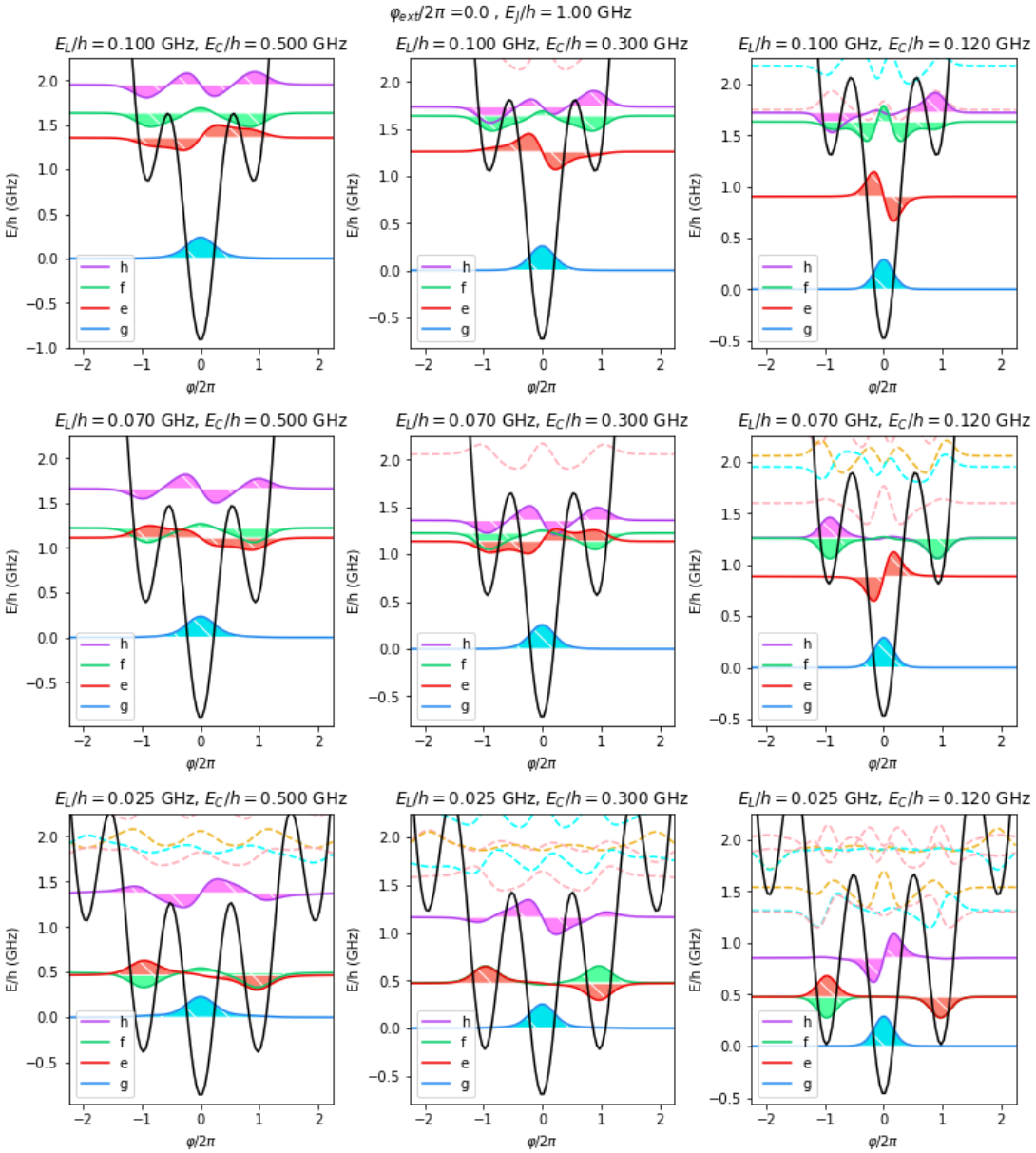

Fig. 2.5 ***Fluxonium-regime:*** *lower energy states for different values of the ratios E_C/E_J and E_L/E_J (with $E_J = 1$ GHz) at zero external flux φ_{ext}. The ratio E_C/E_J decreases from the left column to the right column, corresponding to an increasing number of trapped states inside the central well increases: 1 trapped state (left), 2 trapped states (center), 3 trapped stated (right). The ratio E_L/E_J decreases from the top row to the bottom row, it controls the energy difference between the first state in the central well and the first state in the adjacent wells. There is an additional condition to consider only when operating at zero flux: $2\pi^2 E_L < \sqrt{8E_C E_J}$. It means that the second state inside the central well should be higher in energy than the first state in the adjacent wells. In the ideal case when $4\pi^2 E_L \approx \sqrt{8E_C E_J}$, these three levels hybridize resulting in a maximum anharmonicity (non-linearity of the low-frequency spectrum).*

2.3 Spectrum of the fluxonium circuit

This section provides the fundamental ideas to understand the low-energy spectrum of the fluxonium.

2.3.1 Plasmon/fluxon transitions

On the fluxonium low-frequency spectrum we can identify two kinds of transitions (see Figure 2.6): the plasmon-like transitions, that are transitions within the same flux-well (blue and red arrows in Figure 2.6), and the fluxon-like transitions that are transitions between different wells (black, green, orange and purple arrows in Figure 2.6). In the case of the plasmon-like transitions, we approximate the potential around the center of the well as a parabola with energy $\frac{E_J}{2}\varphi^2$. Then, the energy difference between the first and second state within the well is approximately $\hbar\omega_{\text{plasmon}} = \sqrt{8E_C E_J}$. Note that the plasmon transitions, do not depend on φ_{ext}.

The parabolic term in the potential changes the relative heights between the depths of adjacent wells, such that contrary to plasmon-like transitions, the frequencies of the fluxon-like transitions depend linearly on φ_{ext}. Let us consider the first fluxon-like transition, that is the transition between the first state in the central well and the first state in the adjacent well that is the closest in energy. Notice that the location of the lowest-energy state in the adjacent well (the right well in Figure 2.6) is $\varphi_{\text{R}}/2\pi \approx 1$. Thus, the energy difference

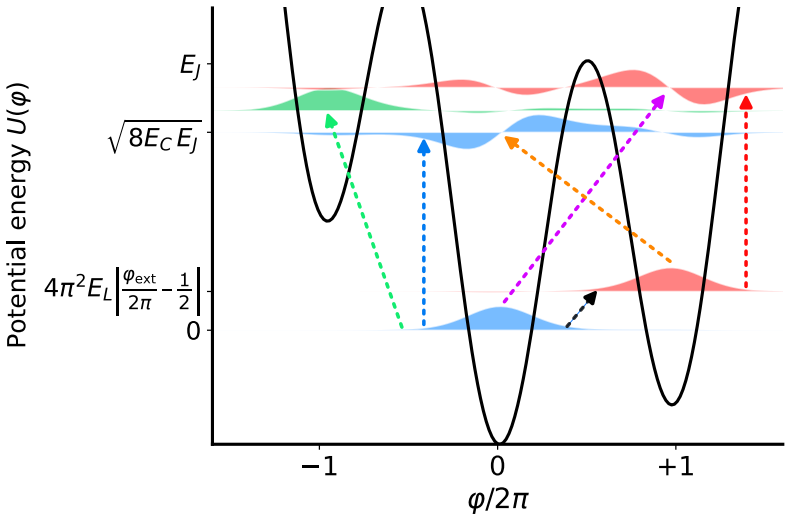

Fig. 2.6 ***Fluxonium transitions:*** *lower energy states. Two categories of transitions can be identified: the plasmon-like transitions that are transitions within the same potential well, and the fluxon-like transitions that are transitions between different wells. In this case, the plasmon transitions are for instance, represented by the blue and red arrows, while the fluxon transitions correspond to the black, green, orange and purple arrows. The fluxon transition are very sensitive to the relative energy height between the corresponding wells, which is determined by the external flux φ_{ext} threading the fluxonium loop.*

between the first state of the central well and the first state of the adjacent well is given by:

$$\hbar\,\omega_{\text{fluxon}} \approx \frac{E_L}{2}\left[(2\pi-\varphi_{\text{ext}})^2-\varphi_{\text{ext}}^2\right] = 4\pi^2 E_L\left|\frac{\varphi_{\text{ext}}}{2\pi}-\frac{1}{2}\right|. \tag{2.13}$$

The frequency of this transition reaches a maximum of $2\pi^2 E_L$ when the external flux is equal to zero, $\varphi_{\text{ext}} = 0$. Conversely, it reaches a minimum at the so-called flux-frustration point when $\varphi_{\text{ext}} = \pi$. In general, at these two interesting values of the external flux, pairs of wells are at the same relative energy level, allowing their localized states of equal energy to hybridize, resulting in avoided crossings.

2.3.2 Flux frustration point

In this section we discuss the low-frequency transition spectrum of the fluxonium around the flux frustration point, $\varphi_{\text{ext}}/2\pi = 0.5$, which will be the main working point in the experimental part of this thesis. As seen in Section 2.3.1, at zero external flux and at the flux frustration point, $\varphi_{\text{ext}} = \pi$, there are pairs of trapped states with the same energy belonging to different wells. Trapped states with mean flux $\langle\varphi\rangle \neq 0$ represent states of frictionless current circulating in the fluxonium loop, the so-called fluxons. These states hybridize at the avoided crossing resulting in superpositions of different states of frictionless current circulating the fluxonium loop. In particular, at the flux frustration point, the potential is a symmetric double well potential and the ground state $|g\rangle$ and the first excited state $|e\rangle$ are symmetric and anti-symmetric superpositions of the localized states of two adjacent wells (left and right).

Figure 2.7 shows the low-frequency transition spectrum of the fluxonium around the flux-frustration point, $\varphi_{\text{ext}}/2\pi = 0.5$. Slightly away from the flux-frustration point (dotted purple line in subpanel 2.7a), the energy difference between $|g\rangle$ and $|e\rangle$, $\hbar\omega_{ge}$, varies linearly with the external flux φ_{ext} according to Equation 2.13 and these states are localized in different wells (see subpanel 2.7c). At the flux-frustration point (dotted gray line in subpanels 2.7a and 2.7b), the energy splitting $\hbar\omega_{ge}$ reaches a minimum value, which is proportional to the tunneling rate of fluxons from one well to the other E_T/h. The states $|g\rangle$ and $|e\rangle$ become delocalized over the two wells (see panel 2.7d), left and right. Note that at the flux frustration point, for these two lower states, the problem reduces to the textbook problem of the ammonia molecule. There is a similar scenario happening for the second states (the first plasmon-like states) of the two adjacent wells at the flux frustration point $|f\rangle$ and $|h\rangle$. These states hybridize resulting in symmetric and anti-symmetric superpositions. However, the energy splitting between these higher energy states $\hbar\omega_{fh}$ is higher compared to $\hbar\omega_{ge}$ (see panel 2.7b) since the effective energy barrier seen by $|f\rangle$ and $|h\rangle$ is smaller (see panel 2.7d).

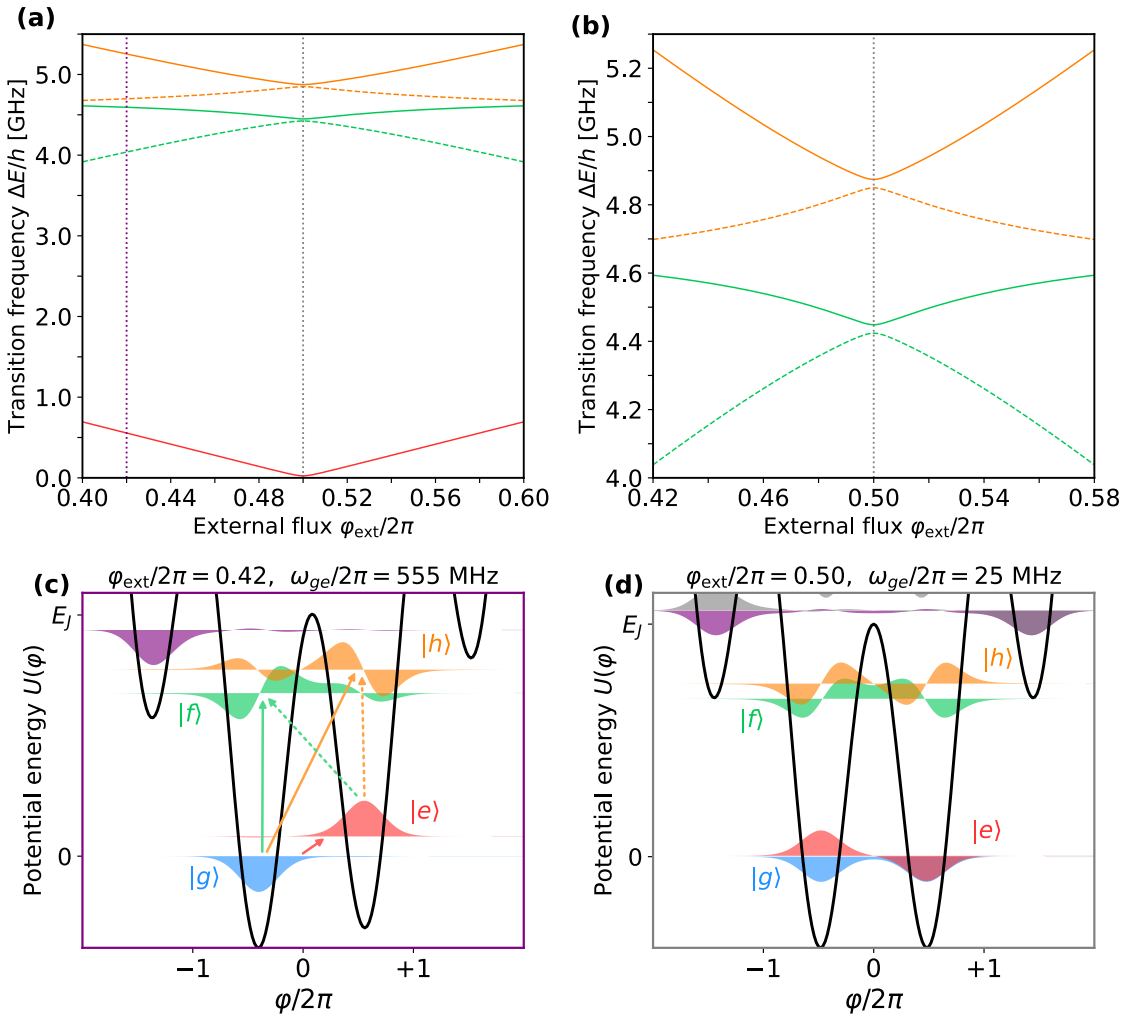

Fig. 2.7 ***Fluxonium spectrum around the flux frustration point:*** *(a) transition frequencies around the flux-frustration point, $\varphi_{\text{ext}}/2\pi = 0.5$. The solid (dashed) lines represent the transitions from the ground state $|g\rangle$ (first excited state $|e\rangle$). (b) Zoom into smaller frequency span. The difference between the frequencies of the "$|e\rangle \rightarrow |f\rangle$" transition (dashed-red) and the "$|g\rangle \rightarrow |f\rangle$" transition (solid-red) is the frequency of the "$|g\rangle \rightarrow |e\rangle$" transition (solid-blue line in subpanel a). The frequency of the "$|g\rangle \rightarrow |e\rangle$" transition, approximately 20 MHz, is two orders of magnitude smaller than the frequencies of the next pair of transitions "$|e\rangle \rightarrow |f\rangle$" (dashed-red) and "$|g\rangle \rightarrow |f\rangle$" (solid-red) that are around 4.45 GHz. (c) Slightly away from the flux frustration point, $\varphi_{\text{ext}}/2\pi = 0.42$, the lowest-energy states, $|g\rangle$, $|e\rangle$, $|f\rangle$ and $|h\rangle$, localized within a well. The energy splitting between $|g\rangle$ and $|e\rangle$ are symmetric and anti-symmetric super-positions of the localized states of the two adjacent wells (left and right) (d) At the flux frustration point, $\varphi_{\text{ext}}/2\pi = 0.5$, the lowest-energy states, $|g\rangle$, $|e\rangle$, $|f\rangle$ and $|h\rangle$, are symmetric and anti-symmetric super-positions of the localized states of the two adjacent wells (left and right). The parameters of the numerically simulated hamiltonian are $E_J = 5.00$ GHz, $E_C = 0.750$ GHz, $E_L = 0.185$ GHz.*

2.3.3 Heavy-fluxonium regime

As discussed in the previous section, at the flux-frustration point, $\varphi_{\text{ext}}/2\pi = 0.5$, the energy splitting between the ground $|g\rangle$ and first excited state $|e\rangle$ is given by the tunneling rate E_T/h between the left and right fluxon states. In the heavy-fluxonium regime, corresponding to $\frac{E_J}{E_C} \gg 1$, the barrier height $2E_J$ becomes much larger than the typical energy of the fluxon-states, such that the transition frequency decreases significantly compared to other circuit transitions. Figure 2.8 illustrates the scaling of the few first transition frequencies of the fluxonium, in particular as a function of the ratio between the Josephson energy E_J and the capacitive energy E_C.

To understand more quantitatively the scaling of the fundamental transition frequency, we can approximate the potential experienced by the fluxon states as quasi-parabolic, expressed as $\frac{E_J}{2}(\hat{\varphi} \pm \pi)^2$. In this approximation, the left- and right-well state wavefunctions $\psi_\pm(\varphi)$ are Gaussian wave-packets located at the center of their corresponding wells ($\pm\pi$) with zero-point fluctuations $\varphi_{\text{zpf}} = \sqrt[4]{8E_C/E_J}$.

$$\psi_\pm(\varphi) = (\pi\varphi_{\text{zpf}})^{-1/4} \exp\left(-\frac{1}{2}\left(\frac{\varphi \mp \pi}{\varphi_{\text{zpf}}}\right)^2\right). \tag{2.14}$$

The overlap between them, and thus, the energy splitting between $|g\rangle$ and $|e\rangle$, scales as:

$$E_T \sim e^{-\sqrt{\frac{\pi^4}{8}\frac{E_J}{E_C}}}. \tag{2.15}$$

From these basic considerations, we can already envision that the transition frequency between $|g\rangle$ and $|e\rangle$ at the flux-frustration point decreases exponentially as a function of the ratio $\frac{E_J}{E_C}$. Taking into account the parabolic correction due to the inductive energy, one can derive a better approximation of the fluxon tunneling rate:

$$E_T \approx \sqrt{8E_C\,E_J}\left(\frac{2E_J}{\pi^2 E_C}\right)^{1/4} \exp\left(-\sqrt{\frac{8E_J}{E_C}} + \frac{14\,\zeta(3)\,E_L}{\sqrt{8E_C\,E_J}}\right), \tag{2.16}$$

where $\zeta(3) \sim 1.202$ is Riemann's zeta function evaluated at the integer 3. This expression, derived using the Wentzel–Kramers–Brillouin (WKB) method [5], accurately matches the numerically diagonalized results of the Fluxonium Hamiltonian, as shown by the black dotted line in Figure 2.8e.

The exponential dependence of $E_T = \hbar\omega_{ge}$ as a function of the ratio E_J/E_C is in stark contrast with the scaling of the plasmon-like transitions $\omega_{\text{gh}} \sim \omega_{\text{ef}} \sim \sqrt{8E_C E_J}$. Consequently, the qubit anharmonicity, can reach extremely large values in the heavy-fluxonium regime:

$$\alpha \approx \frac{\sqrt{8E_C E_J}}{E_T} \gg 1. \tag{2.17}$$

We will next discuss the implications of this distinctive energy spectrum in the context of hybrid quantum devices.

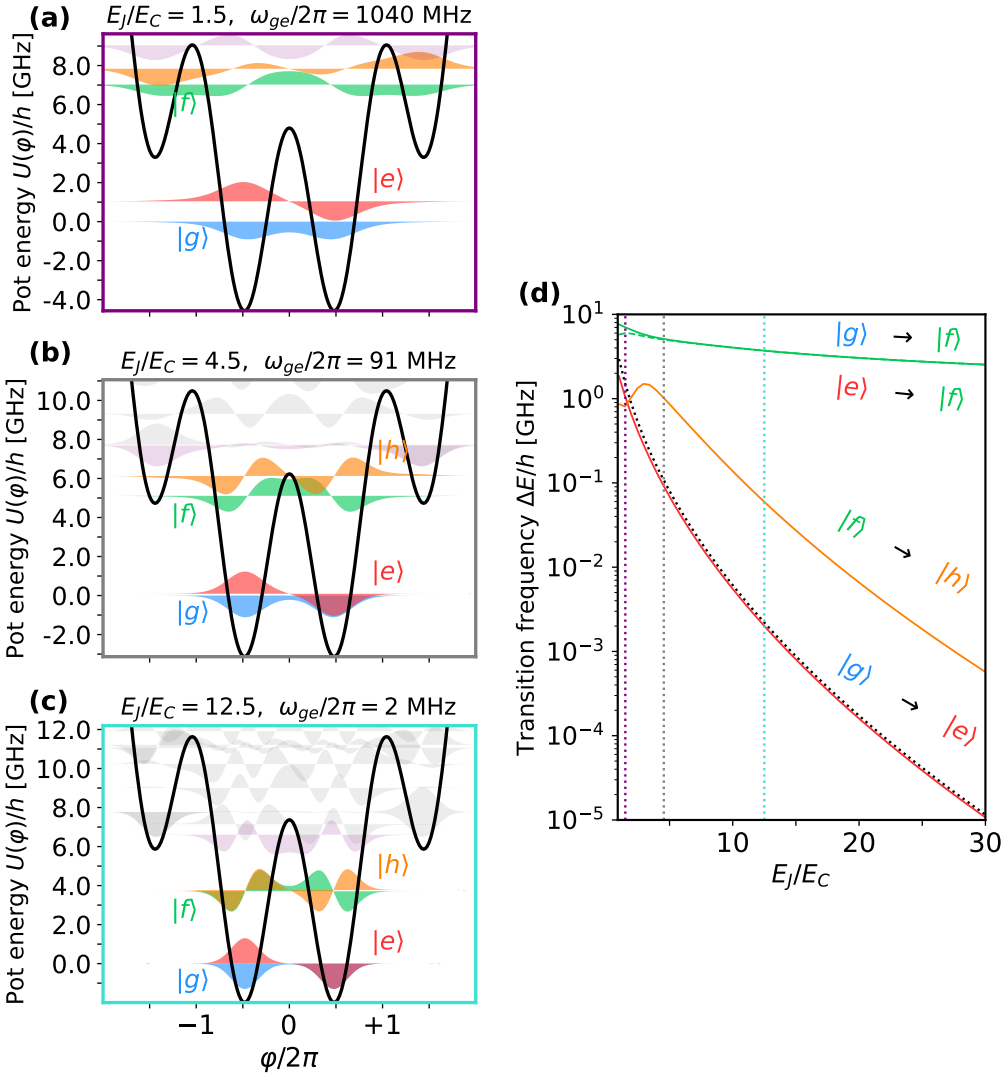

Fig. 2.8 ***Heavy-fluxonium regime.*** *Panels a, b and c show the wave functions of the first energy levels for different values of the ratio E_J/E_C. Here, the Josephson energy $E_J = 5.18$ GHz and the inductive energy $E_L = 0.207$ GHz are fixed while the capacitive energy E_C, thus the ratio E_J/E_C, increases from panel a to panel c. The states $|g\rangle$ (blue) and $|e\rangle$ (red) are symmetric and anti symmetric superpositions of the localized states at the bottom of the adjacent wells (left and right). At increasing ratio E_J/E_C, the wave functions become more confined towards the centers of the wells, and thus, the energy splitting between $|g\rangle$ and $|e\rangle$ decreases dramatically. This is not the case for the transitions from the g-e manifold to the next pair of excited states $|f\rangle$ (green) and $|h\rangle$ (orange), since they are plasmon like-transitions and their frequencies decrease more slowly as $\sqrt{8E_C E_J}$. (d) First transition frequencies of the fluxonium spectrum as a function of the ratio E_J/E_C. The black dotted line represents the asymptotic expression in the semi-classical limit obtained by the WKB-method.*

2.4 The heavy-fluxonium as a novel quantum device

As detailed in section 2.3.3, the low-energy spectrum of the heavy fluxonium at the flux-frustration point is characterized by a strong anharmonicity which depends on the ratio between the junction characteristic energy E_J and the capacitive energy E_C. This section explores the potential applications of the heavy-fluxonium's rich non-linear spectrum in the field of hybrid quantum devices, which is central to this experimental work. Additionally, these properties have been identified as an interesting resource to facilitate rapid qubit gate operations that extend beyond the rotating wave approximation.

2.4.1 A superconducting qubit at MHz frequency

The qubit frequency, as seen in Section 2.3.3, has an exponential dependence on the ratio E_J/E_C, that translates into significant tunability from the GHz range down to the few MHz range. This unique capability offers the possibility to bring the frequency of the heavy-fluxonium qubit close to resonance with other interesting quantum systems. For instance, the silicon nitride micro-mechanical resonators that have been developed in the context of optomechanics [43, 74] exhibit extremely large coherence times of the order of seconds with characteristic frequencies on the order of 1-10 MHz. Lowering the fluxonium-qubit frequency down to the few MHz range can be achieved in practice by increasing the capacitance C shunting the junction by approximately one order of magnitude compared to typical fluxonium experiments. An example is provided in Figure 2.8 (b), which shows the situation for a parameter regime close to the experimental setup used in this thesis, with $E_J/E_C \approx 10$. In this setup, the frequency of the $|g\rangle \rightarrow |e\rangle$ transition is reduced by three orders of magnitude with only a tenfold change in the E_J/E_C ratio.

Furthermore, the higher plasmon-like transitions such as $|g\rangle \rightarrow |h\rangle$ and $|e\rangle \rightarrow |f\rangle$, can serve as ancillary to readout the population in the qubit manifold, with easily accessible GHz techniques. This approach was first demonstrated by Zhang *et al* in 2020 [81]. By employing an optimized measurement chain, including a quantum-limited parametric amplifier, we have significantly improved the readout sensitivity and achieved a single-shot readout of the qubit state, detailed in the experimental section of this thesis (see chapter 5).

In addition, the highly non-linear spectrum of the fluxonium is advantageous as it enables the initialization of the qubit in its ground state. Despite the typical temperatures of a dilution cryostat, where a MHz transition would normally couple to a "hot" environment with a large thermal population, the higher-excited states can essentially be used as a cold reservoir enabling to extract the entropy from the qubit state. This active reset protocol is also described in details in the experimental section (see chapter 6).

2.4.2 Charge-matrix element of the heavy-fluxonium

In order to assess the potential of the heavy-fluxonium in hybrid quantum systems, we need to consider a possible coupling scenario. The coupling mechanism that we have chosen in the mecaflux project is a dipolar interaction, where the mechanical motion induces a modulation of the charge offset $n_g(t)$ in equation 2.3. For a sinusoidal modulation $n_g(t) = n_\mathrm{d} \cos(\omega_\mathrm{ge} t)$,

resonant with the qubit transition, and with a small amplitude $n_{\mathrm{d}} \ll 1$, the quadratic capacitive energy term $4E_C(\hat{N}-n_g(t))^2$ can be linearized and projected in the qubit manifold yielding an interaction term:

$$\hat{H}_{\mathrm{int}} = \frac{\hbar\Omega_r}{2}\hat{\sigma_x} \tag{2.18}$$

Here, $\Omega_r = 8E_C|\langle N\rangle_{ge}|n_{\mathrm{d}}$ represents the frequency of the Rabi oscillations induced by the resonant charge drive. Hence, the sensitivity of the qubit to the external charge modulation is determined by the magnitude of the charge matrix element $|\langle N\rangle_{ge}|$.

From the fluxonium hamiltonian 2.3, we can deduce the following relation between the charge $\langle N\rangle_{ge}$ and the flux $\langle\varphi\rangle_{ge}$ matrix elements:

$$|\langle g|\left[\hat{\varphi},\,\hat{H}\right]|e\rangle| = \hbar\,\omega_{ge}\,|\langle\varphi\rangle_{ge}| = 8E_C|\langle N\rangle_{ge}| \tag{2.19}$$

By substituting the second equality in the expression of Ω_r, one obtains:

$$\Omega_r = n_{\mathrm{d}}\,\omega_{\mathrm{ge}}|\langle\varphi\rangle_{\mathrm{ge}}| \tag{2.20}$$

This expression, valid for any capacitively shunted qubit under a resonant charge drive, shows that the Rabi frequency for a given drive amplitude and frequency is solely governed by the magnitude of the flux matrix element $|\langle\varphi\rangle_{\mathrm{ge}}|$. As such, maximizing this parameter is the only way to increase the sensitivity to such a signal in a resonant coupling scenario.

Owing to the peculiar nature of the heavy fluxonium eigenstates at the flux-frustration point–the flux-wavefunctions resemble a Schrödinger-cat-state with the phase being localized around $\varphi = \pm\pi$– the overlap between the wavefunctions is nearly optimal, at a value of $|\langle\varphi\rangle_{\mathrm{ge}}| = \pi$, leading to the final expression for the Rabi frequency:

$$\Omega_r \sim \pi\omega_{\mathrm{ge}}n_{\mathrm{d}} \tag{2.21}$$

The analysis indicates that even if practical issues such as readout and state preparation were resolved for a MHz frequency charge qubit, its charge sensitivity would still be inferior to that of a heavy fluxonium operating at the same frequency.

In chapter 7, we build on the large dipole moment of the fluxonium operated at the flux-frustration point to turn the heavy-fluxonium into a nearly resonant charge-sensor, and compare its sensitivity–expressed in "elementary charges/$\sqrt{\mathrm{Hz}}$"–to that of more conventional charge sensors [68].

2.4.3 Applications in quantum computing

In a different context, when the fluxonium is intended to be used as a qubit for quantum information processing, the extremely large anharmonicity α is a desired feature, but it comes at the price of an extremely small qubit frequency $\omega_{ge} = E_{ge}/\hbar$. At first sight, the small qubit frequency seems to limit the duration of quantum gates performed on the qubit, since they are typically implemented with Rabi oscillations (in the weak driving-amplitude limit). In fact, this apparent problem can be circumvented by exploiting the very large dipole moment of the heavy-fluxonium qubit (Equation 2.21). Such large dipole moment means that even a weak charge modulation of a fraction of a Cooper pair, $1/\pi \approx 0.31$, is translated into a driving amplitude comparable to the qubit frequency, $\Omega_{\mathrm{r}} \approx \omega_{ge}$ (Equation

2.21). This peculiarity, in combination with the large anharmonicity α, allows reaching very strong driving amplitudes beyond the rotating-wave approximation, that can be used for implementing fast-gates with a duration of the order of the Larmor period of the qubit $T_{\mathrm{g}} \approx 2\pi/\omega_{ge}$ [17, 18, 81].

Chapter 3

Fluxonium design

In this chapter, we discuss the circuit design and optimization. We first give a brief description of the main circuit components which include the fluxonium circuit, control lines, and readout resonator. In order to precisely adjust the characteristics of these elements, we rely on classical electromagnetic simulations, the principles of which are presented in section 3.2. These simulations are crucial for determining the optimal geometry of the circuit elements. Specifically, in section 3.2.1, we describe how the resonant frequency of these components and their coupling to the control lines are adjusted using eigenmode electromagnetic simulation. Further, in section 3.2.2, we explore a simple method to determine the coupling between the readout resonator and the fluxonium mode through the observation of anti-crossing in the frequencies of the normal modes. This process involves conducting repeated simulations while varying the frequency of one of the circuit elements. While this method provides a simple way to adjust the coupling in our circuit, it is time-consuming, and doesn't provide a full analytical understanding of the quantum circuit Hamiltonian. Finally, in section 3.3, we take one step forward in the complexity of the design process by discussing an approach to estimate the full circuit Hamiltonian from a single circuit simulation. This approach builds on the energy-participation method, introduced earlier in the context of weakly anharmonic qubits [54].

3.1 Circuit design

The Figure 3.1 shows the design of our fluxonium circuit. In the following, we provide a brief description of its different elements:

- **Fluxonium loop:** The main component of the fluxonium circuit. It is made of a small Josephson junction (red) shunted to a superinductance (dark blue). In practice, the superinductance is realised by an array of about 360 large-area junctions in serial connection. All the circuit junctions are aluminum-oxide-aluminum Dolan style junctions and their fabrication process is described in Section 4.1.2.

- **Fluxonium co-planar capacitor (green):** The large circular plate connected to one side of the fluxonium loop represents a large capacitance to ground (white) shunting the

small junction. It is also used to couple the fluxonium to the ancillary resonator and to drive the fluxonium by applying a voltage modulation via the charge-drive electrode.

- **Ancillary resonator (Purple):** It is a $\lambda/4$ coplanar-wave (CPW) resonator. It is shorted to ground at one end, while the other end is left open. This open end features a U-shaped termination that acts as a shunting capacitance between the resonator and the fluxonium. The resonator is used to readout the state of the qubit state, via the dispersive shift of the resonator resonance frequency that is caused by the plasmon-like mode.

- **Charge drive (light blue):** It is a superconducting electrode that we use to set the potential on the fluxonium capacitor pad. In particular, by applying a voltage modulation with frequency ω_{d}, we can resonantly drive the various fluxonium transitions.

- **Flux line (orange):** This component consists of a coplanar waveguide that terminates with two wires connected to ground. The flux-line is slightly off-centered with respect to the fluxonium loop, such that a current flowing symmetrically in the two wires generates a magnetic flux through the fluxonium loop. The external flux can thus be controlled precisely by driving this line with a DC- or AC-current.

The large-size elements are implemented in the co-planar superconducting-circuit architecture. They are made of niobium over a silicon substrate (gray) and their fabrication process is described in Section 4.1. The gap and track size of all coplanar-waveguide elements are such that the waveguide impedance is 50 Ohm. The circuit design for this project utilized HFSSdrawpy, a Python library initially developed by Raphael Lescanne [48] and maintained by the company Alice and Bob. This tool enables the programmable definition of circuit geometries, facilitating the creation of precise layouts for experimental setups. The library supports the generation of "gds" files for lithography machines, essential for the fabrication process. Additionally, it allows for direct integration with the simulation software HFSS (High Frequency Structure Simulator), aiding in the verification and adjustment of the design parameters before the physical manufacturing begins.

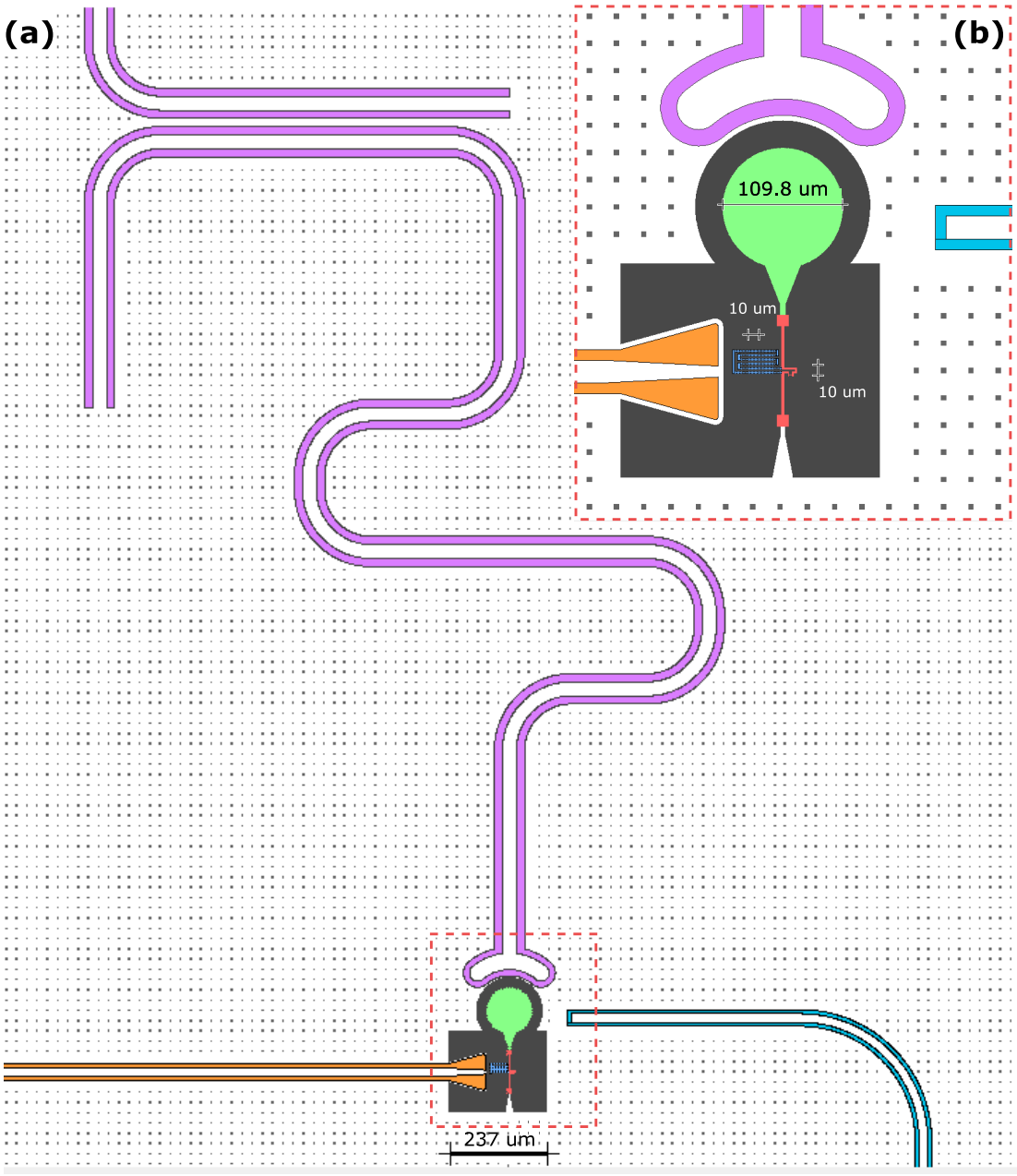

Fig. 3.1 ***Drawing of the grounded fluxonium circuit:*** *(a) The circuit is made of a coplanar capacitor (green), an ancillary resonator(purple), a charge drive (light blue) and a flux line (orange) and the fluxonium loop. (b) Zoom into the fluxonium loop area: The loop is composed by a small junction (red) and a junction-chain implementation of a superinductance (dark blue).*

3.2 Simulations of the circuit

Before starting the sample fabrication, we need to adjust the various circuit parameters such that it matches our design requirements. We recall that the fluxonium circuit has three characteristic elements (see Equation 2.3): a superinductance with energy $E_L = \Phi_0^2/L$, a capacitance with energy $E_C = e^2/2C$ and a Josephson junction with energy E_J (non-linear element). These 3 parameters determine the spectrum of the fluxonium, and in particular, the frequency of the qubit transition ω_{ge}. In practice, we typically use the *scqubits* python-package for diagonalizing the fluxonium hamiltonian with parameters E_C, E_L and E_J, and obtain the low-energy spectrum of the fluxonium circuit.

Ultimately, these parameters can be traced back to the circuit geometry. For instance, the fluxonium capacitance C is related to the geometry of the fluxonium co-planar capacitor (green in Figure 3.1), and it can be accurately predicted from an electromagnetic simulation of the circuit design. On the other hand, the tunneling energy E_J and the inductance of the chain L not only depend on the area of the individual junctions composing them, but also crucially on the thickness of the oxyde layer. As such, we typically do not attempt to extract these parameters from a simulation, but rather empirically adjust these values via a physical sweep of the junction area and a resistance characterization at room temperature (see 4.3 for details).

The second element of our circuit is the ancillary resonator that is used to readout the fluxonium state. It is a co-planar waveguide $\lambda/4$-resonator that is coupled to the fluxonium via a co-planar capacitor represented by a shunting capacitance C_S. The frequency of the ancillary resonator ω_{R} can be traced back to the length of the CPW resonator. Furthermore, its coupling to the fluxonium circuit is governed by the mutual capacitance C_S between the resonator and the fluxonium electrode. These two parameters are also precisely adjusted via an electromagnetic-field simulations using the circuit geometry as the input.

3.2.1 Normal-modes simulation

In practice, we perform the EM-field simulations with the software *ansys HFSS* (see Figure 3.2). This software allows us to retrieve the eigenmodes of the electromagnetic problem (i.e. the electric and magnetic fields), and the real and imaginary parts of their eigen-frequency (i.e. their frequency and losses). Of course, this classical simulation software cannot simulate non-linear elements such as Josephson junctions. However, one can include a "linearized" version of these elements, by replacing them with a lumped-element inductance $L_J = \Phi_0^2/E_J$. In practice, this is equivalent to replacing the non-linear term in the Josephson energy $-E_J \cos(\phi)$ by a quadratic potential $\frac{E_J}{2}\phi^2$. This is particularly relevant in situations where the non-linearity of the junction is only a weak perturbation to the linear circuit spectrum. For instance, by replacing the small junction and super-inductance with a linear inductance L_J, the EM-field simulation reproduces the physics of one of the plasmon-like fluxonium transition coupled to the readout resonator (see Fig. 3.2).

In order to account for the various loss channels, and make sure they are sufficiently suppressed, a $50\,\Omega$ lumped-impedance is added at the end port of the flux line, the charge drive and the resonator drive. This allows us to determine the quality factor of the ancillary resonator, which affects the efficiency of the readout process, and the quality factor of the plasmon-like mode of the fluxonium, which is related to the rate of Purcell losses of the

fluxonium. We can immediately deduce the fluxonium capacitance C from the plasmon-like mode ω_{q} frequency as $C = 1/L_J\,\omega_{\mathrm{q}}^2$, where L_J is the value of the lumped-element inductance replacing the small junction of the fluxonium.

The results of this simulation are summarized in the table of Figure 3.2e. We typically choose a readout resonator frequency around 5.5 GHz, at the lower end of our detection bandwidth. The quality factor of the readout resonator $Q = \omega_r/\kappa_r$ is adjusted to a value close to $5 \cdot 10^3$ by adjusting the gap between the resonator and the drive waveguide. This value is a good compromise between the readout speed (the time to load the resonator with a resonant readout pulse is given by $1/\kappa_r$) and state-selectivity. The plasmon-like frequency of 4.03 GHz is slightly overestimated compared to the measured value of 3.7 GHz (see Chapter 5). This correction likely results from the junction anharmonicity being ignored in this classical simulation. The total plasmon-like loss rate through the 3 loss-channels of 4.43 kHz sets an upper limit of 36 µs to the lifetime of this mode. The experimentally measured lifetime of 8 µs (see chapter 5) indicates that material absorption is dominating over Purcell-like losses.

We finalize this section with a few closing remarks to consider for designing a fluxonium circuit. In general, the fluxonium parameters E_C, E_L and E_J must satisfy the conditions given by Equation 2.5. The condition $E_J \ll E_L$ essentially means that the superinductance $L = \varphi_0^2/E_L$ should be as large as practically possible. Moreover, the condition $E_J > E_C$ sets a minimum value for the fluxonium capacitance $C = e^2/2E_C$. Additionally, the values of E_C, E_J and E_L are limited by practical constrains. For instance, the typical capacitance C of a co-planar capacitor over a silicon substrate is in the range between 10 fF and 100 fF. Furthermore, the tunneling energy E_J of an aluminum-oxide-aluminum junction is typically in the range between 2 GHz·h and 100 GHz·h. Finally, the large-area junctions that build up the superinductance L usually have individual inductances $L_{J\,n}$ of the order of 3 nH.

3.2.2 Coupling between the normal modes

In the previous section we have shown how the parameters E_C and ω_R could be extracted from a single simulation of the circuit's normal modes. Since the energies E_J and E_C are adjusted separately, the main unknown parameter to be determined is the coupling between the fluxonium circuit and readout resonator. It is important to adjust this parameter properly since a too small coupling could result in an insufficient dispersive shift to perform a projective readout of the circuit state. On the other hand, a too large coupling might compromise the qubit coherence properties via Purcell effect and resonator shot noise.

For a very non-linear circuit, like the heavy-fluxonium, the dispersive shift depends in a convoluted manner of the circuit parameters, for instance, the coupling g between the resonator and the fluxonium and the frequency of the ancillary resonator ω_{R} with respect to the various fluxonium levels [82]. In practice, we haven't tried to model precisely the expected dispersive shift as a function of all possible parameters. Since the readout protocol involves a transmon-like transition to a plasmonic excited state, we rather adjusted the geometry of the U-shaped capacitor ending the resonator to achieve a value of $g/2\pi \approx 150$ MHz, which is typical of dispersive readouts in circuit QED [81].

In this section we describe a simple approach to estimate the coupling g via simulations of the normal-modes of the circuit.

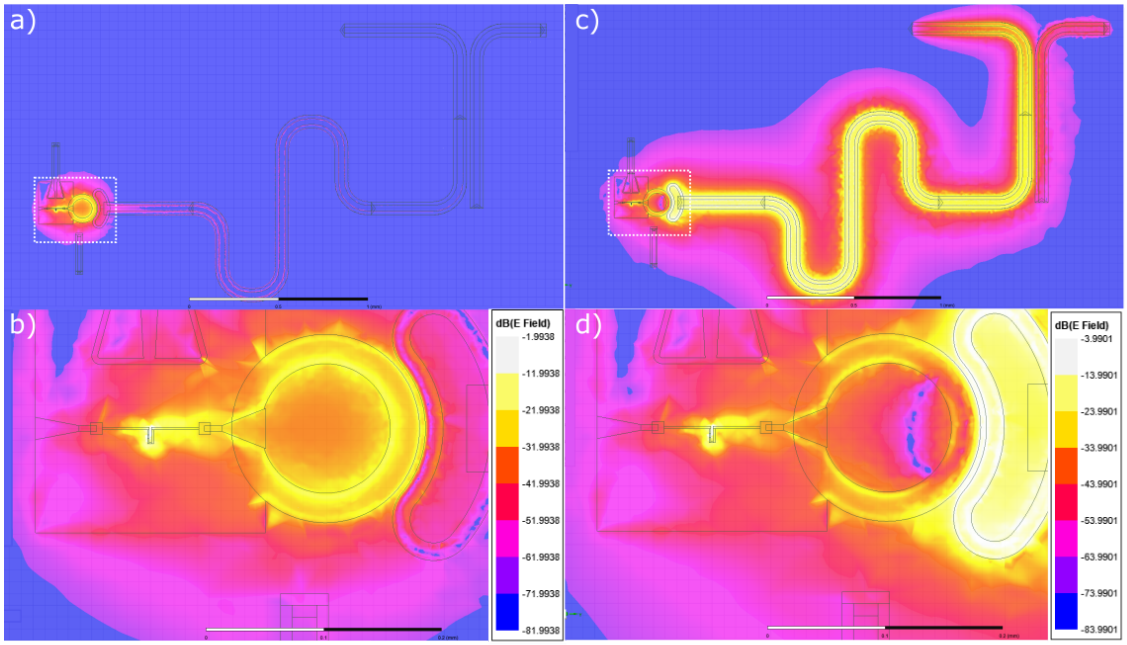

e)

Plasmon-like mode: frequency	$\omega_q/2\pi$	4.03 GHz
Fluxonium-like mode: capacitance	C_q	49.4 fF
Plasmon-like mode: loss rate via readout port	$k_{q\to R}/2\pi$	0.703 kHz
Plasmon-like mode: loss rate via flux line	$k_{q\to F}/2\pi$	72.0 Hz
Plasmon-like mode: loss rate via charge drive	$k_{q\to C}/2\pi$	2.38 kHz
Plasmon-like mode: total loss rate	$k_q/2\pi$	4.43 kHz
Resonator-like mode frequency	$\omega_r/2\pi$	5.60 GHz
Resonator-like mode: loss rate via readout port	$k_{r\to R}/2\pi$	1.30 MHz
Resonator-like mode: loss rate via flux line	$k_{r\to F}/2\pi$	4.0 Hz
Resonator-like mode: loss rate via charge drive	$k_{r\to C}/2\pi$	0.505 kHz
Resonator-like mode: total loss rate	$k_r/2\pi$	1.36 MHz

Fig. 3.2 ***Electrical field simulation, fluxonium and readout resonator***. *Finite element electromagnetic simulation using ANSYS HFFS. The electric field amplitude, obtained by setting 1J in the resonant mode, is plotted respectively for a) and b) the fluxonium plasmon-like mode, c) and d) the ancillary mode. The frequencies and energy decay rates for the first five eigen-modes of the circuit are reported in table e).*

3.2.2.1 Avoided-crossing method

The Figure 3.3a shows the lumped-element schematics of the circuit design that was presented in the Figure 3.2. Furthermore, the "linearized" version of the circuit, used in classical electromagnetic simulations, is represented in Figure 3.3b. One of the modes is related to the ancillary resonator while the other mode is a "linearized" fluxonium mode, corresponding to the so-called plasmon mode. The bare frequency of the resonator mode is $\omega_R = 1/\sqrt{L_R C_R}$ (purple in Figure 3.3a) and the bare frequency of the plasmon mode is $\omega_0 = 1/\sqrt{L_J C}$, where C is the fluxonium capacitance (green in Figure 3.3a) and $L_J = \Phi_0^2/E_J$ is the equivalent linear-inductance of the small junction (red in Figure 3.3a). The two bare modes are capacitively coupled to each other via the shunting capacitance C_S. In general, a system of

two coupled modes can be modeled up to a good approximation by the following quantum hamiltonian:

$$\hat{H} = \hbar\omega_0 \left(\hat{a}_{\mathrm{Q}}^{\dagger}\hat{a}_{\mathrm{Q}} + \frac{1}{2}\right) + \hbar\omega_{\mathrm{R}} \left(\hat{a}_{\mathrm{R}}^{\dagger}\hat{a}_{\mathrm{R}} + \frac{1}{2}\right) - \frac{1}{2}\hbar g \left(\hat{a}_{\mathrm{Q}} + \hat{a}_{\mathrm{Q}}^{\dagger}\right)\left(\hat{a}_{\mathrm{R}} + \hat{a}_{\mathrm{R}}^{\dagger}\right) \tag{3.1}$$

Where $\hat{a}$ and its hermitian self-adjoint are the so-called ladder operators. The term on the RHS of Equation 3.2.2.1 is responsible of mixing together the two bare modes. In general, the eigen-modes of the hamiltonian 3.2.2.1 correspond to linear combinations of the bare modes. They are referred to as the normal modes of the joint-system. In the dispersive coupling regime, when the difference between the frequencies of the bare modes is much larger than the coupling, $\omega_{\mathrm{R}} - \omega_0 \gg g$, then, the hybridization is minimal and the normal modes resemble the bare modes, and the frequencies of the normal modes ω_+ and ω_- are very similar to the frequencies of the bare modes: $\omega_+ \approx \omega_{\mathrm{R}}$ and $\omega_- \approx \omega_0$. This is the regime in which the simulations presented in Figure 3.2 have been achieved, such that we could label the normal modes as resonator-like and plasmon-like modes, respectively. However, when the coupling g is comparable to $\omega_{\mathrm{R}} - \omega_0$, the hybridization of the normal modes is significant. The maximum hybridization is reached at the resonance condition, when the frequencies of the bare modes are equal, $\omega_{\mathrm{R}} = \omega_0$. The eigen-modes of the hamiltonian 3.2.2.1 are then symmetric and anti-symmetric combination of the bare modes. At this condition, the difference between the frequencies of the normal modes is $\omega_+ - \omega_- = g$.

3.2.2.2 Practical implementation of the method

In order to extract g, we perform a "parametric sweep", where the value L_t of the lumped-element inductance that replaces the small junction is varied around the resonance condition

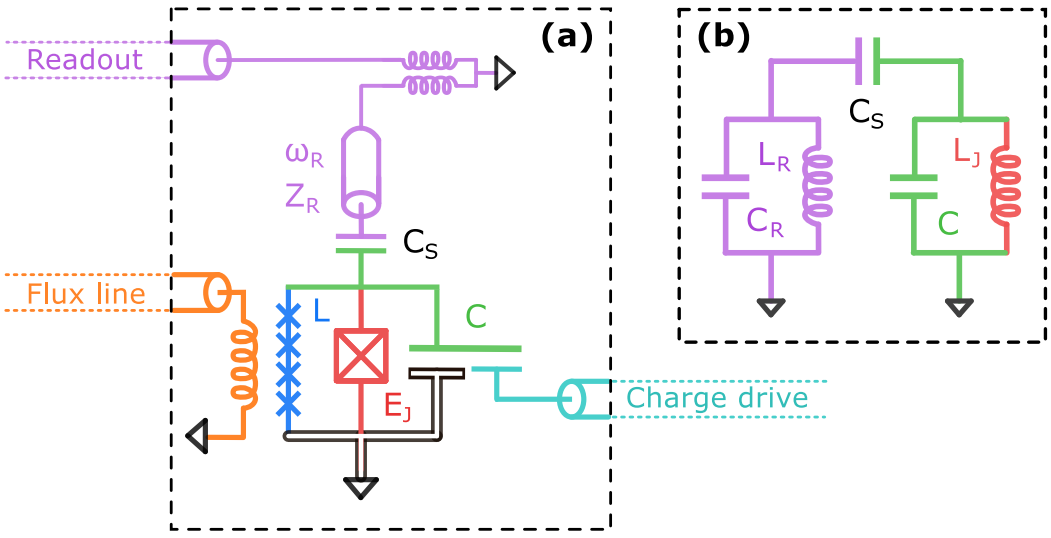

Fig. 3.3 ***Schematics of the circuit design*** *(a) Minimalist equivalent circuit containing the main elements of the circuit design. (b) Simpler version of the circuit corresponding to a pair of coupled LC resonators: One of them is related to the ancillary resonator (purple) and the other one is a "linearized" fluxonium mode, where* $L_J = \Phi_0^2/E_J$.

$\omega_q = \omega_R$, with $\omega_q = 1/\sqrt{L_t C}$. In order to maximize the efficiency of the simulations, we use the same pre-optimized mesh as the initial mesh for all the variations of the junction inductance L_J. This pre-optimized mesh is obtained by performing several adaptive passes (7 to 8) of a given variation of L_J corresponding to a high-frequency plasmon mode, for instance 6.5 GHz. In this way, we ensure that the pre-optimized mesh captures quite well the spatial variations of the plasmon mode at lower frequencies (corresponding to a higher values of the junction inductance L_J). Next, for each variation of the junction inductance L_J, we perform at least four extra adaptive passes on the initially pre-optimized mesh. From the size of the avoided-crossing at the resonance condition between readout mode and bare plasmon resonance, we deduce the coupling g.

Figure 3.4 shows the result of this parametric sweep, where the two normal mode frequencies $\omega_\pm$ are represented in blue (red respectively) as a funtion of L_t. The bare mode frequencies, ω_R and $\omega_\mathrm{q} = 1/\sqrt{L_t C}$ are represented as a dashed (resp. full) black line. By using the avoided-crossing method, we found that the fluxonium capacitance is approximately $C \approx 52.5\,\mathrm{fF}$, the bare resonator frequency is about $\omega_\mathrm{R}/2\pi \approx 5.58\,\mathrm{GHz}$ and the coupling between the resonator and the plasmon mode is about $g/\pi \approx 140\,\mathrm{MHz}$. The avoided-crossing approach is thus a simple method to estimate the relevant circuit parameters, ω_R, C and g, at the expense of performing multiple normal-modes simulations of the circuit design.

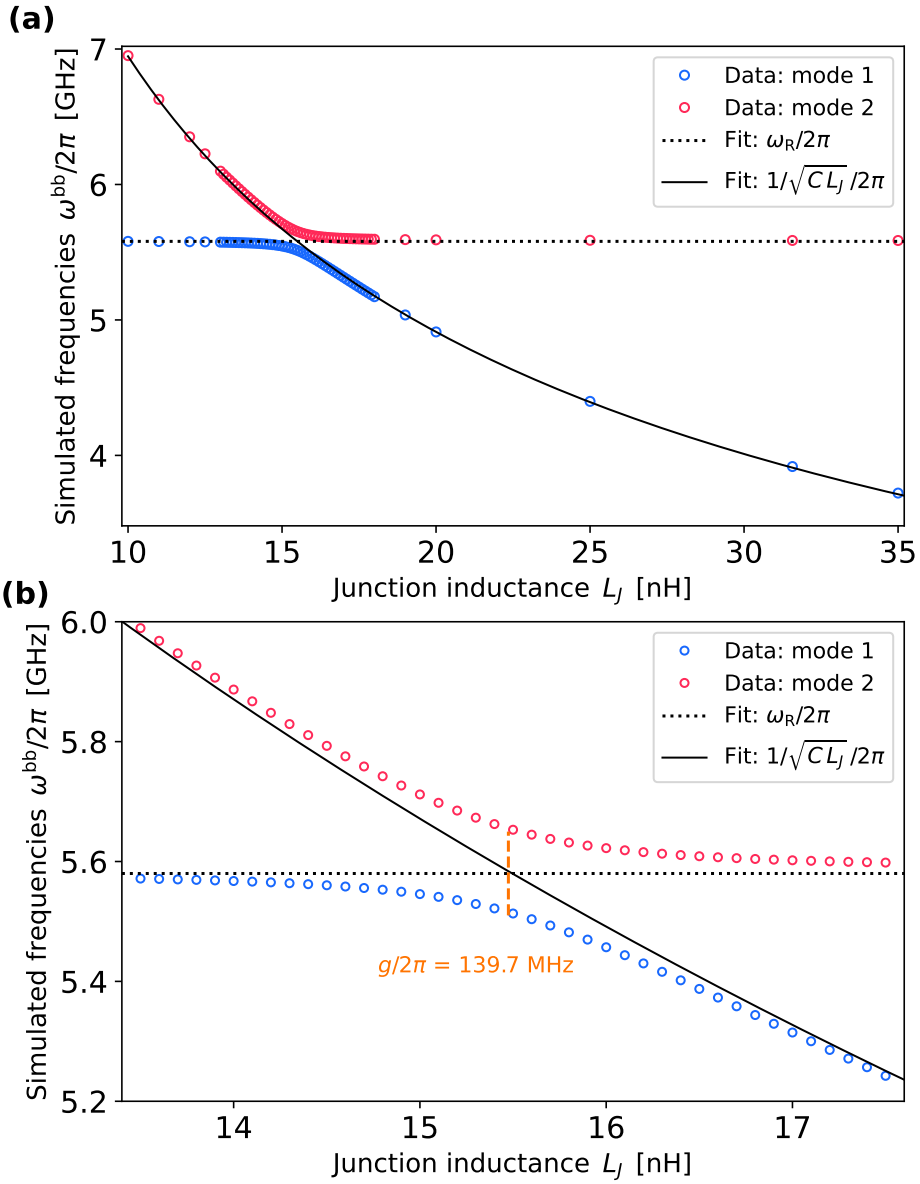

Fig. 3.4 ***Avoided crossing method*** *(a) Frequencies of the simulated normal modes as functions of the equivalent linear inductance L_J of the junction. (b) Zoom into the region of the anti-crossing. The dashed orange line represents de minimum energy splitting between the two frequencies which is the coupling $g/2\pi$. The blue and read open bullets correspond to the frequencies of simulated the normal modes while the black lines represent the asymptotic behaviour of the plasmon-mode (solid) and the resonator mode (dotted) in the zero-coupling limit*

3.3 Advanced design method: quantization of the capacitively shunted fluxonium

In Section 3.2.2, we have discussed a simplistic but useful approach for estimating the relevant parameters of the circuit via normal-modes simulations. The avoided-crossing method, although very useful as a first try, fails to provide a clear connection between the coupling "g" of the bare circuit modes and the dispersive shift χ. This section provides an alternative approach to estimate the relevant circuit parameters coming from a different conceptual point of view. This alternative approach draws inspiration from the energy-participation (EP) method of Minev *et al* [54]. While the avoided-crossing method (Section 3.2.2.2) relies only on the frequencies of the simulated normal modes, the EP-method introduces an additional quantity for each normal mode: the energy participation ratio p, which is the percentage of the total energy of the mode that it is stored in a given element of the circuit, in this case, a lumped element inductance. The EP-method uses the set of the frequencies ω and the energy-participation ratios p of the normal modes obtained from a single simulation to retrieve the relevant circuit parameters. This is in contrast with the avoided-crossing method which relies on performing multiple simulations of the circuit design to infer the relevant circuit parameters. Moreover, the EP-method provides a more explicit connection between the circuit design and the effective quantum hamiltonian that describes the behavior of the real circuit at cryogenic temperature.

3.3.1 Equivalent lumped-element circuit

When designing a superconducting circuit, we typically find the scenario described in the Figure 3.5a: there is a non-linear element, a Josephson junction E_J, whose ports are shunted to a microwave environment. In the case of the capacitively shunted fluxonium, the microwave environment includes, the fluxonium co-planar capacitor, the readout port, the charge drive electrode, the flux line and the CPW resonator with the shunting coplanar capacitor (see Figure 3.1). We then face the problem of finding an appropriate lumped-element equivalent circuit representing the circuit design (junction plus microwave environment). For instance, a minimalist representation of the circuit design was shown in the Figure 3.3. Ideally, the equivalent circuit must be as simple as possible, but at the same time, it must be involved enough to predict with sufficient accuracy the behaviour of the real circuit under the experimental conditions.

The most popular approach that is used for weakly non-linear circuits is shown in Figures 3.5b and 3.5c. It consists of decomposing the junction into a linear inductance $L_J = \Phi_0^2/E_J$ and a non-linear inductance L_{nl}, which incorporates to the circuit all the non-linear effects that are induced by the junction. In the simulations of the circuit design, the junction is thus replaced by the equivalent lumped-element inductance L_J. The linearized joint-system of the microwave environment and the junction (dotted black box in Figure 3.5c) is represented by a pair of capacitively coupled linear modes (LC-resonators), one corresponding to the ancillary-resonator mode and the other one corresponding to a "linearized" mode of the fluxonium (the plasmon mode). The results of one simulation then yield the normal modes of the linearized joint system.

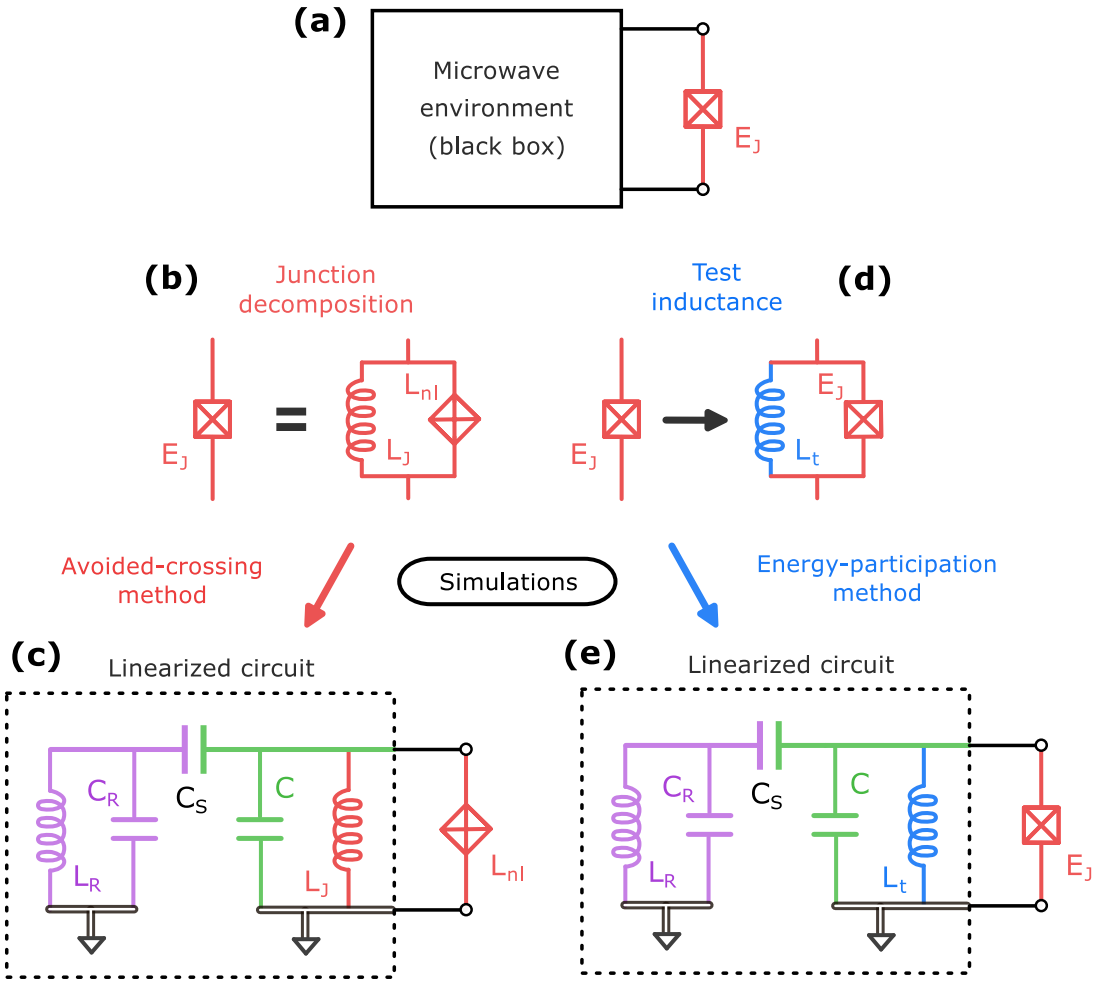

Fig. 3.5 ***Finding the equivalent circuit corresponding to the circuit design:*** *(a) General representation of the circuit design as a Josephson junction shunted to a microwave environment. Then, we consider two approaches for finding an equivalent lumped-element circuit that predicts the behaviour of the circuit design. Avoided-crossing method: (b) In the first approach, the junction is decomposed as a linear inductance L_J and a non-linear inductance L_{nl}. (c) A simulation yields the normal modes of the linearized circuit (dotted black box) in which the junction has been replaced by its equivalent linear inductance L_J. The non-linear effects induced by L_{nl} are later taken into account in a perturbative fashion. Energy-participation method: (d) In the second approach, the junction is shunted by a fictitious test inductance L_{t} which acts as probe for the microwave environment. (e) A simulation yields the normal modes of the linearized circuit (dotted black box) in which the junction has been replaced by the test inductance L_{t}. From here, there are two possible paths to proceed: In the first one, if the test inductance L_{t} is set equal to the fluxonium superinductance L, the parameters of the simulated normal modes can be used to synthesize an effective quantum hamiltonian of the circuit design (more details in the main text). In the second path, the value of test inductance L_{t} is irrelevant, and the parameters of the simulated normal modes are just used to retrieve the parameters of the microwave environment shunting the junction (more details in the main text).*

By finding the coupling g between the bare modes of the system, for instance, via the avoided-crossing method (Section 3.2.2.2), we can then account for the effects induced by the non-linear inductance L_{nl} in a perturbative fashion. This method works quite well for weakly non-linear circuits, such as the transmon, since the contribution of the non-linear inductance L_{nl} is small. However, in the case of very non-linear circuits, like the heavy fluxonium operated at the flux frustration point $\phi_{\mathrm{ext}}/\Phi_0 = \pi$, the contribution of the non-linear inductance is very significant. In general, the contribution of the non-linear inductance L_{nl} to the potential energy of the circuit is:

$$U_{\mathrm{nl}}(\phi) \equiv -E_J \cos\left(\frac{\phi - \phi_{\mathrm{ext}}}{\Phi_0}\right) - \frac{(\phi - \phi_{\mathrm{ext}})^2}{2L_J} \approx -\frac{E_J}{24\Phi_0^4}(\phi - \phi_{\mathrm{ext}})^4 \tag{3.2}$$

Where $\phi = \Phi_0\varphi$ is the equivalent flux across the junction and ϕ_{ext} is the external flux threading the fluxonium loop[1]. By looking at Equation 3.2, we identify that when the fluctuations of the flux across the junction are large, $\phi_{\mathrm{zpf}}/\Phi_0 \gg 1$, the energy related to the non-linear inductance diverges to $-\infty$. Nonetheless, the coupling "g" still modulates the non-linear effects on the resonator that are indirectly induced by the junction, for instance the dispersive shift χ. However, the relation between the coupling g and the dispersive shift χ is more involved.

In the energy-participation approach, the whole fluxonium loop is replaced by a lumped-element test inductance L_{t}, which acts as a probe for the microwave environment. A simulation then yields frequencies ω_n^{bb} and the energy-participation ratios p_n of the normal modes of the linearized equivalent circuit including the microwave environment and the test inductance (dotted black-box in Figure 3.5d). If the value of the test inductance L_{t} is set equal to the fluxonium superinductance L, then, the parameters of the simulated normal modes can be directly related to an effective hamiltonian of the circuit design. However, in the general case, the parameters of the normal modes that are obtained from the simulations do not have a direct physical meaning, and they are just used to retrieve the characteristic parameters of the microwave environment: the fluxonium capacitance C, the bare resonator frequency ω_{R}, and the shunting capacitance C_{S}. Up to a good approximation, these parameters are independent from the value of the test inductance L_{t}. The contribution of the fluxonium loop, in particular, the non-linearity induced by the Josephson junction as a whole, is later taken into account.

3.3.2 Calculating the energy-participation ratios from simulations

In the energy-participation approach, we rely not only on the frequencies ω_n^{bb} of the normal modes, but also in their energy participation ratios (EPR) p_n. This section provides a description of the EPRs of the normal modes and the method to calculated them from the electromagnetic-fields simulations.

[1]Notice that in the case of a transmon, there is no loop, thus, no external flux ϕ_{ext}. However, in the case of a fluxonium circuit, or in general, a circuit where the Josephson junction belongs to a loop, the external flux ϕ_{ext} threading the loop must be taken into account.

The energy-participation ratio p_n of a normal mode "n" is defined as the energy percentage of the mode that is stored in a particular element of the circuit, in this case, the test inductance L_t[2]. On the one hand, the magnetic energy E_n^{mag} of a normal mode "n" has two contributions: The energy stored in the magnetic field $E_n^{\text{H-field}}$ and the energy stored in the (lumped-element) test inductance E_n^{ind},

$$E_n^{\text{mag}} = E_n^{\text{ind}} + E_n^{\text{H-field}} \tag{3.3}$$

On the other hand, the electric energy E_n^{elec} of the normal mode "n" is all stored in the electric field $E_n^{\text{E-field}}$ [3]. Because of detailed balance, the electric and magnetic energies of a normal mode must be equal:

$$E_n^{\text{mag}} = E_n^{\text{elec}} \tag{3.4}$$

Thus, the energy participation ratio p_n of the normal mode "n" on the test inductance L_t can be computed as:

$$p_n \equiv \frac{E_n^{\text{E-field}} - E_n^{\text{H-field}}}{E_n^{\text{E-field}}} \tag{3.5}$$

The energy stored the electric and magnetic fields is computed by integrating the respective field over the entire simulation volume, taking into account the different dielectric regions, and then, taking the time average [54]. In the practice, the energies of the fields, $E_n^{\text{E-field}}$ and $E_n^{\text{H-field}}$, are obtained with the aid of the *pyEPR* python-environment, which was developed by Zlatko Minev and Zaki Leghtas. Then, the EPRs of the simulated normal modes are calculated with Equation 3.5.

With the set of the energy-participation ratios $\{p_1, p_2\}$ and the frequencies $\{\omega_1^{\text{bb}}, \omega_2^{\text{bb}}\}$ of the simulated normal modes, we can follow two possible paths for finding the equivalent circuit that predicts the behaviour of the real circuit under the experimental conditions. In the first one, we set the value of the test inductance L_t equal to the fluxonium superinductance L (see Figure 3.5c), and then, the EPRs p_n and frequencies ω_n^{bb} of the simulated normal modes can be directly used to synthesize an effective quantum hamiltonian of the circuit. This path is explained in more detail in the Section 3.3.3. In the second path, the value of the test inductance is irrelevant L_t, since it is just a tool to probe the microwave environment shunting the junction (see Figure 3.5e). The EPRs p_n and frequencies ω_n^{bb} of the simulated normal modes are just used to retrieve the parameters of the microwave environment, which are in principle independent of the value of the test inductance L_t. This path is explained in more detail in the Section 3.3.4.

3.3.3 Energy-participation quantization

The energy-participation quantization (EPQ) method of Minev *et al* [54] uses the frequencies ω_n^{bb} and the energy-participation ratios p_n of the simulated normal modes to synthesize an effective quantum hamiltonian of the circuit design $\hat{H}_{\text{epq}}$. This process can be thought of as the quantization of the Foster equivalent circuit corresponding to the circuit design. The

[2] Here, we only consider the case of a single lumped element in the circuit, being L_t.

[3] When the circuit contains both lumped-element inductances and capacitances, the energy stored in the lumped element capacitances E_n^{cap} must be taken into account in the electric energy E_n^{elec}

effective hamiltonian $\hat{H}_{\text{epq}}$ is composed by a linear part $\hat{H}_0$ and a non-linear part $\hat{H}_{\text{nl}}$. The linear part of the hamiltonian is:

$$\hat{H}_0 \equiv \sum_n \hbar\,\omega_n^{\text{bb}} \left(\hat{a}_n^\dagger \hat{a}_n + \frac{1}{2}\right) \tag{3.6}$$

This hamiltonian represents a set of decoupled linear modes, which are nothing but the simulated normal modes of the linearized circuit (see dotted black-box in Figures 3.5c and 3.5d). The parameters ω_n^{bb} are the frequencies of the simulated normal modes. In the conventional EPQ method, which works very well for weakly non-linear circuits, the Josephson junction is decomposed into a linear inductance L_J and a non-linear inductance L_{nl}. The linear inductance L_J is included in the simulations of the normal modes, thus, it is already accounted for in the linear part $\hat{H}_0$ of the hamiltonian. Next, the non-linear hamiltonian $\hat{H}_{\text{nl}}$ corresponds to the energy of the non-linear inductance L_{nl} (Equation 3.2):

$$\hat{H}_{\text{nl}} \equiv -E_J \left[\cos\left(\frac{\hat{\phi}}{\Phi_0} - \varphi_{\text{ext}}\right) - \frac{1}{2}\left(\frac{\hat{\phi}}{\Phi_0} - \varphi_{\text{ext}}\right)^2\right] \approx -\frac{E_J}{24}\left(\frac{\hat{\phi}}{\Phi_0} - \varphi_{\text{ext}}\right)^4 \tag{3.7}$$

Where the operator $\hat{\phi} = \Phi_0\,\hat{\varphi}$ is related to the effective flux across the junction, with $\hat{\varphi}$ corresponding to the superconducting phase difference between the two ports of the junction. However, the conventional EPQ method does not work very well for very non-linear circuits, such as the heavy fluxonium. In this case, we replace the whole fluxonium loop by the test inductance L_{t}, which is set equal to the fluxonium superinductance L. Thus, the non-linear hamiltonian $\hat{H}_{\text{nl}}$ actually is:

$$\hat{H}_{\text{nl}} \equiv -E_J \cos\left(\hat{\varphi} - \varphi_{\text{ext}}\right) \tag{3.8}$$

The phase operator $\hat{\varphi}$ in terms of the ladder operators of the normal modes $\hat{a}_n$ and $\hat{a}_n^\dagger$ is written as:

$$\hat{\varphi} \equiv \sum_n \varphi_n^{\text{zpf}} \frac{\left(\hat{a}_n^\dagger + \hat{a}_n\right)}{\sqrt{2}} \tag{3.9}$$

Where φ_n^{zpf} represents the phase zero-point fluctuations in the junction that are induced by the corresponding normal mode n. The φ_n^{zpf} are related to the impedances Z_n^{bb} of the normal modes as seen by the junction as:

$$\varphi_n^{\text{zpf}} \equiv \frac{1}{\Phi_0}\sqrt{\hbar\, Z_n^{\text{bb}}} = \sqrt{\frac{Z_n^{\text{bb}}}{2\, r_{\text{Q}}}} \tag{3.10}$$

Where $r_Q = \frac{\hbar}{2e^2}$ is the reduced resistance quantum. The amplitude of the phase zero-point fluctuations φ_n^{zpf} can be traced to the energy-participation ratio p_n of the corresponding normal mode as:

$$\varphi_n^{\text{zpf}} = \sqrt{p_n \frac{\omega_n^{\text{bb}}/2\pi}{E_L/h}} \tag{3.11}$$

Where E_L is the energy corresponding to the test inductance $E_L = \Phi_0^2/L_{\text{t}}$. The hamiltonian $\hat{H}_{\text{epq}} = \hat{H}_0 + \hat{H}_{\text{nl}}$ is the effective quantum hamiltonian of the circuit design. Diagonalizing this hamiltonian yields the spectrum the fluxonium capacitively shunted to the ancillary resonator. In the practice, the hamiltonian $\hat{H}_{\text{epq}}$ can be diagonalized using the *scqubits*

python-environment [40]. Alternatively, one can follow, for instance, the method described by Smith *et al* in [71], where the matrix elements of the cosine potential are explicitly calculated in the energy basis (the basis of the bare hamiltonian $\hat{H}_0$), and then, the resulting hamiltonian $\hat{H}_{\mathrm{epq}}$ is diagonalized numerically.

3.3.4 Probing the microwave environment shunting the junction

In this Section, we describe an alternative application of the energy-participation method to model the microwave environment shunting the junction as an equivalent lumped-element circuit with a small set of characteristic parameters (see Figure 3.5a, 3.5d and 3.5e). In the practice, we replace the junction E_J by a test inductance L_{t}, and then, we simulate the normal modes of the linearized circuit including the microwave environment and the test inductance. The output data from one simulation are the frequencies ω_n^{bb} and energy-participation ratios p of the normal modes. These parameters are functions of the test inductance L_{t}, however, they can be traced to the characteristic parameters of the microwave environment, which are in principle independent from the test inductance L_{t}. The characteristic parameters of the microwave environment are: the fluxonium capacitance C, the bare resonator frequency ω_{R} and the shunting capacitance C_{S}.

For each normal mode, the energy-participation ratio p_n is related to the impedance Z_n^{bb} as seen at the ports of the test inductance as it follows:

$$Z_n^{\mathrm{bb}} = L_{\mathrm{t}}\, \omega_n^{\mathrm{bb}}\, p_n \tag{3.12}$$

With the frequencies $\{\omega_1^{\mathrm{bb}},\, \omega_2^{\mathrm{bb}}\}$ and the impedances $\{Z_1^{\mathrm{bb}},\, Z_2^{\mathrm{bb}}\}$ of the simulated normal modes, we can then synthesize the Foster (lumped-element) equivalent circuit corresponding to the circuit design, as it is shown in the Figure 3.6b. Alternatively, we can make the reasonable consideration that the circuit design can be represented by the bare (lumped-element) circuit that is shown in Figure 3.6a.

The objective then is finding the equations connecting the parameters of the two representations of the circuit design. On the one side, there are the parameters of the Foster equivalent circuit $\{\omega_1^{\mathrm{bb}},\, \omega_2^{\mathrm{bb}},\, Z_1^{\mathrm{bb}},\, Z_2^{\mathrm{bb}}\}$, which are obtained from the simulation of the normal modes but depend on the test inductance L_{t}. On the other hand, we have the bare parameters of the microwave environment $\{C,\, \omega_{\mathrm{R}},\, C_{\mathrm{S}}\}$, which are independent of the test inductance L_{t}. For this proof of concept, we re-use the same set of simulated data that was used before for the avoided-crossing method described in Section 3.2.2.2. In the first place, we extract the energy-participation ratios p_n and the frequencies ω_n^{bb} of the simulated normal modes as functions of the test inductance L_{t}, and then, we try to model all the obtain results with an unique set of parameters characterizing the microwave environment $\{C,\, \omega_{\mathrm{R}},\, C_{\mathrm{S}}\}$. Next, we test the efficiency of the energy-participation method to retrieve the characteristic parameters of the microwave environment shunting the Josephson junction from only one simulation of the normal modes, for an arbitrary value of the test inductance L_{t}.

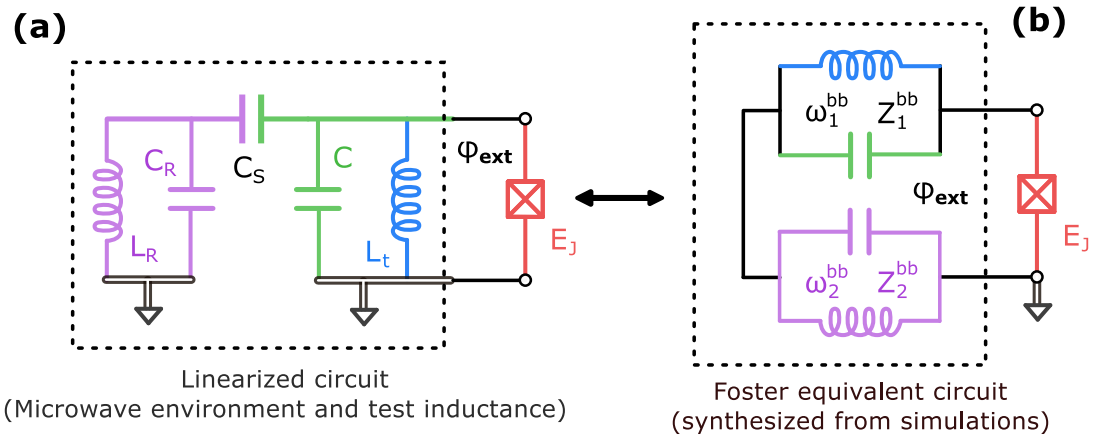

Fig. 3.6 ***Two lumped-element representations of the circuit design.*** *(a) Bare (equivalent) circuit: a non-linear resonator (the fluxonium) capacitively shunted to a linear resonator (purple). The non-linear resonator consists of an inductance (blue) and a capacitance (green) in parallel connection to the Josephson junction (red). (b) Foster equivalent circuit: the Josephson junction is shunted to a chain of two independent linear resonators, that represent the normal modes of the circuit design. Notice that a simulation yields the parameters of this circuit representation,* Z_n^{bb} *and* ω_n^{bb}.

3.3.4.1 Forward transform: going from the bare circuit to the Foster equivalent circuit

In this section we provide the equations relating the parameters of the Foster equivalent circuit, that are obtained from the simulations $\{\omega_1^{\mathrm{bb}}, \omega_2^{\mathrm{bb}}, Z_1^{\mathrm{bb}}, Z_2^{\mathrm{bb}}\}$, as functions of the parameters of the bare circuit, which include the parameters of the microwave environment. Here we just provide the results of the analytic derivations, check out the appendix A3 for more detailed information on the derivation of all the formulas. We then use these equations to model the same data set that was used before for the avoided-crossing method described in Section 3.2.2.2.

The frequencies of the normal modes ω_n^{bb} as functions of the parameters of the bare circuit are:

$$\begin{aligned}
\frac{1}{(\omega_1^{\mathrm{bb}})^2} &= \frac{1}{2}\left(\frac{1}{\omega_0^2}+\frac{1}{\omega_{\mathrm{R}}^2}\right)+\frac{1}{2}\sqrt{\left(\frac{1}{\omega_0^2}-\frac{1}{\omega_{\mathrm{R}}^2}\right)^2+\frac{4}{G^4}} \\
\frac{1}{(\omega_2^{\mathrm{bb}})^2} &= \frac{1}{2}\left(\frac{1}{\omega_0^2}+\frac{1}{\omega_{\mathrm{R}}^2}\right)-\frac{1}{2}\sqrt{\left(\frac{1}{\omega_0^2}-\frac{1}{\omega_{\mathrm{R}}^2}\right)^2+\frac{4}{G^4}}
\end{aligned} \tag{3.13}$$

Where:

$$\begin{aligned} \omega_0 &\equiv \frac{1}{\sqrt{C\,L_{\mathrm{t}}}} \\ \omega_{\mathrm{R}} &\equiv \frac{1}{\sqrt{C_{\mathrm{R}}\,L_{\mathrm{R}}}} \\ \frac{1}{G^2} &\equiv \frac{C_{\mathrm{S}}}{\sqrt{C\,C_{\mathrm{R}}}}\frac{1}{\omega_0\,\omega_{\mathrm{R}}} \end{aligned} \tag{3.14}$$

The parameters ω_{R} and ω_0 are the bare frequencies of the resonator mode and the linearized fluxonium mode, respectively. The parameter G depends on the shunting capacitance C_{S} and it is related to the coupling g between the two bare modes.

The impedances of the normal modes Z_n^{bb} as functions of the bare circuit parameters are given by:

$$\begin{aligned} Z_1^{\mathrm{bb}} &= \frac{1}{2}L_{\mathrm{t}}\,\omega_1^{\mathrm{bb}}\,\left[1+\cos\left(\theta\right)\right] \\ Z_2^{\mathrm{bb}} &= \frac{1}{2}L_{\mathrm{t}}\,\omega_2^{\mathrm{bb}}\,\left[1-\cos\left(\theta\right)\right] \end{aligned} \tag{3.15}$$

Where $\cos\left(\theta\right)$ is given by:

$$\cos(\theta) \equiv \frac{\left(\frac{1}{\omega_0^2}-\frac{1}{\omega_{\mathrm{R}}^2}\right)}{\sqrt{\left(\frac{1}{\omega_0^2}-\frac{1}{\omega_{\mathrm{R}}^2}\right)^2+\frac{4}{G^4}}}\,, \qquad \tan(\theta) = \frac{\frac{2}{G^2}}{\frac{1}{\omega_0^2}-\frac{1}{\omega_{\mathrm{R}}^2}} \tag{3.16}$$

Thus, the energy-participation ratios p_n of the normal modes can be simply related to the angle θ as:

$$\begin{aligned} p_1 &= \frac{1}{2}\,\left[1+\cos\left(\theta\right)\right] \\ p_2 &= \frac{1}{2}\,\left[1-\cos\left(\theta\right)\right] \end{aligned} \tag{3.17}$$

Notice that G (Equation 3.14) depends on the frequency of the linearized fluxonium mode ω_0, and this quantity depends of the test inductance L_t. Thus, G is not a good parameter to characterize the microwave environment. In the ideal scenario, we would like determine the values of both the shunting capacitance C_S and bare resonator capacitance C_{R}. However, the equations only depend of the ratio $C_{\mathrm{S}}/\sqrt{C_{\mathrm{R}}C}$ and not on the individual values of C_S and C_{R}. Thus, we define this ratio as the last parameter characterizing the microwave environment:

$$\gamma_{\mathrm{S}} \equiv \frac{C_{\mathrm{S}}}{\sqrt{C_{\mathrm{R}}C}} \tag{3.18}$$

We will refer to γ_{S} as the relative shunting capacitance. Therefore, the good set of characteristic parameters of the microwave environment are $\{C,\,\omega_{\mathrm{R}},\,\gamma_{\mathrm{S}}\}$. The Figure 3.7 shows the results of applying the formulas 3.13-3.18 to fit the frequencies ω_n^{bb} and the energy-participation ratios p_n of the simulated normal modes as functions of the test inductance L_{t}.

We fitted the frequencies ω_n^{bb} of the normal modes around the anti-crossing, $L_{\mathrm{ac}} \approx 15.50\,\mathrm{nH}$ (panel 3.7b), obtaining the three parameters related to the microwave environment, $\{C, \omega_{\mathrm{R}}, \gamma_{\mathrm{S}}\}$. These parameters were then used to calculate the expected energy-participation ratios p_n of the normal modes as functions of test inductance L_{t} (panel 3.7c), and the expected phase fluctuations φ_n^{bb} at a junction shunting the test inductance (panel 3.7d). We found that the Equations 3.13-3.18 with a single set of fixed parameters representing the microwave environment are in a good agreement with the simulations for a wide range of values of the test inductance L_{t}.

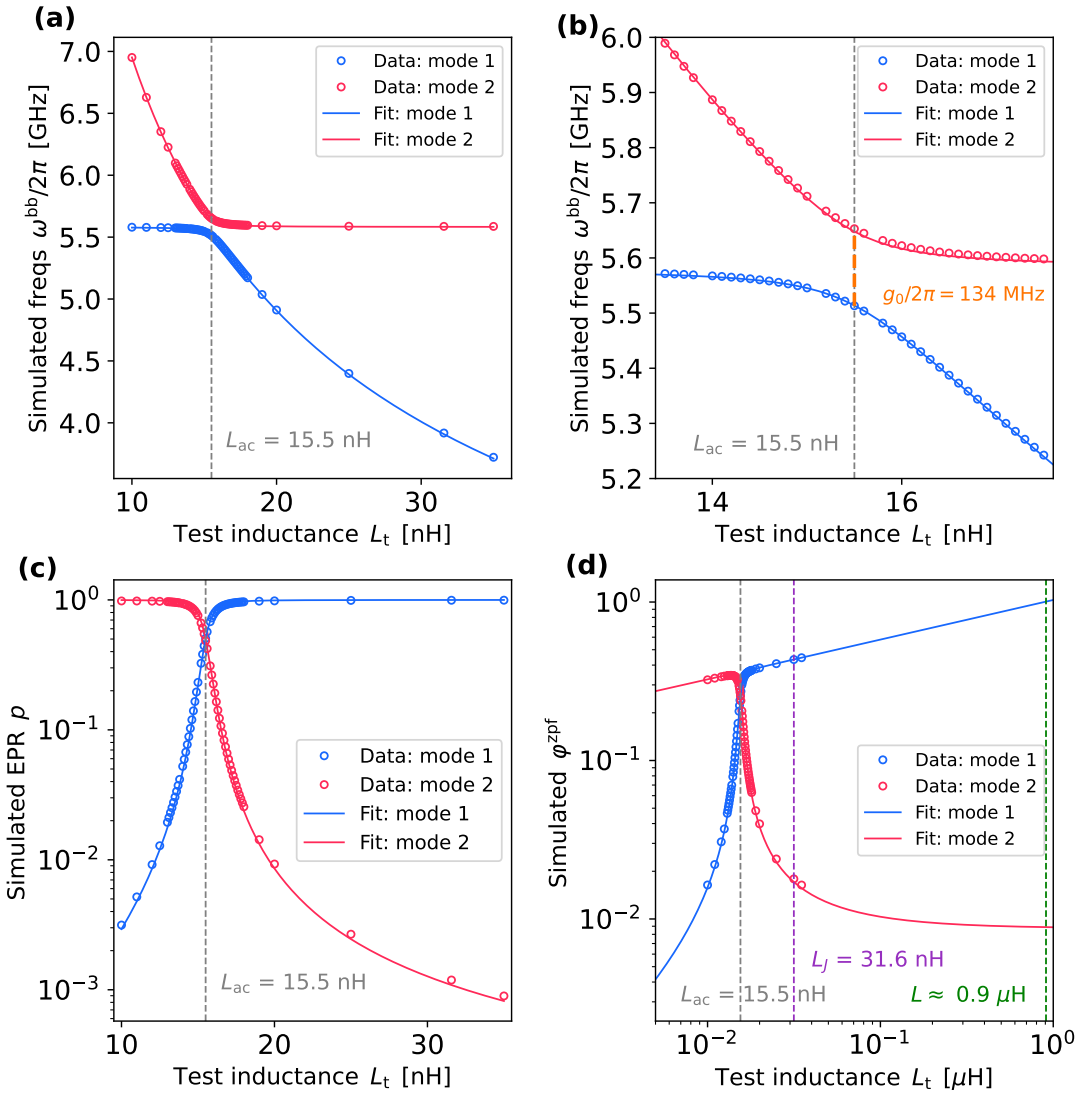

Fig. 3.7 ***Parameters of the simulated normal modes as functions of the test inductance:*** *(a) Frequencies ω_n^{bb} of the simulated normal modes. (b) Zoom-in at the anti-crossing between the modes. The orange dashed line represents the amplitude of the coupling at the anti-crossing g_{ac} that was deduced from the fit. (c) Energy-participation ratios p_n of the normal modes. (d) Expected amplitude of the phase zero-point fluctuations φ_n^{zpf} at a junction shunting the test inductance that are induced by each normal mode. The purple dashed line represents the value of the test inductance L_t corresponding to the linear inductance of the junction L_J. The green dashed line represents the value of the test inductance L_t corresponding to the superinductance of the fluxonium, of the order of 1 µH. The red and blue open bullets correspond to the data obtained from the simulations, while the solid lines are the calculated values using the equations described in the main text and the fitted parameters of the microwave environment: $\{C, \omega_R, \gamma_S\}$. This parameters were founded by fitting the frequencies of the normal modes ω_n^{bb} around the anti-crossing $L_{ac} \approx 15.50$ nH, yielding $C = 52.2$ fF, $\omega_R/2\pi = 5.57$ GHz and $\gamma_S = 0.024$.*

3.3.4.2 Reversed transform: retrieving the parameters of the microwave environment shunting the junction from one simulation

The good agreement between theory and simulations that was found in section 3.3.4.1 suggests that it is possible to retrieve the parameters of the microwave environment shunting the junction from the results of a single simulation of the normal modes. This chapter provides such equations, moreover, we test them with the simulated data that was used in sections 3.3.4.1 and 3.2.2.2.

By inverting the Equations 3.13-3.18, we obtain a set of equations to express the characteristic parameters parameters of the microwave environment $\{C, \omega_{\mathrm{R}}, \gamma_{\mathrm{S}}\}$ as functions of the frequencies ω_n^{bb} and the energy participation ratios p_n obtained from one simulation. Here we just provide the results of the calculations,a more detailed explanation on the derivation of the equations can be found in the appendix A3. Firstly, we express the bare frequencies of the modes ω_0 and ω_{R} in terms of the frequencies ω_n^{bb} and the energy participation ratios p_n of the simulated normal modes:

$$\begin{aligned}
\frac{1}{\omega_0^2} &= \frac{1}{2}\left(\frac{1+(p_1-p_2)}{(\omega_1^{\mathrm{bb}})^2} + \frac{1-(p_1-p_2)}{(\omega_2^{\mathrm{bb}})^2}\right) \\
\frac{1}{\omega_{\mathrm{R}}^2} &= \frac{1}{2}\left(\frac{1-(p_1-p_2)}{(\omega_1^{\mathrm{bb}})^2} + \frac{1+(p_1-p_2)}{(\omega_2^{\mathrm{bb}})^2}\right) \\
\frac{1}{G^2} &= \frac{C_{\mathrm{S}}}{\sqrt{C_{\mathrm{R}}\,C}}\,\frac{1}{\omega_0\omega_{\mathrm{R}}} = \left|\frac{1}{(\omega_1^{\mathrm{bb}})^2} - \frac{1}{(\omega_2^{\mathrm{bb}})^2}\right|\sqrt{p_1 p_2}
\end{aligned} \tag{3.19}$$

Where $\omega_1^{\mathrm{bb}} < \omega_2^{\mathrm{bb}}$, and the parameter G is related to the coupling g between the bare modes. From these three parameters, we extract the bare capacitance of the fluxonium C and the relative shunting capacitance γ_{S}:

$$\begin{aligned}
C &= \frac{1}{\omega_0^2\, L_{\mathrm{t}}} \\
\gamma_{\mathrm{S}} &\equiv \frac{C_{\mathrm{S}}}{\sqrt{C\,C_{\mathrm{R}}}} = \frac{\sqrt{p_1\,p_2}}{\sqrt{\left(\frac{\omega_1^{\mathrm{bb}}\,\omega_2^{\mathrm{bb}}}{(\omega_1^{\mathrm{bb}})^2-(\omega_2^{\mathrm{bb}})^2}\right)^2 + p_1\,p_2}}
\end{aligned} \tag{3.20}$$

The coupling between the bare modes g is related to the relative shunting capacitance γ_{S} as:

$$g = \gamma_{\mathrm{S}}\sqrt{\omega_0\,\omega_{\mathrm{R}}} \tag{3.21}$$

While γ_{S} only depends on the fixed parameters of the microwave environment, the coupling rate g depends on the bare frequency of the plasmon mode ω_0, which is a function of test inductance L_{t}, thus, it varies at each iteration of the simulations. The coupling at the anti-crossing g_0, when the bare frequencies of the modes are equal $\omega_0 = \omega_{\mathrm{R}}$, is related to γ_{S} as:

$$g_0 \equiv \gamma_{\mathrm{S}}\omega_{\mathrm{R}} \tag{3.22}$$

The Figure 3.8 shows the results of applying the reversed Equations 3.19-3.22 to retrieve the characteristic parameters of the microwave environment shunting the junction from the four

normal-modes parameters, $\{\omega_1^{\mathrm{bb}}, \omega_2^{\mathrm{bb}}\}$ and $\{p_1, p_2\}$, obtained from a single simulation. We calculate a set of microwave environment parameters for each iteration of the simulations (that were already display in Figure 3.7), which correspond to a variation of the test inductance L_{t}.

The calculated parameters of the microwave environment are: the capacitance of the fluxonium C (subpanel 3.8a), the bare frequency of the ancillary resonator ω_{R} (subpanel 3.8b) and the relative shunting capacitance γ_{S} (subpanel 3.8c). We also plot the coupling rate at the anti-crossing g_0 (Equation 3.22) that is obtained for each value of the test inductance L_{t} (subpanel 3.8d). The dotted lines represent the ideal values that were obtained by fitting the frequencies ω_n^{bb} of the simulated normal modes around the anti-crossing (see Figure 3.7b).

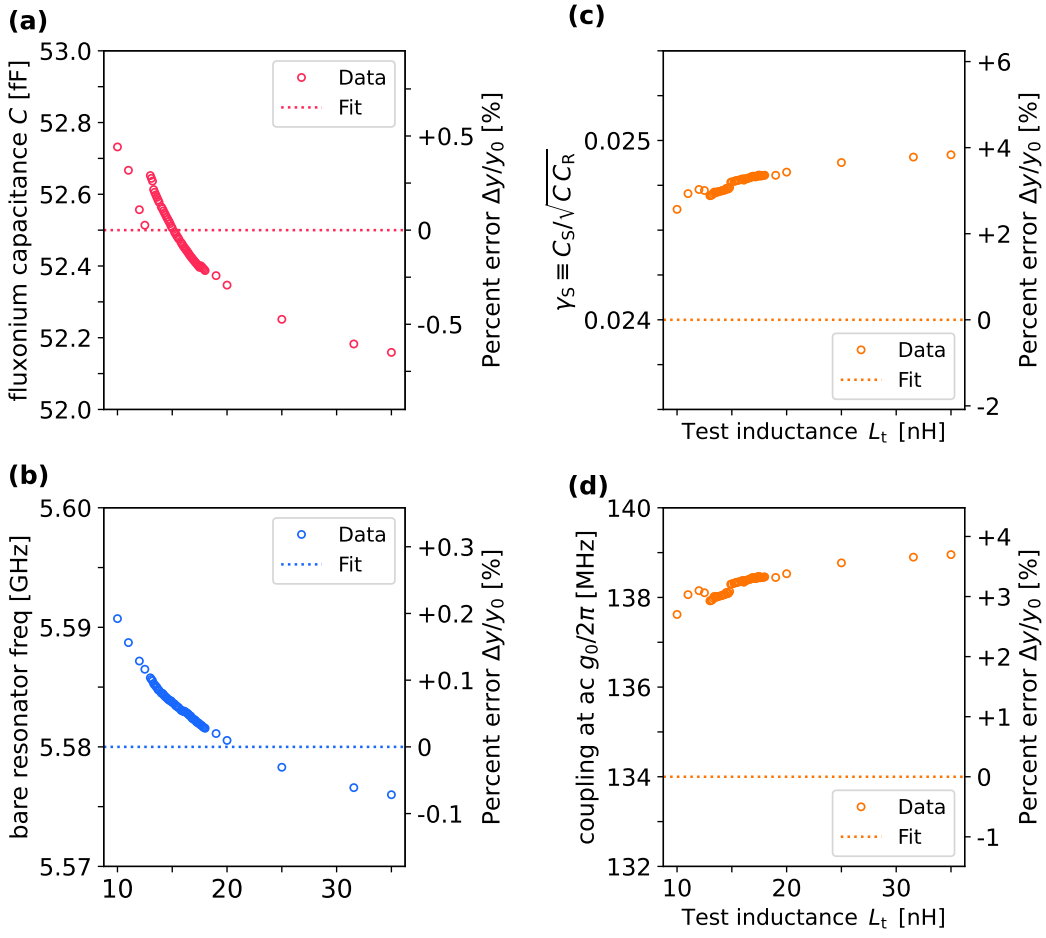

Fig. 3.8 ***Parameters of the microwave environment retrieved from the energy-participation method:*** *(a) fluxonium capacitance C, (b) bare resonator frequency ω_{R}, (c) relative shunting capacitance γ_{S}, and (d) coupling rate g_0 at the anti-crossing. Each point corresponds to one simulation with one variation of the test inductance L_{t}. The dotted lines represent the ideal values obtained by fitting the frequencies ω_n^{bb} of the simulated normal modes around the anti-crossing, $L_{\mathrm{ac}} \approx 15.50$ nH.*

We found that the parameters of the microwave environment depend slightly on the value of the test inductance L_t, nevertheless, their variations are rather small compared to the best values (dotted lines). The agreement between theory and simulations is in fact good enough such that we can estimate the parameters of the microwave environment from the frequencies ω_n^R and energy participation ratios p_n of the normal modes obtained from one simulation. The quality of the estimation decreases when the frequencies of the bare modes are away from from the avoided crossing, however, this constrained can be relaxed a bit by increasing the precision of the simulations. Thus, we can fairly assume that the microwave environment shunting the junction can be well represented by the bare equivalent circuit shown in Figure 3.6a. This equivalent circuit only contains three free parameters of characterizing the microwave environment, the fluxonium capacitance C, the bare resonator frequency ω_R and the relative shunting capacitance γ_S, which are up to a good approximation independent from the value of the test inductance L_t that takes the place of the junction during the simulations.

Chapter 4

Fabrication and experimental setup

This chapter covers experimental techniques that are central to the realization and operation of superconducting circuits. In particular, I describe in details various characterization techniques used to extract the geometric and electrical properties of the circuit's key element: the Josephson junctions. The chapter is divided in 5 sections: in the first one, I describe the various steps to fabricate the fluxonium circuit in the cleanroom. In the second one, I present various imaging techniques used to extract the geometry of the Josephson junctions. In section three, I describe an experimental setup used to measure the resistivity of the junctions at room-temperature. Guided by these characterization tools, I then explain the process through which the precise design choices for the various junctions in the circuit are made. Finally, I present the cryogenic setup used to operate the circuit at low-temperature. In the last section of the chapter I show a first low-temperature characterization of the junction chain allowing us to extract the plasma frequency of the fabricated junctions: a key parameter for the Josephson junction chains employed in the fluxonium circuit.

4.1 Circuit fabrication

This section describes fabrication process of the fluxonium circuit. The circuit is two-dimensional: it consists of a set of metal and oxide layers that are deposited on an insulating silicon substrate. It is fabricated in two steps. First, the circuit components that are larger than a few micrometers in size (including the coplanar wave-guide readout resonator, the flux line, the charge-drive coplanar resonator, and the fluxonium capacitor pad are etched with a plasma in a Niobium (Nb) layer following a UV-laser lithography. Next, the smaller circuit components, i.e. , mainly the Josephson junctions, are created using the conventional Dolan approach, which involves electron-beam lithography, metal deposition and oxidization, concluding with a lift-off process.

4.1.1 Large structures fabrication: UV-laser lithography

The process flow of the UV laser lithography (UV-litho) is sketched in Figure 4.1,

1. **Substrate:** the initial substrate for the fabrication of the circuit is a silicon (Si) wafer with (100)-orientation and 280 μm thickness and resistivity greater than 20 kΩ·cm.

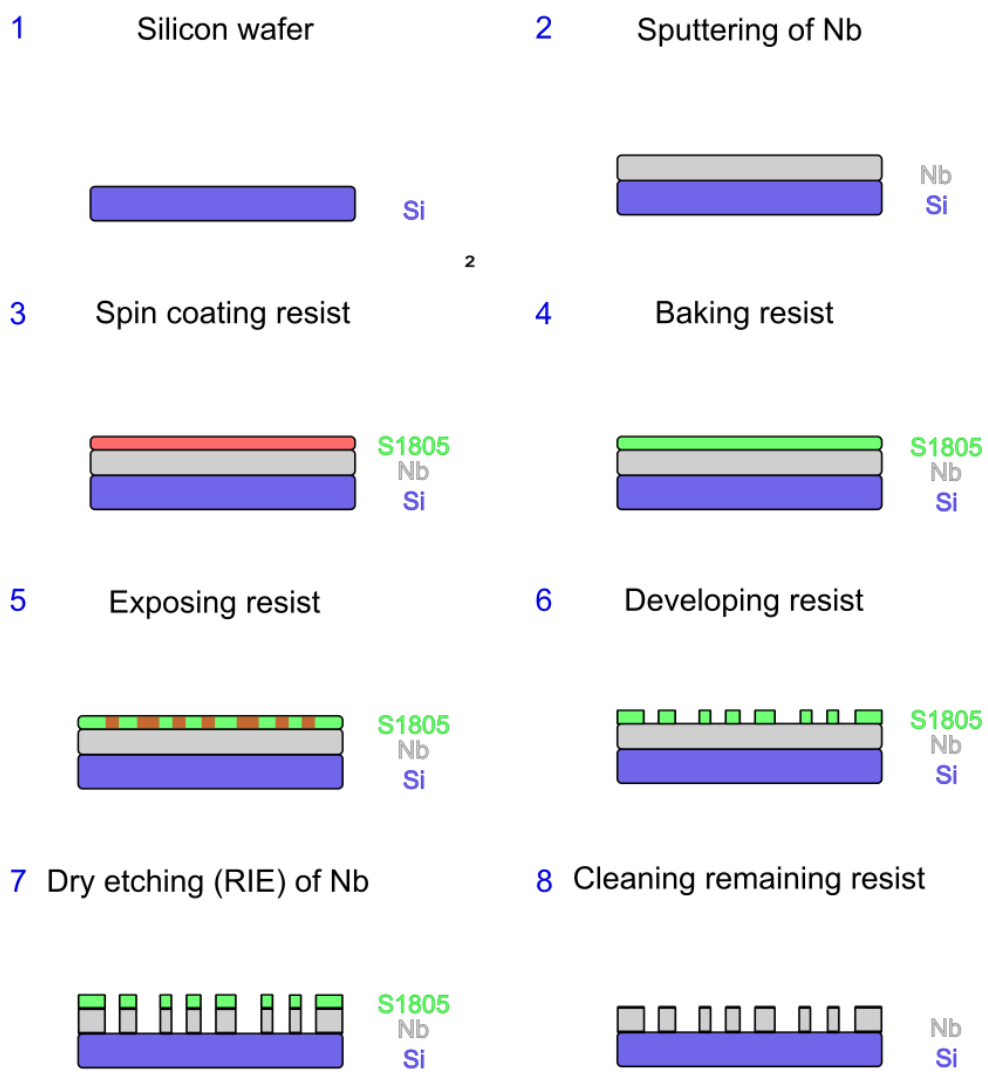

Fig. 4.1 ***Laser lithography process flow:*** *The initial substrate for the circuit is a 280-μm-thick silicon wafer with (100) orientation and a resistivity greater than 20 kΩ·cm (panel 1), then, a thin layer of niobium (Nb) with 150 nm-thick layer is deposited on one side of the wafer (panel 2). Next, a thin layer of the photo-sensitive resist S1805 is deposited over the Nb surface via spin coating (panel 3) then baked at 115 °C for 1 min (panel 4). The resist is exposed with an UV laser with a dose of 100 mJ/cm^2, (panel 5), next, the exposed resist areas are etched away by rinsing the wafer into MF-319 developer for 1 min (panel 6), any developer remainders are cleaned within a deionized water (di-H_2O) bath for 1 min before the wafer is dried with N_2 gas. The exposed areas of the Nb surface are etched (via reactive ion etching, RIE) with a SF_6 plasma (panel 7), with 20 extra seconds for Si etching. Finally, the resist remainders are removed following the standard wet cleaning procedure (panel 8): Firstly, the wafer is rinsed a hot bath of acetone at 50 °C for 15 min with low-power ultrasound, then, the wafer is cleaned within a bath of IPA at room temperature, finally, the wafer is dried with N_2 gas.*

2. **Sputtering of Nb:** An uniform niobium (Nb) layer with 150 nm thickness is deposited on top of the Si wafer via sputtering.

3. **Spin coating resist:** First, the Nb surface is cleaned by the standard wet cleaning, which consists in rinsing the wafer into a hot bath of acetone at 50 °C for approx 10 min, then, with the wafer still inside the bath, pouring hot acetone uniformly with a pipette over the whole Nb surface. Immediately after the hot acetone bath, the wafer is rinsed in IPA for about 20 s with gentle agitation, and finally the wafer is dried with N2 gas. Next, a thin layer of UV-sensitive S1805 positive resist is deposited over the Nb-coated surface of the wafer by spin coating with an angular speed of 4000 RPM for 1 min.

4. **Baking resist:** The resist is then baked at 115 °C for 1 min.

5. **Exposing resist (UV-laser lithography):** The wafer alignment is performed by manually matching the center of the wafer (physical origin) with the origin of the circuit drawing. The sample holder of the lithography machine has a X-Y positioning system with sub μm-precision that is used for raster scanning the sample surface with a focused UV-laser beam. During a typical scan, the laser is briefly unblanked at the points determined by the circuit drawing (mask), exposing locally the resist with a dose of 100 mJ/cm^2 at each point. The laser beam is focused by a microscope-objective that is mounted right above the sample holder. The objective mount has a Z positioning system with sub μm-precision for adjusting the position of beam focus on the vertical (Z) axis. The wafer surface is not completely flat and might be tilted, such that a correction of the beam focus is performed prior to resist exposure. This focus correction starts by manually optimizing the beam focus at some (at least three) key locations properly distributed over the wafer surface. The coordinates $Z_m(X_m,\ Y_m)$ of these points, are then interpolated to infer the wafer height at each position, and correct for the beam focus position.

6. **Developing resist:** The exposed resist is etched away into a bath of MIF-319 developer for 1 min.

7. **Dry-etching of Nb:** Next, the Nb-layer parts that were left uncovered are removed via reactive ion-etching (RIE) with SF_6 plasma for about 50 s, with extra 20 s for etching a bit of Si to ensure that the circuit will be deposited on a clean surface.

8. **Cleaning remaining resist:** The resist remainders are removed following the standard wet cleaning procedure: Firstly, the wafer is rinsed in a hot bath of acetone at 50 °C for 15 min with low-power ultrasound, then, the wafer is rinsed in IPA for about 15 s and immediately after it is dried with N_2 gas.

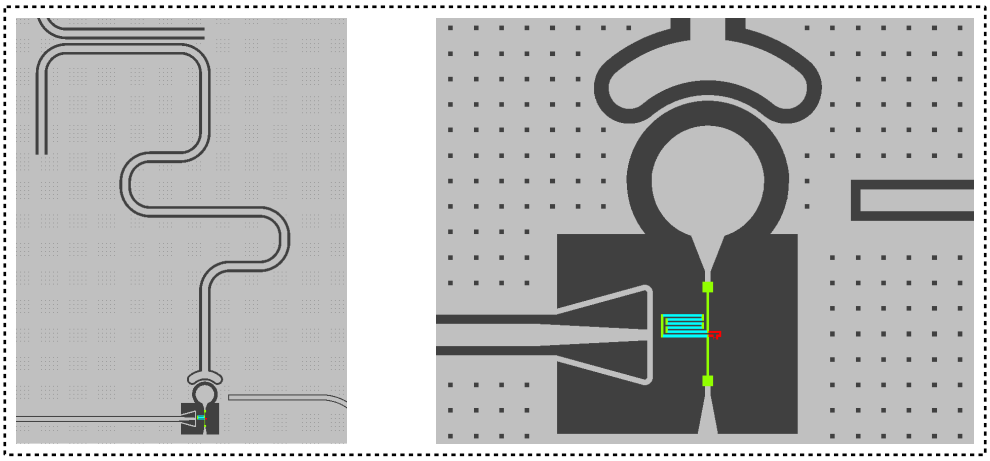

Fig. 4.2 ***Fluxonium circuit mask:*** *This Figure shows the actual mask that was used to fabricate the fluxonium circuit. The left panel shows all the larger circuit elements: the coplanar readout resonator plus its driving coplanar wave-guide (top), the fluxline (bottom left), the charge drive (bottom right), the circuit capacitor pad (circle in the bottom) and last but not least the ground plane. The right panel is a zoom into the smaller circuit structures: a superinductance made of few chains of large junctions (blue) and a small "black-sheep" junction (red), they are both shunted in parallel to the circuit capacitance to ground.*

4.1.2 Josephson junction fabrication: Electron beam lithography

The previous section described the fabrication of the large circuit elements via laser lithography, although they comprise most of the circuit, we are still missing two smaller but key elements: the super inductance, which is made of few chains of large junctions, and a small "black sheep" junction that acts as the main non-linear element of the fluxonium circuit.

We remind the reader that a S-I-S Josephson junction is a multi-layer structure that is made of two superconducting layers separated by an intermediate insulating layer, e.g., an oxide layer. The overlap between the three layers covers an area A, meaning that the Cooper pairs have to tunnel through the insulating barrier to hop between the two superconducting layers. For this project, we had chosen to fabricate Dolan-bridge style junctions [29], although this is not the only known style of Josephson junctions.

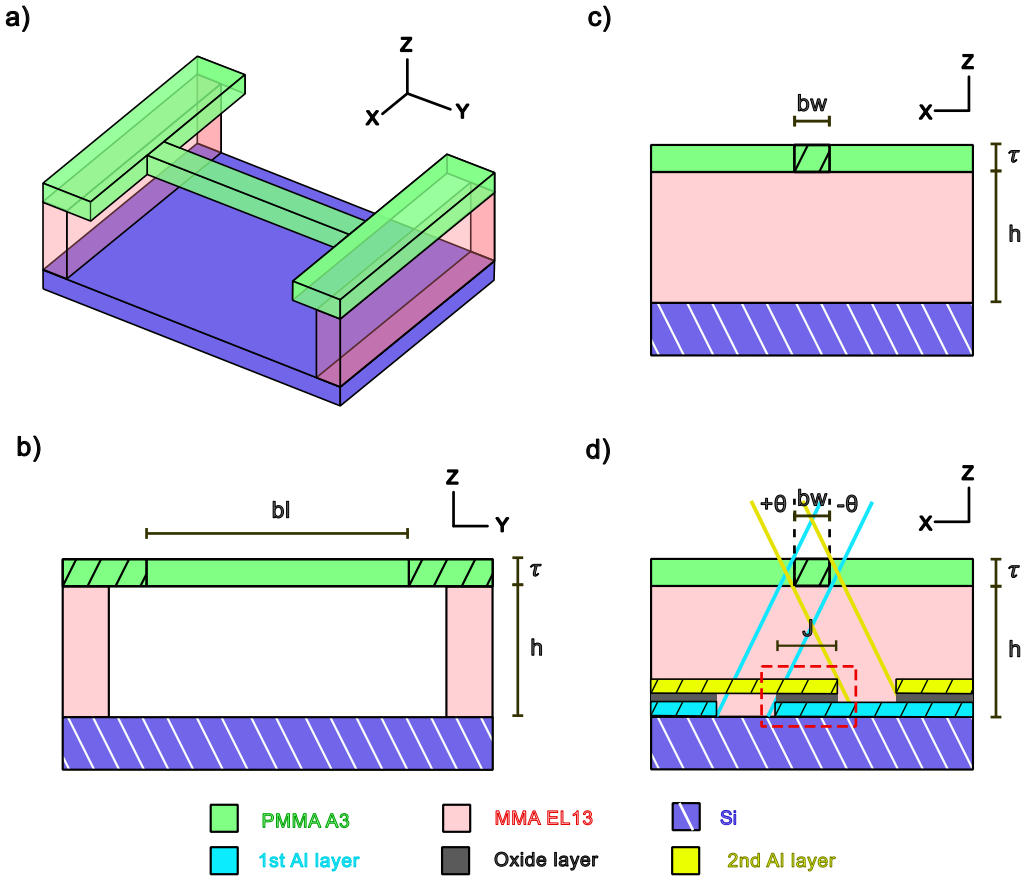

Fig. 4.3 ***Dolan-brige:*** *a) Isometric view of a Dolan bridge in a stack of two resist layers. The bridge is actually a beam in the top resist layer (PMMA, green) that is suspended above the substrate surface (purple) thanks to the bottom resist layer (MMA, red) acting as a support. b) Front view of the Dolan bridge, the bidge has a length bl and a height τ corresponding to the thickness of the top resist layer, and it is kept at a height h from the substrate that corresponds to the thickness of the bottom resist layer. Notice that the undercut in the bottom resist layer extends a bit beyond the lenght of the bridge bl. c) Side view of the Dolan bridge, the width of the bridge is bw, typycally 150 nm d) Example of the fabrication of an overlap structure, an S-I-S junction, by using the Dolan bridge and depositing two thin superconducting layers at different angles with respect to normal incidence. The first thin superconducting layer (light blue) is deposited at an angle of $-\theta$, then, an oxide layer (gray) is created on top the first layer via passive oxidation, finally the second thin superconducting layer (yellow) is deposited at an angle $+\theta$, with respect to normal incidence. The final overlap structure has a length J and a width roughly the same as bl.*

In a nutshell, the Dolan's (e-beam) lithography technique allows producing multi-layer structures with sub-micron scale features using a single mask and having only one lift-off processing [29], this goal is achieved by having a suspended mask [1], i.e., free standing above the substrate surface, that can be used to deposit different layers each one at a different angle with respect to normal incidence. [2] Particularly, the free standing mask is suspended at a height h, such that a layer deposited at an angle θ has also a horizontal offset S (in plane) with respect to a film deposited at normal incidence (see panel d) of Figure 4.3).

In the particular case of a Josephson junction, the fabrication process via the Dolan's approach is as follows: Firstly, a thin film of a superconducting metal (for example, aluminum) is deposited at an angle $-\theta_1$, then, an insulating layer is generated on top by passive oxidation, and finally another thin film of the superconducting metal is deposited at an angle θ_2. The S-I-S junction is then a stack of three layers where the overlap area A, the junction area, is determined by the deposition angles of the two superconducting films θ_1 and θ_2.

The key element for the junction fabrication via the Dolan's approach are free-standing resist bridges, as shown in Figure 4.3, the so-called Dolan bridges. The free-standing bridges are implemented by electron-beam lithography on a stack of two electro-sensitive resist layers, where the bottom (MMA) layer is more electro-sensitive than top (PMMA) layer. The amount of electrons (dose) that is used to expose the resist according to the design mask has to be well calibrated such that, upon development, a large area of the bottom layer is etched away, while only a small bridge from the top layer remains free-standing without collapsing (see panel a) of Figure 4.3).

This implementation of the free-standing bridges via laser lithography is further complicated because of the secondary electrons that are generated by inelastic scattering of the main electron beam (or primary electrons) which causes indirect exposing of the regions in the proximity of the lithographic patterns, we commonly refer to this additional and undesired dose as "proximity effects". After a lot of practical experience, we have managed to keep the proximity effects under control by defining two distinct layers in the lithographic masks, such that each one is related to a different lithographic pattern and a different dose. The main lithographic patter, referred to as the "main" design layer, corresponds to the regions of resist stack where both resist layers should be etched away, while the second lithographic patter, referred to as the "undercut" design layer, corresponds to the areas of the resist stack where only the bottom (MMA) layer is supposed to be etched away. The undercut design layer is exposed with a lower dose compared to the main design layer, e.g., the undercut dose is typically between 20 % and 30 % of the main dose.

4.1.2.1 Electron beam lithography

1. **Resist bilayer processing:** Firstly, a thin layer of the electro-sensitive resist MMA

[1] The suspended mask is actually a suspended resist layer with a lithographic pattern of holes acting as hard mask during the evaporation.

[2] Notice that the conventional lithography technique, where the mask is not suspended from the substrate surface, is only optimal for deposition at normal incidence so that a clean break of the deposited is ensured during the lift-off process.

EL13 is deposited via spin-coating with a speed 5000 RPM for 1 min, then, it is baked at 195 °C for 1 min. Next, a thin layer of the electro-sensitive resist PMMA A3 is deposited on top of the first layer via spin-coating with a speed 4000 RPM for 1 min, then, it is baked at 195 °C for 30 min. This long baking time is intended to evaporate as much water as possible from the top resist layer to ensure the stability the free standing bridges.

2. **Electron-beam lithography:** We load the sample into the lithography machine and pump it until reaching a working pressure of about 2×10^{-5} mbar. We set the working voltage of the e-beam at 25 kV and we then expose the the lithographic patthern corresponding to the main design layer with a dose of 0.85 times 280.00 μC/cm^2 and a spot size (d-step) of (10 nm)x(10 nm). The lithographic pattern corresponding to the undercut design layer is next exposed with a lower dose, 0.25 times 280.00 μC/cm^2, but same spot size with respect to the main lithographic pattern. The Figure 4.3 shows the design mask that was actually used to fabricate a fluxonium circuit, notice that the undercut design layer comprises areas surrounding the areas of the the main design layer, for example, the middle area of the free standing bridges.

3. **Resist developing:** Once the e-beam lithography has been completed, we develop the exposed resist with a mixture of $\mathrm{di}-\mathrm{H_2O}$ and IPA 1:3 at 6 °for 90 s with steady agitation, immediately after we rinse the wafer in IPA at room temperature for 10 more seconds, finally we dry the wafer with $\mathrm{N_2}$ gas.

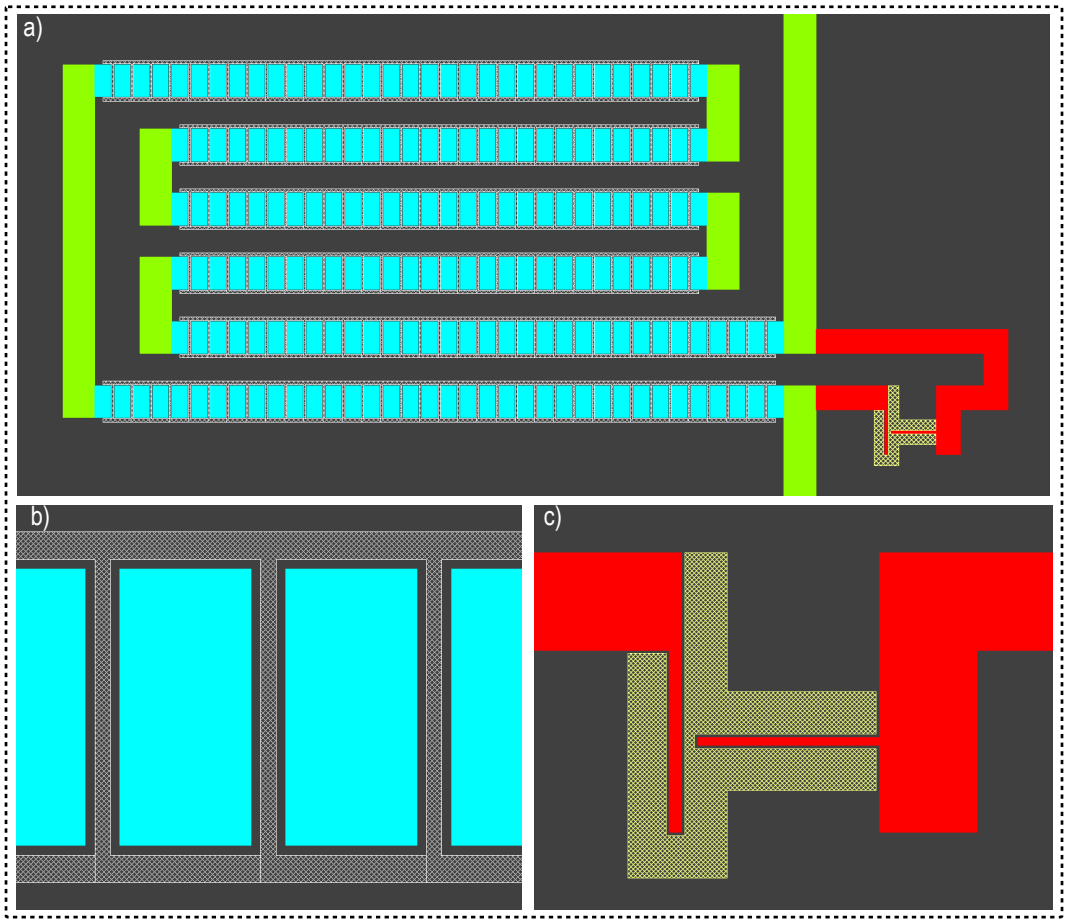

Fig. 4.4 ***E-beam lithography of the fluxonium circuit with doses:*** *a) Fluxonium circuit mask: there are three main structures, the junction arrays (blue), the small cross junctions (red) and the wires (green) connecting both of them. The distinction between them is needed to avoid underdosing or overdosing problems, e.g., the big array junctions are stacked so closed together that a junction chain receives some significant indirect exposition from the adjacent junction chains (on top and below), thus, the junction arrays (blue) require a smaller dose, 0.85 dose factor, compared to the wires (green), 0.90 dose factor. On the contrary, the small cross junctions (red) are too narrow, about 200 nm, and they are far away from other structures so that they require a higher dose, 1.05 dose factor, compared to the wires. Notice that a dose factor of 1.0 corresponds to 280.0 $\mu C/cm^2$. The panel b) shows a zoom into a junction array, the dashed white layer has a smaller dose factor of 0.25, the purpose of this undercut-layer is properly defining the undercut in the bottom resist layer, i.e., while the blue layer represents the holes in the top resist layer, the white dashed layer is related to the undercut in the bottom resist layer. The panel c) shows a zoom into a small cross junction, the dashed yellow layer has a smaller dose factor of 0.30. The importance of the undercut layers must not be underestimated, they allow to obtain well defined junction geometries and avoiding dosing problems, for example, collapsing of the free standing bridges (overdosing) or unwanted resist remainders below the bridges (underdosing).*

4.1.2.2 Al evaporation

The final step in the junction fabrication is the aluminum evaporation, we make the S-I-S junctions by evaporating two aluminum layers at different angles, with an oxidation step in between to make an oxide layer separating the two aluminum layer.

1. **Preliminary preparations:** After creating the suspended bridges in the resist stack,the wafer is loaded into the evaporation machine, and then, it is pumped (overnight) until reaching a pressure of about 5.0×10^{-7} mbar.

2. **Ti deposition:** Before starting the first evaporation, a bit of titanium (Ti) is evaporated (with the sample shutter closed) at a rate of 0.2 nm/s in order to pump down the chamber down to 5×10^{-5} mbar.

3. **Ion milling:** Next, the native oxide layer is etched from the wafer surface with the aid of ion milling with a voltage of 100 V and a flow of argon (Ar) corresponding to a pressure of 3×10^{-4} mbar for 6 s.

4. **1st Al layer deposition:** The first Al layer is evaporated with a tilt angle of -22°(with respect to a horizontally aligned wafer, i.e., normal incidence) at a rate of 1 nm/s amounting for a thickness of 31 nm.

5. **Passive oxidation:** Then, an insulating layer is created by oxidizing the top of the first Al layer via passive oxidation at 200 mbar for 10 min. Before evaporating the last Al layer, the evaporation chamber is pumped back for about 1 h until reaching a pressure of about 5×10^{-7} mbar.

6. **2nd Al layer deposition:** Next, the second Al layer is evaporated with a tilt angle of +22°at a rate of 1 nm/s amounting for a thickness of 100 nm. The thickness of the second layer has to be greater than the thickness of the first layer to avoid unwanted discontinuities in the layers, therefore, resulting in, for example, opened junction chains.

7. **Lift-off and cleaning:** Finally, the unwanted aluminum and the remaining resist are lift-off by rinsing the wafer in hot bath of NMP at 80 °C for 20 min, continuing with a bath of acetone at 50 °C for 10 min. The wafer is then dried with N_2 gas after rinsing it in IPA.

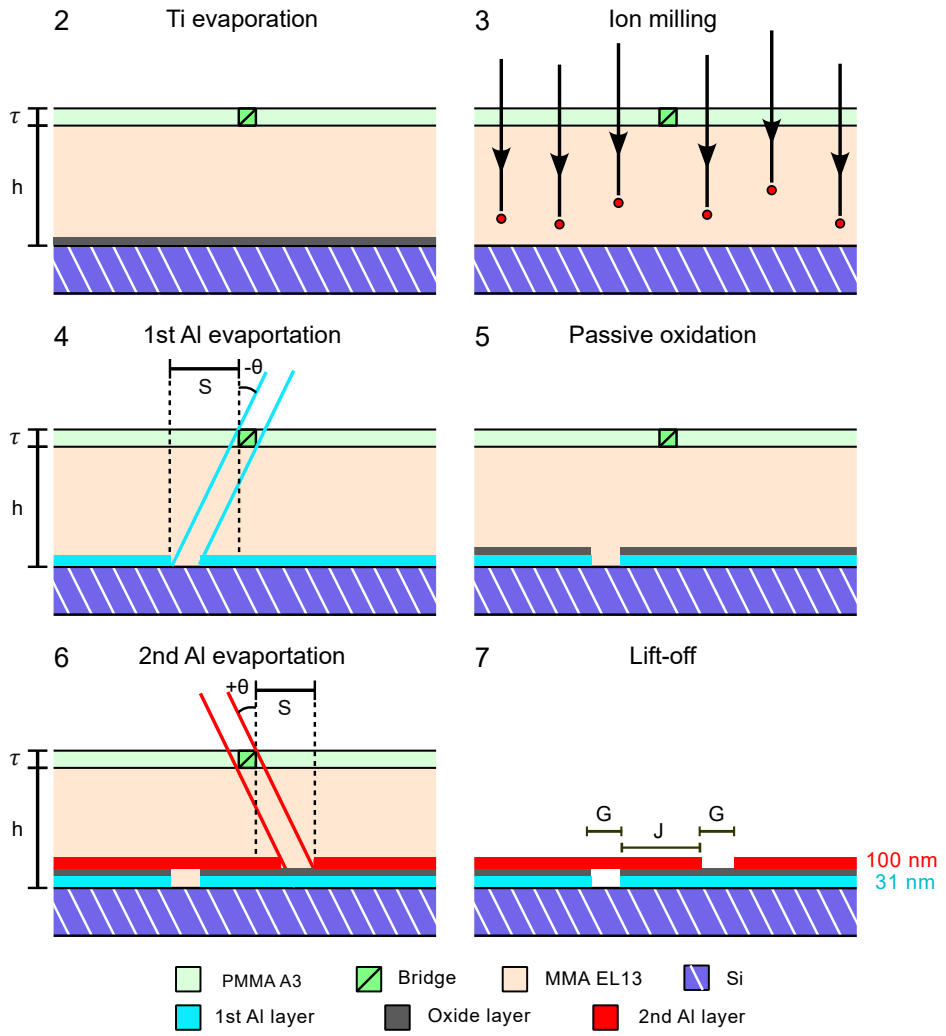

Fig. 4.5 ***Junction evaporation:*** *As preliminary step (1, not shown), the substrate is loaded into the evaporation machine and pumped down to about* 9×10^{-7} *mbar. Next, a bit of Ti is evaporated in the sample chamber (panel 2) at a rate of 0.2 nm/s, with the sample shutter closed, in order to reduce the vacuum down to about* 5×10^{-7} *mbar. Then, the native oxide layer (gray) is removed from the Si substrate (purple) by ion milling with Ar plasma at a voltage of 100 V and a pressure of Ar flow of* 3×10^{-4} *mbar for 6 s. Next, the first Al layer is evaporated (panel 4) at an angle* $-\theta$ *with a rate of 1.0 nm/s until reaching a thickness of 31 nm. Then, an oxide layer is created by passively oxidizing the surface of the first Al layer (panel 5) with a mixture of Ar and* O_2 *9:1 at a static pressure of 200 mbar for 10 min. Next, the second Al layer is evaporated at an angle* $+\theta$ *with a rate of 1.0 nm/s until reaching a thickness of 100 nm. Finally, the resist stack of MMA (orange) and PMMA (green) as well as the Al remainders are removed during the lift-of (panel 7): first, the sample is rinsed in a hot bath of NMP at 80°for about 20 min removing most of the resists and the unwanted Al remainders, next, the wafer is rinsed in a bath of acetone at 50°for about 20 min, and lastly, the wafer is rinsed in a bath a IPA at room temperature and dried with* N_2 *gas.*

4.1.2.3 Junction-chain geometry formulas

The Josephson junction chain is obtained during the same evaporation steps as those used for the small "black sheep" junction of the fluxonium. In practice, a 1-dimensional array of N Dolan bridges is used to form a compact array of Josephson junctions, as it can be seen in Figure 4.5. In the following, we estimate the final junction-chain geometry from the relevant geometric parameters of the mask used for its fabrication: the width of each resist bridge b_w, the spacing between adjacent bridges b_s, the thickness of the MMA and PMMA layers, h and τ, respectively, and the angles of the two successive deposition steps $-\theta$ and θ (for simplicity, both angles are assumed to be equal in magnitude but with opposite directions).

As visible in panel c) of Figure 4.5, the first (blue) and second (yellow) Al layers are not continuous but they contain several gaps, each one of them being created by the "shadow" of one free-standing bridge. Furthermore, the two Al layers are shifted with respect to one another by an offset

$$S = (2h + \tau)\tan(\theta) \tag{4.1}$$

The width G of a bridge shadow is slightly wider compared to the actual bridge width because of the the bridge height, or rather the thickness of the PMMA layer τ:

$$G = b_w + \tau\tan(\theta) \tag{4.2}$$

We remark that we only consider the relevant parameter regime where the bridge shadows of one layer do not overlap with the bridge shadows of the other one, such that the superposition of the two Al layers forms a periodic array of bilayer-strips interconnected by monolayer-strips, these last ones correspond to the bridge shadows. The junction-chain can then be seen as an array of $2N - 1$ Josephson junctions connected in series, where N is the number of bridges. In other words, a Cooper–pair would need to tunnel through those $2N - 1$ bilayers in order to traverse the chain from one end to the other.

One can identify two families of junctions in the chain: the first family consists of the junctions centered below each bridge of index k, those are bounded at their left and right edges by the shadow of bridge k in the Al layer 1 and the shadow of the same bridge in Al layer 2, respectively. We denote by J_1 the width of those junctions. Via elementary trigonometric considerations, we arrive at

$$J_1 = 2h\tan(\theta) - b_w \tag{4.3}$$

From the fact that the spatial periodicity of array of bridges $P = b_w + b_s$ transfer to the Al layers and the junction chain, we get the following equation

$$J_1 + J_2 + 2G = P \tag{4.4}$$

The second family of junctions appears in between successive bridges: those junctions are bounded at the left edge by the shadow of the bridge indexed k in Al layer 1, and at the right edge by the shadow of the bridge indexed $k + 1$ in Al layer 2. The width of these junctions is denoted as J_2. By plugging Equation 4.2 and 4.3 into 4.4, we obtain

$$J_2 = b_s - 2(h + \tau)\tan(\theta) \tag{4.5}$$

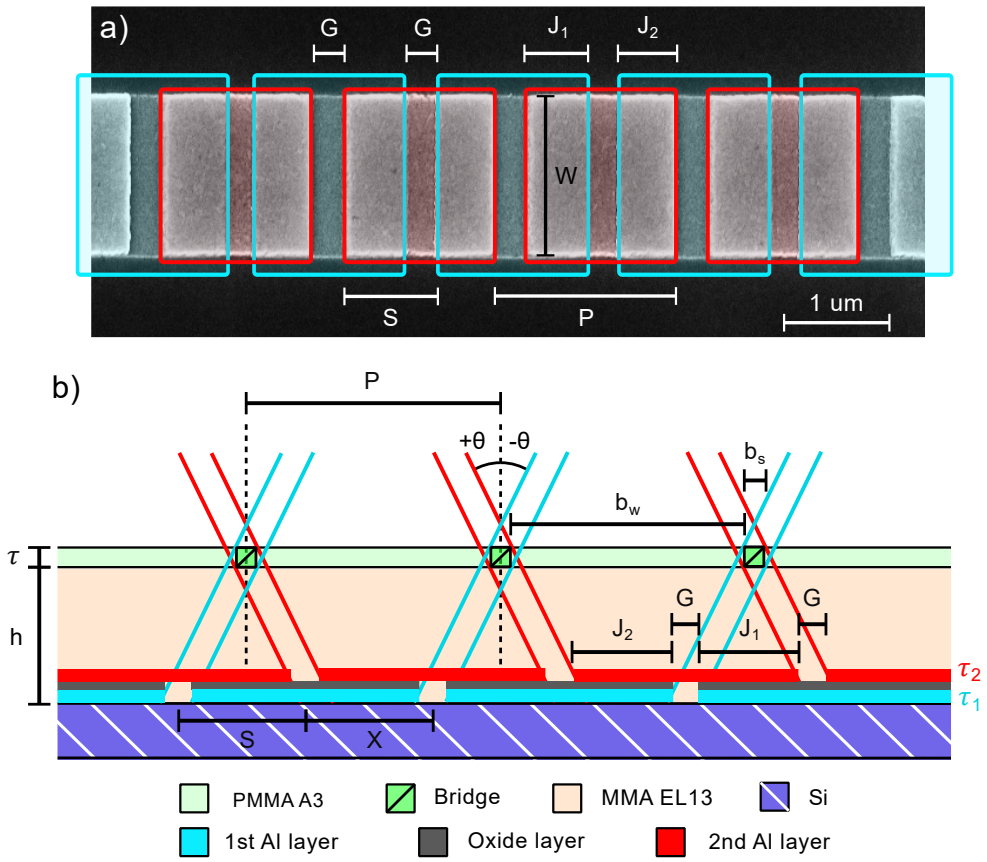

Fig. 4.6 ***Geometrical parameters of Dolan-style junction chains:*** *The panel a) shows an SEM picture of an actual Dolan-style junction chain, the bottom (first) and top (second) Al layers are highlighted by the blue and red rectangles, respectively, matching the colors used in panel b). The junction width is denoted by w, the length of the bridge shadows is G, the widths of the junctions are denoted by J_1 (first junction family) and J_2 (second family), the offset between the Al layers is S, and the period of the junction chain is P, which is the same as the period of each Al layer as well as the period of the array of suspended bridges. The panel b) shows a drawing with the relevant geometrical parameters related to the fabrication of Dolan-style junction chains. The junctions are created by evaporating-oxidizing-evaporating Al at the angles $-\theta$ and $+\theta$. Each Al layer is not continuous but it is interrupted by the "shadows" of the suspended bridges, such that the centers of two adjacent "shadows" are separated by P, the period of the array of suspended bridges. The two Al layers are shifted with respect to each other by S which depends on the evaporation angles $-\theta$ and $+\theta$ and the thicknesses of the resist layers τ and h. The length of a bridge shadow G is slightly grater than the bridge width b_w because of the finite thickness τ of the suspended bridges. Two families of junctions are created from the overlap between the Al layers: The junctions from the first family, whose length is denoted by J_1, are created at the horizontal position of the bridges, such that $J_1 = S - G$, while the junctions from the second family, whose length is denoted by J_2, are created at the intermediate horizontal position between two adjacent bridges, such that $J_2 = X - G$, where $P = S + X$. The condition of symmetric junctions is achieved when, $X = S$, meaning that $P = 2S$. Notice that a total of $2N - 1$ junctions are generated from an array of N suspended bridges.*

Finally we must consider the case of symmetric junctions, i.e., both junction families in the chain having the same width $J = J_1 = J_2$, this case is typically the most important one from the practical point of view. We derive an expression for difference between the widths of both families of junctions using Equations 4.3 and 4.5

$$J_2 - J_1 = P - 2S \tag{4.6}$$

Therefore, the condition of equal junctions $J_1 = J_2$ is fulfilled when $P = 2S$, i.e., the period P of the array of bridges (same as the one of the chain) is equal to twice the offset S between the deposited Al layers

$$P = 2S = 2(2h + \tau)\tan(\theta) \tag{4.7}$$

4.1.2.4 Guidelines for designing Dolan-style junction chains

We finalize the considerations on the junction-chain geometry by providing few practical considerations, from the fabrication point of view, in order to fulfill the following constraints on the final junction-chain geometry:

1. The portions of the chain consisting of monolayers increase the stray capacitance of the chain without significantly contributing to the total (kinetic) inductance of the chain. Consequently, the approach should be minimizing the width G of these elements compared to the width $J = J_1 = J_2$ of the junctions.

2. Both families of junctions should have the same area (i.e. the same width $J_1 = J_2 = J$ in this 1-dimensional model). Otherwise, the smallest junctions would constitute a weak link for phase slips, leading to sub-optimal chain properties.

From criterion 1, it follows that the resists used for the lithographic mask must be chosen such that the thickness of the top resist layer τ is as small as possible compared to the thickness of the bottom resist layer h. Also, the width of the free standing bridges b_w is chosen to be approximately equal to the thickness of the top resist layer τ. Indeed, reducing b_w further only has a marginal impact on the gap G, as visible on Equation 4.2, while it would weaken the free-standing PMMA bridge. Notice that the value of τ can be estimated from the resist data sheet, for example, PMMA A3, by knowing the angular speed used for the spin-coating.

Satisfying criterion 2 requires that both junction families in the chain have the same width, this case was already discussed at the end of the previous subsection, essentially the $P = 2S$ must be fulfilled, meaning that the periodicity P [3] of the bridge pattern should be set to twice the offset between the 2 deposited aluminum layers. Notice that the offset S depends on τ and h and the deposition angle θ. However, in practice it is not necessary to determine to high precision τ and h to set the period P of the array of bridges since the offset S between the two Al layers can be easily measured via scanning electron microscopy (SEM). Thus, once we have chosen the deposition angle to be θ, we only have to set the period P equal to twice the measured offset between the Al layers $2S$. Finally, once we

[3] The periodicity $S = b_w + b_s$ is perfectly defined by the lithographic mask, contrary to the individual parameters b_w and b_s that depend on the precise dose and development conditions, making it a more robust design parameter to consider.

have determined the right period P_a corresponding to a deposition angle θ_a, for example, $\theta_a = 22°$, if the deposition angle is later modified to θ_b, then, the period P_b needs to be adjusted such that

$$\frac{P_b}{P_a} = \frac{\tan(\theta_b)}{\tan(\theta_a)} \tag{4.8}$$

4.2 Junction geometry characterization

Two characterizations need to be performed (at room temperature) after the fabrication of the junctions: measuring the junction resistance and the junction area. There is a remaining characterization to be done at cryogenic temperature (inside the cryostat), the junction plasma frequency measurement, but that will be described in a later section.

4.2.1 Scanning electron microscopy

This section presents the results from the geometric characterization of the junctions via scanning electron microscopy (SEM), specially its area. The Figure 4.6 shows two SEM pictures of a junction chain belonging to a fluxonium circuit fabricated in our laboratory, the junctions edges look sufficiently straight and the corners are not too rounded. We remark that throughout this text the dimension of the junctions that is collinear to the wire length is referred to as the junction length, while the dimension orthogonal (in-plane) to the wire length is referred to as the junction width. Notice that the chain is made by pairs of almost equivalent junctions, having lengths of $J_1 = 568$ nm (P2) and $J_2 = 557$ nm (P3), respectively. The width of the junctions is $w = 1.5$ μm (P1). The period of the junction chain is $P = 1.7$ μm (P4), which is the same as the period of the 1-D arrays of bridges that were used to fabricate the junction chains. Although the offset between the Al layers can be seen in Figure 4.6, being $S = 852$ nm (P6), the period was actually measured in advance, from a previously fabricated batch of junction chains via SEM, so that the period for the junction chains displayed in this picture could be set to satisfy $P = 2S$.

This was not the case back when we started fabricating junctions. In the beginning, we were not using extra layers (and doses) to define the undercuts properly and the junctions edges were rounded, specially at the corners, and junction length (dimension parallel to the wire length) was not constant for different width values (the dimension orthogonal to the wire length), which was not expected. Indeed, without an additional layer to define the undercuts, there were resist remainders (from the bottom layer) below the bridges resulting in irregular bridge shapes and effectively thicker bridges. The amount of resist remainders below each bridge was strongly dependent on the bridge length (junction width) due to proximity effects (the indirect and unwanted dosing of a resist area coming from the direct exposure of nearby resist areas), meaning that the effective bridge height was strongly dependent on the bridge length, the consequence of this was that the right periodicity to have equal junctions, $P = 2S$, was bridge-length dependent, making junction fabrication very prone to reproducibility problems. Notice that we also added an additional layer for the "wires" (sections of the fluxonium loop connecting two junction chains or a junction chain and the small "black-sheep" junction). The addition of all the extra layers, see Figure 4.4, each one related to a different exposure dose, had a significant effect in reducing the

proximity affecting the junctions, and it made the junction fabrication more reproducible (less variation in the junction areas after each iteration), and the fabricated junctions were looking better.

The Figure 4.7 shows two SEM pictures of a small junction of the fluxonium circuit. The junction length and width are 244 nm (P4) and 166 nm (P3), respectively. The shift between the two Al layers is approx 850 nm (P2 and P5), Figure 4.7 shows clearly why S is referred to as the offset between the two deposited layers.

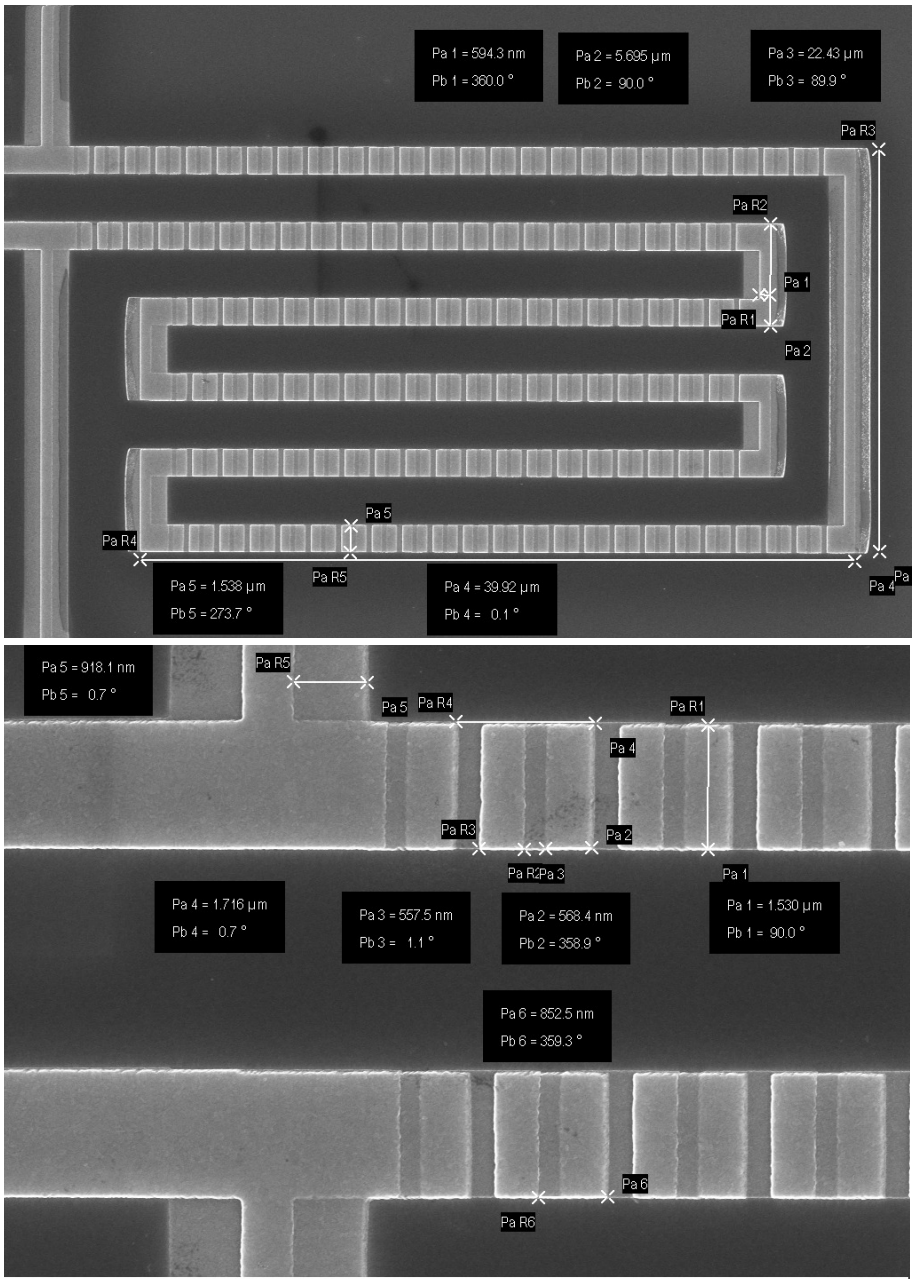

Fig. 4.7 ***Junction array:*** *Top: SEM picture of a junction array in a fluxonium circuit. Bottom: SEM picture with a larger magnification of the same junction array.*

4.2.2 Atomic force microscopy

This section presents the results from the geometric characterization of the junctions via atomic force microscopy (AFM). The atomic force microscopy is useful to obtain information about the relieve of a given surface, in fact, an AFM picture represents a 2-D map of the height as function of the position over the surface, such that each color is associated with a different height value. Notice that the contrast in an SEM picture also can be as-

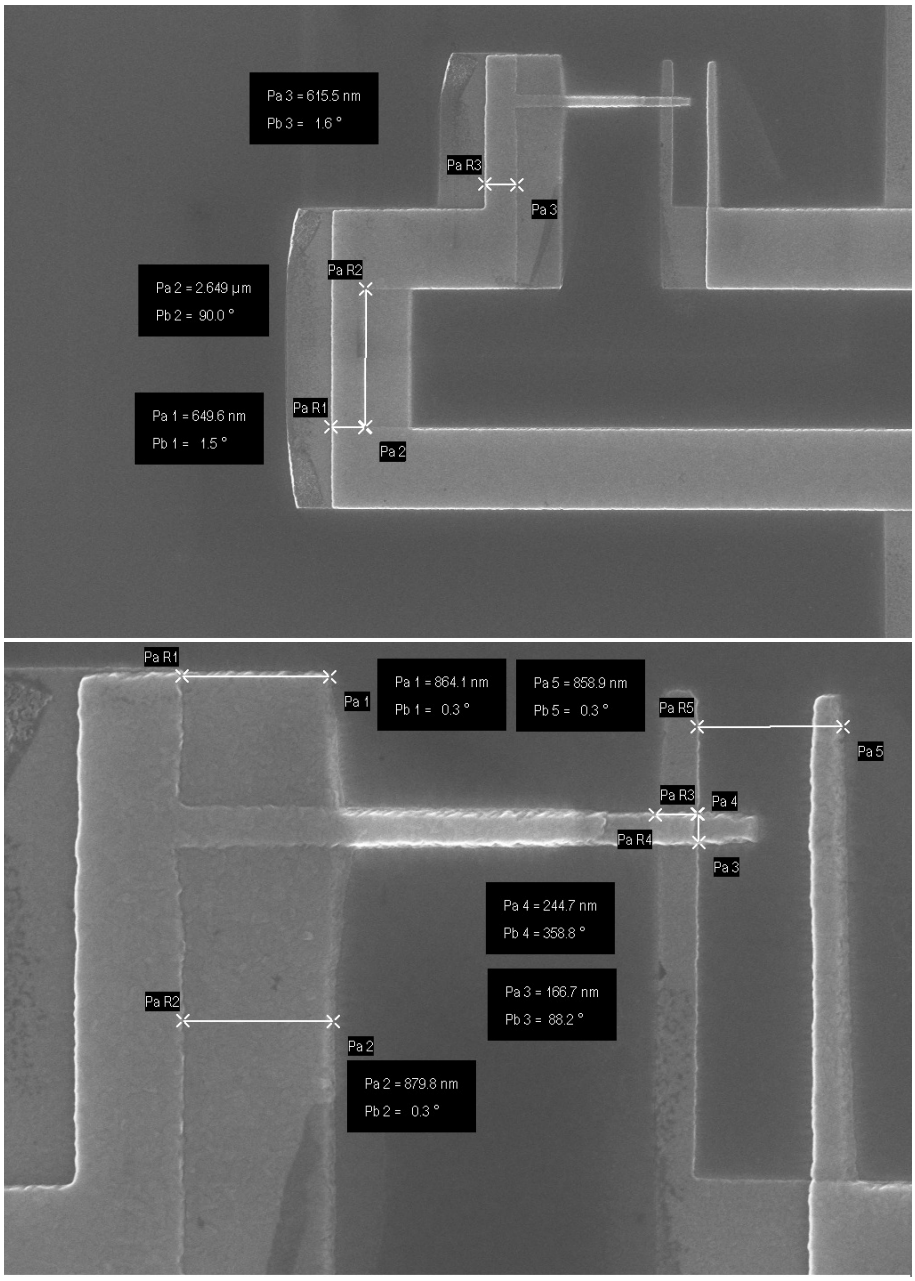

Fig. 4.8 ***Cross junction:*** *Top: SEM picture of a cross junction in a fluxonium circuit. Bottom: SEM picture with a larger magnification of the same cross junction.*

sociated to differences in height over the scanned surface, or rather differences in thickness in the case of a multi-layer structure, nevertheless, there are other things additionally affecting the contrast, after all, different materials interact differently with the electron beam used to acquired the SEM pictures. Moreover, even for multi-layer structures made of the same material, like the Dolan style junctions presented here, there is no simple relation (for example, linear) between the picture brightness and the corresponding surface height, or rather material thickness. Finally, although more information can be inferred from an AFM

picture compared to a SEM picture, the SEM picture is typically more accurate for measuring in-plane distances, and the AFM should rather be used only to scan the surface height.

The Figure 4.8 displays an AFM picture of a junction chain, the 1-D array of bridges used to fabricate this chain has had similar geometric parameters as the array of bridges used to fabricate the junction chain in 4.6, e.g., the period $P = 1.7$ μs and the bridge width 125 nm, the evaporation angle was also identical, $\theta = 22$ °(and -22 °), however, the bridge length was different for the two chains, which only means that the junction widths are different.

Several white lines were drawn over the picture of the junction chain in panel a) of Figure 4.8, each line represents a trajectory over the surface, the panel b) plots the surface height as function of the distance along the lines, notice that the curves in panel b) are labelled with different colors and not the same as the white lines in panel a). The panel b) also display the information about the height of the Al layers, for example, the lowest part of the cyan line identifies the beginning of the Si substrate underneath the junctions. We see that the thickness of the first layer (deepest valley) is about 25 nm, as measured from the Si substrate surface, on the other hand, the thickness of the second layer is about 70 nm (highest valley). Each white line in panel a) has a pair of marks that are represented by two vertical dashed lines in the panel b), respectively. The panel c) shows the measured horizontal and vertical distances between the two marks of each withe line in panel a).

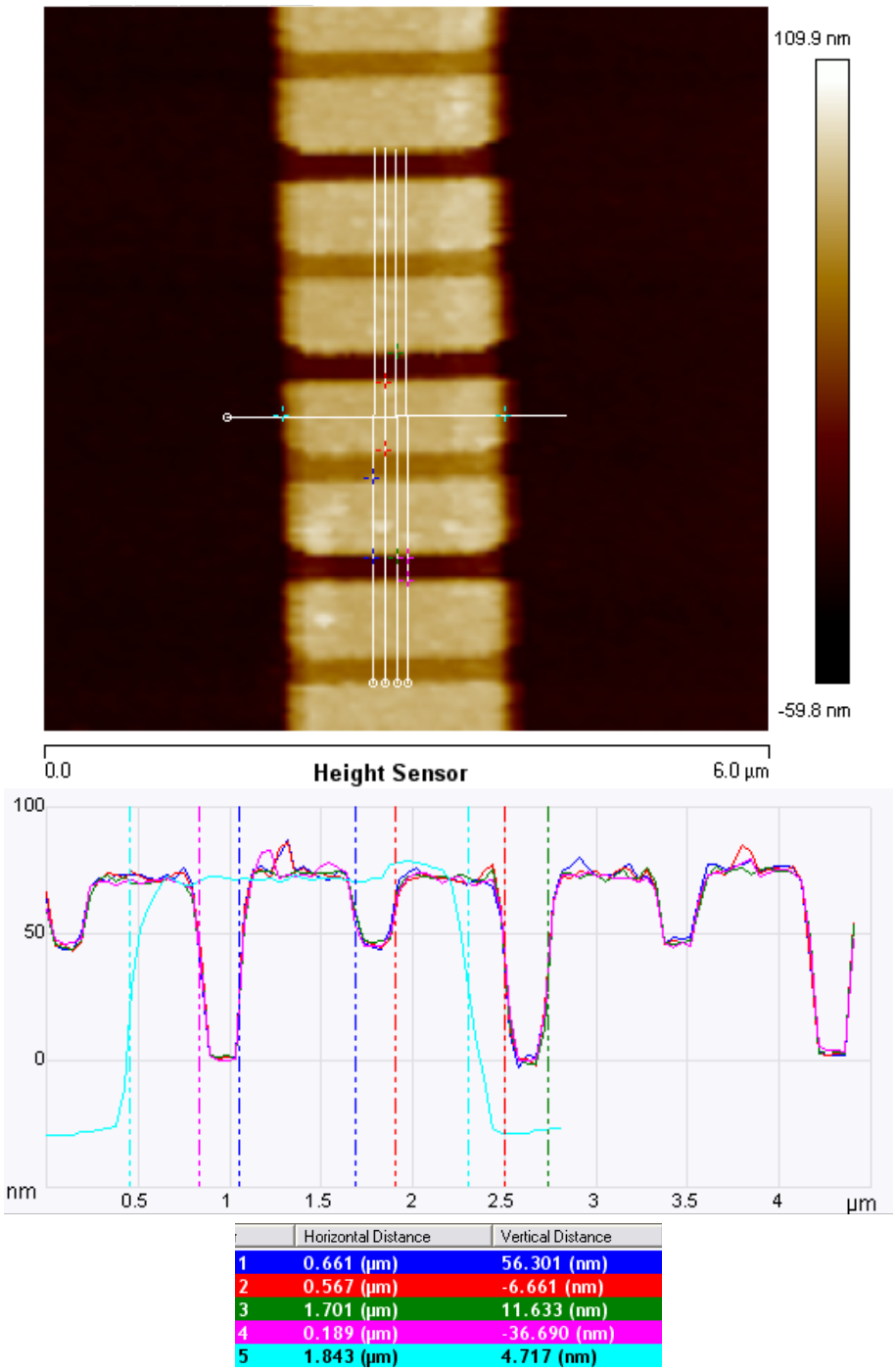

Fig. 4.9 ***AFM picture of a junction array:*** *Top: AFM 2-D scanning of a junction array. Middle: AFM 1-D scanning over the path defined by the lines in the top panel. Bottom: Vertical and horizontal distances between the points in the 1-D scanning lines in the top panel (the pairs of points correspond to vertical lines in the middle panel).*

4.3 Junction resistance measurement

We intend to use the junctions as inductive elements to build up a super-inductance wire, where each junction contributes with a (kinetic) inductance L_J. The linear junction inductance L_J is related to the Josephson energy of the junction E_J as,

$$L_J = \Phi_0^2 / E_J \tag{4.9}$$

Although it might seem quite surprising, it is possible to calculate the junction energy E_J at cryogenic temperatures (the relevant temperature regime for the circuit operation) from a measurement of the DC junction resistance R_n at room temperature (RT). The junction energy E_J is related to the tunneling of a Cooper pair through the junction and it is inversely proportional to the junction resistance R_n, i.e., they are connected via the Ambegaokar-Baratoff relation [3]:

$$E_J = \frac{h\Delta}{8e^2 R_n} \tag{4.10}$$

where Δ is the superconducting gap. Moreover, the junction resistance R_n is inversely proportional to the area A, connecting the junction energy E_J (or the inductance L_J) with its geometrical properties.

As we had just explained, characterizing the junction resistance becomes a priority. We measure the junction resistance using a standard probe station with two thin nails that we galvanically connect to the two electrodes of a junction, one at each end of a junction, respectively. The lumped-element diagram of the resistance measurement setup is shown in Figure 4.9, consisting of a DC volt-meter connected in parallel to a DC current source. In order to measure the junction resistance, for example, in the case of a junction-chain, we connect the two ends of the chain in parallel to both the volt-meter and the current source, then, the voltage drop V_{m} across the junction chain is measured while a constant current is applied, typically $I_0 = 0.1$ μA. As a preventive measure, we set the voltage compliance of the current source to 0.2 V (highest attainable voltage) in order to avoid unwanted voltage peaks specially when connecting the junction electrodes with the probe station tips (when the resistance between the tips effectively passes from nearly infinity to something very small). The resistance of the junction chain is computed as:

$$R_{\mathrm{m}} = \frac{V_{\mathrm{m}}}{I_0} \tag{4.11}$$

However, the measured resistance R_{m} must be adjusted to try to account for the effect of the substrate resistance R_{open} and the stray resistance that is not coming from the junctions R_{short}. The effective resistance R_{eff} of the junction chain is calculated as

$$R_{\mathrm{eff}} = \frac{R_{\mathrm{open}}\, R_{\mathrm{m}} - R_{\mathrm{short}}\, (R_{\mathrm{m}} - R_{\mathrm{open}})}{R_{\mathrm{open}} - R_{\mathrm{m}}} \approx \frac{R_{\mathrm{open}}\, R_{\mathrm{m}}}{R_{\mathrm{open}} - R_{\mathrm{m}}} \tag{4.12}$$

This equation is derived by considering that the total resistance R_{eff} of junctions of the chain is connected in series to the stray resistance of the chain R_{short} while they both are simultaneously connected in parallel to the substrate resistance R_{open}. Normally, the stray resistance R_{short} of the chain is negligible compared the total resistance of the junctions R_{eff},

this is expected since in the end the chain is made of Al which is a good conductor at room temperature. However, the effect of the substrate resistance R_{open} should not be neglected in general, since it can easily result in the overestimation of the junction energy E_J by a factor of 20 %.

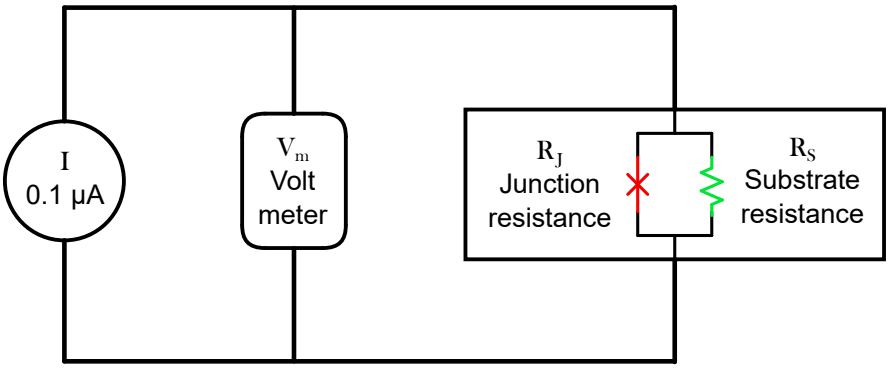

Fig. 4.10 ***Resistance measurement setup:*** *This figure shows the lumped-element diagram of the resistance measurement setup. We use a standard probe station that consists of a DC current source and a volt-meter connected in parallel to each other. Additionally, the probe station has a pair of thin tips to be connected to the two junction electrodes, respectively. After contacting galvanically the tips with the junction electrodes, the junction is effectively connected in parallel to both the current source and the volt-meter, such that we can measure the voltage drop V_{m} across the junction while we apply a constant current I_0. The measured resistance is calculated as $R_{\text{m}} = V_{\text{m}}/I_0$, however, in order to estimate the actual junction resistance, the effects of the stray resistance R_{short} and the substrate resistance R_{open} must be accounted out. The stray resistance R_{short} comes from the fact that the junction is made of metal in the end, R_{short} can be safely neglected since it is normally to small compared to the actual junction resistance R_{eff}. We can consider that the substrate resistance R_{open} is connected in parallel to the actual junction resistance R_{eff}, thus, the effect of R_{open} should not be neglected because it can easily shift the measured junction resistance by 30 % compared to the real value.*

In general, trying to measure the resistance of the whole super-inductance belonging to a fluxonium circuit is not practical at all, firstly, there are hundreds of junctions making up the super-inductance so that its resistance is normally too large, exceeding the typical voltage compliance. Secondly, we must not forget about the parallel resistance of the substrate, in the case of a Si substrate its resistance is of the order of 200 kΩ, which limits the maximum resistance that can be easily measured. Last but not least, in order to ensure proper galvanic connection between the probe station tips and the junction electrodes, the tips have to scratch slightly the surface of the junction electrodes to go through the native oxide layer covering the electrodes. In the case of a junction forming part of an actual circuit, if the contacting between the tips and electrodes is not done carefully enough, it might cause devastating damage to the circuit itself. It is then clear from the previous considerations that measuring the whole resistance of a super inductance is not a good idea. Instead, the approach should rather be:

1. Calculating the inductance of an individual junction L_J from the resistance measure-

ment of some "test" chains with few junctions, such that the test chain resistance is at least 1 order of magnitude smaller compared to the substrate resistance.

2. Approximating the total inductance L_{Tot} of the super-inductance as N times L_J, the inductance of an individual junction.

Notice that the junctions in the test chains must have the same geometrical parameters (same area) as the junctions in the final circuit super-inductance.

4.4 Junction parameter optimization

We have seen in the section 4.1.2 "Josephson junction fabrication" the various necessary elements to realize Dolan-style junctions, for both the small cross junctions and the chains of large junctions. However, there are various parameters that need to be determined empirically in order to succeed at fabricating the junctions:

1. The electron dose corresponding to each design layer.

2. The geometry of the lithographic patterns corresponding to each design layer, i.e., the bridge width and the bridge period in the particular case of the junction chains.

This empirical optimization is implemented by fabricating a batch of "test circuits" such that their junctions have one particular set of design parameters, i.e, main dose, undercut dose, bridge width, and period in the case of the junction chains. We refer to this preliminary fabrication step as a "dose-test", even though the doses are not the only parameters to be scanned. The objective of the dose test is two-fold: On one hand, identifying the safe parameter range in order to obtain functional junctions, in the worse case scenario, for example, a non optimal dose leads to the partial or complete collapse of the suspended bridges. On the other hand, the dose test allows us to determine empirically the relationship between the junction area A_J and the junction energy E_J.The final geometry of the junctions of the test circuits is characterized via SEM microscopy, as described in section 4.2, while the junction energies E_J are systematically extracted via the procedure described in section 4.3. Notice that there must be two kinds of test circuits: one for optimizing the parameters of the chains of large junctions, and another one for optimizing the parameters of the small cross junctions.

In practice, we fabricate a large batch of test circuits that are almost identical variations of the final circuit, in the section 4.4.1, practical considerations on the design of the dose test are provided. Next, the geometry of the junctions (the area) is inspected via SEM imaging, in the in the section 4.4.2, we give some example micrographs obtained for various choices of parameters (underdose, nominal dose, overdose). Next, the resistance of the junctions is systematically measured in the room temperature setup described in section 4.3, allowing us to obtain a relationship between the junction area A_J and the junction energy E_J to finally choose the optimal design parameters for junctions in the real sample. This is described in the final section 4.4.3.

4.4.1 Practical considerations for the test junctions

We use the familiar term "dose test" to refer to a batch of test junctions. In the following, we discuss some considerations to be taken into account when designing a dose test.

- **Basic considerations:** The main objective of the dose test is determining the junction energy E_J as function of the junction area A_J, within a significant range of areas. This goal is achieved by sweeping the junction width w in the dose test. In the case of junction chains, recalling the discussion of the subsection *guidelines for designing Dolan-style junction chains*, the junction length J is uniquely determined once the evaporation angle is chosen, for example, $\theta = 22°$. However, the junction width w is still a free parameter that can be used to vary the junction area A. Notice that the period P of a junction chain is not a free parameter, since it must be fixed at $P = 2S$ to ensure the condition of equal junctions, $J_1 = J_2$. Nevertheless, one might sweep the period P within a small range around the optimal value in the dose test, just as a kind of "sanity check" to verify that indeed the chosen period P is the optimal one. In the case of the small cross junctions, the junction width w again is the only free parameter that can be varied to sweep the junction area A_J.

- **Other considerations:** As the name suggests, in a dose test one needs to optimize the electron dose that is used to expose the resists in the junction fabrication. When the dose is not enough (underdosing), there might be resist remainders where they are not meant to, for example, in the rectangular holes between two successive free standing bridges. Then, the produced junctions might have irregular shapes and smaller areas than expected, and in the worse case when the Al layers making the junctions are deposited over a film of resist remainders instead of being deposited on the substrate surface, the junctions might be completely washed away during the lift-off step. In the opposite case, when the dose overpasses the optimal value (overdosing), the free standing bridges might be thinner than expected, again resulting in an undesired variation of the junction shapes and areas, and in the worse case when the dose is completely overloaded, one might expect the collapse of the free standing bridges.

  Notice that we use two separate layers, each one related to a different electron dose, to fabricate each junction kind in the fluxonium circuit, i.e., two layers for the junction chains, and two layers for the small cross junctions. This means that 2 different dose values have to be swept for each kind of junctions, amounting a total of 4 dose values to sweep in the dose test.

  The purpose of the additional undercut layers is addressing the significant problem of proximity effects, i.e., the additional and unwanted dose that a part of resist receives when other nearby resist parts are exposed during the e-beam lithography. For example, in the less but still concerning cases, the proximity effects might cause the two families of junctions in a junction chain to have different lengths, $J_2 - J_1 \neq 0$. In general, overdosing due to proximity effects causes narrower bridges, thus, resulting in

an undesired variation of the junction shapes and areas. In worse case, when there is too much overdosing due to proximity effects, the free standing bridges might collapse. Therefore, proximity effects must always be taken into account when designing compact structures, like the junction chains and the very super inductance made of several of them in a fluxonium circuit. The addition of the undercut layers in the circuit mask, which are exposed with a lower dose than the one used to expose the main circuit layer, helps a lot to keep the proximity effects under control. For example, the bridges are more stable and preserve their shapes for a large range of junction widths w, for example, from 1.0 μm to 2.5 μm.

Summarizing, 3 parameters need to be swept in the dose test for each one of the two junction kinds of the fluxonium circuit, the parameters are the junction width, the main-layer dose, and the undercut layer dose. An extra parameter can be added for the junction chains, the period P, just as a "sanity check". Thus, a total of 6 or 7 parameters have to be optimized in a dose test (see Figure 4.11), which means fabricating and characterizing lots of junctions before moving forward to the fabricating of the final fluxonium circuit, beware of that :). We finalize this subsection with one remark: in order to account properly for proximity effects, the test junctions have to be as similar as possible as the junctions used in the final circuit, for example, the super-inductance of the fluxonium circuit is made of several junction chains that are closely packed to each other, e.g., the separation between two adjacent chains is fixed at about 2.0 μm, therefore, each test junction chain in the dose test must be surrounded by other "dummy" chains that only have the purpose of accounting for proximity effects. Although these measures might seem a bit exaggerated in the beginning, they fulfill their purpose correctly, these measures resulted from our empirical experience in debugging and optimizing the junction fabrication, we suggest the reader to keep them in mind.

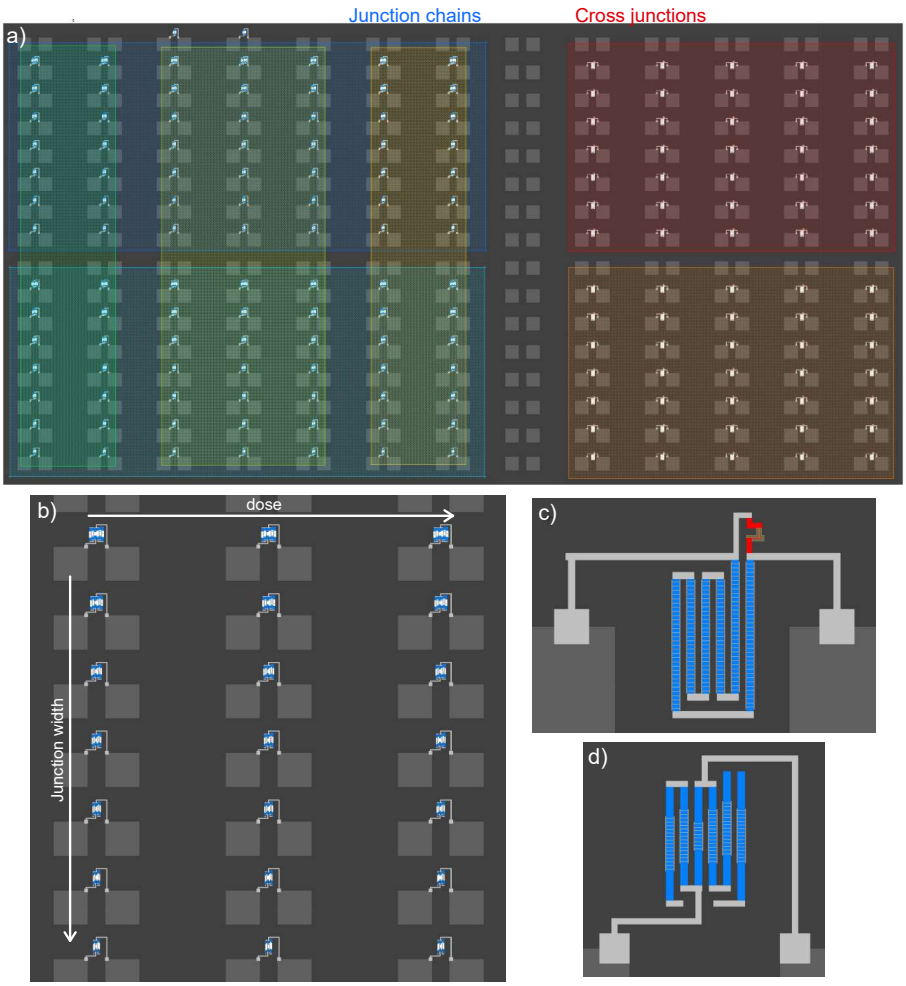

Fig. 4.11 ***Dose test example:*** *This figure shows an example of a design mask that is used to fabricate a dose test. a) displays the whole mask: a typical dose test chip contains an array of Nb pads that are connected to each other by either a junction chain (left) or a small junction (right). The chip consists of several "blocks" each one being characterized by a set of junction design parameters. For example, on the side of the junction chains (left), the light-blue (top) and the dark blue rectangle rectangle (bottom) stand for an undercut dose of 0.15 and 0.20 (times 280 $\mu C/cm^2$), respectively, while the dark green rectangle, light green rectangle and yellow rectangle correspond to a junction-chain period of 1.1 μm, 1.2 μm, and 1.3 μm, respectively. On the side of the small junctions (right), the red rectangle (top) and the orange rectangle rectangle (bottom) are related to an undercut dose of 0.25 and 0.30 (times 280 $\mu C/cm^2$), respectively. b) shows a zoom into the block with undercut dose of 0.20 and a period 1.2 μm (which was the optimal period for an angle of 22 °), this block is signaled by the overlap between the light green rectangle and the light blue rectangle. Inside this block, each column is related to a different main dose, for example, 0.8 (left), 0.9 (mid) and 1.0 (right), while each row corresponds to a different value of the junction width, in this case 1.2 μm (bottom), 1.6 μm, 2.0 μm, 2.5 μm, 3.0 μm, 4.0 μm and 5.0 μm (top). c) show a zoom into the design used for the small junctions while d) shows the design used for junction-chains.*

4.4.2 Geometrical characterization of the test junctions

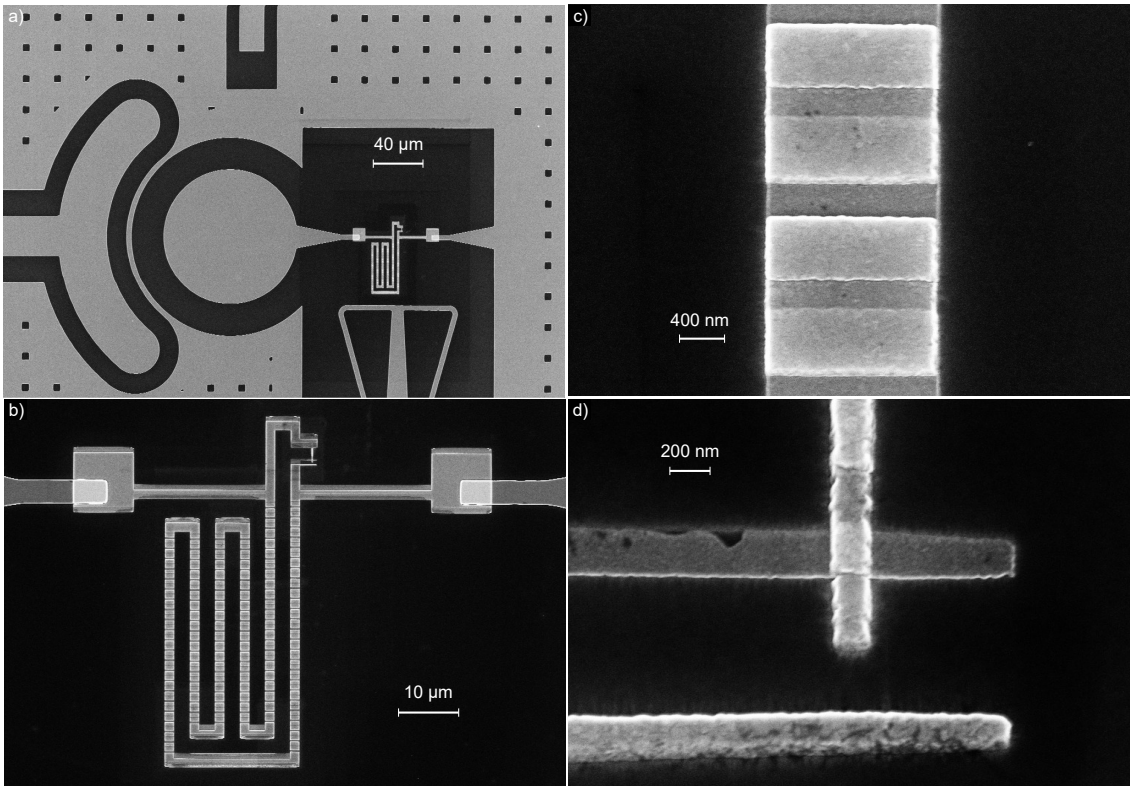

Fig. 4.12 ***SEM pictures of a functional fluxonium circuit:*** *a) An integral view of the circuit elements, including both the large ones and the smaller ones. The large circuit elements are the capacitor pad, the readout resonator, the flux line, the charge drive and the ground plane. The small circuit elements are the small cross junction and the super-inductance made of few chains of large junctions. b) Zoom into the fluxonium loop, made of both the small cross junction and the super-inductance in parallel connection to each other and to the capacitance to ground. c) Zoom into two pairs of junctions of a junction chain of the super-inductance. d) Zoom into the small cross junction.*

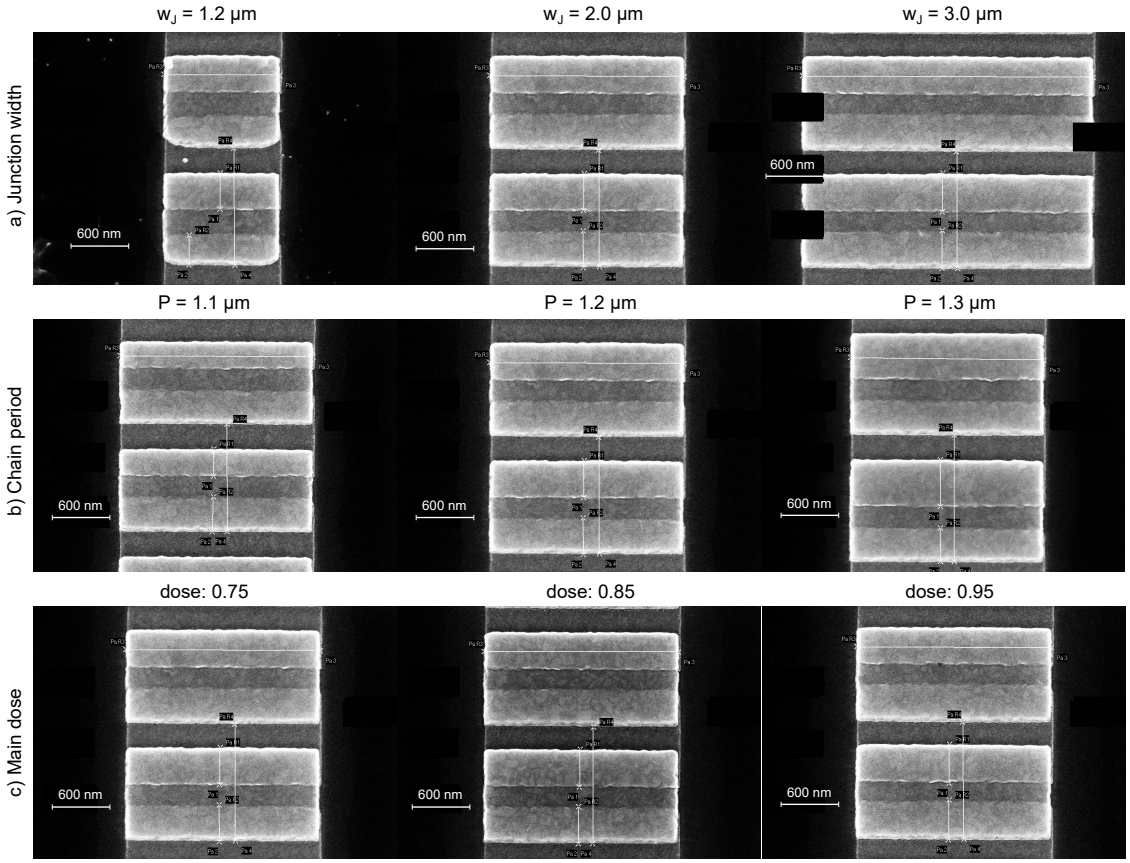

Fig. 4.13 ***Examples of test junction chains:*** *Each row corresponds to the sweep of one design parameter: junction width (top), period (middle) and electron dose of the main design layer (bottom). In the top row, the period and dose are fixed at 1.2 µm and 0.75, respectively, while the junction chain is varied. Notice that for the narrower junction width, one junction from each pair has rounded corners indicating that the used dose was sub-optimal. The rounded junctions are actually the kind of junctions created bellow the suspended resist bridges, and the rounded corners indicate that there were some resist remainders from the bottom resist layer below the suspended bridges, i.e., arc bridges instead of flat bridges. In the middle row, the junction width and dose are fixed at 2.0 µm and 0.75, respectively, while the period is varied. Notice that the length of one junctions of each pair is increasing from the left panel to the right panel, this is expected since the length of one junctions depends on the period (distance between consecutive bridges), while the length of the other junction only depends on the thicknesses of the resist layers and not on the period. Finally, in the bottom row, the junction width and period are fixed at 2.0 µm and 1.2 µm, respectively, while the dose is varied. Notice that the junction edges are almost flat and the corners are not rounded in the dose range scanned here, although it might seem trivial in the beginning, actually shows the stability of the suspended bridges to variations of the electron dose, which is a result of fabricating the bridges with two lithographic patters and two different doses, one for each lithographic pattern, i.e., "main" dose and "undercut" dose. In the case where only one lithographic pattern is uses (and one dose) on typically finds that the shape of the bridges, and consequently the length of the junctions, is very sensitive to variations of the electron dose.*

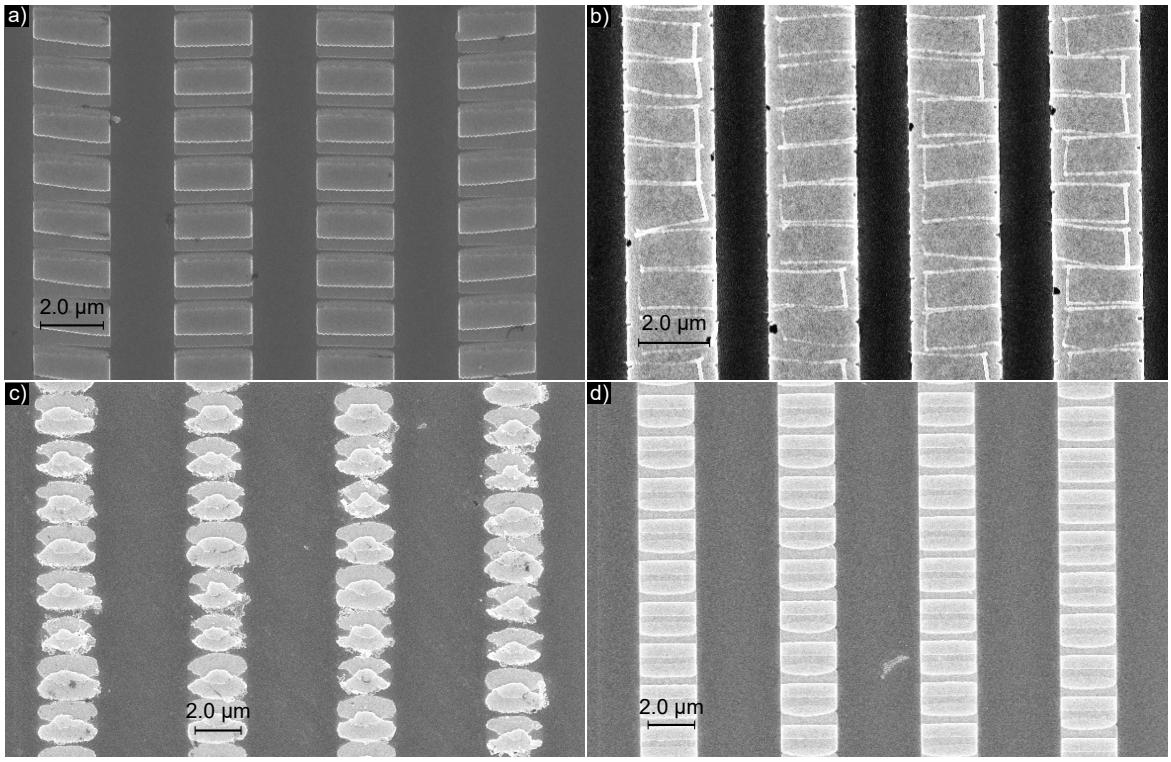

Fig. 4.14 ***Examples of junctions chains with non-optimal dosing:*** *a) The proximity effects between adjacent chains were so strong that the whole bottom resist layer was etched, even the parts between adjacent chains, this caused that the top resist layer acquired some curvature due to gravity, which translates into a bridge height that varies for each chain. Notice however that the suspended resist bridges did not collapse in spite of the strong proximity effects. The test junction chains shown in a) were fabricated with an old recipe where onmy one lithographic pattern (and one dose) where used during the ebeam-lithography. b) The dose used was way too high above the optimal value, resulting in the complete collapse of the bridges. c) The dose used for these test junction chains was way below the optimal value, such that the resist below the bridges was not etched and the bridges were not really suspended. d) In this case, the dose used for fabricating the test junction chains was slightly below the optimal value, causing one junction from each pair to have rounded corners, because of the suspended bridges having an arc shape, instead of being almost flat as in the optimal case.*

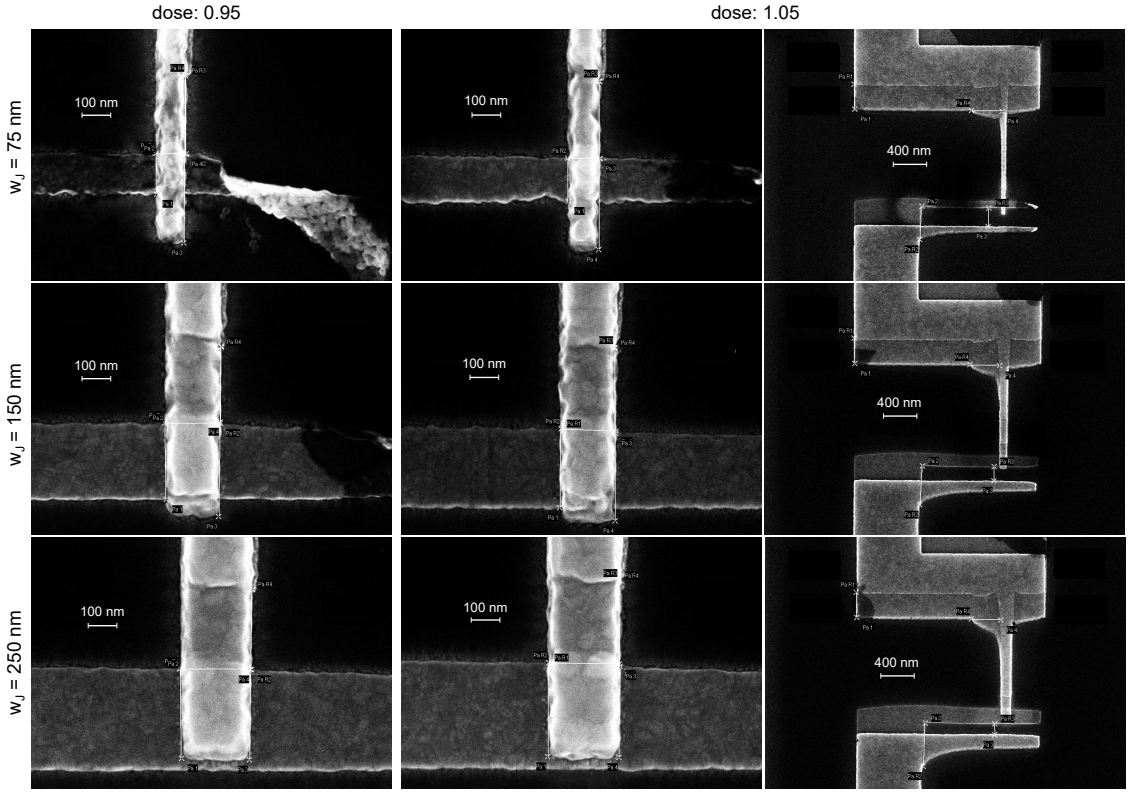

Fig. 4.15 ***Examples of cross junctions:*** *Each frame corresponds to a variation of the design parameters of the small cross junctions, such that within a row (column) the dose (junction width) is swept while the junction width (dose) is fixed.*

4.4.3 Results and chosen parameters

As mentioned previously, one objective of the junction parameter optimization (the "dose test") is determining the relation between the energy E_J (or the inductance L_J) of the fabricated junctions and the design parameters, specially the junction area A_J. The Figure 4.16 displays the results obtained for 5 different dose tests, each one with a particular set of passive oxidation parameters: static pressure and time. The junction areas were measured via SEM as shown in Section 4.2.1, while the junction energies E_J were determined as described in Section 4.3. Notice that for a given dose test iteration, the junction energy E_J and the junction area A_J follow a linear relation. It is particularly surprising that the same linear fit works pretty fine for both the small cross junctions, with areas as small as 0.25 μm^2, and the large junctions of the chains, with areas as big as 0.7 μm^2. Indeed, the linear relation between E_J and A_J holds for almost 3 orders of magnitude of A_J.

We can get some intuition on this result from the fact that the junction energy E_J is inversely proportional to the junction resistance R according to the Ambegaokar-Baratoff relation (Equation 4.10), and for a S-I-S junction with area A_J made of two superconducting layers separated by an insulating layer, the junction resistance R should be inversely proportional to the junction area A_J. Similarly, the junction resistance R should be proportional to the thickness of the insulating layer, however, it does not seem to be the case by looking at the Figure 4.16, since one would expect that larger values of the product oxidation pressure-duration should correspond to thicker oxide layers, and thus, smaller values of the ratio E_J over A_J. Actually, the slope corresponding to each dose test iteration appears to be somehow random and not correlated to the product oxidation pressure-duration. This later result put in evidence a reproducibility problem in our junction fabrication, which we assumed to be related to lack of reproducibility of the passive oxidation step (oxide layer thickness). We addressed this problem by fabricating several copies of our final circuit at once, i.e., wafer scale instead of chip scale, such that each copy had a different value of the area of both kinds of junctions: the small cross junction and the large junctions of the chains.

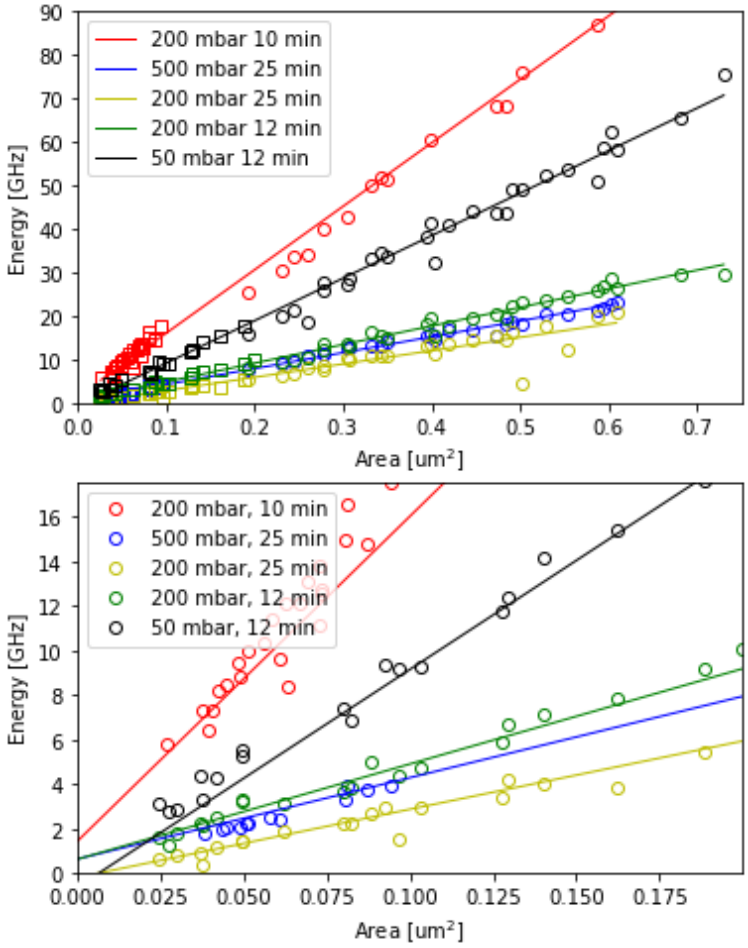

Fig. 4.16 ***Energy vs area of the fabricated junctions:*** *This figure shows the results of the measured energies E_J and areas A_J of the junctions corresponding to a total of 5 different dose tests, each one with a different value of the product oxidation pressure-time. The top panel displays energies E_J and the areas A_J of both the small cross junctions and the large junctions of the chains, while the bottom panel only shows the energies E_J and the areas A_J of the small cross junctions.*

4.5 Experimental setup

In this section I will briefly explain the experimental setup used for the characterization and manipulation of the fluxonium circuit. It consists of two parts: A cryogenic part (see Figure 4.17), i.e., inside the dilution cryostat, that will be explained in the following section, and a room temperature part (see Figure 4.18) that will be explained in the next section.

4.5.1 Cryogenic setup

In our experiments, we used a suspended dilution cryostat LDXX provided by the bluefors cryogenics company. Our cryostat typically reaches a working temperature as low as 8 mK. Such low temperatures are normally required when working with microwave superconducting circuits in order to reduce the negative effects of environment on the coherence properties of the circuit components, for example, the qubit and its readout resonator. Notice that the negative effects of the temperature are enhanced according to the quantity

$$r = \exp\left(-\frac{h\nu_0}{k_{\mathrm{B}}T}\right) \tag{4.13}$$

Where Boltzmann constant is $k_{\mathrm{B}} \approx 20.84\ h{\cdot}\mathrm{GHz}{\cdot}\mathrm{K}^{-1}$, and ν_0 is the relevant transition frequency, e.g., a circuit transition. This expression tell us that we should maximize the ratio $h\nu_0/k_{\mathrm{B}}T$ to maximize the coherence properties of our circuit components. Considering a typical circuit frequency of $\nu_0 = 5$ GHz, the value of r is practically equal to $0.9992 \approx 1$ at room temperature (300 K), notice that the maximum value of r is indeed 1. However, inside a dilution cryostat environment at a temperature of 8 mK, $r \approx 9.4 \times 10^{-14} \approx 0$.

Coming back to the cryogenic part of the setup that is shown in Figure 4.17, the fluxonium device, consisting of the fluxonium circuit, the ancillary readout resonator plus the readout drive line (both purple), the charge drive line (green) and the fluxline (dark yellow), is right at the bottom of the cryostat at the level of 8 mK (red rectangle). [4]. In this way, there are 4 input lines descending through the cryostat corresponding to the flux line (dark yellow), the charge drive line (green), the input readout line (purple), and the TWPA pump line (black). On the other hand, there is only one output line, the one of the readout resonator (purple).

- **Flux line (dark yellow):** This line is used for both driving the fluxonium transitions, and setting the external flux in the fluxonium loop, thus setting the working point of the fluxonium, e.g., the sweet spot. This line is galvanically connected to a DC voltage source at room temperature end. This line has 40 dB of attenuation at 4 K to decrease the amplitude of the current noise descending from the room temperature environment. It also has two high pass filters, the VLFX 500 and the SLP 1.9+, to prevent the high frequency noise of affecting the higher order transitions of the fluxonium circuit.

[4] The circuit is packaged in a JAWS (circuit box) that is inside a magnetic field shield

- **Charge drive line (green):** This line is used for driving the fluxonium via the charge operator by applying an AC voltage pulse at the room temperature end. This line has a total of 70 dB attenuation: 20 dB at 4 K, 10 dB at 800 mK and 40 dB at the bottom of the cryostat, at 8 mK. This line is not galvanically connected with the outside of the cryostat to prevent DC noise from affecting the fluxonium spectrum.

- **TWPA pump line (black):** This line is used to pump the cryogenic amplifier, the TWPA (traveling-wave parametric amplifier), that is at the level of 8 mK. The pump signal is combined with the reflected signal from the ancillary readout resonator via a directional coupler with a 50 ω termination, preventing the TWPA pump to be reflected back to the fluxonium circuit. This input line has a total of 50 dB attenuation: 20 dB at 4 K, 10 dB at 800 mK and 20 dB at 8 mK due to the directional coupler. This line is not galvanically connected with the outside of the cryostat to prevent DC noise from affecting the fluxonium spectrum.

- **Readout input line (purple):** This line is used to probe the ancillary readout resonator to access the fluxonium state via dispersive shift. This line has a total of 70 dB attenuation: 20 dB at 4 K, 10 dB at 800 mK and 40 dB at the bottom of the cryostat, at 8 mK. This line is not galvanically connected with the outside of the cryostat. This line only allows signals to go down the cryostat and it prevents ascending pulses, like the reflected signal, thanks the pairs of circulators plus a 50 ω termination in the first one, they are located at the bottom of the line at 8 mK before the line is connected to readout port of the fluxonium device.

- **Readout output line (purple):** This line is used to read out the fluxonium state, in reflection-configuration, thanks to the dispersive shift that the different states produce on the ancillary readout resonator. In this way, once the readout resonator is probed by an input signal, the reflected component is directed towards the output line by the pair of circulators at the end of the readout input line. This line has no filtering to avoid any reflected signal from the fluxonium to be further attenuated, thus worsening the signal-to-noise ratio (contrast). First the reflected signal is added with with the TWPA pump by a directional coupler with a 50 ω termination. Next, the combination of the two signals feeds a cryogenic amplifier, the TWPA, and the amplified signal goes through a high-pass filter K&L with a cutoff frequency of 8 GHz, and then the signal goes through a pair of circulators, each one with a 50 ω termination in one port. The circulators prevent the signals from the room temperature level to descend down the line to be amplified by the TWPA and lastly the affecting the fluxonium circuit. Finally, the reflected signal is further amplified by a HEMT (high-electron mobility transistor) at 4 K, before reaching the outside of the cryostat. This line is not galvanically connected with the outside of the cryostat. There is an additional amplifier at the room temperature level, but this will be shown latter in the room temperature setup.

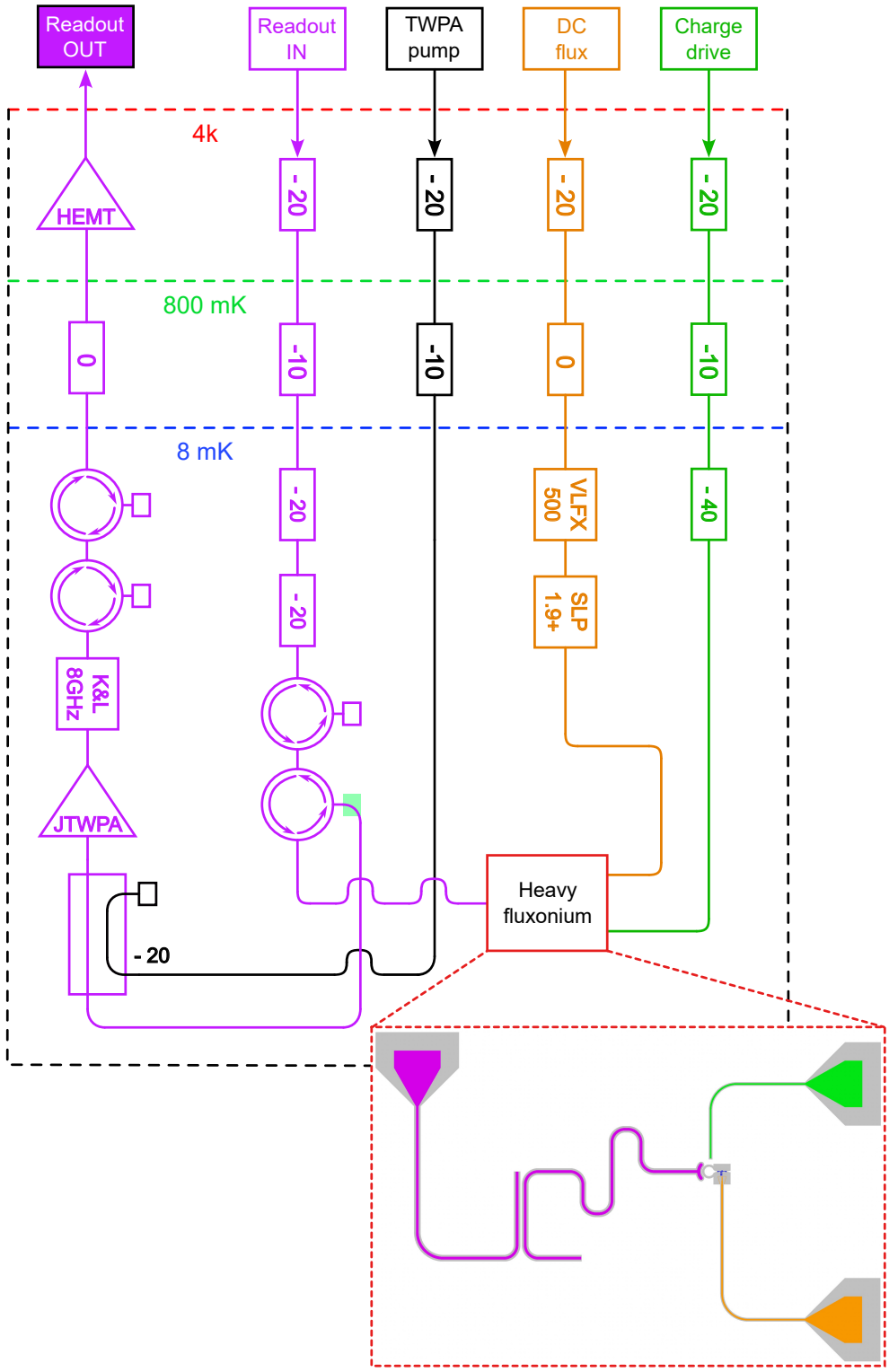

Fig. 4.17 ***Resistance measurement setup:*** .

4.5.2 Room temperature setup

The room temperature part of the setup is shown in Figure 4.18, here we can see the part of the input lines and the output line that is outside the cryostat at room temperature. As we have seen early, there are 4 input lines descending down the cryostat corresponding to the flux line (dark yellow), the charge drive line (green), the input readout line (purple), and the TWPA pump line (black). On the other hand, there is only one output line, the one of the readout resonator (purple). At the end of the room temperature side of the lines, there is either one output port of the microwave source (Anapico APMS40G) or the output port of the DC source (Ykowaga) or one analog output port of the quantum machine operator X (OpX), that is used to generate AC-voltage pulses with a maximum amplitude of 0.5 V and a carrier frequency within the interval of -350 MHz to 350 MHz In fact, the AC-signals that are sent down the cryostat are the combination of a high frequency pulse from an output of the microwave source with a lower frequency pulse generated by an output of the OpX via an IQ-mixer.

- **Flux line (dark yellow):** This line is essentially used for setting the external flux in the fluxonium loop, which sets the working point of the fluxonium, e.g., at the sweet spot. This line adds the DC voltage from the output of the Yokowaga source with the voltage that is output by port 2 of the OpX via a conventional power combiner, i.e., a pair of resistances that are connected at one end. While the output of the DC-voltage source is typically fixed at the sweet spot, the voltage that is output by the OpX is used to sweep the total voltage within a small range, for example, around the sweet spot. The port of the OpX can also output an AC-voltage, this particularly important to drive the fluxonium transitions via the flux operator. The resulting voltage after the power combiner generates a constant current that descends down the cryostat, notice that this is the only line that galvanically connects the input and the output of the cryostat.

- **Charge drive line (green):** This line combines three different AC-voltage signals into one, each of the signals optimized to drive a particular transition of the fluxonium circuit. On the one hand, the output 3 of the Anapico microwave source is mixed with the outputs 5 and 6 of the OpX by means of an IQ-mixer generating one of the mentioned signals, on the other hand, the output 1 of the Anapico microwave source is mixed with the outputs 7 and 8 of the OpX by means of an IQ-mixer generating another of the mentioned signals. These two signals are added up by a power splitter connected backwards, and the resulting signal is added with the signal coming from the output 1 of the OpX by a 10 dB directional, such that the signal coming from the power splitter is attenuated by 10 dB. The low-frequency signal from the output 1 of the OpX is used to drive the qubit transition, which is typically of the order of few MHz. The high-frequency signal that is generated by the combination of the output 3 of the Anapico and the outputs 5 and 6 of the OpX is used to drive a higher frequency fluxonium transition around 3 GHz, that is used as an ancillary transition for the single-shot readout of the low-frequency qubit. Finally, the high-frequency signal that is generated by the combination of the output 1 of the Anapico and the outputs 7 and 8 of the OpX is used to drive a readout-assisted transition around 5 GHz that is used

for the initialization of the low-frequency qubit (side-band cooling. Notice that there are multiple DC-blocks to prevent DC-signals to go down the line into the cryostat.

- **TWPA pump line (black):** This line is used to pump the cryogenic amplifier, the TWPA, that is inside the cryostat. This line is particularly simple, it has a DC-block right after the outside of the cryostat, and at the end of the room temperature level the level, there is the output 4 of the Anapico microwave source, which is typically on always and fixed at the frequency that produces the maximum gain of the TWPA (approximately 6.9 GHz).

- **Readout input line (purple):** This line is used to probe the ancillary readout resonator to access the fluxonium state via dispersive shift. This line mixes the outputs 3 and 4 of the OpX with the output 2 of the Anapico microwave source by means of an IQ-mixer. Notice that there is 10 dB attenuation at each output of the OpX, and also notice that the signal from the output 2 of the Anapico source is splitted into two by a power splitter: one of the resulting signals is used to generate the high-frequency signal to probe the readout resonator, while the other resulting signal is used to demodulate the reflected signal from the readout resonator. Notice that there are multiple DC-blocks to prevent DC-signals to go down the line into the cryostat.

- **Readout output line (purple):** This line is used to read out the fluxonium state, in reflection-configuration, thanks to the dispersive shift that the different states produce on the ancillary readout resonator. Starting at the room temperature level, the signal ascending out from cryostat goes through a DC block right after exiting the cryostat, then, the signal signal is further amplified by a conventional room-temperature microwave amplifier that is pumped by a current of 0.13 A at a constant voltage of 15 V. Next, the amplified signal is demodulated by an image-reflected (IR) mixer, where the local oscillator port is connected to the output 2 of the Anapico source, the resulted low-frequency signal finally reached the analog input 1 of the OpX at the top end of the line. As previously mentioned, the signal from the output 2 of the Anapico source is used for both generating the high-frequency signal to probe the readout resonator and demodulating the reflected signal coming from the readout resonator. Notice that there are multiple DC-blocks to prevent DC-signals to go down the line into the cryostat.

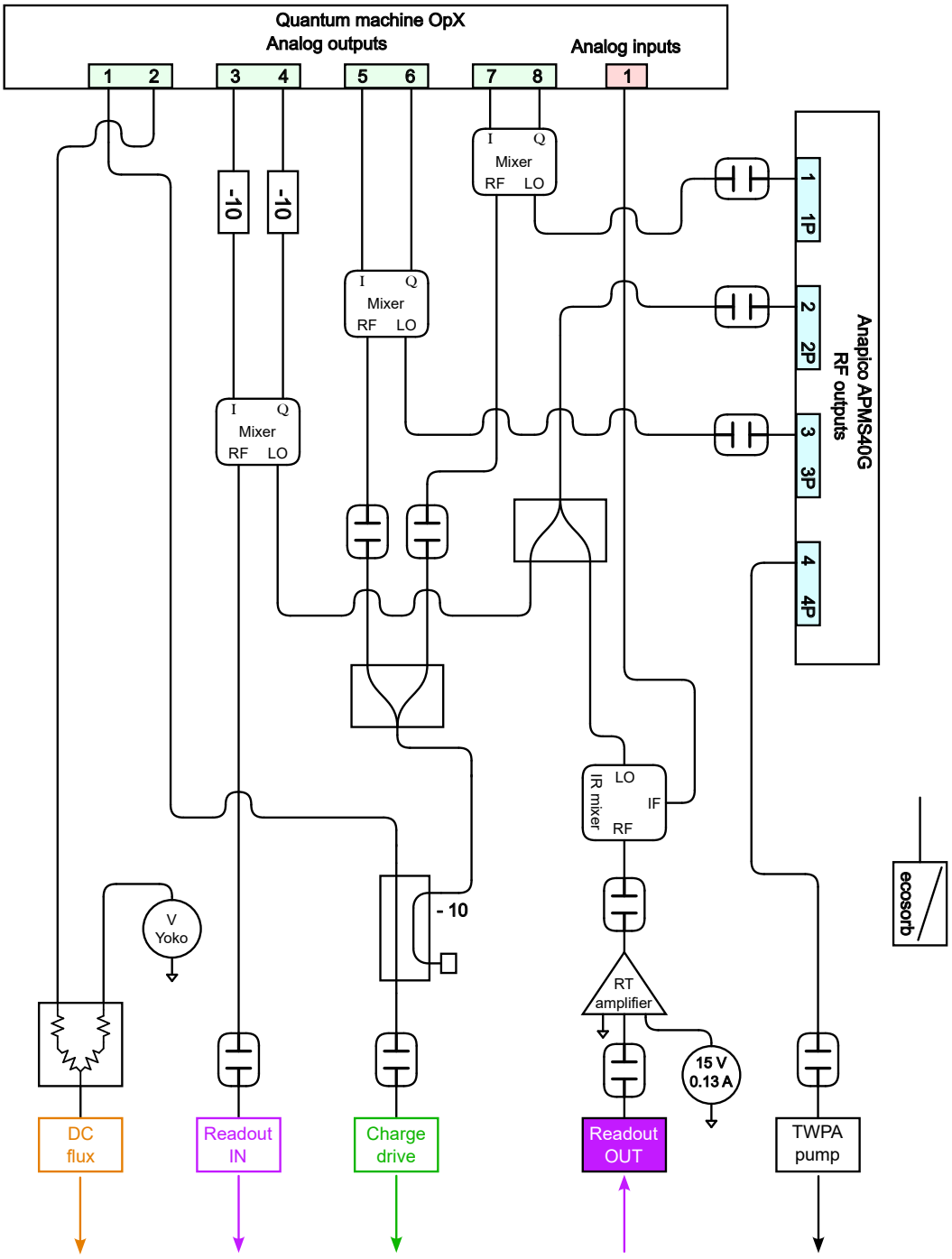

Fig. 4.18 ***Resistance measurement setup:*** .

4.6 Plasma frequency measurement

We remark that the junctions have a self resonance at the frequency ω_p, which is referred to as the junction plasma frequency. This can be understood by viewing the S-I-S junction as a kind of parallel plate capacitor, where the oxide-layer is separating the two superconducting plates. Then, it becomes evident that a S-I-S junction has a self-capacitance C_J, in addition to an inductance L_J, such that its self-capacitance C_J is proportional to its area A. Thus, the junction plasma frequency $\omega_p = 1/\sqrt{L_J C_J}$ is independent of the junction area, this comes from the fact that $L_J \propto R_n \propto 1/A$ as well as $C_J \propto A$. Nevertheless, the plasma frequency does depend on the thickness of the oxide layer, meaning that this is an important parameter to keep in mind. In the case of Al-Ox-Al junctions, the most popular physical implementation of a Josephson junction, the plasma frequency is of the order of 10 GHz, and this value can be increased (decreased) by augmenting (diminishing) thickness of the oxide-layer, corresponding to an increment (reduction) of the passive oxidation time or pressure.

In order to characterize the junction plasma frequency, we fabricate a linear resonator made of several junctions, which is nothing that a large junction chain that is opened at both ends. We then find the frequencies of the collective chain modes via two-tone spectroscopy: Firstly, the resonator is driven by a probe (first) tone at the frequency of the lowest chain mode, then, the amplitude of the reflected probe signal is measured while an additional tone, the pump tone, is used to drive higher order modes of the chain. Thus, we keep track of the reflected probe tone amplitude while sweeping the frequency of the pump tone.

The Figure 4.19 shows the results of the characterization of the junction plasma frequency. According to the linear model of a junction chain that is described in the fluxonium design chapter, the frequency of the chain modes should saturate at the plasma frequency as soon as the mode number increases. This is precisely the behavior that we observe for the frequency of the chain modes as function of the mode number. From the fit, we determine that the saturation frequency, i.e., the plasma frequency of the junctions, is approximately 17.9 GHz.

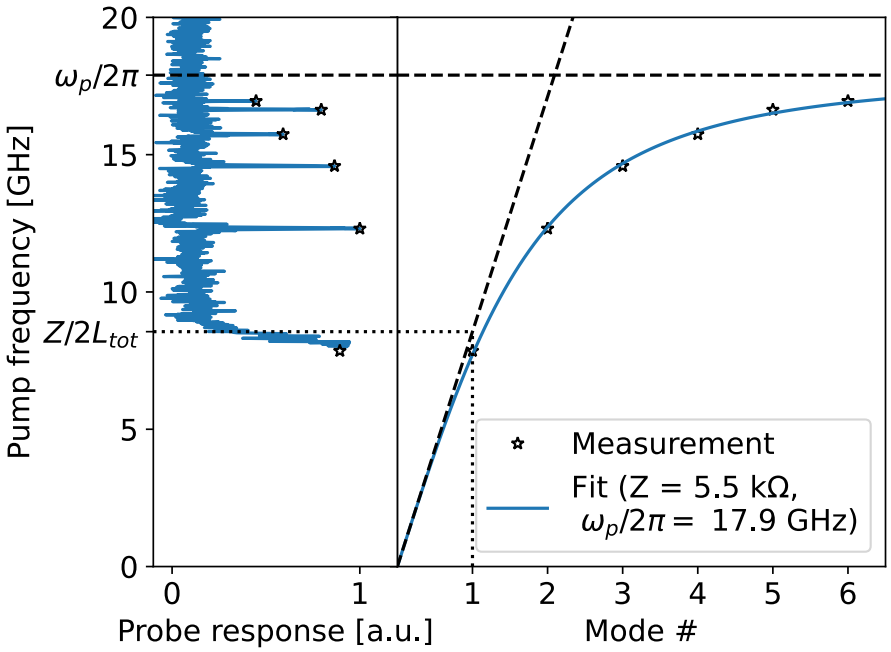

Fig. 4.19 ***Junctions plasma-frequency characterization:*** *Left: Reflected probe tone amplitude as function of the frequency of the pump tone. Right: The stars represent the measured frequencies of the chain modes as function of their mode number, and the solid blue line is the corresponding fit obtained by using the model of the linear junction chain described in the fluxonium design chapter.*

Chapter 5

Basic characterization of the fluxonium device

This chapter describes the basic characterization of the fluxonium device. It is organized as some sort of manual for future students working on the experiment. In particular, the order of the sections closely follows the typical sequence of measurements within the logbook used to characterize new samples as they are cooled within our dilution cryostat. The first section is about the frequency-domain characterization of the readout resonator that is coupled to the fluxonium circuit. This step is vital since the only information that we ever extract from the fluxonium state is obtained indirectly via the readout resonator. The main component of the fluxonium circuit is a superconducting loop made by the super-inductance and the small junction in series. In order to quickly check the integrity of these components, we rapidly verify that the readout resonator has a periodic response as a function of applied external flux. This single-tone resonator spectroscopy is described in section 5.1. Immediately after this quick verification, we perform a pump-probe measurement that is used to characterize the various fluxonium transitions, via the frequency-change of the readout resonator, when particular qubit states are populated. This so-called "two-tone spectroscopy" is the subject of section 5.2. The final section of this chapter is about the optimization of the indirect readout through the resonator. The main goal being to perform a projective measurement of the qubit state, that is able to distinguish between them in a single-shot experimental realization.

5.1 Single tone spectrum

In this section, we undertake the fundamental characterization of the initial circuit element accessible to us: the readout resonator. This component is a coplanar waveguide resonator, with a $\lambda/4$ configuration, directly coupled to a measurement line. Furthermore, it is linked to the fluxonium circuit in such a way that its precise frequency provides valuable insights into the state of the fluxonium.

5.1.1 Readout spectroscopy

The resonator is probed in reflection configuration, as it is described in Section 4.5.2. The resonator probe pulse is generated by up-converting a MHz signal from the OpX (quantum

machine) to the GHZ range with the aid of an IQ mixer and a microwave source (see Figure 4.18). The reflected signal from the resonator is then down-converted by an image-reject mixer, and the resulting MHz signal is demodulated by the OpX yielding as output the two quadratures of the complex reflection coefficient S_{11}.

The Figure 5.1 shows the resonator spectrum, i.e., the amplitude and phase of the reflection coefficient S_{11} as function of the probe frequency ν and for a fixed value of the external flux φ_{ext} (typically $\varphi_{\text{ext}} = 0$).

The curves are fitted simultaneously by a complex lorentzian $z_{\text{L}}(\omega)$, as described for instance in Ref. [33]:

$$z_{\text{L}}(\omega) = \left(A_0\, e^{i\phi_0} - \frac{A\, e^{i\phi}}{i\left(\frac{\omega-\omega_0}{k/2}\right) + 1} \right) e^{i(\omega-\omega_0)\,\tau_{\text{d}}}, \tag{5.1}$$

where $k/2\pi$ is the linewidth (full-width at half maximum, FWHM) of the peak centered at the frequency $\omega_0/2\pi$ and τ_{d} is the delay-time of the signal because of propagation through the coaxial lines through which the readout pulse is propagating.

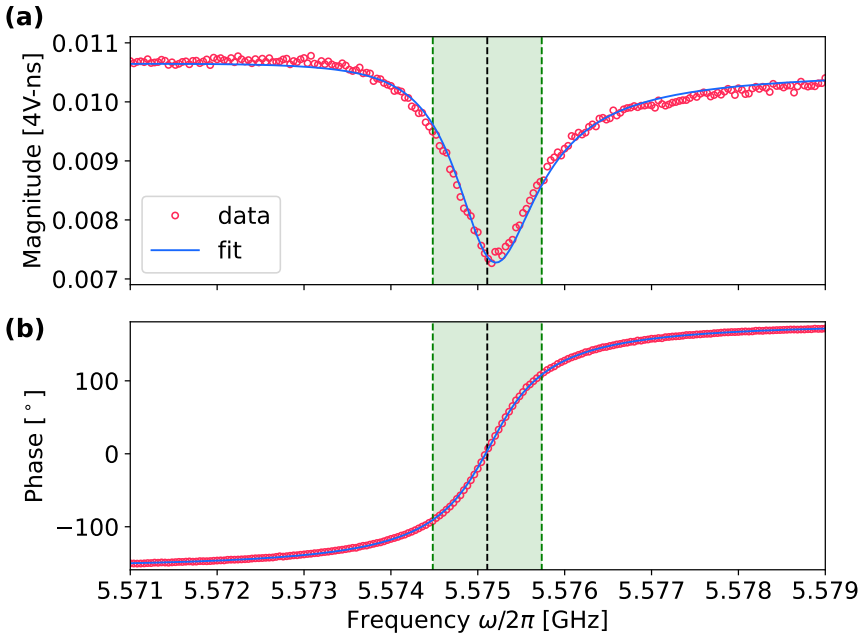

Fig. 5.1 ***Single-flux resonator spectrum:*** *Reflection response of the readout resonator. (a) Magnitude of the complex reflection coefficient S_{11}. The magnitude units correspond to the raw values output by the OPX, where the factor 4 is related to the 4ns-sampling rate of the analog to digital converter (ADC). (b) Phase of the complex reflection coefficient S11. Red dots are the measured data points and the solid line is a fit according to Equation 5.1 of the main text. The fit yields the central frequency $\omega_0/2\pi = 5.5751$ GHz (dotted black line) and the linewidth of $k/2\pi = 1.254$ MHz.*

5.1.2 Flux-dependence of the readout response

The Hamiltonian of the fluxonium coupled to the readout resonator (Equation 2.3) shows a periodic dependence upon the external flux φ_{ext}. This periodicity is directly traceable to the presence of a closed superconducting loop in the circuit. The loop, constituted of the 360 junctions of the superinductor in series with the small junction, is the most sensitive element of the circuit, since a single open junction in the loop would compromise this property of the Hamiltonian. Consequently, once the readout resonator has been characterized, we perform a rapid check of the circuit by scanning the response of the resonator as function of the external flux.

The Figure 5.2 displays the reflection coefficient S_{11} of the resonator for different values of the external flux control (in volts), which we refer to as the resonator single-tone spectrum. The spectrum is flat for most of the external-flux control values, except at some specific values, for instance, $V \approx$ -14 V, -7 V and +8 V, where we observe abrupt variations. At these points, the frequency of a given fluxonium transition crosses that of the resonator, leading to an anti-crossing in the spectrum. For each value of the external flux control, we fit the resonator response with the Equation 5.1. Notice that a quantitative analysis of the resonator spectrum as a function of the external flux can be very involved, because of the complex interplay between qubit-resonator detuning, mutual coupling strength, and the absence of selection rules in the fluxonium leading to a variety of virtual transitions that significantly affect the dispersive shifts [82]. However, we identify two clear symmetry points that correspond to the symmetries $\hat{H}(\varphi_{\text{ext}}) = \hat{H}(-\varphi_{\text{ext}})$ and $\hat{H}(\varphi_{\text{ext}}) = \hat{H}(2\pi - \varphi_{\text{ext}})$ (see the vertical dashed lines in Figure 5.4c). These two symmetries are consequences of the main features of the fluxonium hamiltonian, being both even and periodic (see Equation 2.3). The presence of these two symmetries are the clear signature of the circuit containing a closed-loop. Then, we can identify the voltage values $V_{\varphi_{\text{ext}}=0}$ and $V_{\varphi_{\text{ext}}=\pi}$ corresponding to the external flux values $\varphi_{\text{ext}} = 0$ and $\varphi_{\text{ext}} = \pi$, respectively, which we use to rescale the x-axis in terms of the external flux φ_{ext} for all subsequent measurements.

In practice, we are interested to operate the fluxonium at $\varphi_{\text{ext}} = \pi$, the so-called flux frustration point. At this particular point, the frequency of the lowest transition of the fluxonium is minimal and the fluxonium is first-order insensitive to variations of the external-flux. The last feature means that the decoherence related to external-flux fluctuations is minimal at the flux frustration point.

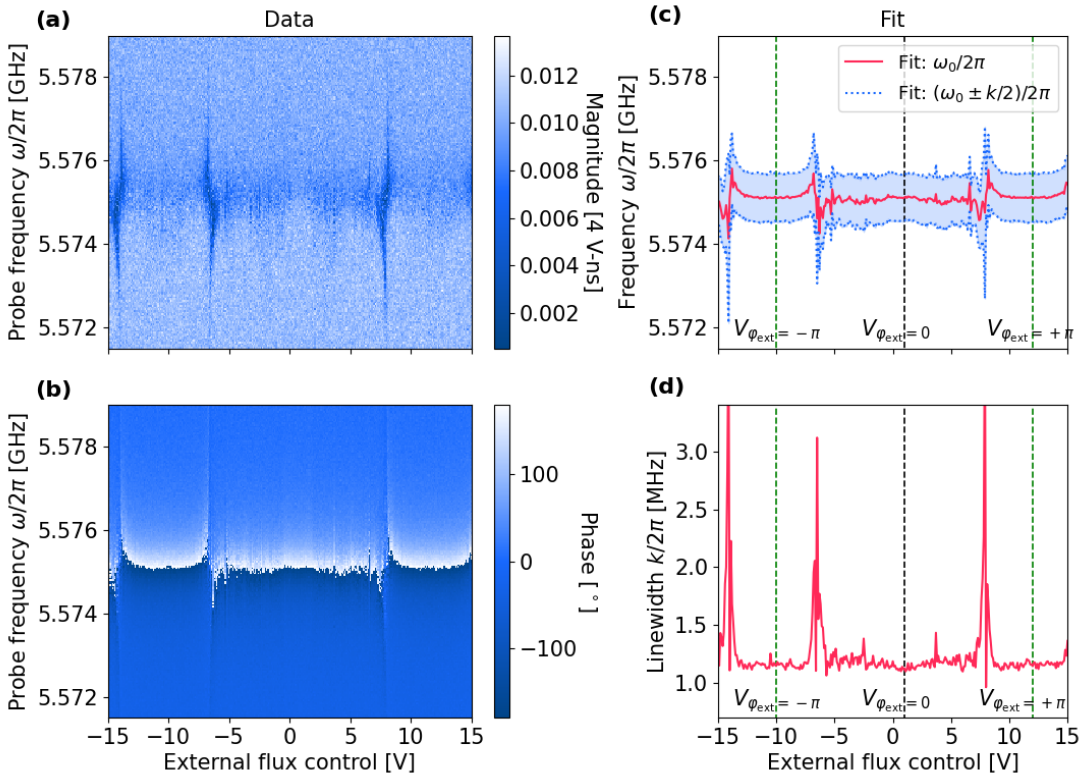

Fig. 5.2 ***Resonator single-tone spectrum:*** *Reflection response of the readout resonator as function of the external flux control (x-axis) and the probe tone frequency (y-axis). (a) Magnitude of the complex reflection coefficient S_{11}. (b) Phase of the complex reflection coefficient S_{11}. (c) Fit parameters according to Equation 5.1, the red solid line is the fitted central frequency of the complex Lorentzian as function of the external flux control while the blue-filled region represents the fitted linewidth as function of the external flux control. (d) Fitted linewidth of the complex Lorentzian as function of the external flux.*

5.2 Two tone spectrum

The next step is characterizing the fluxonium circuit transitions in the frequency domain around the already identified flux frustration point. For this purpose we perform a pump-probe experiment, referred to as two-tone spectroscopy. The first tone (pump), applied to the charge driving port, is scanned over a wide frequency range such that it populates higher fluxonium excited states whenever the pump frequency matches a particular transition. The different fluxonium states can be detected through their dispersive interaction with the readout resonator. Thus, the response of the resonator $S_{11}(\omega_0)$ is monitored with a second tone (probe) whose frequency is fixed close to the unperturbed resonator central frequency ω_0.

The result from the two-tone spectroscopy is shown in Figure 5.3[1]. The color scale encodes the magnitude of the change of the complex reflection coefficient of the probe field $S_{11}(\omega_0)$ as a function of the external flux φ_{ext} and the pump frequency ω_{pump}. The various

[1]The magnitude units correspond to the raw values output by the OPX.

transitions of the fluxonium appear as blue lines in this graph. The red dotted lines correspond to a fit of the various transition frequencies, obtained by numerically diagonalizing the 1D hamiltonian 2.3 [40]. In spite of the apparent complexity of the circuit, being composed of more than 360 Josephson junctions, we note the remarkable agreement between theory and measurements. Thus, the physics of the system is well captured by a 3 parameters lumped-element equivalent circuit (Equation 2.3). The fit parameters $E_J = 5.178$ GHz, $E_C = 0.414$ GHz, $E_L = 0.180$ GHz. In the practice, the parameter E_C can be inferred from an EM-field simulation of the circuit design as it only depends on geometric parameters of the circuit (see Section 3.1). The junction-related parameters E_L and E_J are estimated prior to cooling down the circuit in the dilution cryostat from resistance measurements at room-temperature (see Section 4.3).

Away from the flux-frustration point, $\varphi_{\text{ext}} \neq \pm\pi$, the fluxonium wave functions in the position-like variable φ are well localized within each of the potential wells (see Figure 5.3c right). These states, with small quantum fluctuations around a given value of φ are referred to as fluxons. They can be thought of as states of a persistent current flowing through the superconducting loop in either clockwise or counter-clockwise direction. Away from the flux frustration point, we can distinguish two families of transitions according to their behavior with respect to the external flux (see 2.7): The intra-well or plasmon transitions ($|e\rangle \rightarrow |h\rangle$ and $|g\rangle \rightarrow |f\rangle$), which are mostly independent on the external flux φ_{ext}, and the inter-well or fluxon transitions ($|g\rangle \rightarrow |h\rangle$ and $|e\rangle \rightarrow |f\rangle$), whose frequency varies linearly as a function of φ_{ext}. As the external flux approaches closely to the flux frustration point, the two neighboring potential wells become nearly degenerate and the left-well and right-well states hybridize (see Figure 6.5 left). This leads to a double avoided crossing at the flux frustration point. There are two characteristic frequencies, one of them given by the tunneling rate across the central barrier for the excited states of each well $|h\rangle$ and $|f\rangle$), and the tunneling rate as experienced by the bottom states of the wells ($|g\rangle$ and $|e\rangle$). The wavefunctions of the excited states of the wells are more spread over the position-like variable φ, and thus, their overlap is larger than the overlap between the wavefunctions of the bottom states of the wells. The larger wavefunction overlap for excited states leads to an avoided crossing of 60 MHz between $|f\rangle$ and $|h\rangle$ versus only 1.8 MHz between $|g\rangle$ and $|e\rangle$ (See Figure 5.3a and 5.3b). Notice that the frequency of the $|g\rangle \rightarrow |e\rangle$ transition is minimal at the flux frustration point, while the anharmonicity, the ratio between the frequency of the $|g\rangle \rightarrow |e\rangle$ transition and the frequency of the transition to the next level $|f\rangle$, is maximal, being of the order of 10^3.

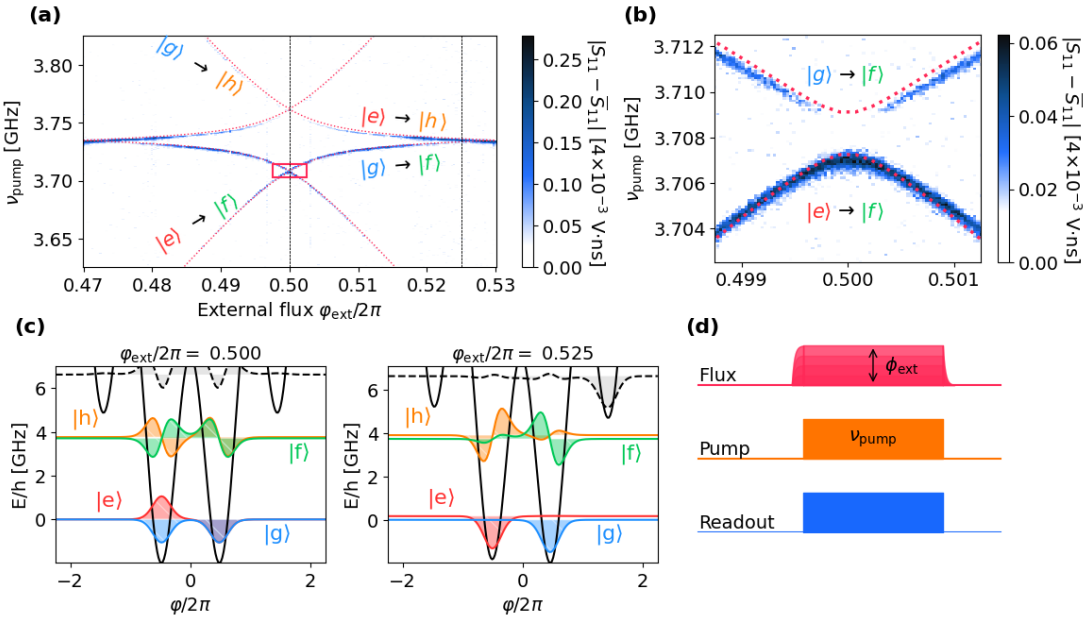

Fig. 5.3 ***Fluxonium two-tone spectrum:*** *Reflection response of the readout resonator as function of the external flux (x-axis) and the pump-tone frequency (y-axis) for a fixed value of the readout probe frequency. (a) Magnitude of the complex reflection coefficient S_{11}. The red dotted lines are the first transition frequencies obtained from the lumped-element hamiltonian of the fluxonium with the parameters $E_J = 5.178$ GHz, $E_C = 0.414$ GHz, $E_L = 0.180$ GHz. The label of each red dotted line indicates the two levels involved in the corresponding transitions. (b) Zoom into panel (a) at the region indicated by the red rectangle, the difference between the two red dotted lines is actually the frequency of the ground to first exited state transition, which is about 1.8 MHz at the flux frustration point ($\varphi_{ext}/2\pi = 0.5$). (c) Wavefunctions of the first 4 energy eigen-states of the fluxonium at the flux frustration point (left) and at close to the flux-frustration point (right). (d) Pulse sequence used to perform the measurement: firstly, the external flux threading the fluxonium loop is set with the aid of the OPX, then, a 5 µs-long pump pulse is applied at a given frequency, and simultaneously the readout is probed with a 5 µs-long pulse.*

5.3 Single shot readout

In the previous sections, we have learned how to probe experimentally the various transitions of the circuit, extract the Hamiltonian parameters E_J, E_C, and E_L, and adjust the magnetic flux to operate the circuit at the flux frustration point $\varphi_{\text{ext}} = \pi$. At this particular operation point, we have identified a low-frequency manifold $\{|g\rangle, |e\rangle\}$, that we refer to as the qubit transition in the following. Ultimately, the goal of this work is to use the low frequency transition as a nearly resonant probe for the electric field generated by other physical systems. However, extending the range of operation of circuit QED to the radio-frequency (MHz) domain comes with distinct challenges: In the first place, the qubit transition is coupled to a thermal environment with a large occupation $n_{\text{th}} \sim k_{\text{B}}T/\hbar\omega_{\text{eg}} \gg 1$, such that at equilibrium, the populations in $|e\rangle$ and $|g\rangle$ are nearly equal. Secondly, due to the large frequency difference between the microwave readout resonator and the radio-frequency qubit transition, the state-dependent dispersive shift of the cavity is typically too weak to readout the qubit state in a single-shot manner [81]. In order to overcome these challenges, we rely on the highly non-linear structure of the fluxonium spectrum (see, for instance, section 2.3.3): the transition to the second excited state being in the microwave domain, it can be easily manipulated and probed using standard circuit QED techniques. Moreover, the dispersive shift of the ancillary readout resonator due to the higher energy states is large enough to allow an efficient readout. This approach, where a low-frequency manifold is manipulated thanks to higher-frequency transitions is reminiscent of optical spin manipulation in atomic physics [31], or Nitrogen-Vacancy centers [42, 81]. In response to the first challenge, we will describe in Section 6.1 a protocol based on sideband cooling [26, 72] to deterministically prepare the states $|e\rangle$ or $|g\rangle$. In the following sections, we rather focus on the second challenge: in order to readout the qubit state, we address a selective transition to a higher-energy level of the fluxonium circuit, as previously demonstrated in reference [81]. This ancillary level (either $|f\rangle$ or $|h\rangle$) isn't typically populated at the operational temperature of the dilution cryostat and they exhibit a significant dispersive shift impacting the readout resonator. In the following, we describe the readout protocol using the higher energy state $|f\rangle$ as the ancillary state, but the experiment has given similar results with using $|h\rangle$ as the ancillary state instead. We start by characterizing the frequency of the ancillary transition $|e\rangle \rightarrow |f\rangle$ in section 5.3.1. In the next section 5.3.2, we characterize the dispersive shift of the ancillary resonator related to the $|e\rangle \rightarrow |f\rangle$ transition (at the flux frustration point) and we describe the procedure to set the single-shot readout of the quibit transition using the ancillary state $|f\rangle$. The coherence properties of the $|e\rangle \rightarrow |f\rangle$ transition are characterized in section 5.3.3. Finally, we demonstrate the single-shot readout in the qubit manifold using the ancillary transition in section 5.3.2.

5.3.1 Characterization of the ancillary transition frequency

The first step consists in performing a selective π-pulse in order to transfer as efficiently as possible the population from one of the lower levels either $|g\rangle$ or $|e\rangle$ to one of the higher fluxonium excited states, for instance, $|f\rangle$ or $|h\rangle$. At the flux-frustration point $\varphi_{\text{ext}} = \pi$, the wavefunctions are either even-parity ($|g\rangle$, $|f\rangle$) or odd-parity ($|e\rangle$, $|h\rangle$). Consequently, the selection rule forbids the direct $|g\rangle \rightarrow |f\rangle$ and $|e\rangle \rightarrow |h\rangle$ transitions (the matrix element for

the flux operator φ, governing the strength of the transition, is strictly 0 at the flux frustration point). This fact explains the vanishing of the corresponding lines in the two-tone spectroscopy (see Figure 5.3). We thus aim for calibrating a π-pulse on either the $|g\rangle \rightarrow |h\rangle$ and $|e\rangle \rightarrow |f\rangle$ transition. In the first place, we perform a coarse scan of the frequency and the duration of the pump pulse. The Figure 5.4 shows the measured readout signal (the quadratures of the reflection coefficient S_{11}) as a function of the frequency and the duration of the pump pulse. We clearly distinguish two sets of fringes (familiarly designated as "chevrons") that are centered around 3.705 GHz and 3.760 GHz. Each chevron represents the coherent oscillation of the occupation probabilities between two levels of the fluxonium, the so-called Rabi oscillations. We associate to the Rabi fringes to the $|e\rangle \rightarrow |f\rangle$ and $|g\rangle \rightarrow |h\rangle$ transitions, respectively. The contrast of the Rabi oscillations is maximum when the pump pulse frequency matches the resonance frequency of a given fluxonium transition (black dotted lines). As the detuning increases, we observe simultaneously a reduction of the contrast and an increase of the oscillation frequency. The geometric interpretation is that during the excitation pulse, the pseudo-spin representing the two involved fluxonium levels rotates around an effective pseudo-magnetic field $\propto \Omega_r/2\hat{e}_x + \Delta/2\hat{e}_z$, where $\Delta \equiv \omega_{\text{transition}} - \omega_{\text{pump}}$ is the detuning and Ω_r is the Rabi frequency at resonance, leading to a Rabi oscillations frequency $\sqrt{\Omega_r^2 + \Delta^2}$. From these graphs, we infer the approximate duration of the π-pulses (approximately 25 ns with this drive amplitude), and at the same time, we can estimate the optimal drive frequency to achieve resonance (3.705 GHz and 3.760 GHz for the $|e\rangle \rightarrow |f\rangle$ and $|g\rangle \rightarrow |h\rangle$ transitions respectively).

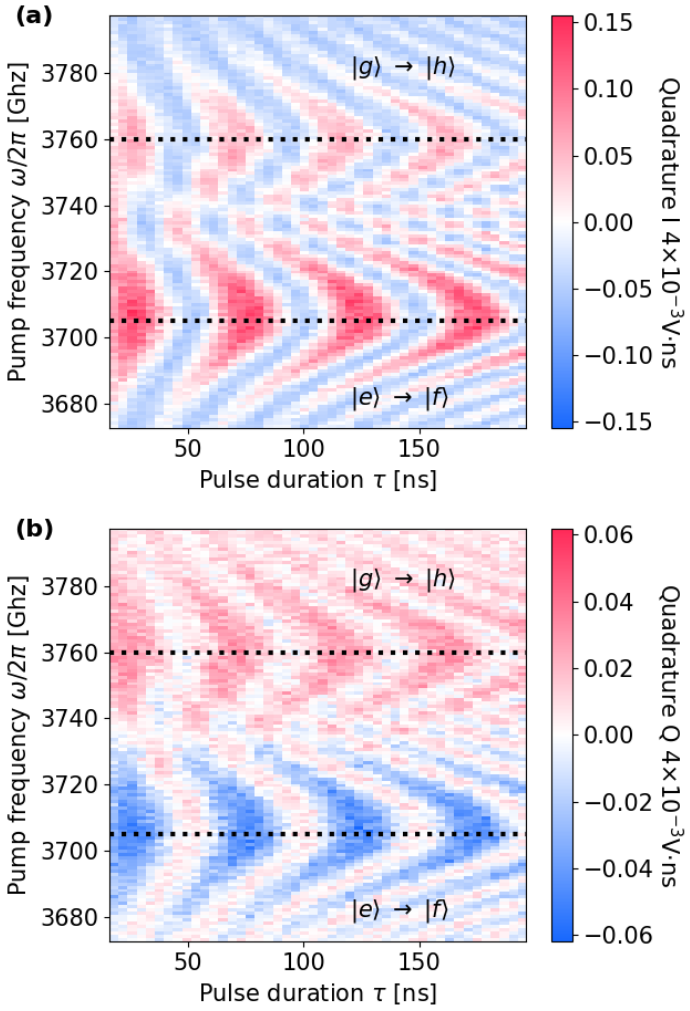

Fig. 5.4 ***e-f Rabi chevron:*** *Reflection response of the readout resonator as function of the pump-tone duration (x-axis) and frequency (y-axis) for a fixed value of the readout probe frequency (at the flux frustration point, $\varphi_{\text{ext}}/2\pi = 0.5$). (a) Magnitude of the complex reflection coefficient S_{11}. The horizontal dotted lines are placed at the frequencies of the $|e\rangle \rightarrow |f\rangle$ and $|g\rangle \rightarrow |h\rangle$ transitions, respectively. (b) Phase of the complex reflection coefficient S_{11}.*

Next, we typically sweep the amplitude of the pump pulse, while keeping the duration fixed, in order to more precisely adjust the pulse amplitude to perform a π-pulse on the chosen ancillary transition. We recall that a π-pulse corresponds to a nearly perfect population exchange between the two states involved in the transition, e.g., $|e\rangle$ and $|f\rangle$. For instance, the Figure 5.5 shows one of the quadratures of the reflection coefficient S_{11} as a function of the contrast the amplitude of the pump pulse. In this case, the frequency of the pump pulse was set in resonance with the $|e\rangle$ and $|f\rangle$ transition. Thanks to a sinusoidal fit (blue line in Figure5.5b), we precisely infer the amplitude corresponding to a π-pulse (here $V_\pi = 0.056$ mV). These settings (frequency, amplitude and duration) of the pump pulse

maximize the population transfer, for instance, from the lower state $|e\rangle$ to the excited state $|f\rangle$. We assume that initially, prior to the pump pulse, both states of the qubit transition, $|g\rangle$ and $|e\rangle$, are equally populated while the higher energy state $|f\rangle$ is typically empty. Then, the final state of the fluxonium, after the pump pulse, should resemble a statistical mixture with states $|g\rangle$ and $|f\rangle$ equally populated while the state $|e\rangle$ is now empty. This is precisely the transition that we use as ancillary in the following to set the single-shot readout of the qubit transition.

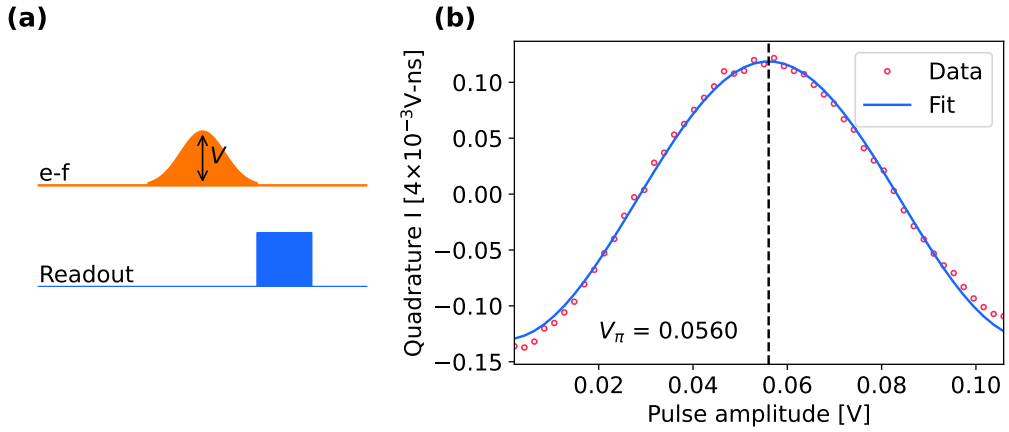

Fig. 5.5 ***e-f Rabi power:*** *Reflection response of the readout resonator as function of the pump-tone amplitude (x-axis) while its duration and frequency are fixed and the external flux is set at the sweet spot ($\varphi_{\text{ext}}/2\pi = 0.5$). (b) Magnitude of the complex reflection coefficient S_{11}. The vertical dotted lines is placed at the amplitude corresponding to a π-pulse. (a) Pulse sequence used to perform the measurement: First, a pulse with with a varying amplitude V, and then, the readout probe pulse.*

5.3.2 Readout histograms and single-shot readout

The readout signals that we have discussed so far were extracted from a large number of identical experimental realizations. The two quadratures I and Q of the complex reflection coefficient S_{11} were averaged over the statistical ensemble of measured data, yielding a pair of values expressed in an arbitrary unit (4 V·ns), which depends on the details of the amplification and measurement chain. We are now interest in the fluctuations of the readout signals over different iterations of the experiment. The Figure 5.6 shows a bi-dimensional histogram of the quadrature values obtained for about 10^5 realizations of the same experiment. In the subpanels (c) and (e), the readout pulse is applied at the circuit being at thermal equilibrium. An idle time of around 50 µs, about three times the thermal relaxation time of the level $|f\rangle$, was set between consecutive iterations of the experiment to ensure that the circuit returns to thermal equilibrium. In this case, mostly the levels $|g\rangle$ and $|e\rangle$ are populated while the other states, like $|f\rangle$ and $|h\rangle$, are mainly empty. This is a consequence of the very non-linear spectrum of a heavy fluxonium at the flux frustration point. Typically, the frequency of the qubit transition, $|g\rangle \rightarrow |e\rangle$, is so low that is below the environment energy represented by $k_{\mathrm{B}}T$ (see 5.6a). On the contrary, the next level of the fluxonium, $|f\rangle$, has a transition frequency 3 orders of magnitude larger compared to the qubit transition, such that the level $|f\rangle$ is above the environment energy (just like the other levels of the fluxonium). The differential frequency shift of the readout resonator is too small to resolve between these two-levels: in other words, the average shift in the quadratures I and Q between the realizations where the qubit is in state $|e\rangle$, compared to those realization where it is in state $|g\rangle$, is much smaller than the standard deviation due to readout noise. This explains why the histograms in Figure 5.6c and 5.6e are very close to a single Gaussian peak. However, two well separated Gaussian peaks are visible when π-pulse on the $|e\rangle \rightarrow |f\rangle$ transition precedes the readout pulse (see subpanels (d) and (f)). This bi-modal histogram clearly indicates that the circuit occupies discrete states that can be resolved in a single readout realisation (single-shot readout).

Notice that one of the quadratures, Q in this case, does not provide any useful information on the fluxonium state and it is only the quadrature I that enables the labeling of the $|f\rangle$ state and the ensemble of $|g\rangle$ and $|e\rangle$. Beware that this is not the normal case, typically the centers of the two gaussians are aligned along an arbitrary direction in the complex I-Q plane that not necessarily matches any of the default coordinate axis. This is easily solved in practice by performing a global-translation followed by a rotation in the complex I-Q plane, e.g., a subtraction of z_{offset} and a multiplication by $e^{i\theta_0}$, where both the complex offset z_{offset} and the phase θ_0 are characteristic of a given transition. The Figure 5.6 also shows 1-D histograms of the measurement results only as a function of the relevant quadrature I. By looking at them, it becomes evident that, with an appropriate threshold, it is possible to distinguish between the state $|f\rangle$ and the ensemble of states $|g\rangle$ and $|e\rangle$ by a single-shot measurement of the quadrature I. However, this shingle-shot readout is not perfect since there is a small overlap between the tails of the distributions corresponding to $|f\rangle$ and the ensemble of $|g\rangle$ and $|e\rangle$, this overlap is small nonetheless. Thus, under the reasonable assumption that the ancillary level $|f\rangle$ is typically empty, by applying a π-pulse between the states $|e\rangle$ and $|f\rangle$ (transferring all the population of state $|e\rangle$ to $|f\rangle$) before probing the readout resonator, we can actually resolve between the states of the qubit-manifold, $|g\rangle$ and $|e\rangle$, in a single

iteration of the experiment. We refer to this indirect readout of the qubit state through an ancillary fluxonium level plus the readout resonator as the single-shot readout.

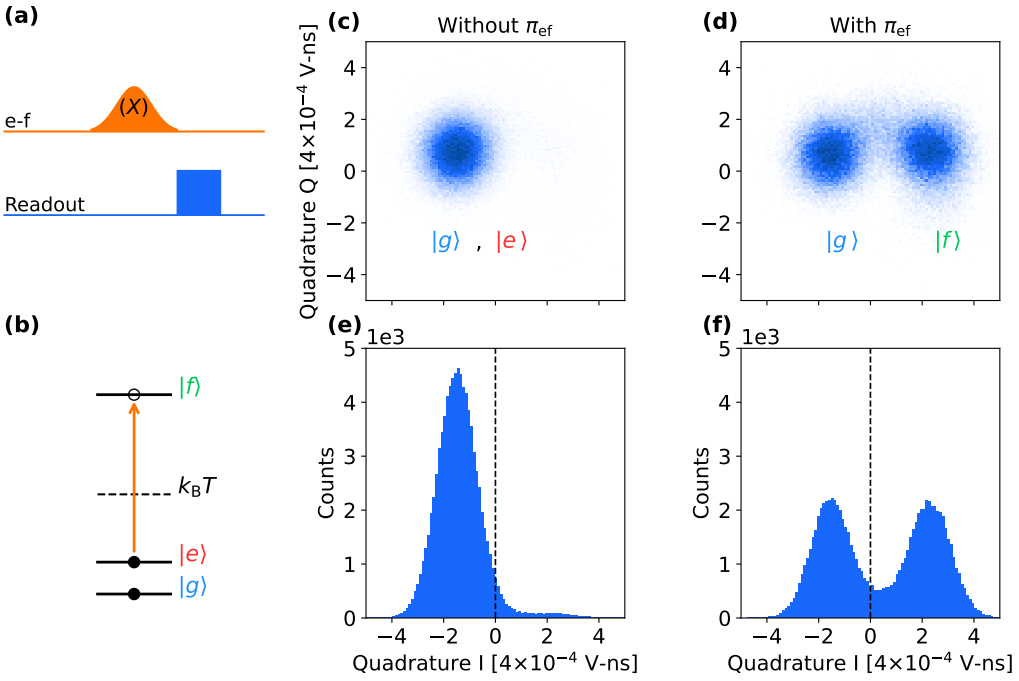

Fig. 5.6 ***Readout histograms:*** *real (I) and imaginary (Q) parts of the complex reflection coefficient S_{11}. (a) Pulse sequence used to perform the measurement: In one case, the readout resonator is probed while the fluxonium is at thermal equilibrium, and in the second case, a π-pulse (labeled as "X") at the frequency of the $|e\rangle \rightarrow |f\rangle$ transition is applied before probing the readout resonator. (b) Level diagram of the low-frequency spectrum of the fluxonium at the flux-frustration point: The $|g\rangle \rightarrow |e\rangle$ transition is so low, approximately 1.8 MHz, that is is typically below the environment energy represented by k_BT. This means that both levels $|g\rangle$ and $|e\rangle$ are equally populated at thermal equilibrium, while the next level $|f\rangle$, that is several GHz away from the ground state $|g\rangle$, remains practically unpopulated. The orange line represents the π-pulse applied in the measurement protocol. 2-D histograms of the real (I) and the imaginary (Q) parts of the complex reflection coefficient S_{11} (as measured by a 5 µs resonant pulse), without (c) π-pulse (X) and with (d) π-pulse. 1-D histograms obtained by ignoring the Q-quadrature corresponding to the case without (e) π-pulse (X) and with (f) π-pulse. The vertical dashed lines represents the threshold that we set to implement the single shot read out.*

5.3.3 Coherence properties

We finalize this chapter by completing the characterization of the ancillary transition $|e\rangle \rightarrow |f\rangle$ in time domain, particularly we discuss the measurement of its coherence properties, its thermal relaxation time T_1 and its coherence time T_2. In the first place, the relaxation time of the $|e\rangle \rightarrow |f\rangle$ transition is measured by first applying a π-pulse, and then, probing the resonator after waiting a time τ. The Figure 5.7 shows the results of the T_1 measurement, the results are presented in terms of population in $|f\rangle$, instead of quadratures (or magnitude and phase), now that the single shot has been set. The data follows an exponential fit yielding a decay time (T_1) of 8 µs.

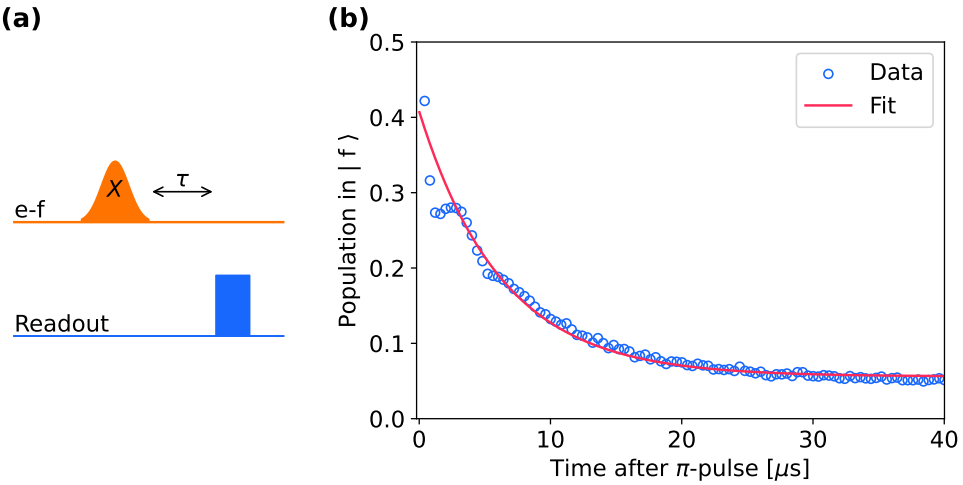

Fig. 5.7 ***T1 e-f:*** *Measurement of the relaxation time of the $|e\rangle \rightarrow |f\rangle$ transition. (a) Measurement protocol: First a π-pulse (X) is applied transferring 50 % of the fluxonium population from the $|g\rangle$, $|e\rangle$ manifold to the $|f\rangle$ state, and then, after an idle time τ, the readout resonator is probed. (b) Population in the $|f\rangle$ state as a function of the elapsed time after the π-pulse (X). The blue empty circles represent the measured data, while the red solid line is obtained by fitting the data with an exponential decay. The fitted T_1 of the $|e\rangle \rightarrow |f\rangle$ transition is* 6.27 µs.

Next, the coherence time (T_2^*) of the $|e\rangle \rightarrow |f\rangle$ transition is measured as it follows: A first $\pi/2$-pulse is applied followed by an idle time τ, during which the qubit pseudo-spin freely evolves in the equatorial plane of the Bloch sphere, and then, a second $\pi/2$-pulse is finally applied in order to map one of the directions of the equatorial plane (x or y) to the z-direction. If the local oscillator controlling the phase of the two $\pi/2$-pulses was precisely set at the natural precession frequency of the qubit ω_{ge}, one would expect a non-oscillatory signal as a function of τ, as the qubit pseudo-spin decays towards the center of the Bloch sphere. However, any detuning $\Delta \neq 0$ between the local oscillator ω_d and the qubit frequency ω_{ge} would result in an oscillatory behavior of the signal. If both the period of these oscillations and the exponential decay had similar characteristic time scales, it would be delicate to fit the signal and extract each parameter independently. Therefore, in order to separate the two timescales, we intentionally dephase the second $\pi/2$-pulse by an angle $\theta(\tau) = \delta_0 \tau$, where δ_0 is the so-called (artificial) Ramsey detuning. Furthermore, in order to remove the ambiguity

between positive and negative detuning Δ, we alternate experimental sequences where the second $\pi/2$-pulse probes the the X quadrature of the qubit pseudo-spin with sequences where the second $\pi/2$-pulse probes the Y quadrature instead. Following this approach, it is possible to reconstruct the precise evolution of the qubit pseudo-spin in the Bloch sphere as a function of the idle time τ. The Figure 5.8 shows the results of the T_2-Ramsey measurement, they are properly fitted by a complex spiral with an exponential decay (T_2^*) of 10.31 µs.

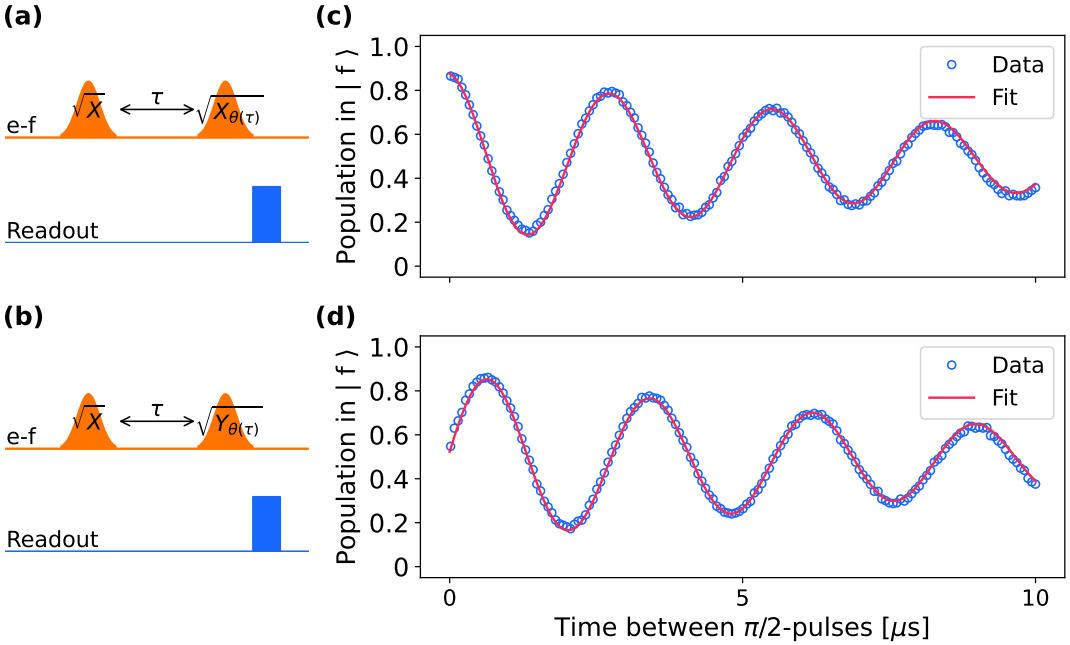

Fig. 5.8 ***T_2 Ramsey e-f:*** *Measurement of the decoherence time of the $|e\rangle \rightarrow |f\rangle$ transition. (a) Measurement protocol: First a $\pi/2$-pulse ($\sqrt{X}$) is applied between the $|e\rangle$ and $|f\rangle$ states, then, after an idle time τ, a second $\pi/2$-pulse is applied. This second pulse has a phase difference $\theta = \delta_0\tau$ with respect to the first pulse, so that it is labeled as $\sqrt{X_{\theta(\tau)}}$. Alternatively, (b) an additional phase difference of $\pi/2$ is added to the second $\pi/2$-pulse, effectively probing the Y-axis of the Bloch sphere, thus, this pulse is labeled as $\sqrt{Y_{\theta(\tau)}}$. Measured population in the $|f\rangle$ state as function of the elapsed time τ between the two $\pi/2$-pulses: (c) $\sqrt{X}$ and $\sqrt{X_{\theta(\tau)}}$, and $\sqrt{X}$ and $\sqrt{Y_{\theta(\tau)}}$. The blue empty circles represent the measured data, while the red solid line is obtained by fitting the data with a complex spiral with an exponential decay. The fitted T_2^* Ramsey of the $|e\rangle \rightarrow |f\rangle$ transition is* 10.31 µs.

This chapter has presented the basic characterization of the circuit, using a higher-energy state of the fluxonium $|f\rangle$ to set a single-shot readout of the qubit-manifold, the states $|g\rangle$ and $|e\rangle$. The next chapter is about the preparation and manipulation of the low-frequency qubit.

Chapter 6

Characterization and manipulation of the low-frequency qubit

As discussed in Section 2.3.2, the heavy-fluxonium operated at the flux-frustration point, has a lowest-energy transition in the range of few MHz, while the next transitions are 3 orders of magnitude higher in frequency (in the GHz range). The two lowest-energy states of the heavy-fluxonium circuit then can be used as a radio-frequency qubit. The associated transition has a large charge matrix element, which allows direct manipulation via charge driving (voltage driving). This chapter is dedicated to describing the preparation and manipulation of this radio-frequency qubit.

As the qubit transition is typically below $k_{\mathrm{B}}T$ where T is the environment temperature, the states $|e\rangle$ and $|g\rangle$ are equally populated. Thus, it is necessary to implement a protocol to prepare the qubit in a pure state ($|g\rangle$ or $|e\rangle$), before any further measurement or manipulation. The first section of this chapter is about the implementation of this protocol that we refer to as the sideband preparation protocol. Then, we continue with the basic manipulation of the qubit, in this case, we perform a Rabi spectroscopy as the first step for optimizing the coherent manipulation of the qubit degree of freedom. The next sections of the chapter are dedicated to the characterization of the qubit coherence properties: its thermal relaxation time T_1 and its coherence time T_2. We conclude the chapter with the characterization of the qubit frequency and coherence time as function of the external flux φ_{ext} around the flux frustration point, $\varphi_{\mathrm{ext}}/2\pi = 0.5$.

6.1 Sideband preparation

As we have seen in section 5.2, the qubit transition $|g\rangle \rightarrow |e\rangle$ has a frequency of approximately 1.8 MHz. This transition is few orders of magnitude below the next fluxonium transitions. For instance, the frequency of the next allowed transition, $|e\rangle \rightarrow |f\rangle$, is around 3.705 GHz, while the frequency of the next next allowed transition, $|g\rangle \rightarrow |h\rangle$, is around 3.760 GHz. The low-energy spectrum of the fluxonium is sufficiently non-linear such that the g-e manifold can be used as a radio frequency qubit. However, the qubit frequency is far below $k_{\mathrm{B}}T$, where T is the environment temperature such that both states have practically the same population at thermal equilibrium. Thus, a reset protocol is required to initialize the qubit in a pure state, either $|g\rangle$ or $|e\rangle$, before proceeding with further manipulations. We drew inspiration from opto-mechanics [72] and took advantage of the coupling between the ancillary resonator and the fluxonium, as schematically shown in Figure 6.1. In practice, we initialize the qubit by driving the resonator at a detuned frequency. More specifically, we use a reset pulse to drive one of the resonator sidebands corresponding to either the transition $|g\,0\rangle \rightarrow |e\,1\rangle$ or the transition $|e\,0\rangle \rightarrow |g\,1\rangle$ (see Figure 6.2). The number "0" represents the vacumm state of the ancillary resonator, while 1 represents the resonator state with 1 quantum of energy. The two sidebands are located at the frequencies $\nu_{\mathrm{s}\pm} = \nu_{\mathrm{resonator}} \pm \nu_{ge}$, respectively.

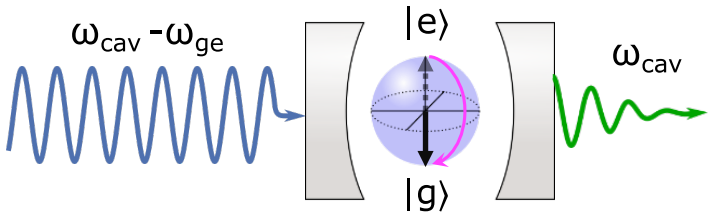

Fig. 6.1 ***Sideband cooling scheme.*** .

The Figure 6.2 shows in more detail the implementation of the reset protocol[1]. As the first step, we performed a pump-probe experiment that we refer to as the sideband spectroscopy. In this experiment, the qubit starts at thermal equilibrium, then, a reset pulse is used to pump one of the sidebands transitions while the change in qubit population is tracked via the single shot readout of the ancillary resonator (see Figure 6.2b). The frequency of the reset pulse is scanned within a few MHz range around the bare resonator frequency $\nu_{\mathrm{resonator}} = 5.64$ GHz. Finally, this measurement is repeated for different values of the external flux around the flux frustration point. The result of the sideband spectroscopy is shown in Figure 6.2c. Notice the two clear transition lines at both sides of the resonator frequency (see dashed horizontal line in Figure 6.2c). We remark that the two sidebands correspond to the transitions $|g\,0\rangle \rightarrow |e\,1\rangle$ and $|e\,0\rangle \rightarrow |g\,1\rangle$, such that the difference between their frequencies is the qubit frequency ν_{ge} (see Figure 6.2a). Away from the flux frustration point, the difference between the frequencies of the two sidebands scale linearly with the external flux. This is traced to the dependence of the $|g\rangle \rightarrow |e\rangle$ transition frequency on the external flux, which roughly goes as $2\pi E_L|\varphi_{\mathrm{ext}}|$. Moreover, this measurement verifies once

[1]The population in $|e\rangle$ is re-scaled to account for the finite readout efficiency

more that the frequency of the transition $|g\rangle \rightarrow |e\rangle$ is minimal at the flux frustration point.

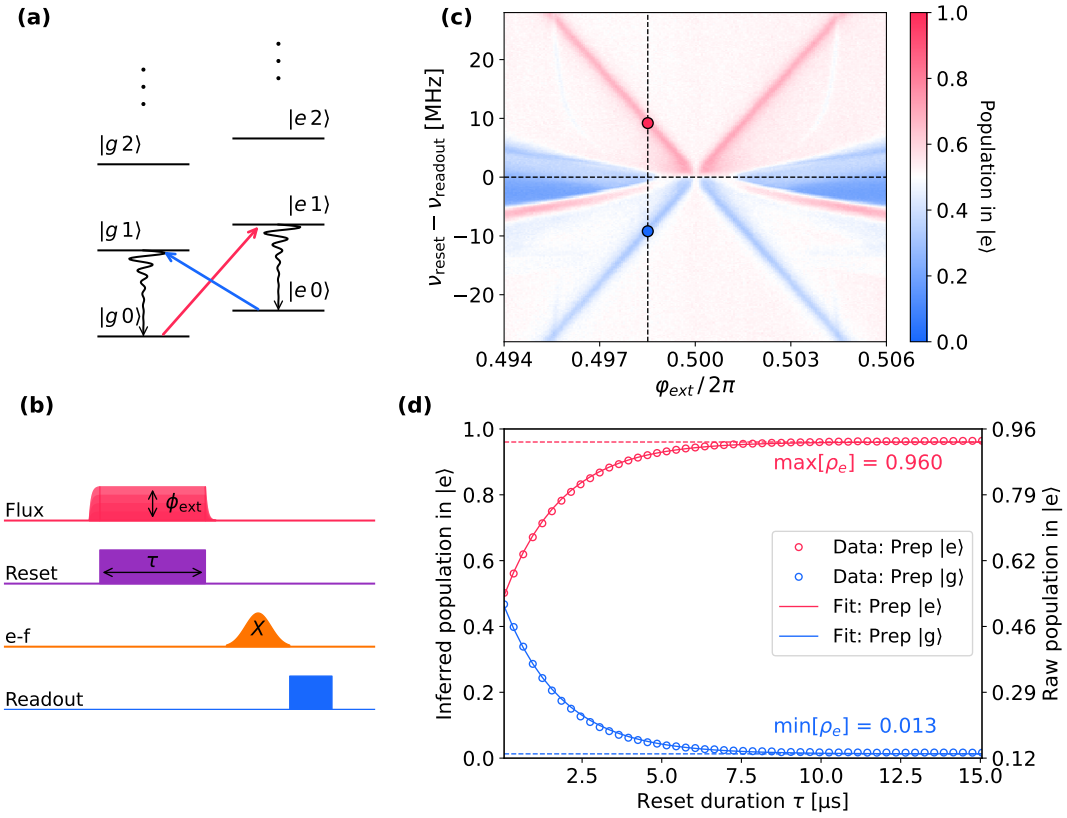

Fig. 6.2 ***Sideband preparation:*** *(a) Level diagram of the sideband preparation. (b) Pulse sequence used for the measurement: Firstly, the reset pulse with duration τ and frequency ν_{reset} is applied, and it is followed by the single shot-readout of the qubit state, consisting of a π-pulse (X) at the $|e\rangle \rightarrow |f\rangle$ transition and the readout pulse to probe the resonator. (c) Spectrum of sideband transitions of the resonator: the frequency of the reset pulse ν_{reset} is varied around the readout resonator frequency ν_{readout} for different external flux values around half flux, $\varphi_{\mathrm{ext}}/2\pi = 0.5$, the population in state $|e\rangle$ at the end of the sequence is represented by the color of each pixel. (d) Optimization of the reset-pulse duration: the external voltage is set at the value indicated by the vertical dashed line in panel (c), the frequency of heating pulse (red branch) is shown by the height of the red dot while the frequency of the cooling pulse (blue branch) is indicated by the height of the blue dot.*

Notice that the two sideband transitions vanish in the vicinity of the flux frustration point. This result is expected since the wavefunctions of the states $|g\rangle$ and $|e\rangle$ have opposite parities at the flux frustration point and the sideband transitions are forbidden in consequence. However, this represents a problem for setting the reset protocol at the flux frustration point, as this is the optimal point for the operation of the low-frequency qubit but the sideband transition are forbidden. We circumvented the issue by first shifting the external flux away from the flux frustration point (see vertical dashed line in Figure 6.2c), then, preparing the qubit in one of the states $|g\rangle$ or $|e\rangle$ by pumping the respective resonator sideband, and finally, shifting the resonator back to the flux frustration point. The external flux is shifted sufficiently slow to avoid non-adiabatic effects, i.e., that the qubit remains in the prepared state for the whole duration of the ramp of the external flux. The duration of the external flux ramp was set to 4 µs. The final step was optimizing the duration of the reset pulse. In Figure 6.2d we scan the duration of the reset pulse and track the change in the quit population. We set the duration of the reset pulse to 10 µs.

We conclude this section by estimating the efficiency of the sideband preparation. As we have discussed in Section 5.3.2, the dispersive shift of the ancillary resonator corresponding to the qubit manifold is negligible, however, we can take advantage of the large dispersive shift of the resonator due to the higher energy levels of the fluxonium to set a single-shot readout of the qubit manifold. The single-shot readout nonetheless is not ideal, meaning that there is some probability of miss-labeling the measured qubit states. In order to estimate the readout efficiency and the preparation efficiency all at once, we perform the following experiment: The qubit is initialized in either a thermal state "th" (in thermal equilibrium), state $|g\rangle$ or state $|e\rangle$, then, the transition $|g\rangle \rightarrow |h\rangle$ is resonantly driven for a fixed duration and an amplitude that is varied over several iterations, and finally, the qubit state readout by probing the ancillary resonator [2]. The results of the experiment are shown in Figure 6.3. By fitting the data (dashed lines), we retrieve the readout efficiency and the sideband-preparation efficiency.

Let's refer to the computational basis as $|0\rangle$ (ground state) and $|1\rangle$ (excited state). In the case of an ideal single-shot readout, the probability of correctly detecting the qubit in state $|e\rangle$ (state $|g\rangle$) is $P\left[|1\rangle \,|\, |e\rangle\right] = 1$ ($P\left[|0\rangle \,|\, |g\rangle\right] = 1$). This means that the probability of wrongly labeling the qubit in state $|e\rangle$ (state $|g\rangle$) is $P\left[|0\rangle \,|\, |e\rangle\right] = 0$ ($P\left[|1\rangle \,|\, |g\rangle\right] = 0$). Notice that the higher energy level, in this case $|h\rangle$, that is involved in the single-shot readout must be taken into account in the analysis. The density matrix of the qubit right after the initialization is:

$$\rho_0 = \rho_g^{\mathrm{x}}(0)\ |g\rangle\langle g| + \left(1 - \rho_g^{\mathrm{x}}(0)\right)\ |e\rangle\langle e| \tag{6.1}$$

Where the symbol "x" refers to the qubit initialization, {"th", "0", "1"}. After resonantly

[2] Notice that for the other experiments involving the qubit we normally use the ancillary fluxonium state $|f\rangle$ for the single-shot readout, as described in Section 5.3.2.

driving the $|g\rangle \rightarrow |h\rangle$ transition with an amplitude V_{d} (in volts), the density matrix becomes:

$$\begin{aligned}\rho_1 =& \frac{\rho_g^{\mathrm{x}}(0)}{2}\left(1+\cos\left(2\pi\frac{V_{\mathrm{d}}}{V_{2\pi}}\right)\right)|g\rangle\langle g| + \left(1-\rho_g^{\mathrm{x}}(0)\right)|e\rangle\langle e| \\ &+ \frac{\rho_g^{\mathrm{x}}(0)}{2}\left(1-\cos\left(2\pi\frac{V_{\mathrm{d}}}{V_{2\pi}}\right)\right)|h\rangle\langle h| \\ &+ \frac{1}{2}\sqrt{\rho_g^{\mathrm{x}}(0)\left(1-\rho_g^{\mathrm{x}}(0)\right)}\sin\left(2\pi\frac{V_{\mathrm{d}}}{V_{2\pi}}\right)\left(|g\rangle\langle h| + |h\rangle\langle g|\right)\end{aligned} \tag{6.2}$$

The probability of detecting the qubit in state $|1\rangle$ is then:

$$\begin{aligned}P\left[|1\rangle\right] =& \frac{\rho_g^{\mathrm{x}}(0)}{2}\left(1+\cos\left(2\pi\frac{V_{\mathrm{d}}}{V_{2\pi}}\right)\right)P\left[|1\rangle\,|\,|g\rangle\right] + \left(1-\rho_g^{\mathrm{x}}(0)\right)P\left[|1\rangle\,|\,|e\rangle\right] \\ &+ \frac{\rho_g^{\mathrm{x}}(0)}{2}\left(1-\cos\left(2\pi\frac{V_{\mathrm{d}}}{V_{2\pi}}\right)\right)P\left[|1\rangle\,|\,|h\rangle\right]\end{aligned} \tag{6.3}$$

Where $P\left[|1\rangle\,|\,|g\rangle\right]$, $P\left[|1\rangle\,|\,|h\rangle\right]$ and $P\left[|1\rangle\,|\,|e\rangle\right]$ are the probabilities of detecting the qubit in the computational state $|1\rangle$ given that the fluxonium is actually in either state $|g\rangle$, $|h\rangle$ or $|e\rangle$, respectively. In the case of the single-shot readout, the amplitude of the resonant drive of the $|g\rangle \rightarrow |h\rangle$ transition is chosen such that $V_{\mathrm{d}}/V_{2\pi} = 0.5$ (a π-pulse). The probability of detecting the qubit in state $|1\rangle$ is after the single-shot readout is then:

$$P_{\mathrm{ssr}}\left[|1\rangle\right] = \left(1-\rho_g^{\mathrm{x}}(0)\right)P\left[|1\rangle\,|\,|e\rangle\right] + \rho_g^{\mathrm{x}}(0)\,P\left[|1\rangle\,|\,|h\rangle\right] \tag{6.4}$$

The efficiency of the readout is given by the coefficients γ_{11} and γ_{00}, where γ_{11} is the probability of (correctly) detecting the computational state $|1\rangle$ given that the qubit was initially in state $|e\rangle$, while γ_{00} is the probability of (correctly) detecting the computational state $|0\rangle$ given that the qubit was initially in state $|g\rangle$:

$$\begin{aligned}\gamma_{11} =& P\left[|1\rangle\,|\,|e\rangle\right] \approx 0.959 \\ \gamma_{00} =& P\left[|0\rangle\,|\,|h\rangle\right] \approx 1 - P\left[|1\rangle\,|\,|h\rangle\right] \approx 0.878\end{aligned} \tag{6.5}$$

Notice that this simple model doesn't take into account explicitly the relaxation of the fluxonium states during the readout of the ancillary resonator. However, the lower efficiency of labeling the qubit as $|0\rangle$, γ_{00}, with respect to the efficiency of labeling the qubit as $|1\rangle$, γ_{11}, can be explained by considering the higher relaxation rate $1/T_1^{hg}$ of the level $|h\rangle$ with respect to the relaxation rate $1/T_1^{eg}$ of level $|e\rangle$. The Equation 6.4 can be inverted to infer the "real" population of state $|e\rangle$ from the measured value $P_{\mathrm{ssr}}\left[|1\rangle\right]$ (raw population) [3]:

$$\rho_e = \frac{P_{\mathrm{ssr}}\left[|1\rangle\right] + \gamma_{00} - 1}{\gamma_{11} + \gamma_{00} - 1} \tag{6.6}$$

Finally, the preparation efficiency is characterized by the coefficient ϵ_0 and ϵ_1, where ϵ_0 is defined as the population of state $|g\rangle$ after the sideband initialization in the ground state $|0\rangle$, while ϵ_1 is defined as the population of state $|e\rangle$ after the sideband initialization in the excited state $|1\rangle$:

$$\begin{aligned}\epsilon_0 =& \rho_g^0(0) \approx 0.991 \\ \epsilon_1 =& \rho_e^1(0) = 1 - \rho_g^1(0) \approx 0.976\end{aligned} \tag{6.7}$$

[3] This equation was used to rescale the axis of Figure 6.2d

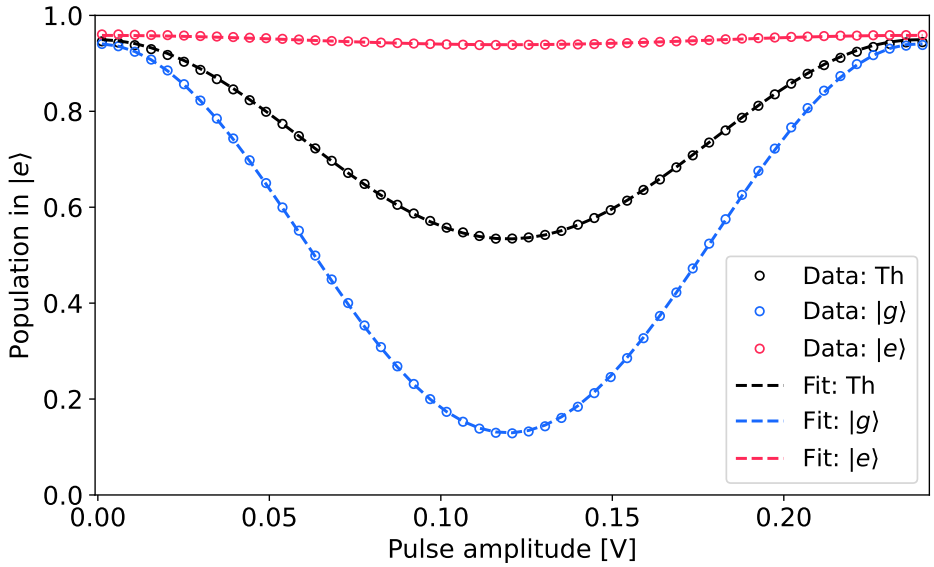

Fig. 6.3 ***Preparation efficiency:*** *Readout efficiency:* $P[1||g\rangle] = 0.94065$, $P[1||e\rangle] = 0.95872$, $P[1||h\rangle] = 0.87809$. *Preparation efficiency:* $\rho_g(0) = 0.99096$, $\rho_e(0) = 0.97630$, $\rho_{g,\,\mathrm{th}} = 0.50764$

6.2 Rabi spectroscopy

With the reset protocol already implemented, we proceed with the characterization of the qubit manifold $\{|g\rangle, |e\rangle\}$. We perform a Rabi oscillations experiment, in which the qubit is initialized in the state $|e\rangle$, and then, an additional pulse is used to drive the coherent population exchange between the states $|e\rangle$ and $|g\rangle$, finally, the population in state $|e\rangle$ at the end of the measurement protocol was measured via the single-shot readout of the ancillary resonator. The Figure 6.4 shows the result of the measurement referred to as Rabi spectroscopy. The population exchange between the states $|e\rangle$ and $|g\rangle$ is clear and more noticeable when the frequency of the drive (g-e) pulse matches the qubit frequency (see dashed line in Figure 6.4b).

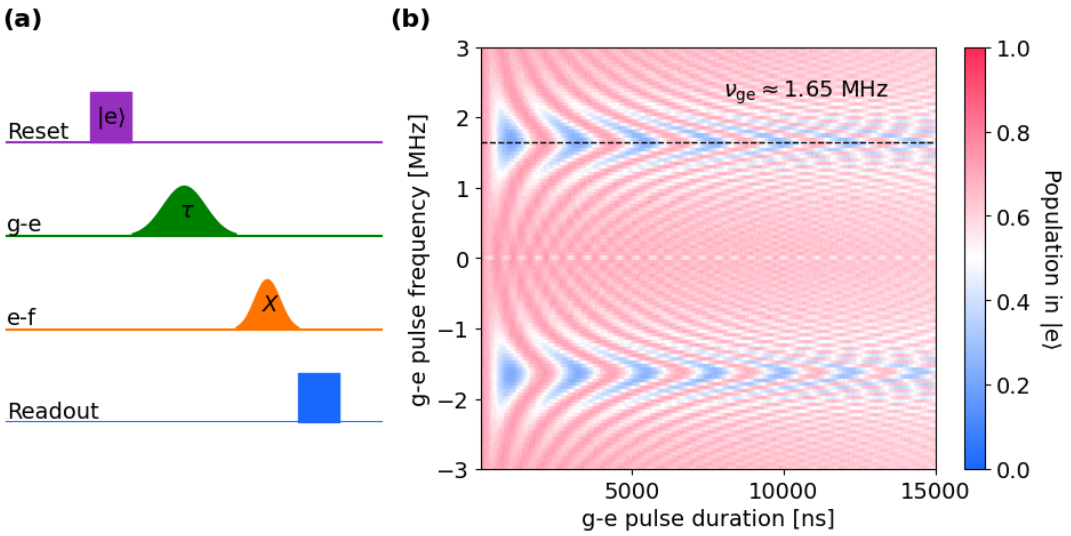

Fig. 6.4 ***g-e Rabi chevron:*** *(a) Pulse sequence used in each experimental realization: Firstly, the qubit is initially prepared in the state $|e\rangle$ by applying the sideband reset pulse, then, the drive pulse with duration τ is applied at the frequency of the $|g\rangle \rightarrow |e\rangle$ transition, and finally, the projective measurement of the qubit state is performed by applying the π-pulse (X) at the $|e\rangle \rightarrow |f\rangle$ transition and concluding with the readout pulse to probe the resonator. (b) Rabi chevron of the g-e transition: The coordinates of each pixel indicate the values of the $g-e$ pulse frequency (y-axis) and duration (x-axis) while the color of each pixel indicates the represents the qubit population at the end of each measurement realization.*

6.3 Relaxation time

The next step in the qubit characterization is measuring the relaxation time T1. In this experiment, the qubit is initialized in one of the states of the qubit manifold, either $|e\rangle$ or $|g\rangle$, and after a delay time τ, the final quit population is measured.

6.3.1 Qubit relaxation time at 10 mK

The Figure 6.5 shows the results of the experiment. In either case, we notice the clear exponential decay of the population in $|e\rangle$ towards the thermal equilibrium value 0.5.

In general, when a qubit interacts with a thermal environment of occupation n_{th}, it is exposed to two loss channels, described by the operators $\Gamma_{\uparrow}\sigma^{+}$ and $\Gamma_{\downarrow}\sigma^{-}$, such that $\Gamma_{\uparrow} \propto n_{\text{th}}$ and $\Gamma_{\downarrow} \propto n_{\text{th}} + 1$ [41]. In the case of a low-frequency transition, such as the $\{|e\rangle\ ,\ |g\rangle\}$ manifold, the large environmental occupation $n_{\text{th}} \approx k_{\text{B}}T_{ge}/\hbar\omega_{ge}$, with T_{ge} being the environmental temperature associated to the 1.8 MHz transition, results in $\Gamma_{\downarrow} \approx \Gamma_{\uparrow} \equiv \Gamma$, leading to an exponential relaxation towards the statistical mixture $\rho_{\text{th}} = (|e\rangle\langle e| + |g\rangle\langle g|)/2$ at a rate 2Γ. By fitting exponential curves to the data of Figure 6.5, we obtain $T_1 = 1/2\Gamma = 34\,\mu\text{s}$. This value is below the the reported values of other state-of-the-art qubit implementations [81].

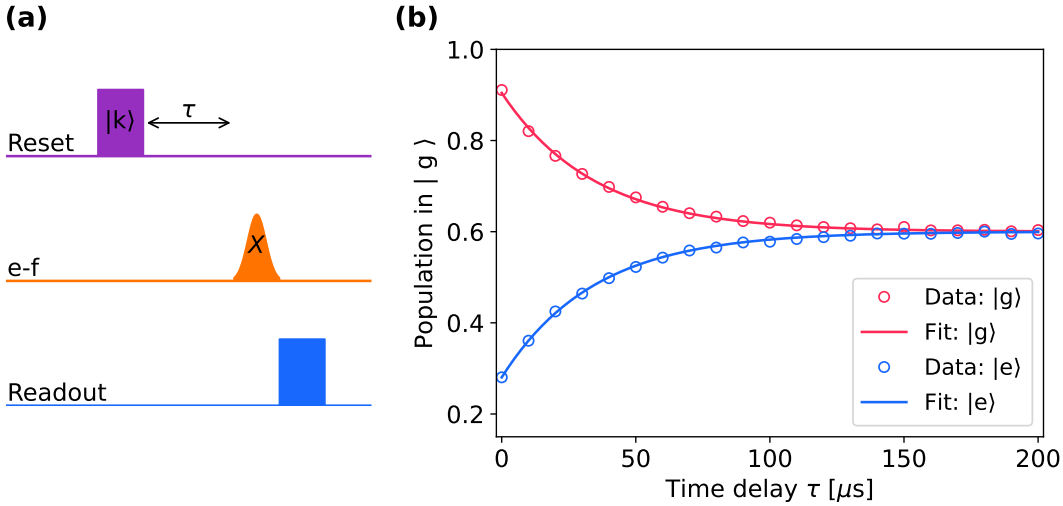

Fig. 6.5 ***T1 g-e:*** *Measurement of the relaxation time of the $|g\rangle \rightarrow |e\rangle$ transition. (a) Pulse sequence used for the experimental realization: The qubit is initially prepared in either $|g\rangle$ or $|e\rangle$ with the aid of the reset pulse, and then, after waiting a time τ, the qubit state is determined by the projective measurement consisting of a π-pulse (X) at the $|e\rangle \rightarrow |f\rangle$ transition and the readout pulse to probe the resonator. (b) Population in the state $|e\rangle$ at the end of each realization as function of the waiting time τ after the qubit preparation. The empty circles represent the measured data while the solid lines are obtained by fitting the data with an exponential decay. The blue and red colors correspond to a qubit preparation in state $|g\rangle$ or $|e\rangle$, respectively. The fitted $T1$ of the $|g\rangle \rightarrow |e\rangle$ transition is* 34 µs.

6.3.2 Qubit relaxation time vs cryostat temperature

As the qubit frequency explored in the current work extends well below the values reported in the literature so-far [81], it is important to determine whether the qubit transition couples with a thermal environment or is primarily constrained by technical noises (e.g. $1/f$-charge noise). In this section, we study the dependence of the relaxation rate as a function of the temperature. To achieve this, we heat the mixing-chamber of the cryostat with a resistor. The temperature $T_{\mathrm{RuO_2}}$, as measured by a Ruthenium oxide probe built-in with the cryostat (model Bluefors BFLD250) is stabilized thanks to a feedback loop to various setpoints ranging from 7 mK to 100 mK. For each point, we measure the decay rate $2\Gamma^{eg} = 1/T_1^{eg}$ of the states $|e\rangle$ and $|g\rangle$, akin to the measurement shown in the Figure 6.5. We observe a nearly constant decay rate $2\Gamma^{eg} \approx 35\ \mathrm{ms}^{-1}$ in the range 7 mK $\leq T_{\mathrm{RuO_2}} \leq$ 50 mK. Above 50 mK, we observe a linear increase of the decay rate, compatible with an imperfect thermalization of the sample with the mixing chamber. The fact that the assymptote of the curve $\Gamma(T_{\mathrm{RuO_2}})$ does not intersect with the origin is attributed to a possible miscalibration of the cryostat temperature sensor at high temperature. In order to cross check the temperature measurement, we perform an independent temperature measurement by taking into account the residual thermal population of the higher qubit excited states $\{|f\rangle\ , |h\rangle\}$. This signal serves as a local probe, scrutinizing the noise temperature of the circuit at the second transition frequency of 3.7 GHz. In practice, we let the circuit thermalize with its environment, and then record a histogram of the real (I) and imaginary part (Q) of the readout cavity reflection coefficient, as visible on Figure 6.6. Three peaks are visible on the histogram, corresponding to the

population in the manifold $|g\rangle$, $|e\rangle\}$, the state $|f\rangle$ and the state $|h\rangle$ respectively. We assume a Boltzmann distribution for the population in the various qubit states: $pk \propto e^{-kbT_{\text{eff}}/Ek}$, where E_k is the energy of state k ($k \in |g\rangle, |e\rangle, |f\rangle , |h\rangle\}$. Furthermore, by neglecting the small transition frequencies $\omega_{ge}/2\pi \approx 1.8$ MHz, and $\omega_{fh}/2\pi \approx 50$ MHz, compared to $\omega_{ef}/2\pi \approx 3.7$ GHz, we get $P_{|g\rangle} = P_{|e\rangle} \equiv P_{g,e}/2$ and $P_{|f\rangle} = P_{|h\rangle} \equiv P_{f,h}/2$. We extract the populations $P_{g,e}$ and $P_{f,h}$ by a triple Gaussian fit to the readout histogram, where the Gaussian peaks corresponding to $|f\rangle$ and $|h\rangle$ are constrained to the same area. From the values $P_{g,e}$ and $P_{f,h}$, we determine the effective temperature:

$$T_{\text{ef}} = \frac{\hbar\omega_{ge}}{k_{\text{B}} \log\left(\frac{P_{g,e}}{P_{f,h}}\right)} \tag{6.8}$$

We then plot the decay rate $2\Gamma^{eg}$ as a function of effective temperature T_{ef} in Figure 6.6. We observe a linear dependence on most of the temperature range indicating that the $|g\rangle \rightarrow |e\rangle$ and $|e\rangle \rightarrow |f\rangle$ transitions are coupled to thermal environments with similar noise temperatures, in spite of their 3-orders of magnitude frequency difference.

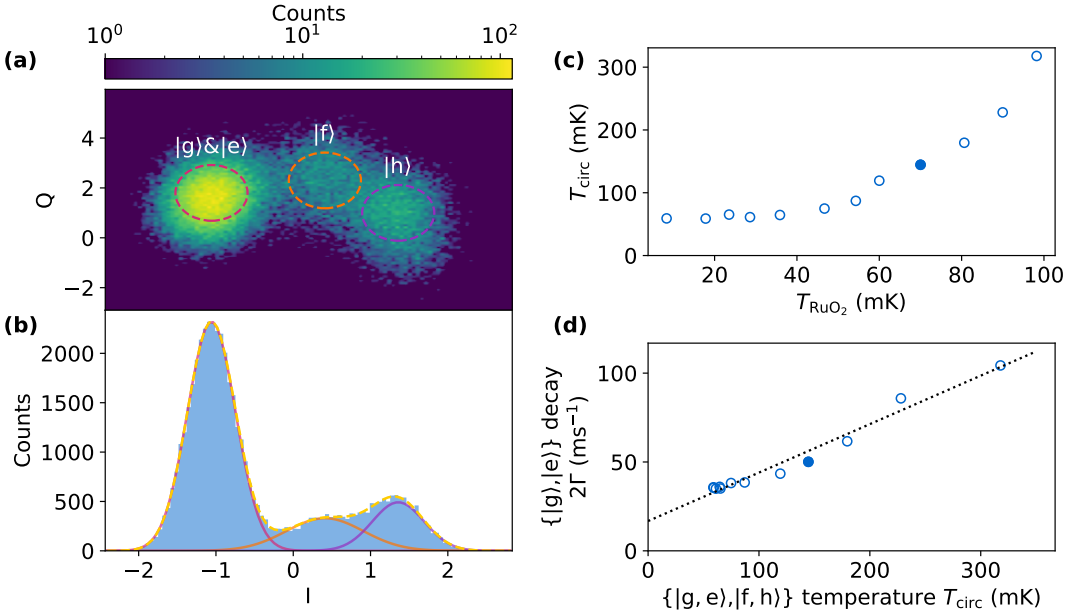

Fig. 6.6 ***Relaxation rate vs temperature:*** *(a) 2-dimensional histogram of the I and Q quadratures of the readout reflection coefficients for a qubit at thermal equilibrium with the environment. (b) Histogram of the I quadrature. The population in the manifolds $\{|g\rangle$, $|e\rangle$, $|f\rangle$ and $|h\rangle\}$ are determined by fitting the various peaks with Gaussian functions. (c) Energy decay rate 2Γ in the $\{|g\rangle, |e\rangle\}$ manifold measured via T_1^{x} relaxometry (see Figure 6.5), as a function of cryostat temperature. (d) The same data are plotted as a function of the effective temperature of the $|e\rangle \rightarrow |f\rangle$ transition, as determined from Equation 6.8). The filled point is the one extracted from the histograms in (a) and (b). The dashed line is a guide to the eyes highlighting the linear dependency above $T_{\text{ef}} = 100$ mK.*

6.4 Coherence time

The next step in the qubit characterization is measuring the dephasing time T_2^* thanks to a Ramsey spectroscopy (see Chapter 1 section 1.5.3). Compared to the sequence described in the first chapter, the second $\pi/2$ pulse is applied with a phase difference $\theta(\tau) = \theta_0 + 2\pi\delta\tau$ (see figure 6.7), with the respect to the first pulse, in order to generate an artificial oscillation between the states to simplify the fitting procedure.

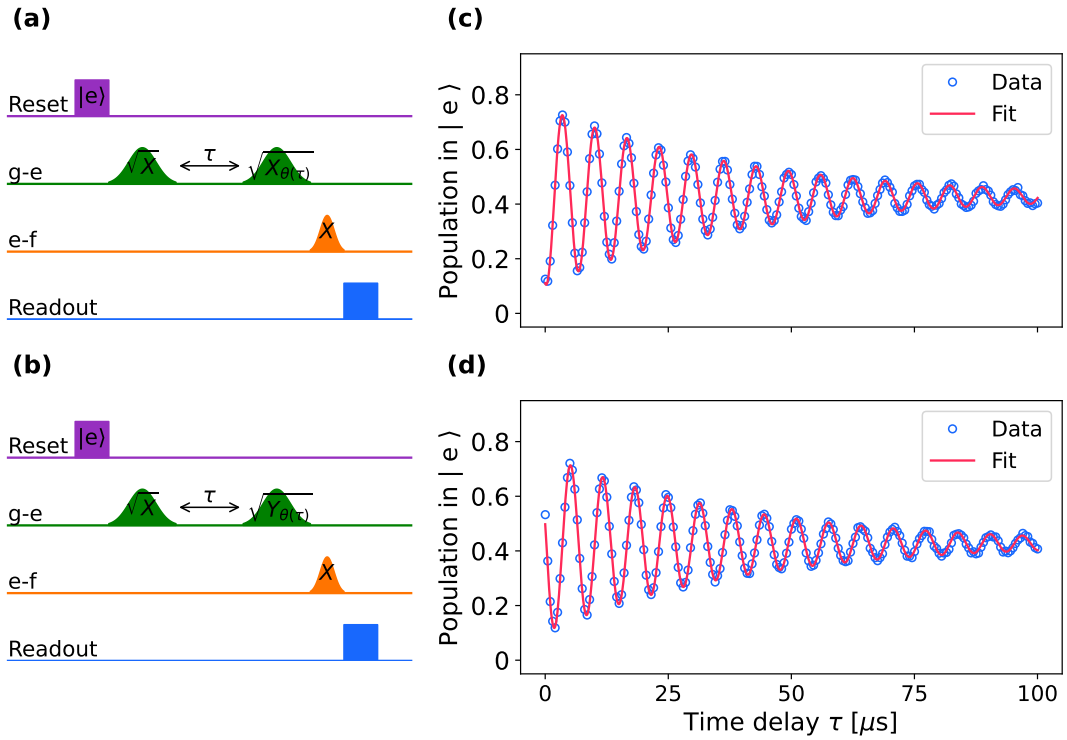

Fig. 6.7 ***g-e T2 Ramsey:*** *Measurement of the decoherence time of the $|g\rangle \rightarrow |e\rangle$ transition. (a) Pulse sequence used for the experimental realization: The qubit is initially prepared in state $|e\rangle$, and then, the first $\pi/2$-pulse ($\sqrt{X}$) between $|g\rangle$ and $|e\rangle$ is applied, and after a delay time τ, the second $\pi/2$-pulse between $|g\rangle$ and $|e\rangle$ is applied, however, this second pulse has a phase difference $\theta(\tau)$ with respect the first one, such that $\theta = \delta_0\tau$, thus, the second pulse is labeled as $\sqrt{X_{\theta(\tau)}}$. Alternatively, (b) an additional phase difference of $\pi/2$ is added to the second $\pi/2$-pulse, effectively probing the y-axis of the Bloch sphere, thus, the second pulse is labeled as $\sqrt{Y_{\theta(\tau)}}$. Finally, the qubit state is projectively measured by first applying a π-pulse between $|e\rangle$ and $|f\rangle$ and then probing the resonator with the readout pulse. The population of the state $|e\rangle$ at the end of the pulse sequence in the case of the pulses $\sqrt{X}$ and $\sqrt{X_{\theta(\tau)}}$ is shown in (c), while the population of the state $|e\rangle$ at the end of the pulse sequence in the case of the pulses $\sqrt{X}$ and $\sqrt{Y_{\theta(\tau)}}$ is shown in (d). The blue empty circles represent the measured data, while the red solid lines are obtained by fitting the data with a complex spiral times an exponential decay. The fitted T2 Ramsey of the $|g\rangle \rightarrow |e\rangle$ transition is* 39.7 µs.

We perform the measurement sequence twice for each value of the delay time τ, each iteration corresponds to a different value of the initial phase difference θ_0 between the pulses.

The two values of θ_0 are shifted with respect to each other by $\pi/2$. In this way, we effectively probe two orthogonal axis on the Bloch sphere. The Figure 6.7 shows the results of the Ramsey spectroscopy at the flux frustration point. We fit the obtained results with a complex spiral, which is nothing but a rotation in the complex plane times an exponential decay. The fitted decay time, corresponding to the decoherence time T_2^* of the qubit, was 39.7 µs. Notably, the measured coherence is not too far from the upper limit of $2T_1$, suggesting a pure dephasing rate of $\Gamma_\varphi = 1/2T_1 - 1/T_2^* = (97\,\mu\text{s})^{-1}$.

6.5 Ramsey spectroscopy vs external flux

The final step of the qubit characterization is the measurement of the coherence time T2 around the flux frustration point. We recall the fluxonium circuit is supposed to be insensitive to first-order flux fluctuations at the flux frustration point. For this purpose, we perform the experimental sequence described in section 6.2, for different values of the external flux φ_{ext} in a vicinity around the flux frustration point. We fitted the data corresponding to each value of the external flux obtaining a relation between the qubit frequency and decoherence time as function of the external flux. The Figure 6.8 shows the measurement results. We can distinguish two clear regions in the plot according to the behaviour of the curves. On the one hand, we notice that, in a very small vicinity around the flux frustration point, the qubit frequency remains almost constant as function of the external flux, with a local minimum at the flux frustration point. On the contrary, within this same region around the flux frustration point, the decoherence time varies abruptly as function of the external flux reaching a local maximum at the flux frustration point. On the other hand, when the external flux shifts away from the flux frustration point, the qubit frequency varies almost linearly as function of the external flux. Nonetheless, the decoherence time varies very slowly as function of the external flux away from the flux frustration point.

We can infer from these results that the qubit dephasing away from the flux frustration point takes place via two mechanisms. Therefore, we can express the total dephasing rate $1/T2$ as the sum of the dephasing rates of the two mechanisms. We can attribute one of the dephasing mechanisms to the imperfect qubit preparation because of unwanted and uncontrollable external flux fluctuations. This means that if the target operation point is $\varphi_{\text{ext}} = \varphi_0$, the effective operation point for a particular measurement iteration is actually $\varphi_{\text{ext}} = \varphi_0 + \delta\varphi$, with $\delta\varphi$ being a random variable for each measurement iteration, in consequence, the qubit frequency is also a random variable for each measurement iteration. This means that the measured data corresponding to two measurement iterations have a random phase difference $\delta\theta$ with respect to each other. When the measured data of all the iterations is averaged, at a fixed operation point, the random phases add up and the signal contrast is reduced. Moreover, the phase difference $\delta\theta$ increases with the delay time τ, thus, the signal contrast becomes worse the longer the delay time τ. This dephasing mechanism is less dominating at the operation points where the qubit frequency varies less as function of the external flux. Therefore, when the qubit is operated at the flux frustration point, where the qubit frequency is minimal, the dephasing related to external flux fluctuations is also minimal.

The results of the Ramsey spectroscopy vs external flux confirm that the flux frustration point is the optimal point for operation the low frequency qubit.

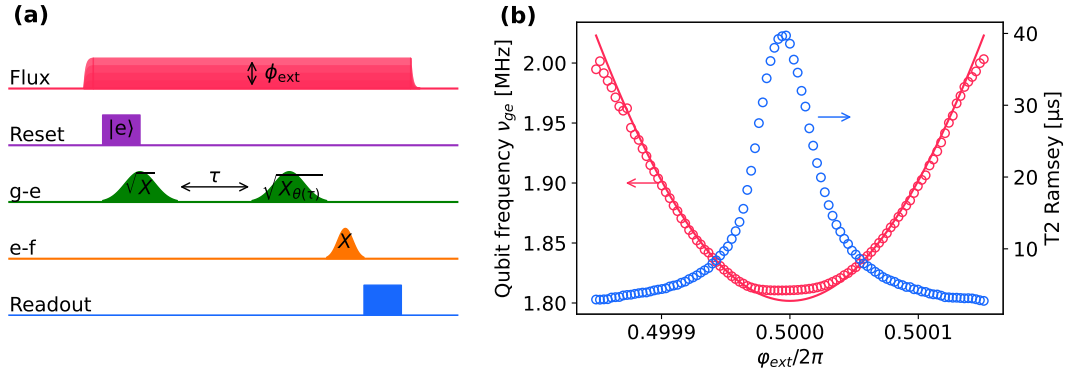

Fig. 6.8 ***T2 g-e vs external flux:*** *(a) Pulse sequence used for the experimental realization: Firstly, the external flux φ_{ext} is set to a given value, and then, the qubit is initially prepared in $|e\rangle$, next, the first $\pi/2$-pulse ($\sqrt{X}$) between $|g\rangle$ and $|e\rangle$ is applied, and after a delay time τ, the second $\pi/2$-pulse ($\sqrt{X_{\theta(\tau)}}$) between $|g\rangle$ and $|e\rangle$ is applied with a phase difference $\theta(\tau)$ with respect the first one, finally, the qubit state is projectively measured by first applying a π-pulse between $|e\rangle$ and $|f\rangle$ and then probing the resonator with the readout pulse. (b) Qubit frequency (red) and decoherence time T2 (blue) as function of the external flux φ_{ext}. Both the frequency and T2 of the qubit are obtained by fitting the measured Ramsey fringe, corresponding to each value of the external flux φ_{ext}, with a complex spiral with an exponential decay. The red solid line is a plot of the qubit frequency as function of the external flux obtained from the fluxonium hamiltonian whose parameters were previously determined.*

Chapter 7

AC-charge sensitivity of the low-frequency qubit

The superconducting-circuits platform offers the possibility of designing artificial quantum systems with desired properties for interesting applications. A typical superconducting circuit is engineered to have a sufficiently an-harmonic transition to be used as a qubit, which can be easily manipulated and read-out thanks to its strong (dipolar) interaction with electromagnetic fields. The property of having a strong dipole moment is particularly interesting for interfacing a superconducting circuit with other quantum systems. For instance, fluorescence from individual electronic spins was successfully detected using a superconducting qubit-based microwave-photon detector [79] operating close to 7 GHz. Additionally, in the realm of circuit quantum acousto-dynamics (cQAD), the coupling between a qubit and a piezoelectric resonator is used to detect and manipulate the phononic state, typically within the 2-10 GHz range [6, 23, 59, 67]. However, adapting these sensing schemes to lower frequencies, below the conventional operating frequency of superconducting qubits, introduces distinct challenges. First, superconducting qubits are read out thanks to the dispersive shift imparted to a nearby superconducting resonator. As the dispersive shift quickly drops for a cavity detuning exceeding the qubit anharmonicity, weakly anharmonic qubits, such as transmons, would require nearly resonant resonators with dimensions scaling inversely with the frequency (as an illustration, a 1 MHz $\lambda/2$-coplanar cavity requires a 100-m-long waveguide). Second, low-frequency systems are coupled to a hot thermal bath with which they exchange photons randomly, quickly turning pure quantum states into statistical mixtures. In recent years, significant progress has been made in overcoming these challenges. Notable contributions include the development of a 14 MHz heavy fluxonium qubit with a long coherence time and fast manipulation through fast-flux gates [81]. Furthermore, operation of a fluxonium qubit dispersively coupled to a 690 MHz piezoelectric mechanical system was demonstrated earlier this year [47].

The fact that the qubit transition has a frequency of $\omega_{ge}/2\pi \approx 1.8$ MHz is interesting for applications in the field of hybrid quantum systems. For example, it could be resonantly coupled to a high quality factor mechanical resonator such as a phononic crystal defect mode (see Figure 7.1a). Typical parameters in such mechanical resonators are: frequencies of the order of few MHz and quality factors of the order of 10^8 at cryogenic temperatures [43, 61].

This device is a thin square silicon nitride film with 1 mm long edges and that is 100 nm thick. It is patterned with a periodic array of holes such that out of plane modes see a large bandgap, which is a frequency range where the system does not have any mode. By breaking the symmetry of the crystal in the center of the structure, a single mode appears within the bandgap. It is spatially localized at the center of the structure (see Figure 7.1b), such that the amplitude of the mode is exponentially decreasing from the center, towards the edges of the membrane. This helps minimizing the bending losses due to the very high curvature of the membrane at the edges, where the connection between the film and the substrate forces the membrane motion to zero. At the same time, the localized defect mode is also protected from environmental noise (see Figure 7.1c and 7.1d). This device is promising for building quantum memories with record times, of the order of few seconds. Moreover, silicon nitride phononic crystal membranes are promising candidates for testing the Penrose gravitational collapse due to its long coherence time and large zero-point fluctuations [36].

The coupling between a SiN membrane and a fluxonium can be achieved by metallizing the SiN membrane, and bring the defect pad in the vicinity of the fluxonium capacitor electrode, making some sort of parallel plate capacitor where the spacing is modulated by the membrane oscillations. In this way, if the membrane is DC-biased, the motion of the membrane produces a charge modulation on the fluxonium capacitor electrode. In the absence of membrane, we can emulate the motion of the membrane by imposing a voltage modulation on the charge-drive electrode of the circuit. For instance, it was used in Section 6.2 to drive Rabi oscillations of the qubit states. Note that the fluxonium qubit not only has a low frequency, but it also features a large charge matrix element $|\langle g|N|e\rangle|$ with respect to the qubit transition frequency ω_{ge}, such that its sensitivity to a charge modulation is extreme. In this chapter we evaluate the sensitivity of the fluxonium to a nearly resonant AC-charge drive. We start by discussing the theoretical advantages of the fluxonium qubit over other qubit implementations, and then, we introduce a practical scheme for detecting a weak AC-charge modulation. We show that our device allows the detection of charge modulations of the order of 10^{-2} Cooper pairs, on a capacitance of the order of 20 fF.

7.1 The fluxonium qubit for sensing weak charge modulations

The fluxonium qubit can be used as a charge sensor. Indeed, a charge modulation induces a Rabi oscillation of the qubit, as seen in Section 1.3.4. The amplitude of the charge modulation can be inferred from the measured Rabi frequency. Since the qubit has a finite relaxation time T_1, the ultimate sensitivity is reached when the charge modulation induces a single Rabi flop during T_1. In more details, let us consider a single-mode qubit with a capacitive energy given by $4E_C\left(N-n_g(t)\right)^2$, which interacts with a classical offset charge $n_g(t)=N_\mathrm{d}\cos(\omega_\mathrm{d}t)$. For small charge modulations $N_\mathrm{d}\ll 1$, the Hamiltonian can be linearized according to the rotating-wave approximation (RWA). In a frame rotating at the drive frequency, the hamiltonian writes:

$$\mathscr{H}_\mathrm{int}=-8E_C N_\mathrm{d}\,\langle e|N|g\rangle\,\sigma_x \tag{7.1}$$

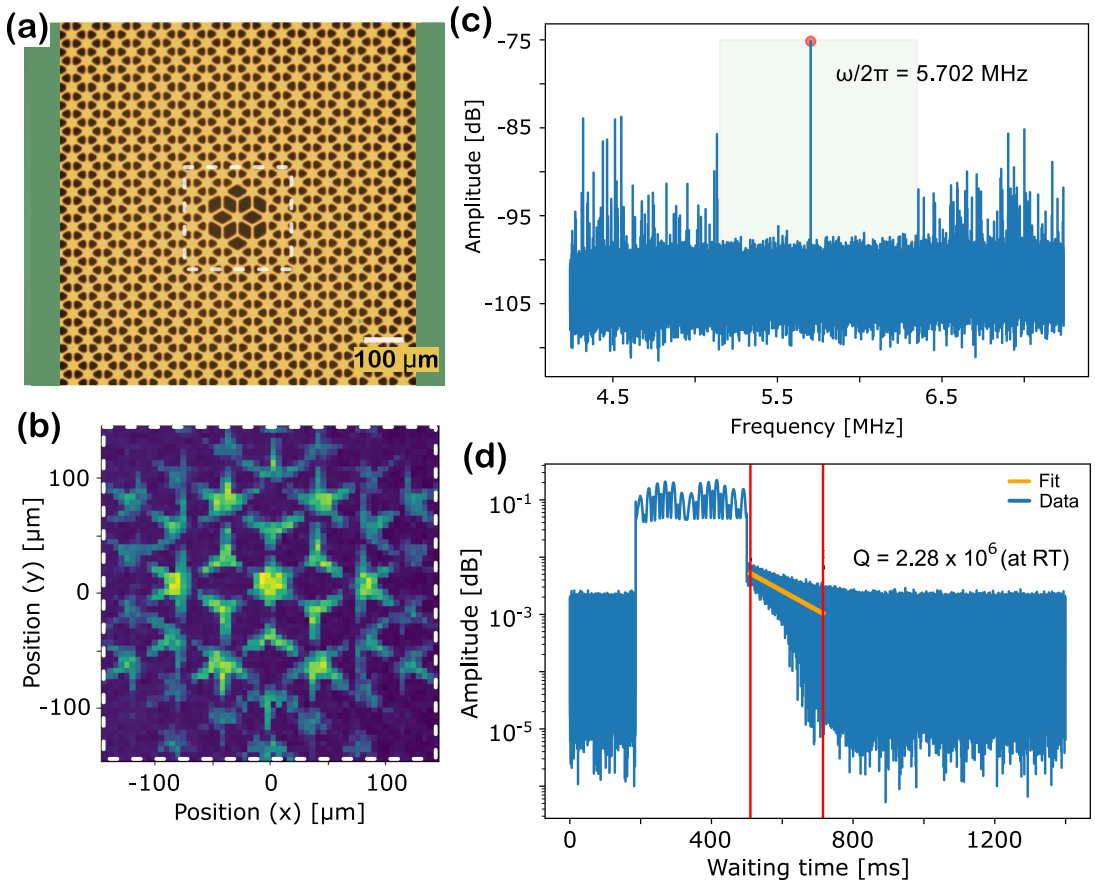

Fig. 7.1 ***Phononic membrane resonator:*** *(a) Micrograph of a phononic-crystal membrane resonator suspended over a silicon substrate (green). The membrane is made of silicon nitride (yellow) with a thickness of about 90 nm. It has a phononic crystal pattern with a defect in the middle (withe dashed-line), resulting in a mode that is both localized in space and frequency (red dot in panel c). (b) Displacement profile of the defect mode, the contrast represents the amplitude of the out-of-plane displacement probed at the mode frequency 5.702 MHz. The x and y axes are in units of position over the membrane surface (panel a). (c) Membrane spectrum probed at the defect center. (d) Ring-down measurement of the defect mode at room temperature, giving a quality factor of 2.28 ×10⁶. This membrane was fabricated and characterized in our lab, but more information about the lotus membrane is provided in [61].*

Using the relation between charge and flux matrix elements, i.e., $8E_C|\langle e|N|g\rangle| = \hbar\omega_{ge}|\langle e|\varphi|g\rangle|$ [53], we derive the Rabi frequency

$$\Omega_\mathrm{r} = 2N_\mathrm{d}\omega_\mathrm{ge}|\langle e|\varphi|g\rangle| \tag{7.2}$$

In a resonant coupling scenario, where the drive frequency ω_d is imposed by the resonance of an auxiliary system to probe, the qubit frequency needs to fulfill $\omega_{ge} = \omega_\mathrm{d}$. In such a situation, maximizing the third factor $|\langle e|\varphi|g\rangle|$ is crucial. Indeed, only this term depends on the specifics of the qubit implementation, while the first two terms N_d and ω_{ge} are characteristics of the auxiliary system to be detected. For instance, in cQAD, the frequency ω_d is

set by the mechanical resonance frequency, whereas the amplitude N_d depends on the details of the mechanical-electrical transduction. In this case, we expect an AC-charge modulation of $N_\mathrm{d} \sim 10^{-2}$ at a resonance frequency of $\omega_\mathrm{d}/2\pi = \Omega_\mathrm{m}/2\pi \approx 2$ MHz (see section 7.1.1). While the matrix element $|\langle e|\varphi|g\rangle|$ is typically suppressed exponentially in the heavy fluxonium regime, a radically different scenario emerges at the flux-frustration point. Here, the wavefunctions recover a large overlap $|\langle e|\varphi|g\rangle| \approx \pi$. This value compares favorably with weakly anharmonic qubits, where $|\langle e|\varphi|g\rangle| \sim (2E_C/E_J)^{1/4} \ll 1$, or even the Cooper-pair box $|\langle e|\varphi|g\rangle| \sim 4E_C/E_J \sim 1$. In essence, the unique characteristics of fluxonium eigenstates at the flux-frustration point, manifesting as Schrödinger cat-like superpositions of persistent current states, endow it with a larger charge sensitivity compared to a transmon or Cooper-pair box operating at the same transition frequency.

In Figure 6.4 of Section 6.2, we directly drive the qubit, biased at $\varphi_\mathrm{ext} = \pi$, with a MHz pulse on the charge drive. We observe a Rabi oscillation pattern with maximum contrast for $\omega_\mathrm{d} = \omega_{ge} = 1.8$ MHz. In a similar experiment, the frequency of the driving pulse was set equal to the qubit frequency, $\omega_\mathrm{d} = \omega_{ge}$, while its amplitude V_d was varied. The Figure 7.2a shows the results of this measurement, each column corresponds to a measured Rabi fringe for one value of the driving pulse amplitude V_d. Then, we fit the measured data with an decaying-cosine function obtaining one Rabi frequency Ω_r for each value of the driving amplitude V_d. The half-periods of the Rabi fringes are well fitted by α/V_d (see black dashed line in Figure 7.2a), representing a linear relation between the Rabi frequency Ω_r and the driving pulse amplitude V_d. The Figure 7.2b shows the measured Rabi frequency $\Omega_\mathrm{r}/2\pi$ as function of amplitude of the driving pulse in terms of either volts V_d (top axis) or number of Cooper-pairs N_d (bottom-axis). The value of N_d corresponding to Ω_r is calculated with Equation 7.2. As expected, we observe a linear relation between the Rabi frequency and the drive amplitude (in terms of N_d or V_d, respectively), up to $\Omega_\mathrm{r}/2\pi \approx 1$ MHz. This result agrees wtht the rotating-wave approximation (RWA) which is valid in the weak-driving-amplitude regime, $\Omega_\mathrm{r} \ll \omega_{ge}$.

We deduce from Equation 7.2 the minimum charge modulation N required to observe a single Rabi flop within T_1:

$$N_\mathrm{min} = \frac{2\pi}{|\langle e|\varphi|g\rangle|\omega_\mathrm{ge}T_1} \approx 5 \times 10^{-3} \quad \text{(Cooper pairs)} \tag{7.3}$$

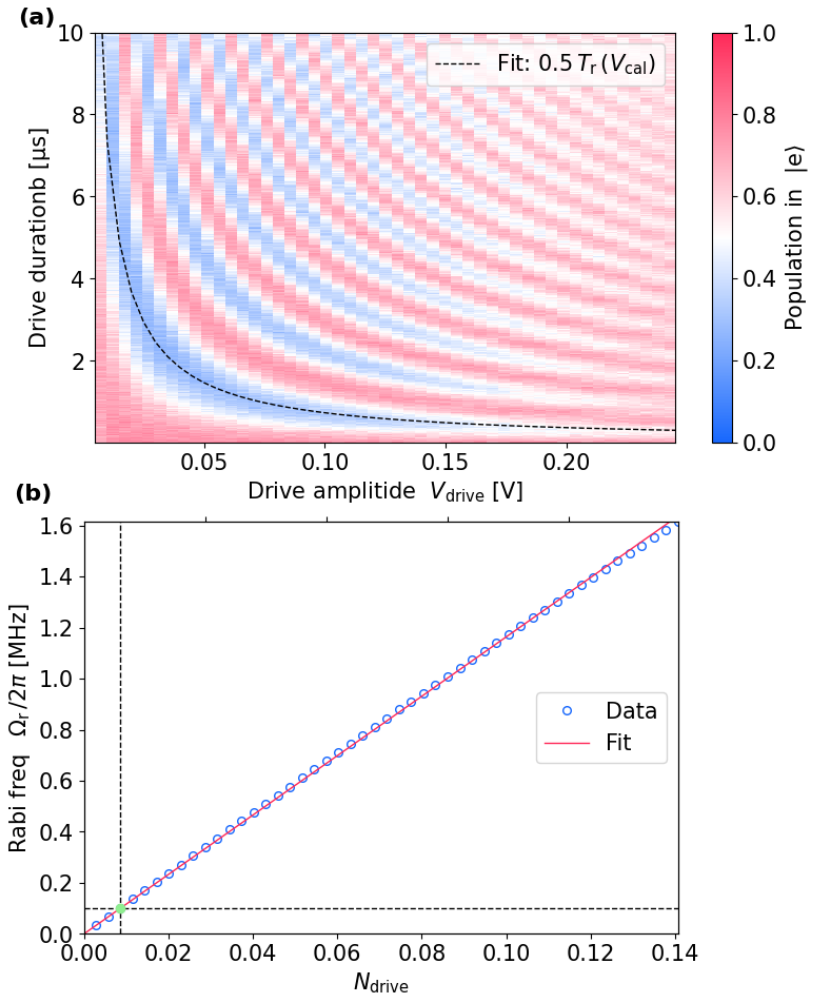

Fig. 7.2 ***Calibration of the Rabi frequency vs charge drive amplitude:*** *(a) Rabi spectroscopy of the qubit transition. The color of each pixel represents the rabi-fringe contrast for a given driving pulse duration (y-coordinate) and amplitude (x-coordinate). In this way, a given column corresponds to rabi oscillation of the qubit at a fixed driving amplitude. The measured data are fitted column by column using a decaying-cosine function. The fit yields the rabi oscillations frequency $\Omega_r/2\pi$ corresponding to the driving amplitude of each column V_d. (b) Qubit Rabi frequency $\Omega_r/2\pi$ as a function of the charge driving amplitude V_d: The data (blue open circles) is fitted with a linear function (red solid line), resulting in a relation between Rabi frequency $\Omega_r(V_d)$ as a function of the charge driving amplitude V_d. Finally, the amplitude of the charge drive in terms of Cooper-pairs number N_d as function of the Rabi frequency $\Omega_r/2\pi$ is obtained by considering that $\Omega_r/2 \approx \pi\omega_{ge}N_d$ (see Equation 7.2). The green dot represents the chosen amplitude of the calibration tone V_{cal} for the AC-charge sensing experiment.*

The ability to manipulate the qubit state with less than one percent of a Cooper-pair shows the extreme sensitivity of the fluxonium to a resonant AC-charge modulation. For instance, this value would be sufficient to reach the strong-coupling regime with a DC-biased mechanical membrane in a resonant coupling scenario as we will discuss in Section 7.1.1. The aforementioned value of 5×10^{-3} Cooper pairs corresponds to a single shot charge sensitivity of 10^{-2} e. However, through the implementation of quantum sensing protocols, like those routinely used in nitrogenvacancy-center magnetometry [13] and similar methodologies [**?**], we are able to accrue substantial statistical data. This allows us to measure charge sensitivity within a one second integration period and subsequently compare these findings with other charge sensing methods.

7.1.1 The meca-fluxonium

In this section, we assess the possibility for the heavyfluxonium to reach the strong-coupling regime with a state-of-the art macroscopic electromechanical systems. For this, we estimate the magnitude of the charge modulation induced by the zero-point fluctuations of a DC-biased vacuum-gap capacitor (see Figure 7.3). In this scenario, we consider that the out-of-plane vibrations of a silicone-nitride membrane modulate the capacitance between two parallel electrodes subjected to a DC bias voltage V_g. Table I summarizes the main geometric parameters of the membrane. The membrane lateral dimensions are chosen such that the fundamental mechanical mode matches the qubit frequency ω_{ge} [80]. The area of the electrodes are chosen to obtain a capacitance $C = 50\,\mathrm{fF}$ matching the value reported in our fluxonium implementation. We assume an electrode separation $\mathrm{w} = 500$ nm, which is a conservative estimate based on flip-chip assemblies already reported in the literature [69].

Membrane length	l	$150\,\mu\mathrm{m}$
Defect-mode frequency	Ω_m	$1.8\,\mathrm{MHz}$
Mode effective mass	m	$3\,\mathrm{ng}$
Zero-point fluctuations	x_zpf	$7\,\mathrm{fm}$
Capacitor plates separation	w	$500\,\mathrm{nm}$
Capacitor plates surface	S	$(90\,\mu\mathrm{m})^2$

Table 7.1: **Estimated parameters of the electro-mechanical system.**

The mechanical resonator undergoes the sum of the restoring force and the electrostatic force:

$$F = m\Omega_m^2\,(\mathrm{w} - z) - \frac{V_g^2\,\epsilon_0 S}{z^2} \tag{7.4}$$

We can estimate the regime of mechanical stability as $V_g < \sqrt{m\Omega_m^2 \mathrm{w}^3/\epsilon_0 S} \approx 50$ V. If we assume a conservative bias voltage $V_g = 5$ V, we obtain

$$N_\mathrm{zpf} = \frac{V_g}{2e}\,x_\mathrm{zpf}\frac{dC}{dx} \approx 0.01 \quad (\text{Cooper pairs}) \tag{7.5}$$

where $x_\mathrm{zpf} = \sqrt{\hbar/(2m\,\Omega_m)}$ is the amplitude of the zero-point fluctuations of the mechanical motion, and $\frac{dC}{dx} \approx C/\mathrm{w}$. The term N_zpf represents the amplitude of the charge fluctuations induced on the small junction of the fluxonium due to the fluctuations of the membrane

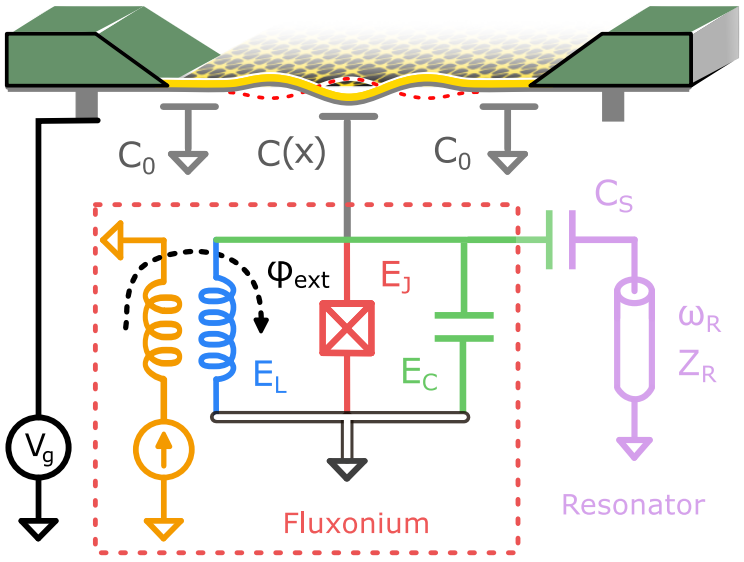

Fig. 7.3 ***Schematics of the mecha-fluxonium.***

position x_{zpf}. Notice that N_{zpf} is larger than the minimal value that is needed to observe Rabi oscillations N_{min} (Equation 7.3), which is set by the relaxation time of the qubit T_1. Thus, this simple calculation with a realistic set of parameters suggests that is possible to use the fluxonium qubit as a sensor for the membrane motion, and in particular, the strong coupling regime between the fluxonium and the membrane can be achieved in principle.

7.2 Frequency-resolved AC-charge sensing experiment

In Section 7.1, we have performed an experiment to measure the sensitivity of the fluxonium qubit to an external charge modulation (see Figure 7.2). Nonetheless, this scheme has two main limitations: In the first place, we intentionally set the frequency of the driving tone ω_{d} emulating the charge modulation equal to the qubit transition frequency ω_{ge}. This maximized the contrast of the Rabi oscillations, thus, maximizing the qubit sensitivity to the charge modulation. In a realistic scenario where the qubit is used as a probe, the frequency of the charge modulation ω_{d} is an arbitrary parameter which is not controlled. In fact, we would be interested in determining both the amplitude and the frequency of the charge modulation in a single experiment. However, the simple scheme used in Section 7.1 does not provide transparent information about the frequency of the charge modulation ω_{d}. In principle, by sweeping the qubit frequency ω_{ge} around the frequency of the charge modulation ω_{d}, we can obtain a map of the frequency of the Rabi oscillations Ω_{r} as a function of the detuning $\Delta = \omega_{ge} - \omega_{\mathrm{d}}$, a so-called Rabi chevron as the one shown in Figure 6.4. By fitting this map $\Omega_{\mathrm{r}}(\Delta)$, we could infer both parameters of the charge modulation. Although the frequency of the qubit ω_{ge} indeed can be tuned by adjusting the external flux φ_{ext} threading the fluxonium loop (see Figure 5.3), this is not practical since at each iteration we would need to adjust the parameters of the pulses that are used to manipulate the qubit. Additionally, the coherence properties of the qubit change drastically outside the flux frustration point

$\varphi_{\text{ext}} = \pi$ (see Figure 6.8), the ideal point for operating the qubit.

This section describes the implementation of a method for detecting both the frequency and the amplitude of a weak AC-charge modulation with using the fluxonium qubit as the probe. In a quantum sensing experiment, we can leverage the ability to swiftly prepare and read out the qubit state to detect a weak charge signal through repeated interaction with the two-level system. This involves preparing the qubit in $|g\rangle$, after which it interacts for an interrogation time τ_{I} with the weak continuous signal to be detected (referred to as the "calibration tone" henceforth), of frequency ω_{cal}, applied to the charge port. For weak enough calibration tone, the Bloch-vector undergoes a small rotation away from the south pole. We then probe this displacement by mapping the transverse component of the Bloch-vector to the σ_z basis with a $\pi/2$-pulse, before performing a single-shot readout of the qubit in the $\{ |g\rangle, |e\rangle \}$ basis. In this scheme, the probability to detect the qubit in $|e\rangle$ slightly deviates from 1/2, by an amount that depends on the phase and amplitude of the calibration tone. Furthermore, the mismatch $\Delta = \omega_{ge} - \omega_{\text{cal}}$ between the calibration tone and qubit frequencies gives rise to a shot-to-shot rotation of the Bloch-vector by an angle $\theta_k = k\Delta\tau_{\text{M}}$, where k is the repetition index and τ_{M} the repetition period of the experiment. Even though each measurement result $m_k \in \{0, 1\}$ only contains one bit of information, the complete measurement record $\{m_k\}_{0 \leq k < N_{\text{tot}}}$ can be used to reconstruct the spectrum of the charge modulation by the periodogram method [2]. Performing the $\pi/2$-rotation along an unique axis would lead to an ambiguity between positive and negative detuning Δ. We thus perform the $\pi/2$-rotation of the qubit along an axis picked up sequentially in the set {+X, +Y , -X, -Y }. This ensures a non-ambiguous correspondence between discrete and continuous time frequencies over the interval $[-\Omega_{N_y}/2, +\Omega_{N_y}/2]$, where Ω_{N_y} is the Nyquist angular frequency $\Omega_{N_y} = \pi/\tau$. In the end, the series of 0 and 1 that is obtained from this protocol contains information on both the amplitude and the frequency of the charge modulation produced by the calibration tone.

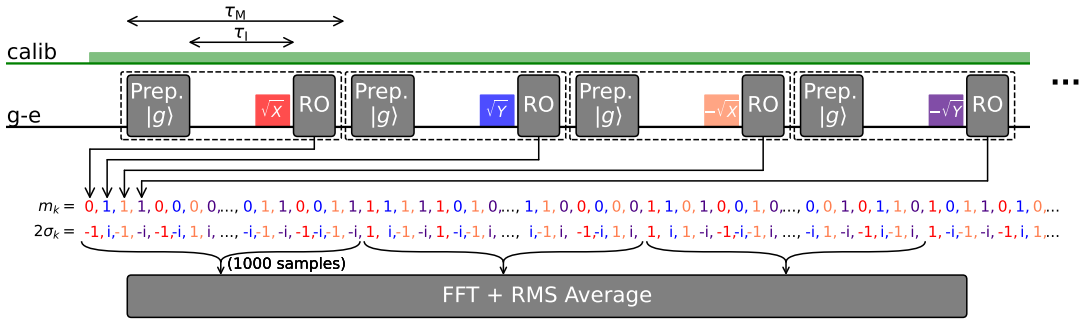

Fig. 7.4 ***Experimental protocol:*** *A weak monochromatic charge-drive (also referred to as calibration tone) is detected thanks to a repeated pulse sequence: The qubit is prepared in* $|g\rangle$*. After interacting for a time* τ_{I} *with the tone, a partial information on the qubit state is obtained by performing a* $\pi/2$ *pulse in one of the 4 directions* $\{+X, +Y, -X, -Y\}$*, followed by a qubit state readout in the ge basis. From the measurement samples* $m_k \in \{0, 1\}$*, a complex telegraphic signal* $\sigma_k = i^k(m_k - 1/2)$ *is constructed. The noise spectrum centered around the qubit frequency is estimated by Bartlett's-method, with periodograms of 1000 non-overlapping consecutive samples.*

Then, by performing a Fourier transform of these results, we can turn the fluxonium qubit into a quantum spectrum analyzer that allows to reconstruct the power spectral density of the charge modulation. This last one is thus obtained by performing fast-Fourier-transforms over consecutive windows of $N = 1000$ consecutive samples. The calibration tone is finally visible as a sinus-cardinal-shaped peak, centered around ω_{cal} and of width $\Omega_{\mathrm{RBW}} = 2\pi/N\tau$. This value is the residual bandwidth of our quantum spectrum analyzer, and it can be tuned by adjusting the window length (the samples per window N).

7.2.1 Qubit evolution during the interrogation time

We first model the evolution of the qubit during the interrogation time, by taking into account the interaction with the calibration-tone, which has a Rabi-frequency Ω_{r} and a finite detuning $\Delta = \omega_{ge} - \omega_{\mathrm{cal}}$. Since the qubit is coupled to a thermal bath with a large occupation, we choose an equal rate Γ for the loss and gain of qubit excitations. From the empirical finding $T_1 \approx T_2$ (see Figure 3), we also assume a dephasing rate $\Gamma_\varphi \approx \Gamma/2$. The full evolution of the qubit's density matrix ρ is thus, in a frame rotating at the drive frequency:

$$\begin{aligned}\frac{d}{dt}\rho = -\frac{i}{\hbar}\left[\mathscr{H},\, \rho\right] &+ \Gamma\left[\sigma_-^\dagger \rho\, \sigma_- - \frac{1}{2}\left(\sigma_-\sigma_-^\dagger\rho + \rho\,\sigma_-\sigma_-^\dagger\right)\right] \\ &+ \Gamma\left[\sigma_+^\dagger \rho\, \sigma_+ - \frac{1}{2}\left(\sigma_+\sigma_+^\dagger\rho + \rho\,\sigma_+\sigma_+^\dagger\right)\right] \\ &+ \Gamma\left[\sigma_z^\dagger \rho\, \sigma_z - \frac{1}{2}\left(\sigma_z\sigma_z^\dagger\rho + \rho\,\sigma_z\sigma_z^\dagger\right)\right]\end{aligned} \tag{7.6}$$

Where the qubit Hamiltonian is $\mathscr{H} = \hbar\Delta/2\sigma_z + \hbar\Omega_{\mathrm{r}}/2\sigma_x$. We proceed by calculating the Bloch equations for the 3 components of the qubit pseudo-spin:

$$\begin{aligned}\frac{d}{dt}\langle\sigma_x\rangle &= -\Delta\langle\sigma_y\rangle - 2\Gamma\langle\sigma_x\rangle \\ \frac{d}{dt}\langle\sigma_y\rangle &= -\Omega_{\mathrm{r}}\langle\sigma_z\rangle + \Delta\langle\sigma_x\rangle - 2\Gamma\langle\sigma_y\rangle \\ \frac{d}{dt}\langle\sigma_z\rangle &= +\Omega_{\mathrm{r}}\langle\sigma_y\rangle - 2\Gamma\langle\sigma_z\rangle\end{aligned} \tag{7.7}$$

This equations describe two simultaneous rotations, one around the z-axis with angular frequency Δ and the other one around the x-axis with angular frequency Ω_{r}, and the isotropic relaxation of the pseudo-spin components towards the origin of the Bloch sphere at a rate Γ. We consider the qubit to be in state $|g\rangle$ as the initial condition, i.e., $\langle\sigma_x\rangle = -1$ and $\langle\sigma_z\rangle = \langle\sigma_y\rangle = 0$. Solving the Bloch equations with the mentioned initial condition leads to:

$$\begin{aligned}\langle\sigma_x\rangle(t) &= e^{-2\Gamma t}\left(\cos\left(t\sqrt{\Omega_{\mathrm{r}}^2+\Delta^2}\right) - 1\right)\frac{\Omega_{\mathrm{r}}\Delta}{\Omega_{\mathrm{r}}^2+\Delta^2} \\ \langle\sigma_y\rangle(t) &= e^{-2\Gamma t}\sin\left(t\sqrt{\Omega_{\mathrm{r}}^2+\Delta^2}\right)\frac{\Omega_{\mathrm{r}}}{\sqrt{\Omega_{\mathrm{r}}^2+\Delta^2}} \\ \langle\sigma_z\rangle(t) &= -e^{-2\Gamma t}\left(\Delta^2 + \Omega_{\mathrm{r}}^2\cos\left(t\sqrt{\Omega_{\mathrm{r}}^2+\Delta^2}\right)\right)\frac{1}{\Omega_{\mathrm{r}}^2+\Delta^2}\end{aligned} \tag{7.8}$$

At the end of the interrogation time τ_{I}, the projection of the Bloch vector on the xy-plane is:

$$|2\,\langle\sigma_{\perp}\rangle\,| = \sqrt{\langle\sigma_x\rangle^2 + \langle\sigma_y\rangle^2} = \Omega_{\mathrm{r}}\,\tau_{\mathrm{I}}\,e^{-2\Gamma\,\tau_{\mathrm{I}}}\,f(\Delta) \tag{7.9}$$

The coefficient $f(\Delta)$ is the response function of the detector, that is given by

$$f(\Delta) = \sqrt{\frac{\Delta^2\,\mathrm{sinc}\left(\frac{\tau_{\mathrm{I}}}{2\pi}\sqrt{\Omega_{\mathrm{r}}^2+\Delta^2}\right)^2 + \Omega_{\mathrm{r}}^2\,\mathrm{sinc}\left(\frac{\tau_{\mathrm{I}}}{\pi}\sqrt{\Omega_{\mathrm{r}}^2+\Delta^2}\right)^2}{\Omega_{\mathrm{r}}^2+\Delta^2}} \tag{7.10}$$

The quantity $|\,\langle\sigma_{\perp}\rangle\,|$ can be think of as the contrast that we would observe in a Rabi spectroscopy, where driving pulse has an amplitude Ω_{r}, duration τ_{I}, and frequency $\omega_{\mathrm{d}} = \omega_{ge} - \Delta$. In the limit $\Delta \gg \Omega_{\mathrm{r}}$, the detector response function simplifies to

$$f(\Delta) \approx \mathrm{sinc}\left(\frac{\Delta}{\Omega_{\mathrm{full}}}\right) \tag{7.11}$$

Where the bandwidth is defined as $\Omega_{\mathrm{full}} =: 2\pi/\tau_{\mathrm{I}}$, and $\mathrm{sinc}(x) = \sin(\pi x)/\pi x$. The Equation 7.11 means that the qubit is not sensitive to the noise that is away from its central frequency ω_{ge} by more than Ω_{full}.

7.2.2 Signal processing

At the end of the interrogation time, a projective measurement of one of the transverse components of the pseudo-spin is performed in the qubit frame. The discrete random variable m_k represents the outcome of the qubit-state measurement at the iteration step k. This is nothing but a "0" if the qubit is found in $|g\rangle$ or a "1" if the qubit is found in $|e\rangle$. The mean value of $\langle m_k\rangle$ is related to the transverse component of the qubit pseudo spin $\sigma_{\perp}$ as:

$$\langle m_k\rangle = \frac{1}{2} + \mathrm{Re}\left[\langle\sigma_{\perp}\rangle\,(-i)^k e^{i\Delta\tau_{\mathrm{M}}k}\right] \tag{7.12}$$

The term $(-i)^k$ encodes for the alternating measurement basis $\{+X,\,+Y,\,-X,\,-Y\,\}$. The term $e^{i\Delta\tau_{\mathrm{M}}k}$ describes the phase difference between the frames of the qubit and calibration tone. Without loss of generality, we can ignore the phase of the pseudo-spin projection $\langle\sigma_{\perp}\rangle$, and assume $\langle\sigma_{\perp}\rangle \in \mathbb{R}^+$, such that:

$$\langle m_k\rangle = \frac{1}{2} + \langle\sigma_{\perp}\rangle\,\mathrm{Re}\left[(-i)^k e^{i\Delta\tau_{\mathrm{M}}k}\right] \tag{7.13}$$

Notice that the sequence of measurement axis as function of the iteration number k (mod 4), $\{+X,\,+Y,\,-X,\,-Y\,\}$, corresponds to an effective clockwise-rotation of the lab frame with angular frequency $\omega_{\mathrm{lab}} = \pi/2\tau_{\mathrm{M}}$. Moreover, this rotation of the lab frame translates into an anti-clockwise-rotation of the pseudo-spin $\langle\sigma_{\perp}\rangle$ with angular frequency $-\omega_{\mathrm{lab}}$. Keep in mind that $\exp(-i\omega_{\mathrm{lab}}\,k\tau_{\mathrm{M}}) = \exp(-i\pi k/2) = (-i)^k$. Then, we can rewrite Equation 7.13 in a way such that this additional rotation of the pseudo-spin shows up explicitly:

$$\langle m_k\rangle = \frac{1}{2} + \frac{\langle\sigma_{\perp}\rangle}{2}\left[e^{i(\Delta-\omega_{\mathrm{lab}})\,k\tau_{\mathrm{M}}} + e^{-i(\Delta-\omega_{\mathrm{lab}})\,k\tau_{\mathrm{M}}}\right] \tag{7.14}$$

The final step in sampling the data sets is applying the following transformation:

$$\sigma_k = i^k \left(m_k - \frac{1}{2} \right) \tag{7.15}$$

Notice again that the term i^k corresponds to a clockwise rotation of the pseudo spin with angular frequency $\omega_{\text{lab}} = \pi/2\tau_{\text{M}}$. Finally, we compute the mean of the generated data σ_k:

$$\langle \sigma_k \rangle = \frac{\langle \sigma_\perp \rangle}{2} \left[e^{i\Delta\, k\tau_{\text{M}}} + e^{i(2\omega_{\text{lab}} - \Delta)\, k\tau_{\text{M}}} \right] \tag{7.16}$$

The mean of the signal σ_k is the sum of two rotations in the complex plane: one with frequency $\omega_+ = \Delta$ and the other with frequency $\omega_- = \pi/\tau_{\text{M}} - \Delta$. The spectrum of a real harmonic-oscillating function, for instance $\cos(\Delta t)$, contains two peaks in the frequency domain: one at $\omega_+ = \Delta$ and the other one at $\omega_- = -\Delta$. This means thay the spectrum is insensitive to the sign of the frequency Δ. We see in Equation 7.16 that the negative component of the signal has been shifted in the frequency domain as $-\Delta \rightarrow (2\omega_{\text{lab}} - \Delta)$, with $\omega_{\text{lab}} = \pi/2\tau_{\text{M}}$. This shift is different depending on the sign of the detuning Δ. On the one hand, if the detuning Δ is positive, both $\omega_+ = \Delta$ and $\omega_- = \pi/\tau_{\text{M}} - \Delta$ are positive, representing clock-wise rotations on the complex plane. On the other hand, if the detuning Δ is negative, both $\omega_+ = -|\Delta|$ and $\omega_- = -\pi/\tau_{\text{M}} + |\Delta|$ (mod $2\pi/\tau_{\text{M}}$) are negative, representing counter-clock-wise rotations on the complex plane. Thus, the sign of the detuning Δ can be inferred from the spectrum of the signal $\langle \sigma_k \rangle$.

Alternatively, we can write Equation 7.16 into a more friendly but less insightful form:

$$\begin{aligned} \langle \sigma_k \rangle &= \langle \sigma_\perp \rangle \cos(k\tau_{\text{M}}\, \Delta) \qquad (k \text{ even}) \\ \langle \sigma_k \rangle &= i\, \langle \sigma_\perp \rangle \sin(k\tau_{\text{M}}\, \Delta) \qquad (k \text{ odd}) \end{aligned} \tag{7.17}$$

The real and imaginary parts of the complex numbers $\langle \sigma_\perp \rangle\, e^{i\Delta t}$ are encoded pairwise on the successive samples σ_k.

7.3 Frequency-domain analysis of the signal

This section is about the analysis of the measured data in frequency domain.

7.3.1 Power spectral density estimation

The sampled data σ_k (see Equation 7.15) are grouped by windows of N = 1000 consecutive samples, the spectrum of each window is obtained via the discrete Fourier transform (DFT), yielding a set of frequencies $\{\omega_n\}$ for each window that is referred to as periodogram. In order to reduce the spacing between Fourier frequencies, the Fourier transform is performed on a 0-padded version of each window $\{z_k\}_{0 \leq k < N_p\, N}$, such that

$$\begin{aligned} z_k &= \sigma_k \quad 0 \leq k \leq N - 1 \\ z_k &= 0 \quad N \leq k < N_p\, N \end{aligned} \tag{7.18}$$

The padding factor N_p represents the number of frequency bins in each measurement bandwidths. We typically use $N_p = 5$.

We denote $\{Z_n\}_{0\leq n<N_p\,N}$ the discrete Fourier transform of the samples of a given window $\{z_k\}_{0\leq k<N_p\,N}$:

$$Z_n = \sum_{k=0}^{N_p\,N-1} z_k \, \exp\left(\frac{-i\,2\pi k\,n}{N_p N}\right) \tag{7.19}$$

In the previous expression k is related to a discrete time $t_k =: k\tau_{\mathrm{M}}$, while n is related to the frequencies ω_n obtained from the DFT. The DFT frequencies are given by

$$\omega_n = \frac{2\pi\,n}{NN_p\,\tau_{\mathrm{M}}} \pmod{2\pi/\tau_{\mathrm{M}}} \tag{7.20}$$

With $n = 0,\, 1,\, 2,\, ...\, NN_p - 1$. Notice that the index $n > NN_p/2$ correspond to a negative frequency. The Fourier frequencies $\omega_n \in (-\pi/\tau_{\mathrm{M}},\, \pi/\tau_{\mathrm{M}}]$, and any two adjacent frequencies are separated by $\delta\omega = 2\pi/NN_p\,\tau_{\mathrm{M}}$.

We evaluate $\langle Z_n\rangle$ that is obtained by averaging the spectra of all the data windows Z_n. By plugging Equations 7.16 and 7.18 into Equation 7.19, we get an expression for $\langle Z_n\rangle$:

$$\langle Z_n\rangle = \frac{\langle\sigma_\perp\rangle}{2} \sum_{k=0}^{N-1} \left[e^{i(\Delta-\omega_n)\,k\tau_{\mathrm{M}}} + e^{i(\pi/\tau_{\mathrm{M}}-\Delta-\omega_n)\,k\tau_{\mathrm{M}}}\right] \tag{7.21}$$

This expressions contains two geometric sums that can be easily simplified. Moreover, we would like to rewrite the previous expression in terms of the Nysquit frequency $\Omega_{\mathrm{Ny}} =: \pi/\tau_{\mathrm{M}}$:

$$\begin{aligned}\langle Z_n\rangle = &\frac{\langle\sigma_\perp\rangle}{2} \exp\left(i\pi(N-1)\,\frac{(\Delta-\omega_n)}{2\Omega_{\mathrm{Ny}}}\right) \frac{\sin\left(\pi\frac{N(\Delta-\omega_n)}{2\Omega_{\mathrm{Ny}}}\right)}{\sin\left(\pi\frac{(\Delta-\omega_n)}{2\Omega_{\mathrm{Ny}}}\right)} \\ &+ \frac{\langle\sigma_\perp\rangle}{2} \exp\left(i\pi(N-1)\,\frac{(\Omega_{\mathrm{Ny}}-\Delta-\omega_n)}{2\Omega_{\mathrm{Ny}}}\right) \frac{\sin\left(\pi\frac{N(\Omega_{\mathrm{Ny}}-\Delta-\omega_n)}{2\Omega_{\mathrm{Ny}}}\right)}{\sin\left(\pi\frac{(\Omega_{\mathrm{Ny}}-\Delta-\omega_n)}{2\Omega_{\mathrm{Ny}}}\right)}\end{aligned} \tag{7.22}$$

The mean of the spectrum $\langle Z_n\rangle$ is periodic with respect to the detuning Δ, with period of $4\Omega_{\mathrm{Ny}}$. Moreover, it contains two families of resonances: the first family appears at $\omega_+ = \Delta \pmod{2\Omega_{\mathrm{Ny}}}$, while the second family appears at $\omega_- = \Omega_{\mathrm{Ny}} - \Delta \pmod{2\Omega_{\mathrm{Ny}}}$. The difference between the center frequencies of the two resonances is $|\omega_+ - \omega_-| = |\Omega_{\mathrm{Ny}} - 2|\Delta||$.

Next, we proceed to analyze the behavior of $\langle Z_n\rangle$ near the first family of resonances. We consider $\omega_n = \Delta + \delta$ such that $|\delta| \ll \Omega_{\mathrm{Ny}}$. In this regime, $\langle Z_n\rangle$ can be approximated as:

$$\langle Z_n\rangle \approx N\,\frac{\langle\sigma_\perp\rangle}{2} \exp\left(i\pi\frac{(\Delta-\omega_n)}{\frac{2\Omega_{\mathrm{Ny}}}{(N-1)}}\right) \mathrm{sinc}\left(\frac{\Delta-\omega_n}{\frac{2\Omega_{\mathrm{Ny}}}{N}}\right) \tag{7.23}$$

Now we analyze the behavior of $\langle Z_n\rangle$ near the second family of resonances. We consider $\omega_n = \Omega_{\mathrm{Ny}} - \Delta + \delta$ such that $|\delta| \ll \Omega_{\mathrm{Ny}}$. In this regime, $\langle Z_n\rangle$ can be approximated as:

$$\langle Z_n\rangle \approx N\,\frac{\langle\sigma_\perp\rangle}{2} \exp\left(i\pi\frac{(\Omega_{\mathrm{Ny}}-\Delta-\omega_n)}{\frac{2\Omega_{\mathrm{Ny}}}{(N-1)}}\right) \mathrm{sinc}\left(\frac{\Omega_{\mathrm{Ny}}-\Delta-\omega_n}{\frac{2\Omega_{\mathrm{Ny}}}{N}}\right) \tag{7.24}$$

Following Bartlett's method, the power spectrum S_n is then estimated by taking the mean-value $\langle |Z_n|^2 \rangle$ over a large number of periodograms. If the two resonances are sufficiently narrow, the power spectrum of the signal, $S_n^{\text{signal}} = |\langle Z_n \rangle|^2$, can be approximated as:

$$S_n^{\text{signal}}(\Delta, \omega_n) \approx N^2 \frac{\langle \sigma_\perp \rangle^2}{4} \left[\text{sinc}\left(\frac{\Delta - \omega_n}{\Omega_{\text{RBW}}} \right)^2 + \text{sinc}\left(\frac{\Omega_{\text{Ny}} - \Delta - \omega_n}{\Omega_{\text{RBW}}} \right)^2 \right] \tag{7.25}$$

Where the residual bandwidth Ω_{RBW} is:

$$\Omega_{\text{RBW}} = \frac{2\Omega_{\text{Ny}}}{N} = \frac{2\pi}{N\tau_{\text{M}}} \tag{7.26}$$

The regime of the two resonances being narrow enough corresponds to the condition $\Omega_{\text{RBW}} \ll |\omega_+ - \omega_-| = |\Omega_{\text{Ny}} - 2|\Delta||$. The residual bandwidth Ω_{RBW} results from the sampling of the measurement data. The Figure 7.5 shows the power spectrum $S_n = \langle |Z_n|^2 \rangle$ of the measured data $\{\sigma_k\}$. We observe the two expected peaks of the signal power spectrum S_n^{signal} (Equation 7.25), at the Fourier Frequencies $\omega_+/2\pi = \Delta/2\pi$ and $\omega_-/2\pi = \Omega_{\text{Ny}}/2\pi - \Delta/2\pi$. Notice that the mean point between the peaks centers is $\Omega_{\text{Ny}}/4\pi = 7.3485$ kHz (see vertical dashed line in Figure 7.5a). The maximum frequency of the spectrum is $\nu_{\max} = \Omega_{\text{Ny}}/2\pi = 14.697$ kHz, corresponding to a measurement repetition time $\tau_{\text{M}} \approx 34.02\,\mu\text{s}$. The Figure 7.5b zooms in around the first peak, whose center frequency is $\omega_+/2\pi = 1.146$ kHz. The residual bandwidth of the peak is $\Omega_{\text{RBW}} \approx 31$ Hz. The peak is fitted according to Equation 7.25, assuming a flat noise level S_n^{noise}. The height of the peak $\max(S_n) \times 4/N^2$ is approximately the projection of the Bloch vector in the xy-plane $\langle \sigma_\perp \rangle$.

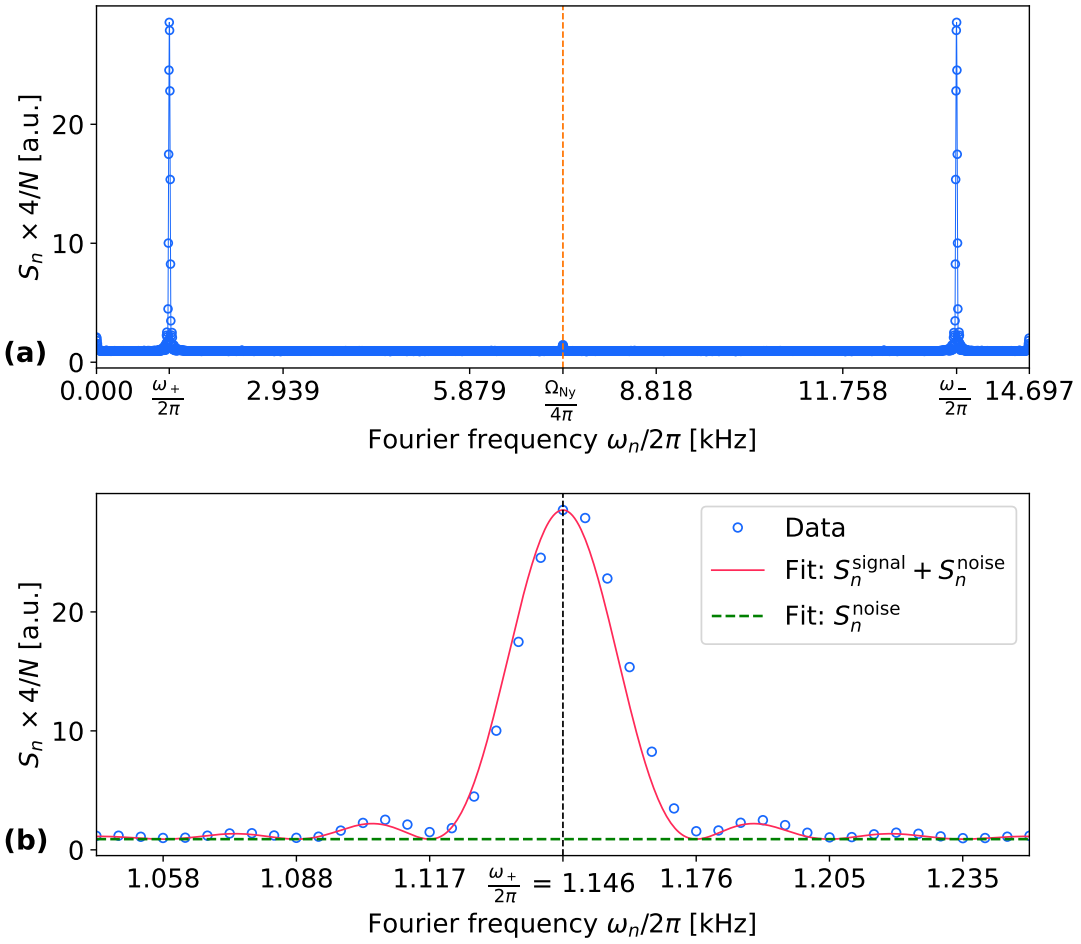

Fig. 7.5 ***Power spectrum of the measured data:*** *(a) Power spectrum* $S_n = \langle |Z_n|^2 \rangle$ *of the measured data. It was obtained by averaging the magnitude-squared of the spectrum of many periodograms. The power spectrum is normalized by the factor* $4/N^2$*, where* $N = 1000$ *is the number of samples per periodogram. (b) Zoom in around the center frequency* $\omega_+/2\pi$ *of the first peak of the power spectrum* $S_n(\omega_n)$*. The amplitude of the peak* A *is related to the mean-value of the in-plane projection of the qubit pseudo spin* $\langle \sigma_\perp \rangle$ *as* $A = \langle \sigma_\perp \rangle^2$*. Blue empty circles are the measured data while the red solid line is a sinc-squared fit according to Equation 7.25. The residual bandwidth of the peak is* $\Omega_{\mathrm{RBM}}/2\pi \approx 31$ *Hz, and the in-plane projection of the qubit pseudo-spin is* $\langle \sigma_\perp \rangle \approx 0.1690$*.*

7.3.2 Response to the calibration tone and frequency aliasing

In the section 7.3 we saw that mean-value of the spectrum $\langle Z_n \rangle$ is actually a periodic function of Δ, with period of $2\Omega_{\mathrm{Ny}}$ (see Equation 7.22). However, the approximation of the power spectrum S_n^{signal} that was provided in Equation 7.25 does not explicitly show this $2\Omega_{\mathrm{Ny}}$-periodicity. Moreover, the power spectrum S_n^{signal} contains two families of resonances that further complicate the analysis. The combination all this factors makes difficult to trace the exact value of the detuning Δ from the center frequency of a measured resonance ω_p. The section is about the analysis of the power spectrum $S_n^{\mathrm{signal}}(\Delta)$ as function of the detuning Δ.

A better approximation of the power spectrum $S_n^{\mathrm{signal}}(\Delta,\, \omega_n) = |\, \langle Z_n \rangle \,|^2$ that shows more explicitly its periodic nature is the following:

$$S_n^{\mathrm{signal}}(\Delta,\, \omega_n) \approx \frac{\langle \sigma_\perp^2 \rangle}{4} \left[\frac{\sin\left(\pi \frac{N(\Delta-\omega_n)}{2\Omega_{\mathrm{Ny}}}\right)^2}{\sin\left(\pi \frac{(\Delta-\omega_n)}{2\Omega_{\mathrm{Ny}}}\right)^2} + \frac{\sin\left(\pi \frac{N(\Omega_{\mathrm{Ny}}-\Delta-\omega_n)}{2\Omega_{\mathrm{Ny}}}\right)^2}{\sin\left(\pi \frac{(\Omega_{\mathrm{Ny}}-\Delta-\omega_n)}{2\Omega_{\mathrm{Ny}}}\right)^2} \right] \tag{7.27}$$

This approximation is obtained from Equation 7.22 in the limit of sufficiently narrow resonances. This condition is equivalent to $\Omega_{\mathrm{RBW}} \ll |\omega_+ - \omega_-| = |\Omega_{\mathrm{Ny}} - 2|\Delta||$, where ω_+ and ω_- are the center frequencies of the two families of resonances that are present in $\langle Z_n \rangle$. More precisely, the previous condition can be translated into:

$$N \gg \frac{2}{|1 - \frac{2|\Delta|}{\Omega_{\mathrm{Ny}}}|} \tag{7.28}$$

For sufficiently large number of samples per window N, the approximation of the power spectrum $S_n^{\mathrm{signal}}(\Delta,\, \omega_n) = |\, \langle Z_n \rangle \,|^2$ given by Equation 7.27 works well everywhere except within a small vicinity around $|\Delta| = \Omega_{\mathrm{Ny}}/2$.

Notice that the the power spectrum $S_n^{\mathrm{signal}}(\Delta,\, \omega_n)$ has two families of resonances that are given by the zeros of $\sin\left(\pi \frac{(\Delta-\omega_n)}{2\Omega_{\mathrm{Ny}}}\right)^2$ and $\sin\left(\pi \frac{(\Omega_{\mathrm{Ny}}-\Delta-\omega_n)}{2\Omega_{\mathrm{Ny}}}\right)^2$. Therefore, the center frequencies of the two families of resonances are located at the Fourier frequencies

$$\begin{aligned} \omega_+ &= \Delta \pmod{2\Omega_{\mathrm{Ny}}} \\ \omega_- &= \Omega_{\mathrm{Ny}} - \Delta \pmod{2\Omega_{\mathrm{Ny}}} \end{aligned} \tag{7.29}$$

In general, we observe that the power spectrum $S_n^{\mathrm{signal}}(\Delta) = |\, \langle Z_n \rangle \,|^2$ is periodic with respect to the detuning Δ, with a period of $2\Omega_{\mathrm{Ny}}$, while the mean-value of the spectrum $\langle Z_n \rangle$ has a period of $4\Omega_{\mathrm{Ny}}$. The difference between the center frequencies of the two resonances is $|\omega_+ - \omega_-| = |\Omega_{\mathrm{Ny}} - 2|\Delta_{\mathrm{mod}_{\Omega_{\mathrm{Ny}}}}||$. Moreover, the two resonances become degenerate, $\omega_+ = \omega_-$, when $\Delta = \pm\Omega_{\mathrm{Ny}}/2$. This suggest that the points $\Delta = \pm\Omega_{\mathrm{Ny}}/2$ are symmetry points of the power spectrum $S_n^{\mathrm{signal}}(\Delta)$.

Firstly, we verify that $\Delta = +\Omega_{\mathrm{Ny}}/2$ is a symmetry point by applying the transformation

$\Delta \to +\Omega_{\mathrm{Ny}}/2 + \Delta$ to the power spectrum S_n^{signal} given by Equation 7.27:

$$S_n^{\mathrm{signal}}\left(\Delta + \frac{\Omega_{\mathrm{Ny}}}{2}, \omega_n\right) = \frac{\langle\sigma_\perp^2\rangle}{4}\left[\frac{\sin\left(\pi\frac{N\left(\frac{1}{2}\Omega_{Ny}-\omega_n+\Delta\right)}{2\Omega_{\mathrm{Ny}}}\right)^2}{\sin\left(\pi\frac{\left(\frac{1}{2}\Omega_{Ny}-\omega_n+\Delta\right)}{2\Omega_{\mathrm{Ny}}}\right)^2} + \frac{\sin\left(\pi\frac{N\left(\frac{1}{2}\Omega_{Ny}-\omega_n-\Delta\right)}{2\Omega_{\mathrm{Ny}}}\right)^2}{\sin\left(\pi\frac{\left(\frac{1}{2}\Omega_{Ny}-\omega_n-\Delta\right)}{2\Omega_{\mathrm{Ny}}}\right)^2}\right] \tag{7.30}$$

Notice that $S_n^{\mathrm{signal}}\left(-\Delta + \frac{\Omega_{\mathrm{Ny}}}{2}, \omega_n\right) = S_n^{\mathrm{signal}}\left(\Delta + \frac{\Omega_{\mathrm{Ny}}}{2}, \omega_n\right)$ meaning that $\Delta = +\Omega_{\mathrm{Ny}}/2$ is indeed a symmetry point of the power spectrum $S_n^{\mathrm{signal}}(\Delta)$. Next, we verify that $\Delta = -\Omega_{\mathrm{Ny}}/2$ is a symmetry point by applying the transformation $\Delta \to -\Omega_{\mathrm{Ny}}/2+\Delta$ to the power spectrum S_n^{signal} given by Equation 7.27:

$$S_n^{\mathrm{signal}}\left(\Delta - \frac{\Omega_{\mathrm{Ny}}}{2}, \omega_n\right) = \frac{\langle\sigma_\perp^2\rangle}{4}\left[\frac{\sin\left(\pi\frac{N\left(-\frac{1}{2}\Omega_{Ny}-\omega_n+\Delta\right)}{2\Omega_{\mathrm{Ny}}}\right)^2}{\sin\left(\pi\frac{\left(-\frac{1}{2}\Omega_{Ny}-\omega_n+\Delta\right)}{2\Omega_{\mathrm{Ny}}}\right)^2} + \frac{\sin\left(\pi\frac{N\left(\left(2-\frac{1}{2}\right)\Omega_{Ny}-\omega_n-\Delta\right)}{2\Omega_{\mathrm{Ny}}}\right)^2}{\sin\left(\pi\frac{\left(\left(2-\frac{1}{2}\right)\Omega_{Ny}-\omega_n-\Delta\right)}{2\Omega_{\mathrm{Ny}}}\right)^2}\right] \tag{7.31}$$

By considering that the period of the power spectrum $S_n^{\mathrm{signal}}(\Delta)$ with respect to the detuning Δ is $2\Omega_{\mathrm{Ny}}$, we therefore find that $S_n^{\mathrm{signal}}\left(-\Delta - \frac{\Omega_{\mathrm{Ny}}}{2}, \omega_n\right) = S_n^{\mathrm{signal}}\left(\Delta - \frac{\Omega_{\mathrm{Ny}}}{2}, \omega_n\right)$, meaning that $\Delta = -\Omega_{\mathrm{Ny}}/2$ is also a symmetry point of the power spectrum $S_n^{\mathrm{signal}}(\Delta)$. Finally, the power spectrum $S_n^{\mathrm{signal}}(\Delta, \omega_n)$ is invariant under the exchange of the variables $\omega_n \leftrightarrow \Delta$, meaning that $\omega_n = \pm\Omega_{\mathrm{Ny}}/2$ are also symmetry points of the power spectrum.

The Figure 7.6 shows the expected behaviour of the power spectrum $S_n^{\mathrm{signal}}(\Delta, \omega_n)$ as function of the detuning Δ. We can observe the central frequencies $\omega_\pm$ of the peaks of the power spectrum S_n^{signal} as function of the value of the detuning Δ (see red and blue lines in Figure 7.6a).

Moreover, we see the symmetry points of the power spectrum. For instance, the centers of the peaks $\omega_\pm$ are symmetrically located with respect to the horizontal lines $\omega_n = \pm\Omega_{\mathrm{Ny}}$ (see the horizontal dashed black lines in Figure 7.6a). The Figure 7.6b shows the expected amplitude of the peaks $S_n^{\mathrm{signal}}(\Delta, \omega_n = \omega_\pm(\Delta))$ as function of the detuning Δ. The decay of the peak amplitude with increasing Δ comes from the in-plane projection of the qubit pseudo-spin $\langle\sigma_\perp\rangle$ according to Equation 7.27. The qubit has approximately a sinc-like response as a function of Δ (see Equations 7.9 and 7.11), with a bandwidth $\Omega_{\mathrm{full}} = \pi/\tau_{\mathrm{I}}$. Finally, the Figure 7.6c displays the response of the power spectrum S_n^{signal} at a fixed Fourier frequency ω_0 when the detuning Δ is swept, i.e., $S_n^{\mathrm{signal}}(\Delta, \omega_n = \omega_0)$.

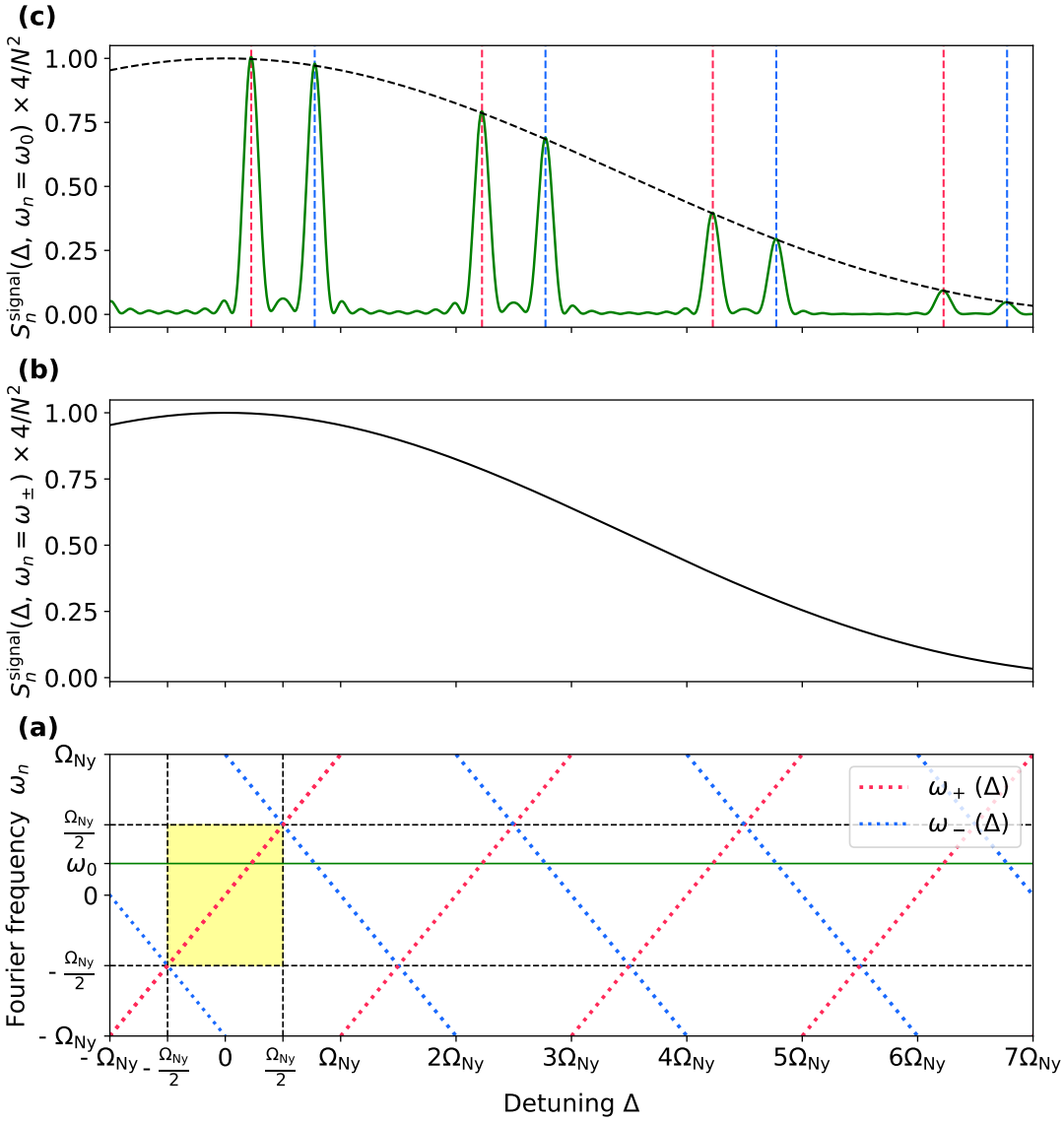

Fig. 7.6 ***Theoretical power spectrum vs detuning:*** *(a) Location of the peaks $\omega_\pm$ of the power spectrum S_n^{signal} in Fourier frequency space ω_n as function of the detuning Δ between the qubit frequency and the calibration-tone frequency. The yellow rectangle represents the ideal region to set and detect the calibration tone without an ambiguity of the relation between the measured peak center ω_+ and the detuning Δ. (b) Amplitude of the peaks $S_n^{\text{signal}}(\Delta, \omega_n = \omega_\pm)$ as function of the detuning Δ. The width of the envelope is approximately $\Omega_{\text{full}} = 2\pi/\tau_1$. (c) Response of the power spectrum at a fixed Fourier frequency ω_0 when the detuning Δ is swept. The width of the peaks is approximately $\Omega_{\text{RBM}} = 2\pi/N\tau_M$.*

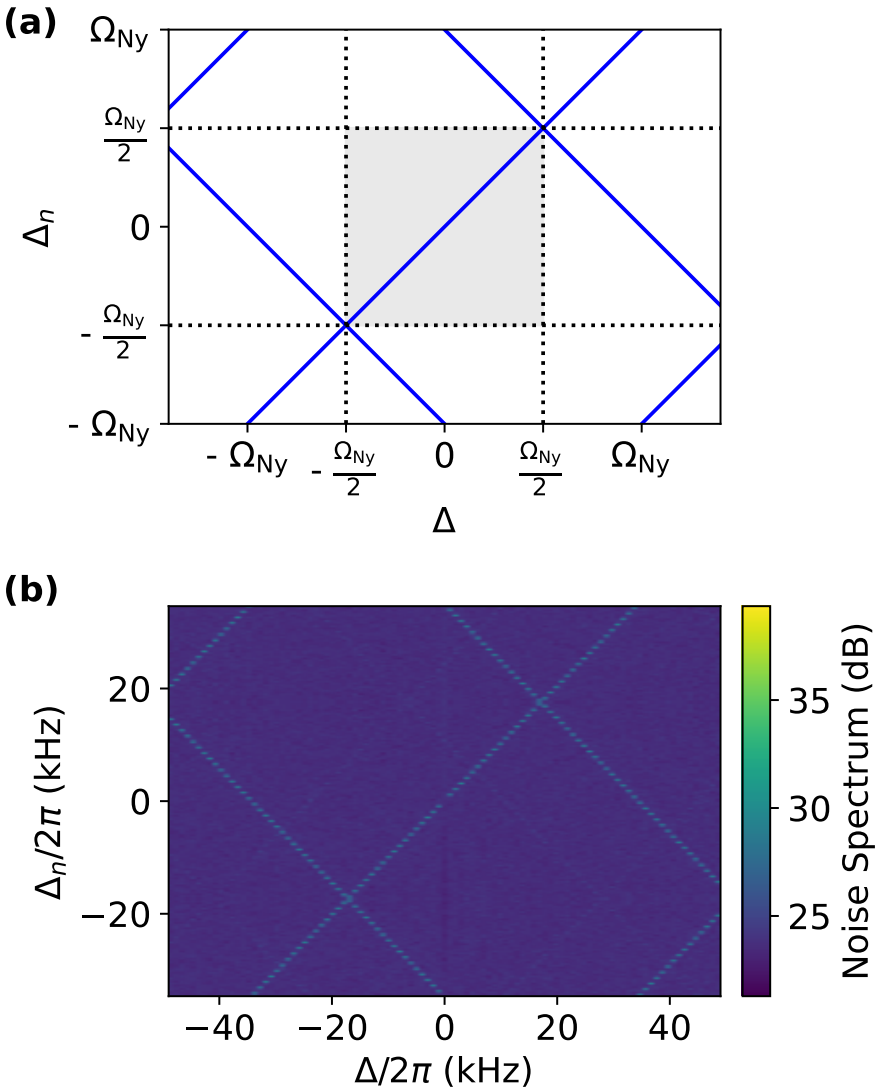

Fig. 7.7 ***Aliasing diagram of the spectrum analyzer:*** *(a) The blue lines indicate the position of the peaks in discrete frequency space ω_n as a function of the continuous frequency Δ of the applied calibration tone, $\omega_+ = \Delta \ (mod\ 2\Omega_{Ny})$ and $\omega_- = \Omega_{Ny} - \Delta \ (mod\ 2\Omega_{Ny})$. (b) Experimental spectrogram with an applied tone of fixed frequency. The detuning Δ is swept by adjusting the qubit frequency. In this particular instance, the repetition time of the experiment was set to $\tau_M = 14.4\,\mu s$, corresponding to a Nyquist frequency $\Omega_{Ny}/2\pi = 35$ kHz.*

7.4 Signal to noise ratio

Owing to the quantum nature of our sensor, the measurement records are in essence discrete, such that a fundamental sampling noise, of spectral shape S_n^{sampling}, affects our measurement. Indeed, the spectrum estimator can be decomposed according to

$$S_n = S_n^{\text{signal}} + S_n^{\text{sampling}} \tag{7.32}$$

with $S_n^{\text{signal}} = |\langle Z_n \rangle|^2$ and $S_n^{\text{sampling}} = \langle |Z_n - \langle Z_n \rangle|^2 \rangle$. To calculate the sampling noise, we can consider the situation when no calibration tone is applied, such that the samples $\{z_k\}_{0 \leq k < N}$ are independent, with $\langle z_k \rangle = 0$ and $\langle z_k z_{k-m}^* \rangle = \delta_{m,0}/4$. Combined with the relation 7.19, we get

$$S_n^{\text{sampling}} = \sum_{k=0}^{N-1} \langle z_k z_{k-n}^* \rangle = \frac{N}{4} \tag{7.33}$$

By combining the relations 7.25 and 7.33, we get the signal-to-noise ratio:

$$\text{SNR} = \sqrt{\frac{\max\left(S_n^{\text{signal}}\right)}{S_n^{\text{sampling}}}} = \sqrt{N}\,\langle \sigma_\perp \rangle \tag{7.34}$$

The signal to noise ratio scales linearly with the in-plane projection of the qubit pseudo-spin $\langle \sigma_\perp \rangle$. By combining Equations 7.9 and 7.10, in the limit of weak driving amplitude, i.e., $\Delta \ll \Omega_\text{r}$, we can simply write $\langle \sigma_\perp \rangle$ with the respect to the interrogation time τ_I, the qubit relaxation time T_1 and the Rabi frequency Ω_r:

$$\langle \sigma_\perp \rangle \approx \frac{1}{2} \sin\left(\Omega_\text{r} \tau_\text{I}\right) e^{-\tau_\text{I}/T_1} \tag{7.35}$$

As the Rabi frequency Ω_r and the relaxation time T_1 are given parameters of the sensor and the singnal, the only adjustable parameter to improve the SNR is the interrogation time τ_I. In order to find the optimum SNR with the respect to the interrogation time τ_I, we perform sequentially several AC-charge sensing experiments varying the interrogation time τ_I at each iteration. In this way, we obtain a set of measured data $\{\sigma_k\}$ for each value of τ_I. Then, we get the power spectrum $S_n(\omega_n) = \langle |Z_n|^2 \rangle$ corresponding to each measured data set (for a given value of τ_I). We find the center frequency $\omega_\pm$ of the peaks of each power spectrum $S_n(\omega_n)$, and we make a sinc-squared fit on one of them, determining the signal amplitude S_n^{signal} an the noise amplitude S_n^{noise}. Finally, we evaluate the signal to noise ratio SNR of each data set according to Equation 7.34. The Figure 7.8 shows the signal to noise ratio SNR as a function of the interrogation time τ_I. The SNR as a function of τ_I is well described by Equation 7.35, where we used the measured qubit relaxation time $T_1 = 1/(2\Gamma) = 24\,\mu\text{s}$ and the Rabi frequency Ω_r corresponding to the amplitude of the calibration tone. Moreover, we added a factor of 84 % to account for non-ideal readout efficiency. The expected SNR showed good qualitative agreement with the measured one (see green solid line in Figure 7.8a). Qualitatively, the SNR increases linearly for $\tau_\text{I} \ll T_1$, as the initial Bloch-vector accumulates a transverse component $2|\langle \sigma \rangle| = \Omega_\text{r} \tau_\text{I}$. On the other hand, due to the interaction with the thermal bath, the Bloch-vector relaxes eventually towards the origin of the Bloch sphere such that the SNR vanishes for $\tau_I \gg T_1$.

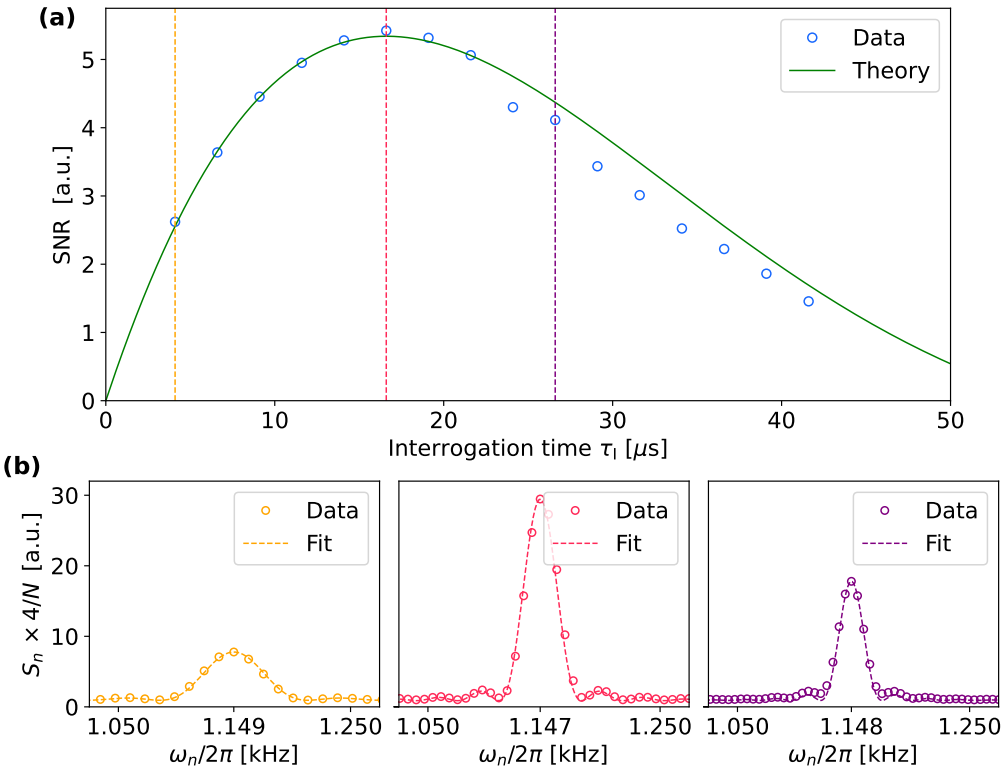

Fig. 7.8 ***Signal to noise ratio vs interaction time:*** *(a) Signal to noise ratio SNR for different values of the interaction time τ_I. The blue open circles represent the measured data while the green solid line is made according to Equation 7.35 with a scale factor of 84 % to account for non-ideal readout efficiency. (b) The normalized power spectrum $S_n = \langle |Z_n|^2 \rangle$ for some values of the interrogation time τ_I that are represented by the vertical dashed lines in panel (a).*

7.5 Approximate expression for the optimal charge sensitivity

The noise spectrum in units of e^2/Hz is calibrated such that the area under the calibration peak matches the known modulation amplitude:

$$\int_0^\infty \frac{d\omega}{2\pi} S_{ee} = (2eN_d)^2 \tag{7.36}$$

The factor of 2 accounts for the number of elementary charges in each Cooper-pair. The left-hand side of Equation 7.27 is approximately given by $S_{ee}[\omega_d]\,\Omega_{RBW}/2\pi$, such that the peak of the noise spectrum is given by:

$$\max\left(S_{ee}^{signal}\right) = (2e\,N_d)^2 \frac{2\pi}{\Omega_{RBW}} \tag{7.37}$$

Where e is the electron charge. We can now use the definition of the signal-to-noise ratio (in conjunction with the linear relationship between S_{ee} and S_n):

$$S_{ee}^{sampling} = \frac{\max\left(S_{ee}^{signal}\right)}{SNR^2} \tag{7.38}$$

Additionally, by combining Equation 7.9 with Equation 7.34, we obtain the approximate expression of the signal-to-noise ratio for a calibration tone well within the detector bandwidth ($\Delta \ll \Omega_{\text{full}}$):

$$\text{SNR}^2 = N \left(\frac{1}{2} e^{-\tau_\text{I}/\text{T}_1} \Omega_\text{r} \tau_\text{I} \right)^2 \tag{7.39}$$

Finally, by inserting Equation 7.30 into Equation 7.29, and using the expressions 7.2 for N_d and the definition of Ω_RBW (Equation 7.20), we derive

$$S_{ee}^{\text{sampling}} = \delta q^2 = \frac{4\tau_\text{M}\, e^2}{(\pi\omega_{ge}\tau_\text{I})^2\; e^{-2\tau_\text{I}/T_1}} \tag{7.40}$$

To minimize δq, it is beneficial to maximize the duty cycle $\tau_\text{I}/\tau_\text{M}$. In our experiment, the total preparation and readout time is approximately amounts to $\tau_\text{prep} \approx 13\,\mu\text{s}$, rendering the total cycle time as $\tau_\text{M} = \tau_\text{I} + \tau_\text{prep}$.

The figure 11 illustrates the evolution of S_{ee}^{sampling} as a function of the interrogation time τ_I for various T_1 values under two distinct scenarios. In the first one (dotted lines), we have considered the ideal case $\tau_\text{prep} = 0\,\mu\text{s}$. In this ideal case, the optimal sensitivity is obtained for $\tau_\text{I} = T_1/2$, reaching a value

$$\delta q_\text{min}^2 = \frac{8\exp(1)\, e^2}{T_1(\pi\omega_{ge})^2} \tag{7.41}$$

Remarkably, δq_min only depends on the qubit frequency ω_{ge} and coherence time T_1. This stems from the observation that at the flux-frustration point, the Rabi frequency depends only on the product $\omega_{ge}N_\text{drive}$ (Equation 7.2), and not on the specific qubit parameters, as long as the systems operates in the heavy-fluxonium regime. In the second scenario (full lines in Figure 11), we consider a realistic preparation and readout time $\tau_\text{prep} = 13\,\mu\text{s}$. As evident from Equation 7.31, for a given interrogation time τ_I, the sensitivity is degraded by a factor $\sqrt{1/\eta}$, where $\eta =: \tau_\text{I}/\tau_\text{M}$ is the non-ideal duty cycle of the experiment, in comparison to the ideal case. The ideal sensitivity is defined as

$$\delta q_\text{min} = \min_{\tau_\text{I}}(\delta q) \tag{7.42}$$

The optimal sensitivity remains close to the ideal one as long as $\tau_\text{prep} \ll T_1$, as visible in Figure 11b.

7.6 Normalized spectrum

In this the final section, we proceed to calculate the normalized spectrum of the measured data. We start from the raw power spectrum $S_n = \langle |Z_n|^2 \rangle$ of the measured data that was displayed in Figure 7.4. There, we have fitted the signal power spectrum $S_n^{\text{signal}} = |\langle Z_n \rangle|^2$ with a sinc-squared function obtaining a good agreement (see red-dashed line in Figure 7.4b). We used the fitted signal amplitude $\max\left(S_n^{\text{signal}}\right)$ and the amplitude of the charge modulation produced by calibration tone N_{cal} (in terms of Cooper-pairs) to determine the scaling factor γ of the power spectrum S_n according to Equation 7.37. The amplitude of charge modulation produced by the calibration tone N_{cal} is computed by taking into account the linear fit shown in Figure 7.2. Next, we transform the power spectrum as $S_n \to \gamma S_n$, after the re-scaling, the power spectrum is in units of $\mu e^2/\text{Hz}$. Finally, we obtain the normalized noise spectrum of the measured data by taking the square-root of the power spectrum S_n. The Figure 7.9 shows the normalized noise spectrum in units of $\mu\text{e}/\sqrt{\text{Hz}}$.

The calibration peak sits on a flat noise background, which is attributable to the sampling noise of the quantum sensor [24]. In practice, when the the AC-charge sensor is operated around its optimal sensitivity ($\tau_{\text{I}} \approx 20\,\mu\text{s}$ in Figure 7.8), the sensor achieves a noise-level as low as $33{\times}10^{-6}\text{e}/\sqrt{\text{Hz}}$. This value approaches that of the most sensitive electrometers such as the radiofrequency quantum point contact (rf-QPC) [19, 64] or the radiofrequency single-electron transistor [68, 83]. Yet, these transport-based sensors are very different in nature from the current qubit-based quantum protocol. The shuntcapacitor on which the charge is detected in our system is typically 2 orders of magnitude larger than the superconducting islands employed in those systems [19, 68]. This is of utmost practical importance when it comes to connecting the sensor to an auxiliary quantum system. As an example, when trying to detect the charge-modulation of an electromechanical system such as [69], the 50 fF capacitor of the vacuum-gap system would perfectly match the value employed in this work, whereas traditional sensors would suffer a large dilution of the signal. The challenge of detecting extremely small charge signals while maintaining a large island capacitance is more directly captured by the energy sensitivity [19] $\delta q^2/2C \approx 2.8\ \hbar$ which is below the sensitivity of any other charge detectors operating at MHz frequencies. Furthermore, in stark contrast with transport-based measurements, featuring a flat frequency response from DC to several tens of MHz, our resonant detector features a narrow frequency response around the qubit frequency, the full bandwidth being given by $\Omega_{\text{full}} = 2\pi/\tau_{\text{I}} \approx 50$ kHz, as obtained from Equation 7.11. This peculiar frequency response is highly advantageous when coupling the fluxonium to a nearly resonant system, as it guarantees perfect immunity to low-frequency environmental charge noise while maximizing charge sensitivity at the MHz region of interest.

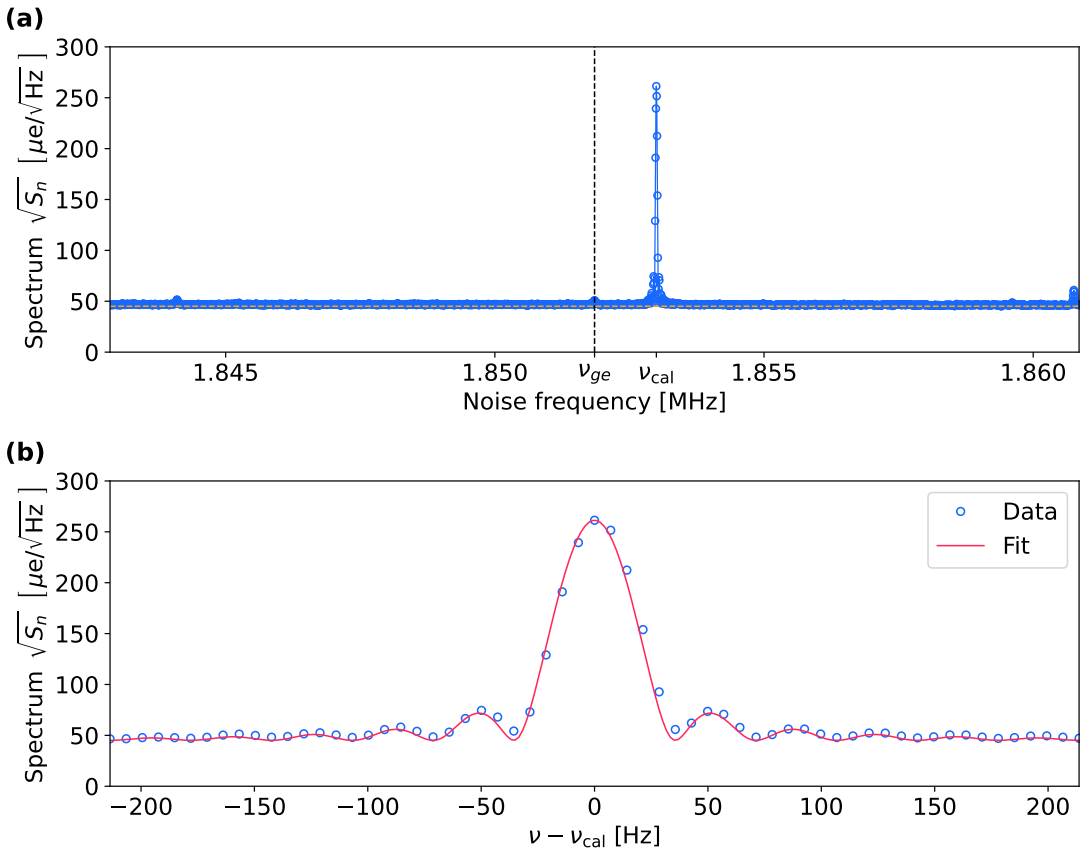

Fig. 7.9 ***Normalized noise spectrum:*** *(a) Normalized spectrum* $\sqrt{S_n} = \sqrt{\langle |Z_n|^2 \rangle}$ *of the measured data. The spectrum is normalized with the aid of the fit of the calibration peak and according to Equations 7.37 and 7.2. (b) Zoom in around the frequency of the calibration peak. Blue empty circles are the measured data while the red solid line is a fit according to Equation 7.25. The residual bandwidth of the calibration peak is* $\Omega_{\text{RBM}}/2\pi \approx 31$ *Hz.*

Chapter 8

Conclusion and perspectives

8.1 Detecting weak charge modulations with a radio-frequency fluxonium qubit

The primary contribution of this thesis is the successful demonstration of the fluxonium superconducting-circuit architecture's capability to develop low-frequency qubits that operate effectively in the few MHz range. Specifically, we designed and operated a heavy fluxonium qubit with a notably low transition frequency of 1.8 MHz and a large dipole moment.

Additionally, the intrinsic non-linearity of the fluxonium circuit has yielded a rich and useful low-frequency spectrum. This spectrum features a high degree of anharmonicity at the qubit transition, with higher energy levels reaching into the GHz range. These properties facilitate the implementation of ancillary states essential for the single-shot readout of the low-frequency qubit transition. We successfully demonstrated resolved sideband cooling, achieving a final ground state population of 97.7 %, which corresponds to an effective temperature of 23 μK. The coherence times measured were $T_1 = 34$ μs and $T_2 = 39$ μs, highlighting the qubit's coherence.

Importantly, our experiments have also shown that the fluxonium's large dipole moment makes it highly sensitive to radio-frequency fields. By employing a capacitively coupled waveguide to directly address the qubit transition, we were able to transform this low-frequency fluxonium qubit into a frequency-resolved charge sensor. Through cyclic qubit preparation and interrogation, we achieved a charge sensitivity of 33 $\mu e/\sqrt{\text{Hz}}$, and an energy sensitivity of 2.8 $\hbar$, rivaling state-of-the-art transport-based devices while maintaining inherent insensitivity to dc-charge noise.

These capabilities position the fluxonium qubit as an exceptionally suitable tool for probing quantum phenomena in the 1–10 MHz range, opening new avenues for exploring interactions in hybrid quantum systems. This constitutes the main directions that the project will undertake in the coming years.

8.2 Future directions

Immediate improvements of the Fluxonium circuit

As our research group looks to enhance the design of the heavy fluxonium, several strategies emerge for improving its performance. Initially, enhancing the coherence properties of the qubit could be achieved by substituting the current silicon substrate with sapphire, which is known for its superior dielectric properties that can reduce decoherence.

Another area of focus could be increasing the fluxonium's insensitivity to flux noise. This might be accomplished by augmenting the value of the superinductance. Practically, this involves modifying the junctions within the superinductance from Dolan-style to Manhattan-style junctions. These junctions have a larger area, which can make them more resilient to quantum coherent-phase-slips, currently a primary limitation in superinductance performance.

Additionally, enhancing the tunability of the qubit frequency presents a significant opportunity for improvement. In the current design, the qubit frequency depends exponentially on the small junction energy (E_J), a parameter challenging to control with a precision greater than $\sim 10\%$ in the micro-fabrication process. This variability complicates the precise design of hybrid systems where the auxiliary system's resonance frequency is predefined. A possible workaround involves replacing the small junction with a tunable junction, such as a SQUID (Superconducting Quantum Interference Device) loop. This modification would allow for *in situ* adjustment of the effective junction potential E_J of the fluxonium (its "weight"), thereby enabling precise control over the transition frequency. Although this solution introduces the need for additional magnetic control, the benefit of achieving exact frequency alignment in hybrid quantum systems could significantly outweigh the complexity added by this extra layer of control.

Strong electro-mechanical coupling: the mecafluxonium

In the main text, we have shown that our heavy fluxonium qubit has the potential to achieve strong resonant coupling with a micro-mechanical phononic-crystal membrane resonator. Our group has successfully fabricated and characterized both quantum devices independently, but integrating them into the unified system known as the mecafluxonium introduces several technological challenges.

One significant challenge is the precise assembly of two chips, each about 1 cm^2, at a sub-micron distance. To minimize dust interference during the flip-chip process, a recess is etched on the chips to reduce the areas in regard, thus lowering the likelihood that dust will prevent successful assembly.

Additionally, it is important to ensure that the mechanical and qubit modes are not affected by energy leakage through the DC bias lines. Robust DC-line filtering strategies are necessary to ensure that AC-fluctuations are effectively reflected back to the circuit.

The ultimate goal of our research is to develop the mecafluxonium, which could have significant applications in fields such as quantum gravity and quantum memories. As depicted in Figure 8.1, our experiment involves configuring the capacitor pad of the fluxonium (green) to overlap with the defect of the metallized membrane, effectively converting mechanical motion into a charge modulation at the fluxonium junction (red). Successful assembly

has been achieved using a flip-chip process with aluminum spacers approximately 600 nm high to ensure separation and maintain galvanic contact.

Himanshu Patange and Kyrylo Gerashchenko, the two PhD students who will continue this project, are focusing on specific aspects of the integration. Himanshu is enhancing the flip-chip process and improving electromechanical integration, while Kyrylo is adapting the fluxonium circuit design for this particular setup. The initial experiment planned–qubit-assisted cooling of the membrane–is relatively straightforward, as it does not require the

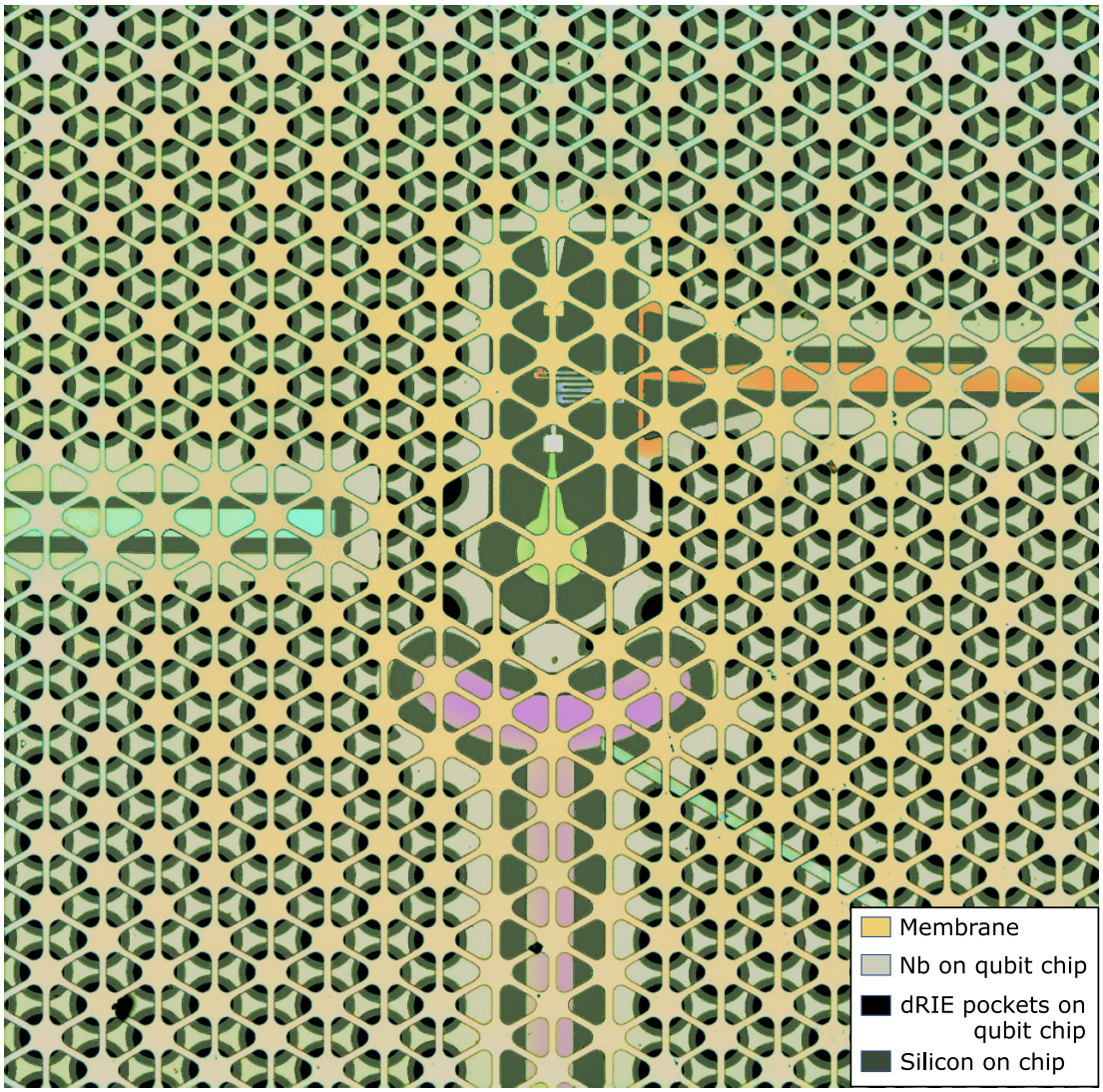

Fig. 8.1 ***Meca-fluxonium (work in progress):*** *False-colored micrograph of silicon nitride phononic crystal membrane resonator on a grounded heavy-fluxonium. The capacitor pad of the fluxonium (green) overlaps with the defect of the metallized membrane resembling a parallel plate capacitor, which transduces the mechanical motion of the membrane into a charge modulation at the fluxonium junction (red). The two chips were successfully assembled via flip-chip with a few aluminum spacers keeping them apart while ensuring galvanic contact between them. The height of the spacers is about* 600 nm.

system to be in the strong coupling regime. This allows the qubit to be operated away from the flux-frustration point, where the T_2 time is typically degraded. As such, we are optimistic about obtaining the first results in the coming months. This experiment is crucial as it sets the stage for more advanced quantum state manipulation of the membrane, paving the way for further explorations of truly non-classical quantum states of the macroscopic mechanical system.

8.3 Summary of activities

During my time as PhD student I was involved in a variety of activities, from circuit design using python for both circuit drawing for electromagnetic-fields simulations (Ansys HFSS) and lithography mask scripting, up to more practical activities like microfabrication and characterization of the designed circuits in both frequency and time domains using a quantum operator X (from Quantum Machines) inside a dilution cryostat. My duties were set to fulfill the requirements and priorities of our main project at the each time, which was fabricating a superconducting fluxonium qubit that was suitable for reaching strong coupling with our micromechanical membrane resonators. In the early days of my PhD work, I focused on fabricating the thin membrane resonators and later trained new PhD students in this task as I transitioned towards participating in circuits-related activities. In this way, I fabricated the first superconducting circuit that was ever fabricated in the Laboratoire Kastler Brossel. I also designed part of the membrane resonator characterization setup using FreeCAD. Finally, towards the later stage of my PhD I became the responsible of the entire microfabrication process and successfully fabricated a superconducting qubit with a then-record low frequency of 1.8 MHz. The qubit achieved high anharmonicity (1000) and strong coherence (40 μm), demonstrating potential for resonant coupling with an ultra-coherent nanomechanical membrane resonator.

8.4 Acknowledgments

This ambitious project would have not been possible without the collaboration of many people that I will briefly try to list here. Thanks to our colleagues Zaki Leghtas (ENS Paris), Clarke Smith (ENS Paris at that time), Marius Villiers (ENS Paris), Emmanuel Flurin (Quantronics CEA) and Philippe Campagne-Ibarcq (INRIA) who provided their guidance and support through the tough process of entering into the field of superconducting circuits from 0 to hero. Thanks to the cleanroom technicians Jose Palomo (ENS Paris), Michael Rosticher (ENS Paris), Aurélie Pierret (ENS Paris), Jean-Loup Smirr (Collège de France) and Pierre-François Orfila (CEA) for their training on the precious art of microfabrication techniques and cleanroom machines and for providing their expertise for debugging frequently emerging problems. Thanks for all their support to the permanent members of my group at LKB Tristan Briant and Pierre-François Cohadon as well as the administrative staff at LKB, David Noel, Laetitia Morel and particularly Stéphanie Dubois who used all of her expertise to save my PhD at several occasions. Thanks to my scientific tutors Saïda Guellati-Khélifa and Igor Dotsenko for their support during my darkest and toughest times. Thanks to the École Doctorale Physique en Île de France for funding my PhD education, special thanks to the EDPIF Director Maria Chamarro and her assistant Nadine Yassine for the support and lots of

patience with the administrative procedures. Thanks to my dear supervisors Igor Dotsenko (master thesis supervisor), Antoine Heidmann, Thibaut Jacqmin, and Samuel Deléglise for all their patience, support and guidance in both scientific and personal matters, sorry for having been too annoying at times, I would have not made it without you <3. Finally thanks to my mother Esperanza Santos-Abrajan, my father Baldomero Najera-Reyes, my brothers Raul-Alberto Najera-Santos, Jose-Rodrigo Najera-Santos and Jimbo and all my family, I owe you all I am today, I love you all.

Appendices

.1 Synthesizing the equivalent circuit from the simulations

In this section, we aim to synthesize an equivalent circuit with the frequencies ω_n and energy-participation ratios p_n of the simulated normal modes. In the first place, the lagrangian $\mathscr{L}_{\text{bare}}$ of the bare equivalent circuit (see Figure 3.6a) is written as:

$$\mathscr{L}_{\text{bare}} = \left[\frac{C\dot{\phi}^2}{2} - \frac{\phi^2}{2\,L} + \frac{C_{\text{R}}\dot{\phi}_{\text{R}}^2}{2} - \frac{\phi_{\text{R}}^2}{2\,L_{\text{R}}} - C_{\text{S}}\dot{\phi}_{\text{R}}\dot{\phi}\right] + E_J\cos\left(\frac{\phi}{\Phi_0} + \varphi_{\text{ext}}\right) \tag{.1}$$

Where $\Phi_0 = \hbar/2e$ is the reduced flux quantum. The linear part of the bare lagrangian $\mathscr{L}_{\text{bare}}$ are the terms inside the brackets. The shunting capacitance C_{S} accounts for the coupling the fluxonium and the resonator. The the capacitance C_{R} and the inductance L_{R} of the ancillary resonator are related to its bare frequency as $\omega_{\text{R}} = 1/\sqrt{C_{\text{R}}L_{\text{R}}}$. Notice that the bare lagrangian $\mathscr{L}_{\text{bare}}$ depends on 6 unknown parameters: $\{L,\, C,\, \omega_{\text{R}},\, Z_{\text{R}},\, C_{\text{S}},\, E_J\}$, where the resonator bare impedance is defined as $Z_n = \sqrt{L_{\text{R}}/C_{\text{R}}}$. The parameters related to the circuit junctions, $L = \Phi_0^2/E_L$ and E_J, are determined by measuring the junctions resistance at room temperature, and then, using the Ambegaokar-Baratoff relation [3] to calculate their tunneling energies. This is described in more detail in Section 4.3.

The next step is decoupling the linear part of the bare lagrangian $\mathscr{L}_{\text{bare}}$. This is achieved by applying a linear transform $\boldsymbol{K}$, such that ϕ and ϕ_{R} are transformed as:

$$\begin{aligned}\phi &\to K_{11}\Phi + K_{12}\Phi_{\text{R}}\\ \phi_{\text{R}} &\to K_{21}\Phi + K_{22}\Phi_{\text{R}}\end{aligned} \tag{.2}$$

Here, the variables ϕ and ϕ_{R} correspond to bare linearized-fluxonium and resonator modes, respectively, while the variables Φ and Φ_{R} are related to the normal modes. The transformation $\boldsymbol{K}$ suppresses the linear coupling term, $C_{\text{S}}\dot{\phi}_{\text{R}}\dot{\phi}$. The resulting lagrangian $\mathscr{L}_{\text{norm}}$ has the form:

$$\mathscr{L}_{\text{normal}} = \left[\frac{C'\dot{\Phi}^2}{2} - \frac{\Phi^2}{2\,L'} + \frac{C'_{\text{R}}\dot{\Phi}_{\text{R}}^2}{2} - \frac{\Phi_{\text{R}}^2}{2\,L'_{\text{R}}}\right] + E_J\cos\left(K_{11}\frac{\Phi}{\Phi_0} + K_{12}\frac{\Phi_{\text{R}}}{\Phi_0} + \varphi_{\text{ext}}\right) \tag{.3}$$

We refer to $\mathscr{L}_{\text{normal}}$ as the normal-modes lagrangian. The linear part of $\mathscr{L}_{\text{normal}}$ is shown inside the brackets. The capacitances C'_x and inductances L'_x in terms of the parameters of the bare equivalent circuit are:

$$\begin{aligned}C'_1 &= K_{11}^2\,C + K_{21}^2\,C_{\text{R}} - K_{11}K_{21}\,C_{\text{S}}\\ C'_2 &= K_{12}^2\,C + K_{22}^2\,C_{\text{R}} - K_{12}K_{22}\,C_{\text{S}}\\ \frac{1}{L'_1} &= \frac{K_{11}^2}{L} + \frac{K_{21}^2}{L_{\text{R}}}\\ \frac{1}{L'_2} &= \frac{K_{12}^2}{L} + \frac{K_{22}^2}{L_{\text{R}}}\end{aligned} \tag{.4}$$

The inductances L'_x and capacitances C'_x of the normal modes are in general different from the ones of the bare lagrangian (see Equation .1), for example, $C' \neq C$. Notice that the EM-fields simulations yield the frequencies of the normal modes, $\omega'_x = 1/\sqrt{L'_x C'_x}$, and not

the frequencies of the bare modes, $\omega_x = 1/\sqrt{L_x C_x}$.

The linear part of the lagrangian $\mathscr{L}_{\text{normal}}$ (see Equation .3) describes two independent modes that can be written, for instance, as:

$$\Phi_x = \Phi_{x,0} \cos(\omega_x t) \tag{.5}$$

The total energy of the mode "x" is then:

$$E_x^{\text{Tot}} = \frac{\Phi_{x,0}^2}{2L'_x} \cos(\omega'_x t)^2 + \frac{1}{2}\omega'^2_x C'_x \Phi_{x,0}^2 \sin(\omega_x t)^2 = \frac{\Phi_{x,0}^2}{2L'_x} \tag{.6}$$

By substituting Equations .2 and .5 into the bare lagrangian $\mathscr{L}_{\text{bare}}$ (Equation .1), we find the energy of the mode "x" that is stored in the lumped element inductance L:

$$E_x^{\text{ind}} = \max_t \left(\frac{\phi^2}{2L}\right) = K_{1x}^2 \frac{\Phi_{x,0}^2}{2L} \tag{.7}$$

It follows that the energy-participation ratio P_x of mode "x" in the inductance L is:

$$P_x = \frac{E_x^{\text{ind}}}{E_x^{\text{Tot}}} = K_{1x}^2 \frac{L'_x}{L} \tag{.8}$$

Thus, by setting $p_x = P_x$, we have found a natural way to connect the energy-participation ratios p_x that are obtained from the simulations (Equation 3.5) and the parameters of the normal-modes lagrangian $\mathscr{L}_{\text{normal}}$ (Equation .3). We substitute the inductance L'_x of a normal modes in terms of its frequency ω'_x and its impedance Z'_x in Equation .8, obtaining a relation between the impedances Z'_x and the simulated energy-participation ratios p_x of the normal modes:

$$Z'_x = \frac{L\,\omega'_x p_x}{K_{1x}^2} \tag{.9}$$

Notice that L in Equation .9 does not represent the junction-chain superinductance L_{c} but it rather corresponds to the test inductance L_{t} that replaces the junction-chain superinductance in the simulations. In general, it is not mandatory to set the value of the test inductance L_{t} equal to the inductance of the junction chain L_{c}, which is determined independently by measuring the resistance of the chain junctions at room temperature as detailed in Section 4.3. The results of simulations can be traced to the parameters of the bare equivalent circuit (Equation .1), independently of the value of the test inductance L_{t}.

The Equation .9, as it is right now, it is not useful, since it relates the simulated energy-participation ratios p_x to two unknown parameters, Z'_x and K_{1x}. We need some extra steps to turn this equation into a more useful form. Firstly, we re-scale the normal flux variables as $\Phi_x = f_x/K_{1_x}$ in the normal-modes lagrangian $\mathscr{L}_{\text{normal}}$ (Equation .3), obtaining

$$\mathscr{L}_{\text{bb}} = \left[\frac{C'_1 \dot{f}_1^2}{2K_{11}^2} - \frac{f_1^2}{2K_{11}^2 L'_1} + \frac{C'_2 \dot{f}_2^2}{2K_{12}^2} - \frac{f_2^2}{2K_{12}^2 L'_2}\right] + E_J \cos\left(\frac{f_1}{\Phi_0} + \frac{f_2}{\Phi_0} + \varphi_{\text{ext}}\right) \tag{.10}$$

This is the lagrangian of the Foster equivalent circuit corresponding to a junction shunted to a "black-box" microwave environment (see Figure 3.6b). The re-scaling of the fluxes

translates into a re-scaling of the inductances and the capacitances as $L_x^{\mathrm{bb}} = L'_x \cdot K_{1x}^2$ and $C_x^{\mathrm{bb}} = C'_x / K_{1x}^2$, respectively. This re-scaling, nonetheless, leaves the frequencies invariant, $\omega_x^{\mathrm{bb}} = \omega'_x$, but it re-scales the impedances as $Z_x^{\mathrm{bb}} = \sqrt{L_x^{\mathrm{bb}}/C_x^{\mathrm{bb}}} = Z'_x \cdot K_{1x}^2$. Thus, we define the frequencies ω_x^{bb} and impedances Z_x^{bb} of the Foster equivalent circuit as:

$$\begin{aligned} \omega_x^{\mathrm{bb}} &= \omega'_x \\ Z_x^{\mathrm{bb}} &= Z'_x \, K_{1x}^2 \end{aligned} \tag{.11}$$

Where ω'_x and Z'_x are the frequencies and impedances of the normal modes, respectively, and K_{1x} are the matrix elements of transform linking the bare flux coordinates ϕ_x and normal flux coordinates Φ_x. By substituting Equations .11 into Equation .9, we obtain the relation between the energy-participation ratios p_x of the simulated normal modes and the parameters of the Foster equivalent circuit:

$$Z_x^{\mathrm{bb}} = L_{\mathrm{t}} \, \omega_x^{\mathrm{bb}} \, p_x \tag{.12}$$

Notice that a single simulation of the normal modes of the circuit design yields the frequencies ω_x^{bb} and the energy-participation ratios p_x of the normal modes. Since the value of the test impedance L_{t} is defined *a priori*, thus, we can use the Equation .12 to obtain the impedances Z_x^{bb} of the Foster equivalent circuit (see Figure 3.6b). Therefore, the EP method allows synthesizing the Foster equivalent circuit from the results of one single simulation of the normal modes of the circuit design. The lagrangian of the Foster equivalent circuit, in terms of the frequencies ω_x^{bb} and impedances Z_x^{bb}, is written as:

$$\mathscr{L}_{\mathrm{bb}} = \left[\frac{\dot{f}_1^{\,2}}{2\,\omega_1^{\mathrm{bb}}\,Z_1^{\mathrm{bb}}} - \frac{\omega_1^{\mathrm{bb}}\,f_1^{\,2}}{2\,Z_1^{\mathrm{bb}}} + \frac{\dot{f}_2^{\,2}}{2\,\omega_2^{\mathrm{bb}}\,Z_2^{\mathrm{bb}}} - \frac{\omega_2^{\mathrm{bb}}\,f_2^{\,2}}{2\,Z_2^{\mathrm{bb}}} \right] + E_J \cos\left(\frac{f_1}{\Phi_0} + \frac{f_2}{\Phi_0} + \varphi_{\mathrm{ext}} \right) \tag{.13}$$

.2 Relations between the bare and the Foster equivalent circuits

In the Section .1, we discussed the equations relating the parameters of the normal modes and the parameters of the Foster equivalent circuit (see Equation .11). Moreover, the parameters of the normal modes are connected to the parameters the bare equivalent circuit via a linear transform $\boldsymbol{K}$ (see Equation .4). This section is about finding the analytical expressions connecting the parameters of the Foster equivalent circuit (see Figure 3.6b) and the parameters of the bare (equivalent) circuit (see Figure 3.6a). The fist step is finding the normal modes of the linear part $\mathscr{L}_0^{\mathrm{bare}}$ of the bare lagrangian $\mathscr{L}_{\mathrm{bare}}$ (Equation .1),

$$\mathscr{L}_0^{\mathrm{bare}} = \frac{C\dot{\phi}^{\,2}}{2} - \frac{\phi^{\,2}}{2\,L} + \frac{C_{\mathrm{R}}\dot{\phi}_{\mathrm{R}}^2}{2} - \frac{\phi_{\mathrm{R}}^2}{2\,L_{\mathrm{R}}} - C_{\mathrm{S}}\dot{\phi}_{\mathrm{R}}\dot{\phi} \tag{.14}$$

The typical approach is finding a transform of the flux coordinates ϕ_x that diagonalizes the lagrangian $\mathscr{L}_0^{\mathrm{bare}}$ [54, 71]. However, the approach here is rather different. Instead of focusing on the lagrangian $\mathscr{L}_0^{\mathrm{bare}}$, we are rather going to decouple the differential equations dominating the flux variables ϕ_x. The set of differential equations generated by the lagrangian $\mathscr{L}_0^{\mathrm{bare}}$ (Equation .1) is:

$$\begin{aligned} C\ddot{\phi} - C_{\mathrm{S}}\ddot{\phi_{\mathrm{R}}} + \frac{\phi}{L} &= 0 \\ C_{\mathrm{R}}\ddot{\phi_{\mathrm{R}}} - C_{\mathrm{S}}\ddot{\phi} + \frac{\phi_{\mathrm{R}}}{L_{\mathrm{R}}} &= 0 \end{aligned} \tag{.15}$$

This set of linear differential equations can be conveniently written in matrix form as:

$$\mathbf{C}\ddot{\vec{\phi}} + \mathbf{L}^{-1}\vec{\phi} = \vec{0} \tag{.16}$$

where $\vec{\phi}$ represents the flux coordinates and $\mathbf{C}$ and $\mathbf{L}$ are the capacitance and inductance matrices:

$$\mathbf{C} = \begin{bmatrix} C & -C_{\mathrm{S}} \\ -C_{\mathrm{S}} & C_{\mathrm{R}} \end{bmatrix}, \quad \mathbf{L}^{-1} = \begin{bmatrix} L^{-1} & 0 \\ 0 & L_{\mathrm{R}}^{-1} \end{bmatrix}, \quad \vec{\phi} = \begin{bmatrix} \phi \\ \phi_{\mathrm{R}} \end{bmatrix} \tag{.17}$$

Notice that the inductance matrix $\mathbf{L}$ is diagonal. It is useful to write the inductance matrix as:

$$\mathbf{L} = \mathbf{S}^2 = \begin{bmatrix} \sqrt{L} & 0 \\ 0 & \sqrt{L_{\mathrm{R}}} \end{bmatrix} \tag{.18}$$

We transform the flux coordinates as $\vec{\phi} = \mathbf{K}\,\vec{\Phi}$, where the transform $\mathbf{K}$ has the form:

$$\mathbf{K} = \mathbf{S}\,\mathbf{U}\,\mathbf{S}^{-1} \tag{.19}$$

Where $\mathbf{U}$ is an unitary matrix. We substitute the *ansatz* of $\mathbf{K}$ (Equation .19) into the Equation .16 and multiply by $\mathbf{K}^{\mathrm{T}}$, obtaining

$$\mathbf{S}^{-1}\left(\mathbf{U}^{-1}\,\mathbf{S}\,\mathbf{C}\,\mathbf{S}\,\mathbf{U}\right)\mathbf{S}^{-1}\ddot{\vec{\Phi}} + \mathbf{S}^{-2}\vec{\Phi} = \vec{0} \tag{.20}$$

We define the matrix

$$\mathbf{W}^{-2} \equiv \mathbf{S}\,\mathbf{C}\,\mathbf{S} \tag{.21}$$

Notice that if $\mathbf{U}$ chosen such that $\mathbf{U}^{-1}\,\mathbf{W}^{-2}\,\mathbf{U} \equiv \boldsymbol{\Lambda}_{\mathbf{W}}^{-2}$ is a diagonal matrix, the Equation .20 becomes:

$$\mathbf{S}^{-2}\,\boldsymbol{\Lambda}_{\mathbf{W}}^{-2}\ddot{\vec{\Phi}} + \mathbf{S}^{-2}\vec{\Phi} = \vec{0} \tag{.22}$$

Since both $\mathbf{S}$ and $\boldsymbol{\Lambda}_{\mathbf{W}}$ are diagonal matrices, the flux variables Φ_x are not coupled. The entries of $\boldsymbol{\Lambda}_{\mathbf{W}}$ are the eigen-values of $\mathbf{W}$, which are nothing but the resonance frequencies ω'_x of the normal modes. The Equation .22 resembles the Equation .16, with $\mathbf{L'}^{-1} = \mathbf{S}^{-2} = \mathbf{L}^{-1}$ and $\mathbf{C'} = \mathbf{S}^{-2}\,\boldsymbol{\Lambda}_{\mathbf{W}}^{-2}$. Thus, the set of differential equations represented by Equation **??** can be associated with the following lagrangian:

$$\mathscr{L}_0^{\mathrm{normal}} = \frac{C'_1\dot{\Phi}_1^2}{2} - \frac{\Phi_1^2}{2\,L_1} + \frac{C'_2\dot{\Phi}_2^2}{2} - \frac{\Phi_2^2}{2\,L_2} \tag{.23}$$

Alternatively, this lagrangian $\mathscr{L}_0^{\mathrm{normal}}$ can be obtained by substituting the transform $\mathbf{K}$ (Equation .19) into the lagrangian $\mathscr{L}_0^{\mathrm{bare}}$ (Equation .1). Notice that the inductances L'_x of the normal modes are the same as the inductances of the bare equivalent circuit L_x. On the contrary, the capacitances C'_x and impedances Z'_x of the normal modes are given by

$$\begin{aligned} C'_x &= \frac{1}{L_x\,\omega'^2_x} \\ Z'_x &= L_x\,\omega'_x \end{aligned} \tag{.24}$$

As discussed in Section .1, the lagrangian $\mathscr{L}_{\mathrm{normal}}$ (Equation .10) results from applying the transform $\mathbf{K}$ (Equation .19) to the lagrangian $\mathscr{L}_{\mathrm{bare}}$ of the bare equivalent circuit (Equation

.10). The lagrangian $\mathscr{L}_{\rm normal}$ can be turned into the lagrangian $\mathscr{L}_{\rm bb}$ of the Foster equivalent circuit (Equation .13) by re-scaling the flux variables as $\Phi_x = f_x/K_{1x}$ corresponding to a re-scaling of inductances $L_x^{\rm bb} = K_{1x}^2\, L'_x$ and the capacitances $C_x^{\rm bb} = K_{1x}^2\, C'_x$. Moreover, the impedances $Z_x^{\rm bb} = \sqrt{L_x^{\rm bb}/C_x^{\rm bb}}$ are re-scaled as

$$Z_x^{\rm bb} = K_{1x}^2\, Z'_x \tag{.25}$$

Notice that the frequencies remain invariant, i.e., $\omega_x^{\rm bb} = \omega'_x$. Thus, in order to find the relation between the parameters of the Foster equivalent circuit, $\omega_x^{\rm bb}$ and $Z_x^{\rm bb}$, and the parameters of bare equivalent circuit, L, C, $C_{\rm S}$, $\omega_{\rm R}$, $Z_{\rm R}$, we must determine both the eigen-values and eigen-vectors of the matrix $\mathbf{W}$,

$$\mathbf{W}^{-2} = \mathbf{S}\,\mathbf{C}\,\mathbf{S} = \begin{bmatrix} L\,C & -C_{\rm S}\sqrt{L\,L_{\rm R}} \\ -C_{\rm S}\sqrt{L\,L_{\rm R}} & L_{\rm R}\,C_{\rm R} \end{bmatrix} \tag{.26}$$

Notice that $\mathbf{W}^{-2}$ is a symmetric matrix, thus, it can be written in the form

$$\mathbf{W}^{-2} = \frac{\epsilon}{2}\,\mathbf{I}_2 + \frac{\Omega}{2}\left[\frac{\Delta}{\Omega}\mathbf{Z} - \frac{2G}{\Omega}\mathbf{X}\right] \tag{.27}$$

Where

$$\mathbf{I}_2 = \begin{bmatrix} 1 & 0 \\ 0 & 1 \end{bmatrix}, \quad \mathbf{Z} = \begin{bmatrix} 1 & 0 \\ 0 & -1 \end{bmatrix}, \quad \mathbf{X} = \begin{bmatrix} 0 & 1 \\ 1 & 0 \end{bmatrix} \tag{.28}$$

$$\begin{aligned} \epsilon &\equiv \frac{1}{\omega^2} + \frac{1}{\omega_{\rm R}^2} \\ \Delta &\equiv \frac{1}{\omega^2} - \frac{1}{\omega_{\rm R}^2} \\ G &\equiv C_{\rm S}\sqrt{L\,L_{\rm R}} = \frac{C_{\rm S}}{\sqrt{C\,C_{\rm R}}\,\omega\,\omega_{\rm R}} \\ \Omega &\equiv \sqrt{\Delta^2 + 4G^2} = \sqrt{\left(\frac{1}{\omega^2} - \frac{1}{\omega_{\rm R}^2}\right)^2 + \frac{4}{G^2}} \end{aligned} \tag{.29}$$

Notice that the Equation .27 represents a spin-matrix. Therefore, the eigenvalues of $\mathbf{W}^{-2}$ are $\lambda_\pm = \epsilon/2 \pm \Omega/2$. As mentioned before, the eigenvalues of $\mathbf{W}$ are the frequencies of the normal modes ω'_x. Thus,

$$\begin{aligned} \frac{1}{\omega'^2} &= \frac{1}{2}\left(\frac{1}{\omega^2} + \frac{1}{\omega_{\rm R}^2}\right) + \frac{1}{2}\sqrt{\left(\frac{1}{\omega^2} - \frac{1}{\omega_{\rm R}^2}\right)^2 + \frac{4}{G^2}} \\ \frac{1}{\omega'^2_{\rm R}} &= \frac{1}{2}\left(\frac{1}{\omega^2} + \frac{1}{\omega_{\rm R}^2}\right) - \frac{1}{2}\sqrt{\left(\frac{1}{\omega^2} - \frac{1}{\omega_{\rm R}^2}\right)^2 + \frac{4}{G^2}} \end{aligned} \tag{.30}$$

The next step is determining the eigen-vectors of $\mathbf{W}$. This is also simple because $\mathbf{W}^{-2}$ is a symmetric matrix. Notice from Equation .27 that it is sufficient to find the eigen-vectors of the matrix:

$$\mathbf{A} = \cos(\theta)\,\mathbf{Z} - \sin(\theta)\,\mathbf{X} \tag{.31}$$

Where

$$\begin{aligned}\cos(\theta) =& \frac{\Delta}{\Omega} = \frac{\left(\frac{1}{\omega^2} - \frac{1}{\omega_{\mathrm{R}}^2}\right)}{\sqrt{\left(\frac{1}{\omega^2} - \frac{1}{\omega_{\mathrm{R}}^2}\right)^2 + \frac{C_{\mathrm{S}}^2}{C\,C_{\mathrm{R}}}\frac{4}{\omega^2\,\omega_{\mathrm{R}}^2}}} \\ \sin(\theta) =& \frac{2G}{\Omega} \\ \tan(\theta) =& \frac{4\,C_{\mathrm{S}}}{\sqrt{C\,C_{\mathrm{R}}}}\frac{\omega\,\omega_{\mathrm{R}}}{\omega_{\mathrm{R}}^2 - \omega^2}\end{aligned} \tag{.32}$$

In this way, the eigenvectors of $\mathbf{A}$ are

$$\hat{u}_1 = \begin{bmatrix}\cos\left(\frac{\theta}{2}\right) \\ -\sin\left(\frac{\theta}{2}\right)\end{bmatrix}, \quad \hat{u}_2 = \begin{bmatrix}\sin\left(\frac{\theta}{2}\right) \\ \cos\left(\frac{\theta}{2}\right)\end{bmatrix} \tag{.33}$$

Where

$$\begin{aligned}\cos\left(\frac{\theta}{2}\right) =& \sqrt{\frac{1 + \frac{\Delta}{\Omega}}{2}} \\ \sin\left(\frac{\theta}{2}\right) =& \sqrt{\frac{1 - \frac{\Delta}{\Omega}}{2}}\end{aligned} \tag{.34}$$

Finally, we obtain the explicit form of the transformation $\mathbf{K}$ (Equation .19):

$$\mathbf{K} = \begin{bmatrix}K_{11} & K_{12} \\ K_{21} & K_{22}\end{bmatrix} = \begin{bmatrix}\cos\left(\frac{\theta}{2}\right) & \sin\left(\frac{\theta}{2}\right)\sqrt{\frac{L}{L_{\mathrm{R}}}} \\ -\sin\left(\frac{\theta}{2}\right)\sqrt{\frac{L_{\mathrm{R}}}{L}} & \cos\left(\frac{\theta}{2}\right)\end{bmatrix} \tag{.35}$$

.3 Calculating the bare circuit parameters from the simulations

An EM-fields simulation of the normal modes of the circuit design yields a set of frequencies ω_x^{bb} and energy-participation ratios p_x that can be related to the impedances Z_x^{bb} of the modes as seen by the test inductance L_t. In this Section we take into account the results of Sections .1 and .2 to connect the simulation results with the bare equivalent circuit parameters.

Substituting $Z'_x = L'_x\omega'_x$ into Equation .9, produces a relation between the energy-participation ratios p_x and the entries of the matrix transform $\mathbf{K}$:

$$p_x = \frac{L_x}{L_t}K_{1x}^2 \tag{.36}$$

Then, by substituting the explicit form of the entries of $\mathbf{K}$ (Equation .35), we obtain a relation between the components of the eigenvectors of the matrix $\mathbf{W}^{-2}$ (Equations .33 and .34) and the energy-participation ratios:

$$\begin{aligned}p_1 =& \cos\left(\frac{\theta}{2}\right)^2 \\ p_2 =& \sin\left(\frac{\theta}{2}\right)^2\end{aligned} \tag{.37}$$

Therefore, we can write the unitary matrix $\mathbf{U}$ (Equation .33) that diagonalizes $\mathbf{W}^{-2}$ in terms of the energy participation ratios as:

$$\mathbf{U} = \begin{bmatrix} \sqrt{p_1} & \sqrt{p_2} \\ -\sqrt{p_2} & \sqrt{p_1} \end{bmatrix} \tag{.38}$$

We recall that the frequencies of simulated normal modes ω_x^{bb} are the eigen-values of the matrix $\mathbf{W}$. As mentioned in Section .2, we denote by $\boldsymbol{\Lambda}_{\mathbf{W}}$ the diagonal matrix containing the eigen-values of $\mathbf{W}$:

$$\boldsymbol{\Lambda}_{\mathbf{W}} = \begin{bmatrix} \omega_1^{\mathrm{bb}} & 0 \\ 0 & \omega_2^{\mathrm{bb}} \end{bmatrix} \tag{.39}$$

We can recover the matrix $\mathbf{W}^{-2}$ (Equation .21) by applying the following transform:

$$\mathbf{W}^{-2} = \mathbf{U}\, \boldsymbol{\Lambda}_{\mathbf{W}}^{-2}\, \mathbf{U}^{-1} \tag{.40}$$

Notice that on the L.H.S. there are only parameters of the bare equivalent circuit and on the R.H.S. there are only results from the simulation of the normal modes:

$$\begin{bmatrix} L_t\, C & -C_{\mathrm{S}}\sqrt{L_{\mathrm{t}}\, L_{\mathrm{R}}} \\ -C_{\mathrm{S}}\sqrt{L_{\mathrm{t}}\, L_{\mathrm{R}}} & L_{\mathrm{R}}\, C_{\mathrm{R}} \end{bmatrix} = \begin{bmatrix} \left(\frac{\sqrt{p_1}}{\omega_1^{\mathrm{bb}}}\right)^2 + \left(\frac{\sqrt{p_2}}{\omega_2^{\mathrm{bb}}}\right)^2 & -\frac{\sqrt{p_1\, p_2}}{\left(\omega_1^{\mathrm{bb}}\right)^2} + \frac{\sqrt{p_1\, p_2}}{\left(\omega_2^{\mathrm{bb}}\right)^2} \\ -\frac{\sqrt{p_1\, p_2}}{\left(\omega_1^{\mathrm{bb}}\right)^2} + \frac{\sqrt{p_1\, p_2}}{\left(\omega_2^{\mathrm{bb}}\right)^2} & \left(\frac{\sqrt{p_2}}{\omega_1^{\mathrm{bb}}}\right)^2 + \left(\frac{\sqrt{p_1}}{\omega_2^{\mathrm{bb}}}\right)^2 \end{bmatrix} \tag{.41}$$

Firstly, we express the bare frequencies of the modes ω_0 and ω_{R} in terms of the frequencies ω_n^{bb} and the energy participation ratios p_n of the simulated normal modes[1]:

$$\begin{aligned} \frac{1}{\omega_0^2} &= \frac{1}{2}\left(\frac{1+(p_1-p_2)}{(\omega_1^{\mathrm{bb}})^2} + \frac{1-(p_1-p_2)}{(\omega_2^{\mathrm{bb}})^2}\right) \\ \frac{1}{\omega_{\mathrm{R}}^2} &= \frac{1}{2}\left(\frac{1-(p_1-p_2)}{(\omega_1^{\mathrm{bb}})^2} + \frac{1+(p_1-p_2)}{(\omega_2^{\mathrm{bb}})^2}\right) \\ \frac{1}{G^2} &= C_{\mathrm{S}}\sqrt{L_{\mathrm{t}}\, L_{\mathrm{R}}} = \frac{C_{\mathrm{S}}}{\sqrt{C_{\mathrm{R}}\, C}}\, \frac{1}{\omega_0 \omega_{\mathrm{R}}} = \left|\frac{1}{(\omega_1^{\mathrm{bb}})^2} - \frac{1}{(\omega_2^{\mathrm{bb}})^2}\right| \sqrt{p_1 p_2} \end{aligned} \tag{.42}$$

Where $\omega_1^{\mathrm{bb}} < \omega_2^{\mathrm{bb}}$, and the parameter G is related to the coupling g between the bare modes. From these three parameters, we extract the bare capacitance of the fluxonium C and the relative shunting capacitance γ_{S}:

$$\begin{aligned} C &= \frac{1}{\omega_0^2\, L_{\mathrm{t}}} \\ \gamma_{\mathrm{S}} &\equiv \frac{C_{\mathrm{S}}}{\sqrt{C\, C_{\mathrm{R}}}} = \frac{\sqrt{p_1\, p_2}}{\sqrt{\left(\frac{\omega_1^{\mathrm{bb}}\, \omega_2^{\mathrm{bb}}}{(\omega_1^{\mathrm{bb}})^2 - (\omega_2^{\mathrm{bb}})^2}\right)^2 + p_1\, p_2}} \end{aligned} \tag{.43}$$

The coupling between the bare modes g is related to the relative shunting capacitance γ_{S} as:

$$g = \gamma_{\mathrm{S}}\, \sqrt{\omega_0\, \omega_{\mathrm{R}}} \tag{.44}$$

[1]Here, we have used the fact that $p_1 + p_2 = 1$.

While γ_{S} only depends on the fixed parameters of the microwave environment, the coupling rate g depends on the bare frequency of the plasmon mode ω_0, which is a function of test inductance L_{t}, thus, it varies at each iteration of the simulations. The coupling at the anti-crossing g_0, when the bare frequencies of the modes are equal $\omega_0 = \omega_{\mathrm{R}}$, is related to γ_{S} as:

$$g_0 \equiv \gamma_{\mathrm{S}} \omega_{\mathrm{R}} \tag{.45}$$

Unfortunately, the energy participation method here described can't associate the results of the simulation, the frequencies ω_x^{bb} and energy-participation ratios p_x of the normal modes, to an unique set of bare circuit parameters. The bare fluxonium capacitance C and the bare resonator frequency ω_{R} can be uniquely determined. However, as it can be seen in Equation .43, the shunting capacitance C_{S} and the bare resonator capacitance C_{R} can't be determined independently from each other. However, with a reasonable estimate of the resonator impedance, for example, $Z_{\mathrm{R}} = 50\,\Omega$, one estimate the shunting capacitance C_{S} using Equation .43.

Bibliography

[1] A Aassime, D Gunnarsson, K Bladh, P Delsing, and R Schoelkopf. Radio-frequency single-electron transistor: Toward the shot-noise limit. *Applied physics letters*, 79(24):4031–4033, 2001.

[2] Oppenheim Alan V, Schafer Ronald W, Buck John R, et al. Discrete-time signal processing (chapter 2: Signal and systems), 1999.

[3] Vinay Ambegaokar and Alexis Baratoff. Tunneling between superconductors. *Phys. Rev. Lett.*, 10:486–489, June 1963.

[4] S. J. Angus, A. J. Ferguson, A. S. Dzurak, and R. G. Clark. A silicon radio-frequency single electron transistor. *Applied Physics Letters*, 92(11):112103, 03 2008.

[5] Waël Ardati, Sébastien Léger, Shelender Kumar, Vishnu Narayanan Suresh, Dorian Nicolas, Cyril Mori, Francesca D'Esposito, Tereza Vakhtel, Olivier Buisson, Quentin Ficheux, and Nicolas Roch. Using bi-fluxon tunneling to protect the fluxonium qubit, 2024.

[6] Patricio Arrangoiz-Arriola, E Alex Wollack, Zhaoyou Wang, Marek Pechal, Wentao Jiang, Timothy P McKenna, Jeremy D Witmer, Raphaël Van Laer, and Amir H Safavi-Naeini. Resolving the energy levels of a nanomechanical oscillator. *Nature*, 571(7766):537–540, 2019.

[7] L. Balembois. *Magnetic resonance of a single electron spin and its magnetic environment by photon counting*. Phd thesis, Service de physique de l'état condensé, 2023.

[8] Charles H Bennett and David P DiVincenzo. Quantum information and computation. *nature*, 404(6775):247–255, 2000.

[9] Audrey Bienfait, Kevin J Satzinger, YP Zhong, H-S Chang, M-H Chou, Chris R Conner, É Dumur, Joel Grebel, Gregory A Peairs, Rhys G Povey, et al. Phonon-mediated quantum state transfer and remote qubit entanglement. *Science*, 364(6438):368–371, 2019.

[10] Marius Bild, Matteo Fadel, Yu Yang, Uwe Von Lüpke, Phillip Martin, Alessandro Bruno, and Yiwen Chu. Schrödinger cat states of a 16-microgram mechanical oscillator. *Science*, 380(6642):274–278, 2023.

[11] Alexandre Blais, Ren-Shou Huang, Andreas Wallraff, S. M. Girvin, and R. J. Schoelkopf. Cavity quantum electrodynamics for superconducting electrical circuits: An architecture for quantum computation. *Phys. Rev. A*, 69:062320, Jun 2004.

[12] Miles P Blencowe and Martin N Wybourne. Sensitivity of a micromechanical displacement detector based on the radio-frequency single-electron transistor. *Applied Physics Letters*, 77(23):3845–3847, 2000.

[13] Cristian Bonato, Machiel S Blok, Hossein T Dinani, Dominic W Berry, Matthew L Markham, Daniel J Twitchen, and Ronald Hanson. Optimized quantum sensing with a single electron spin using real-time adaptive measurements. *Nature Nanotechnology*, 11(3):247–252, 2015.

[14] Cristian Bonato, Machiel S Blok, Hossein T Dinani, Dominic W Berry, Matthew L Markham, Daniel J Twitchen, and Ronald Hanson. Optimized quantum sensing with a single electron spin using real-time adaptive measurements. *Nature nanotechnology*, 11(3):247–252, 2016.

[15] V. Bouchiat, D. Vion, P. Joyez, D. Esteve, and M. H. Devoret. Quantum coherence with a single cooper pair. T76(1):165.

[16] Henrik Brenning, Sergey Kafanov, Tim Duty, Sergey Kubatkin, and Per Delsing. An ultrasensitive radio-frequency single-electron transistor working up to 4.2 K. *Journal of Applied Physics*, 100(11):114321, 12 2006.

[17] Joan J. Caceres, Daniel Dominguez, and Maria Jose Sanchez. Fast quantum gates based on landau-zener-stückelberg-majorana transitions, 2023.

[18] Daniel L. Campbell, Yun-Pil Shim, Bharath Kannan, Roni Winik, David K. Kim, Alexander Melville, Bethany M. Niedzielski, Jonilyn L. Yoder, Charles Tahan, Simon Gustavsson, and William D. Oliver. Universal nonadiabatic control of small-gap superconducting qubits. *Phys. Rev. X*, 10:041051, Dec 2020.

[19] M. C. Cassidy, A. S. Dzurak, R. G. Clark, K. D. Petersson, I. Farrer, D. A. Ritchie, and C. G. Smith. Single shot charge detection using a radio-frequency quantum point contact. *Applied Physics Letters*, 91(22):222104, 11 2007.

[20] Jasper Chan, T. P. Mayer Alegre, Amir H. Safavi-Naeini, Jeff T. Hill, Alex Krause, Simon Groblacher, Markus Aspelmeyer, and Oskar Painter. Laser cooling of a nanomechanical oscillator into its quantum ground state. *Nature*, 478(7367):89–92, October 2011.

[21] Yanbei Chen. Macroscopic quantum mechanics: theory and experimental concepts of optomechanics. *Journal of Physics B*, 46(10):104001, 2013.

[22] Yiwen Chu, Prashanta Kharel, William H. Renninger, Luke D. Burkhart, Luigi Frunzio, Peter T. Rakich, and Robert J. Schoelkopf. Quantum acoustics with superconducting qubits. *Science*, 358(6360):199–202, 2017.

[23] Yiwen Chu, Prashanta Kharel, Taekwan Yoon, Luigi Frunzio, Peter T Rakich, and Robert J Schoelkopf. Creation and control of multi-phonon fock states in a bulk acoustic-wave resonator. *Nature*, 563(7733):666, 2018.

[24] Christian L Degen, Friedemann Reinhard, and Paola Cappellaro. Quantum sensing. *Reviews of Modern Physics*, 89(3):035002, 2017.

[25] Samuel Deleglise, Igor Dotsenko, Clement Sayrin, Julien Bernu, Michel Brune, Jean-Michel Raimond, and Serge Haroche. Reconstruction of non-classical cavity field states with snapshots of their decoherence. *Nature*, 455(7212):510–514, September 2008.

[26] F. Diedrich, J. C. Bergquist, Wayne M. Itano, and D. J. Wineland. Laser cooling to the zero-point energy of motion. *Phys. Rev. Lett.*, 62:403–406, Jan 1989.

[27] Lajos Diósi. Models for universal reduction of macroscopic quantum fluctuations. *Physical Review A*, 40(3):1165, 1989.

[28] Lajos Diósi. Notes on certain newton gravity mechanisms of wavefunction localization and decoherence. *Journal of Physics A*, 40(12):2989, 2007.

[29] G. J. Dolan. Offset mask for lift-off photoprocessing. *Appl. Phys. Lett.*, 31:337–339, 1977.

[30] Nathan Earnest, Srivatsan Chakram, Yao Lu, Nicholas Irons, Ravi K Naik, Nelson Leung, Leo Ocola, David A Czaplewski, Brian Baker, Jay Lawrence, et al. Realization of a λ system with metastable states of a capacitively shunted fluxonium. *PRL*, 120(15):150504, 2018.

[31] I. V. Fedotov, L. V. Doronina-Amitonova, A. A. Voronin, A. O. Levchenko, S. A. Zibrov, D. A. Sidorov-Biryukov, A. B. Fedotov, V. L. Velichansky, and A. M. Zheltikov. Robust all-optical single-shot readout of nitrogen-vacancy centers in diamond. *Nat. Commun.*, 4(5362), 2014.

[32] Francesco Fogliano, Benjamin Besga, Antoine Reigue, Philip Heringlake, Laure Mercier de Lépinay, Cyril Vaneph, Jakob Reichel, Benjamin Pigeau, and Olivier Arcizet. Cavity nano-optomechanics in the ultrastrong coupling regime with ultrasensitive force sensors. *arXiv:1904.01140*, 2019.

[33] K Geerlings, S Shankar, E Edwards, L Frunzio, RJ Schoelkopf, and MH Devoret. Improving the quality factor of microwave compact resonators by optimizing their geometrical parameters. *Applied Physics Letters*, 100(19), 2012.

[34] Mario F Gely, Marios Kounalakis, Christian Dickel, Jacob Dalle, Rémy Vatré, Brian Baker, Mark D Jenkins, and Gary A Steele. Observation and stabilization of photonic fock states in a hot radio-frequency resonator. *Science*, 363(6431):1072–1075, 2019.

[35] Mario F Gely and Gary A Steele. Superconducting electro-mechanics to explore the effect of general relativity in massive superpositions. *arXiv:2103.12729*, 2021.

[36] Mario F. Gely and Gary A. Steele. Superconducting electro-mechanics to test Diósi–Penrose effects of general relativity in massive superpositions. *AVS Quantum Science*, 3(3):035601, September 2021.

[37] Amir H Ghadimi, Sergey A Fedorov, Nils J Engelsen, Mohammad J Bereyhi, Ryan Schilling, Dalziel J Wilson, and Tobias J Kippenberg. Elastic strain engineering for ultralow mechanical dissipation. *Science*, 360(6390):764–768, 2018.

[38] GianCarlo Ghirardi, Renata Grassi, and Alberto Rimini. Continuous-spontaneous-reduction model involving gravity. *Physical Review A*, 42(3):1057, 1990.

[39] MF Gonzalez-Zalba, S Barraud, AJ Ferguson, and AC Betz. Probing the limits of gate-based charge sensing. *Nature Communications*, 6(1):6084, 2015.

[40] Peter Groszkowski and Jens Koch. Scqubits: a python package for superconducting qubits. *Quantum*, 5:583, November 2021.

[41] Serge Haroche and Jean-Michel Raimond. Oxford Univ. Press, 2006.

[42] Dominik M. Irber, Francesco Poggiali, Fei Kong, Michael Kieschnick, Tobias Lühmann, Damian Kwiatkowski, Jan Meijer, Jiangfeng Du, Fazhan Shi, and Friedemann Reinhard. Robust all-optical single-shot readout of nitrogen-vacancy centers in diamond. *Nat. Commun.*, 12(532), 2021.

[43] E Ivanov, T Capelle, M Rosticher, J Palomo, T Briant, P-F Cohadon, A Heidmann, T Jacqmin, and S Deléglise. Edge mode engineering for optimal ultracoherent silicon nitride membranes. *Appl. Phys. Lett.*, 117(25):254102, 2020.

[44] Dustin Kleckner, Igor Pikovski, Evan Jeffrey, Luuk Ament, Eric Eliel, Jeroen Van Den Brink, and Dirk Bouwmeester. Creating and verifying a quantum superposition in a micro-optomechanical system. *NJP*, 10(9):095020, 2008.

[45] Jens Koch, M Yu Terri, Jay Gambetta, Andrew A Houck, David I Schuster, Johannes Majer, Alexandre Blais, Michel H Devoret, Steven M Girvin, and Robert J Schoelkopf. Charge-insensitive qubit design derived from the cooper pair box. *Physical Review A*, 76(4):042319, 2007.

[46] Alexander N. Korotkov and Mikko A. Paalanen. Charge sensitivity of radio frequency single-electron transistor. *Applied Physics Letters*, 74(26):4052–4054, 06 1999.

[47] Nathan R. A. Lee, Yudan Guo, Agnetta Y. Cleland, E. Alex Wollack, Rachel G. Gruenke, Takuma Makihara, Zhaoyou Wang, Taha Rajabzadeh, Wentao Jiang, Felix M. Mayor, Patricio Arrangoiz-Arriola, Christopher J. Sarabalis, and Amir H. Safavi-Naeini. Strong dispersive coupling between a mechanical resonator and a fluxonium superconducting qubit, 2023.

[48] Raphaël Lescanne. *Engineering multi-photon dissipation in superconducting circuits for quantum error correction.* Theses, Université Paris sciences et lettres, February 2020.

[49] Goran Lindblad. On the generators of quantum dynamical semigroups. *Communications in Mathematical Physics*, 48:119–130, 1976.

[50] Wei Lu, Zhongqing Ji, Loren Pfeiffer, KW West, and AJ Rimberg. Real-time detection of electron tunnelling in a quantum dot. *Nature*, 423(6938):422–425, 2003.

[51] Xizheng Ma, Jeremie J Viennot, Shlomi Kotler, John D Teufel, and Konrad W Lehnert. Non-classical energy squeezing of a macroscopic mechanical oscillator. *Nature Physics*, 17(3):322–326, 2021.

[52] Vladimir E Manucharyan, Jens Koch, Leonid I Glazman, and Michel H Devoret. Fluxonium: Single cooper-pair circuit free of charge offsets. *Science*, 326(5949):113–116, 2009.

[53] Vladimir Eduardovich Manucharyan. *Superinductance*. Phd thesis, Yale university, May 2012. Available at `https://qulab.eng.yale.edu/theses/`.

[54] Zlatko K. Minev, Zaki Leghtas, Shantanu O. Mundhada, Lysander Christakis, Ioan M. Pop, and Michel H. Devoret. Energy-participation quantization of josephson circuits, 2021.

[55] B.-L. Najera-Santos, R. Rousseau, K. Gerashchenko, H. Patange, A. Riva, M. Villiers, T. Briant, P.-F. Cohadon, A. Heidmann, J. Palomo, M. Rosticher, H. le Sueur, A. Sarlette, W. C. Smith, Z. Leghtas, E. Flurin, T. Jacqmin, and S. Deléglise. High-sensitivity ac-charge detection with a mhz-frequency fluxonium qubit. *Phys. Rev. X*, 14:011007, Jan 2024.

[56] Leonhard Neuhaus, Samuel Deleglise, and P.-F. Cohadon. Laser cooling of a planck mass object close to the quantum ground state. *arXiv:2104.11648, in review PRL*, 2021.

[57] Michael A Nielsen and Isaac L Chuang. *Quantum computation and quantum information*, volume 2. Cambridge university press Cambridge, 2001.

[58] Tjerk H Oosterkamp and Jan Zaanen. A clock containing a massive object in a superposition of states; what makes penrosian wavefunction collapse tick? *arXiv:1401.0176*, 2013.

[59] A. D. O'Connell, M. Hofheinz, M. Ansmann, Radoslaw C. Bialczak, M. Lenander, Erik Lucero, M. Neeley, D. Sank, H. Wang, M. Weides, J. Wenner, John M. Martinis, and A. N. Cleland. Quantum ground state and single-phonon control of a mechanical resonator. *Nature*, 464(7289):697–703, April 2010.

[60] Roger Penrose. On gravity's role in quantum state reduction. *Gen. Relativity and Gravitation*, 28(5):581–600, 1996.

[61] Eric Planz, Xiang Xi, Thibault Capelle, Eric C. Langman, and Albert Schliesser. Membrane-in-the-middle optomechanics with a soft-clamped membrane at millikelvin temperatures. *Optics Express*, 31(25):41773, November 2023.

[62] Emanuele Polino, Mauro Valeri, Nicolò Spagnolo, and Fabio Sciarrino. Photonic quantum metrology. *AVS Quantum Science*, 2(2), 2020.

[63] Norman F Ramsey. A molecular beam resonance method with separated oscillating fields. *Physical Review*, 78(6):695, 1950.

[64] DJ Reilly, CM Marcus, MP Hanson, and AC Gossard. Fast single-charge sensing with a rf quantum point contact. *Applied Physics Letters*, 91(16), 2007.

[65] Massimiliano Rossi, David Mason, Junxin Chen, Yeghishe Tsaturyan, and Albert Schliesser. Measurement-based quantum control of mechanical motion. *Nature*, 563(7729):53–58, 2018.

[66] D Rugar, R Budakian, H J Mamin, and B W Chui. Single spin detection by magnetic resonance force microscopy. *Nature*, 430(6997):329–332, jul 2004.

[67] Kevin Joseph Satzinger, YP Zhong, H-S Chang, Gregory A Peairs, Audrey Bienfait, Ming-Han Chou, AY Cleland, Cristopher R Conner, Étienne Dumur, Joel Grebel, et al. Quantum control of surface acoustic-wave phonons. *Nature*, 563(7733):661–665, 2018.

[68] RJ Schoelkopf, P Wahlgren, AA Kozhevnikov, P Delsing, and DE Prober. The radio-frequency single-electron transistor (rf-set): A fast and ultrasensitive electrometer. *Science*, 280(5367):1238–1242, 1998.

[69] Yannick Seis, Thibault Capelle, Eric Langman, Sampo Saarinen, Eric Planz, and Albert Schliesser. Ground state cooling of an ultracoherent electromechanical system. *Nature Communications*, 13(1):1507, 2022.

[70] JOHN A Sidles, JOSEPH L Garbini, KJ Bruland, D Rugar, O Züger, S Hoen, and CS Yannoni. Magnetic resonance force microscopy. *Rev. of Mod. Phys.*, 67(1):249, 1995.

[71] W. C. Smith, A. Kou, U. Vool, I. M. Pop, L. Frunzio, R. J. Schoelkopf, and M. H. Devoret. Quantization of inductively shunted superconducting circuits. *Physical Review B*, 94(14), October 2016.

[72] J. D. Teufel, T. Donner, Dale Li, J. W. Harlow, M. S. Allman, K. Cicak, A. J. Sirois, J. D. Whittaker, K. W. Lehnert, and R. W. Simmonds. Sideband cooling of micromechanical motion to the quantum ground state. *Nature*, 475(7356):359–363, July 2011.

[73] John D Teufel, Dale Li, MS Allman, K Cicak, AJ Sirois, JD Whittaker, and RW Simmonds. Circuit cavity electromechanics in the strong-coupling regime. *Nature*, 471(7337):204–208, 2011.

[74] Yeghishe Tsaturyan, Andreas Barg, Eugene S Polzik, and Albert Schliesser. Ultracoherent nanomechanical resonators via soft clamping and dissipation dilution. *Nature Nanotechnology*, 12(8):776, 2017.

[75] E. Verhagen, S. Deleglise, S. Weis, A. Schliesser, and T. J. Kippenberg. Quantum-coherent coupling of a mechanical oscillator to an optical cavity mode. *Nature*, 482(7383):63–67, February 2012.

[76] J. J. Viennot, M. R. Delbecq, M. C. Dartiailh, A. Cottet, and T. Kontos. Out-of-equilibrium charge dynamics in a hybrid circuit quantum electrodynamics architecture. *Phys. Rev. B*, 89:165404, Apr 2014.

[77] J. J. Viennot, X. Ma, and K. W. Lehnert. Phonon-number-sensitive electromechanics. *PRL*, 121:183601, Oct 2018.

[78] Christian Volk, Anasua Chatterjee, Fabio Ansaloni, Charles M. Marcus, and Ferdinand Kuemmeth. Fast charge sensing of si/sige quantum dots via a high-frequency accumulation gate. *Nano Letters*, 19(8):5628–5633, 2019.

[79] Zhiren Wang, Léo Balembois, Milos Rančić, Eric Billaud, Marianne Le Dantec, Alban Ferrier, Philippe Goldner, Sylvain Bertaina, Thierry Chanelière, Daniel Estève, Denis Vion, Patrice Bertet, and Emmanuel Flurin. Single-electron spin resonance detection by microwave photon counting. *Nature*, 619:276–281, 2023.

[80] P.-L. Yu, T. P. Purdy, and C. A. Regal. Control of material damping in high-q membrane microresonators. *Physical Review Letters*, 108:083603, Feb 2012.

[81] Helin Zhang, Srivatsan Chakram, Tanay Roy, Nathan Earnest, Yao Lu, Ziwen Huang, DK Weiss, Jens Koch, and David I Schuster. Universal fast-flux control of a coherent, low-frequency qubit. *Physical Review X*, 11(1):011010, 2021.

[82] Guanyu Zhu, David G Ferguson, Vladimir E Manucharyan, and Jens Koch. Circuit qed with fluxonium qubits: Theory of the dispersive regime. *Physical Review B*, 87(2):024510, 2013.

[83] T. Yu et al ZZ. Li, CH. Lam. Detector-induced backaction on the counting statistics of a double quantum dot. *Scientific Reports*, 3026(3), October 2013.